Jagiellonian University
Faculty of Physics, Astronomy and Applied Computer Science

Doctoral Thesis

# Development of positronium imaging with the 192-strip J-PET detector

Author:
Kamil Dulski

Supervisor: Prof. dr hab. Paweł Moskal
Co-Supervisor: Dr hab. Bożena Jasińska, prof. UMCS

Kraków
May 2, 2022

Wydział Fizyki, Astronomii i Informatyki Stosowanej
Uniwersytet Jagielloński

# Oświadczenie

Ja niżej podpisany Kamil Dulski (nr indeksu 1077826), doktorant Wydziału Fizyki, Astronomii i Informatyki Stosowanej Uniwersytetu Jagiellońskiego oświadczam, że przedłożona przeze mnie ropzrawa doktorska pt. "Development of positronium imaging with the 192-strip J-PET detector" jest oryginalna i przedstawia wyniki badań wykonanych przeze mnie osobiście, pod kierunkiem prof. dr hab. Pawła Moskala oraz dr hab. Bożenę Jasińską, prof. UMCS. Prace napisałem samodzielnie.

Oświadczam, że moja rozprawa doktorska została opracowana zgodnie z Ustawą o prawie autorskim i prawach pokrewnych z dnia 3 lutego 1994 r. (Dziennik Ustaw 1994 nr 24 poz.83 wraz z późniejszymi zmianami).

Jestem świadom, że niezgodność niniejszego oświadczenia z prawdą ujawniona w dowolnym czasie, niezależnie od skutków prawnych wynikających z ww. ustawy, może spowodować unieważnienie stopnia nabytego na podstawie tej rozprawy.

Kraków, dnia Podpis autora pracy

"*People are like stained - glass windows.*
*They sparkle and shine when the sun is out, but when the darkness sets in,*
*their true beauty is revealed only if there is a light from within.*"

- dr. Elisabeth Kubler-Ross

# Abstract

The thesis describes the basics of a new imaging technique - positronium imaging. Positronium imaging is a technique that combines the metabolic information obtained in a standard Positron Emission Tomography (PET) scan with the structural indices examined by the Positron Annihilation Lifetime Spectroscopy (PALS) technique. In particular, proof of concept of the positronium imaging, by means of the 192-strip J-PET detector is presented.

A research hypothesis was formulated which stated that it is possible to simultaneously measure the distribution of the radioisotope inside the sample and to determine the structural index (mean ortho-positronium lifetime) in each part of the sample. According to this hypothesis, it is possible to distinguish samples with a different structure. Therefore, positronium imaging can find application not only in PET scans by delivering additional information, potentially improving PET diagnosis effectiveness, but also in material research as a technique to characterize the nanostructure in every part of the large sample.

In order to demonstrate that positronium imaging can be an important technique and prove the research hypothesis, comprehensive studies were carried out using the 192-strip J-PET detector. To ensure the high quality of the collected data, the J-PET detector was calibrated for time and position reconstruction, and a set of data selection conditions was developed. It was also checked how developed selection criteria and dedicated measurement simulations reflect the measurement conditions and at the same time maintain high purity of the data sample. In order to check how well the J-PET detector is able to examine the properties of positronium, an additional analysis was carried out in terms of the separation of various states and types of positronium decay. The results of the analysis shows the possibilities of the J-PET detector in the context of fundamental studies, on the example of the precise determination of the ortho-positronium decay constant.

The main part of the work focuses on testing the research hypothesis on two systems that covered two potential applications of positronium imaging - material and medical studies. The positronium image of a system composed of samples of different porosity shows that it is possible to distinguish the samples in terms of structure, despite the lack of visible differences on the analogue to the standard image of annihilation density distribution. The developed method of estimating the mean o-Ps lifetime for single voxels allows to obtain quite good agreement, even for voxels with a relatively low o-Ps intensity. A clear separation in terms of structure is also presented in the positronium image from the in-vitro measurement of the human tissues. Measurement setup consisted of four samples of two types of tissue - cardiac myxoma and adipose tissue. Despite relatively low differences in the mean lifetime of o-Ps, the positronium image of these samples also confirms the research hypothesis, successfully separating different types of tissues, with quite good compatibility of tissues of the same type.

# Streszczenie

Praca opisuje podstawy nowej techniki obrazowania - obrazowania pozytonium. Obrazowanie pozytonium to technika, która łączy ze sobą informacje metaboliczne uzyskane w standardowym skanie PET i wskaźniki strukturalne badane przez technikę PALS. W szczególności w pracy przedstawiona jest koncepcja obrazowania pozytonium za pomocą 192-paskowego detektora J-PET.

Sformułowano hipotezę badawczą, zgodnie z którą możliwe jest jednoczesne zmierzenie rozmieszczenia radioizotopu wewnątrz próbki oraz wyznaczenie wskaźnika strukturalnego (średniego czasu życia orto-pozytonium) w każdym obszarze próbki. Zgodnie z tą hipotezą możliwe jest rozróżnienie próbek o różnej strukturze. Obrazowanie pozytonium może więc znaleźć zastosowanie nie tylko w skanach PET przez dostarczenie dodatkowej informacji, potencjalnie poprawiając skuteczność diagnostyki PET, ale także w badaniach materiałowych jako technika charakteryzowania nanostruktury w każdej części dużej próbki.

Aby wykazać, że obrazowanie pozytonium może być ważną techniką i udowodnić hipotezę badawczą, przeprowadzono kompleksowe badania z użyciem 192-paskowego detektora J-PET. Aby zapewnić wysoką jakość zebranych danych, przeprowadzono kalibrację detektora J-PET pod kątem rekonstrukcji czasu i położenia oraz opracowano zestaw warunków selekcji danych. Sprawdzono również, jak dobrze opracowane kryteria selekcji i dedykowane symulacje pomiarowe odzwierciedlają warunki pomiaru przy jednoczesnym zachowaniu wysokiej czystości próbki danych. Aby sprawdzić, na ile dobrze detektor J-PET jest w stanie badać właściwości pozytonium, przeprowadzono dodatkową analizę pod kątem separacji różnych stanów i rodzajów rozpadu pozytonu. Wyniki analizy pokazują możliwości detektora J-PET w kontekście badań podstawowych, na przykładzie precyzyjnego wyznaczenia stałej rozpadu orto-pozytonium.

Główna część pracy koncentruje się na przetestowaniu hipotezy badawczej na dwóch systemach obejmujących dwa potencjalne zastosowania obrazowania pozytonium - badań materiałowych i medycznych. Obraz pozytonium układu złożonego z próbek o różnej porowatości wykazał, że możliwe jest rozróżnienie próbek pod względem struktury, pomimo braku widocznych różnic na analogu do standardowego obrazu rozkładu gęstości anihilacji. Opracowana metoda szacowania średniego czasu życia o-Ps dla pojedynczych wokseli pozwala na uzyskanie dość dobrej zgodności, nawet dla wokseli o stosunkowo niskiej intensywności o-Ps. Wyraźna separacja pod względem struktury jest przedstawiona również na obrazie pozytonium z pomiaru in-vitro tkanek ludzkich. Układ badawczy składał się z czterech próbek i dwóch typów tkanek – śluzaka serca i tkanki tłuszczowej. Pomimo stosunkowo niewielkich różnic w średnim czasie życia o-Ps, obraz pozytonium tych próbek również potwierdza hipotezę badawczą, z powodzeniem rozróżniając różne typy tkanek, przy dość dobrej zgodności dla tkanek tego samego typu.

# Acknowledgement

I would like to express my gratitude to the people without whom this work would not be possible.

First and foremost, I would like to thank Prof. Paweł Moskal for the opportunity to work in J-PET collaboration, in particular with the J-PET detector and participate in the development of positronium imaging. I am especially grateful to Prof. Moskal for support, guidance, motivation and help in understanding and solving any problems that I encountered during my research. Help from Prof. Moskal was invaluable, without which this work would not reach its final shape. I would also like to thank Prof. Jasińska for introducing me to the world of positron lifetime spectroscopy, which was crucial to fully understand the phenomenon of positronium annihilation.

Thanks to my colleagues from the J-PET collaboration for their help and useful suggestions for my research. I would especially like to distinguish dr. Ewelina Kubicz for her exceptional help which introduced me to J-PET collaboration and research. Cooperation with Ewelina on the assembly and commissioning of the system for positron lifetime spectroscopy allowed me to develop in many fields, including the operation of detectors, analysis of experimental data and approaches to their treatment. I have always been able to count on her in testing my analysis software, and her positive attitude, persistence and friendship helped me a lot during my research. I would also like to highlight dr. Michał Silarski, dr. Sushil Sharma, dr. Aleksander Gajos and dr. Wojciech Krzemień. Their support, help in the analysis, very helpful suggestions and comments allowed me to greatly improve the quality of my research. Thanks to them, I could always count on extremely interesting and useful conversations and a friendly atmosphere.

I would like to extend my thanks to Prof. Zbigniew Rudy and Prof. Steven Bass. A useful suggestion from Prof. Rudy and especially his recommendations helped me achieve my research goals. I could also always count on the help of Prof. Bass in terms of consultation and publication of research results. I would also like to mention Dr. Anna Wieczorek, who helped me introducing into the J-PET collaboration and helped me understand the operation of scintillators. I would also like to thank Dr. Bożena Zgardzińska for help in analyzing positron lifetime spectra, which significantly translated into the development of my software for decomposition of positron lifetime spectra.

I also have to thank my friends from studies: Ania, Dariusz, Natalia Łukasz, Piotrek, Weronika and Wojtek and also those I met in other circumstances: Adam, Ania, Justyna, Magda and Tomasz. I have always been able to count on you. Your friendship was and is invaluable to me.

Special thanks and words of gratitude to my family, especially to my mother, sister and grandparents, without whom I could not even think about going to university or doing my doctoral studies. Their support in every aspect over my whole life has translated directly into who I am. Thank you for all their sacrifices that helped me achieve my goals.

My final thanks go to one of the most important person - Monika. Your appearance in my life was the best thing that happened to me and it has helped me and still helps me achieve full happiness. With you, I feel that I can still develop both scientifically and as a human being.

For the sake of completeness, I would also like to thank the funding sources that have allowed my PhD research to be conducted. In particular, this work was supported by the Polish National Science Centre through grants no. 2019/35/B/ST2/03562 and 2021/41/N/ST2/03950, and by the Foundation for Polish Science through the TEAM POIR.04.04.00-00-4204/17 programme.

# Contents

# Introduction

The main objective of the study is to prove that the positronium imaging [1–3] can be successfully used as a separate technique allowing to study the structure in different parts of the sample larger than the voxel size. The positronium imaging characteristics will be presented with the 192-strip J-PET detector [4–6].

Positron Emission Tomography (PET), that is based on the positron-electron annihilation, finds an application in the diagnosis of the metabolic changes in the tissues. Neoplastic tissues in the human body are diagnosed by using PET based on higher density of the radiopharmaceutical labeled with positron emitter. Higher density is implied from a surplus of positrons in a given area correlated with higher metabolism rate ot the malignant cells. The number of positrons in a given area can be estimated from the number of events associated with that area, based on the reconstructed position of the annihilation. The position reconstruction is carried out on the basis of the registration of photons that are formed during the annihilation of a positron with an electron. The registration of a photon may correspond to the position of the detector itself (standard PET), in which it deposited energy, or the position combined with the time of arrival of a given photon to the detection module (Time-of-Flight PET). Therefore, the high spatial resolution of the obtained PET and TOF-PET images is conditioned by the size and large number of detection modules and by the high precision of the timing of the signals, respectively [8,9]. In addition, an important factor in the quality of the obtained images is the correct distinction between primary and scattered photons on the basis of energy deposition in the detection modules. For this reason, the only detectors used in commercial PET scanners are inorganic detectors, in which the energy selection is mainly based on the photoelectric effect, allowing for precise differentiation of primary annihilation photons.

The main objective in the development of the PET scanners is to improve quality of the obtained images, by achieving better and better spatial resolution. To achieve this, solutions using more precise detection elements, faster data acquisition systems, more effective reconstruction algorithms and new configurations are proposed [9–11]. On the other hand, the effectiveness of PET scans as a diagnostic basis results not only from how well the image of the patient's metabolism is reconstructed, but also from how specific and selective contrasts are used during the examination. For now, several types of contrasts, mainly based on $^{18}$F, are used for PET scans based on various radioactive isotopes and their carriers, which allow the selective imaging of various organs of the patient, such as for example lungs or prostate [12]. Recent results show that the additional contrast may come from the positron itself, based on its lifetime in the part of the patient tested in the so-called positronium imaging

[2,3]. The positronium imaging developed for TOF-PET scanners requires the use of specific radioisotopes, like for example $^{44}$Sc or $^{66}$Ga, that emit an additional photon [13–15] just after positron emission which can be used as a start signal and in effect allows the lifetime of individual positrons to be measured. It should be emphasized that positronium imaging could be performed together with a standard PET scan, which would not increase the radiation dose to which the patient is exposed during the examination. The use of additional contrast derived from the average lifetime of positrons may allow to increase the effectiveness of diagnostics based on PET images.

In order for positronium imaging to be realized, the PET scanner should be characterized by a very good time resolution of the detectors (in the order of 100 ps) to properly estimate positron lifetime and have data acquisition system (DAQ) to detect multiple photons coming from a single event. The answer to this demand is the J-PET detector consisting of many detection modules based on long plastic scintillating strips, ensuring a relatively large detection area - 0.14 m$^3$ for the 192-strip prototype [4–6] and 1 m$^3$ for total-body design [7]. Despite the fact that organic scintillators, such as plastic scintillators used in the J-PET detector, do not allow for precise measurement of the photons energy (practically only by Compton effect), their high time resolution (in the order of 150 ps) allows to maintain high imaging resolution, and additional estimation of the time duration of the signals can be a successful energy discriminator [16]. DAQ based on FPGA architecture allows the J-PET detector to operate in trigger-less mode [17, 18], which ensures multi-photon detection and reconstruction during a single event. In addition, the study of positron-electron annihilation through the Compton effect, and thus scattered photons, allow the J-PET detector to extend basic imaging application to include research on basic interactions in matter [19–24].

In addition to the medical use of positron, the mean lifetime of the positron-electron bound state (positronium), is also an extremely sensitive structural indicator in materials research. The dependence of the mean lifetime of ortho-positronium (o-Ps) on the radius of free volumes (pores) is the basis of the Positron Annihilation Lifetime Spectroscopy (PALS) [25–28]. This allows not only to characterize the porosity in the tested sample, but also to study changes in structure as a function of temperature or pressure, and in particular to determine the conditions of phase transitions. This has found several application in the study of porous materials, defects and the characterization of thin layers of dielectrics [27–29].

For the purposes of the study, a research hypothesis was formulated that positronium imaging can be used to simultaneously measure the distribution of the radioisotope inside the sample and to determine the structural index, coming from the mean o-Ps lifetime in each part of the sample. Hypothesis was tested by means of the 192-strip prototype of the J-PET detector [6]. The research hypothesis can be additionally extended in the field of diagnostics by the statement that positronium lifetime can serve as an additional indicator differentiating various types of tissues, and in particular distinguishing neoplastic tissues from normal ones. It will be shown that the positronium imaging, created by the J-PET detector is sensitive to differences in structure between exemplary tissues, measured in-vitro - cancer (cardiac myxoma) and normal (adipose tissue) [1, 30].

Thesis is divided into 6 chapters. Chapter 1 will briefly introduce the topic of positron, positronium and their interactions with matter. Special emphasis will be placed on the dif-

ferences between the two positronium states - para-positronium and ortho-positronium. In addition, a short description of techniques that benefit from positron-electron annihilation - PET, PALS will be given along with the idea of connection of those two techniques by means of positronium imaging. Next, in Chapter 2 the experimental description of the J-PET detector used for positronium imaging will be covered. In particular, its construction, data reconstruction and analysis will be discussed in more detail. In Chapter 3, a detailed procedures for time and position calibration will be presented. Results from the calibration of the J-PET detector will be also shown, with additional discussion of the obtained resolution parameters. Chapter 4 presents the evaluation of the developed analysis methods and algorithms, that were used in the data reconstruction and in the final analysis. In addition, the sensitivity of the J-PET detector and purity of the data sample will be assessed at different stages of the analysis, along with the differentiation of background types. Chapter 5 will show the first results of the positronium properties analysis based on the measurement with the J-PET detector. The method of selecting different positronium decay channels will be shown first, following the positron lifetime distributions for different types of events. By using the position reconstruction methods, the resulting distributions of annihilation points for the decays of positronium into two and three photons will be presented. At the end of the chapter, comparing the positron lifetime distributions for different decays will allow an estimate of the ortho-positronium decay constant. The last, Chapter 6 will show the final results of the thesis covering the topic of the positronium imaging with the J-PET detector and allow to test the research hypothesis. The positronium images for two different phantoms will show the possibilities of the J-PET detector for the analysis of positronium images and answer the question about their usefulness in the context of structural imaging. The two phantoms used consisted of three materials of different porosity (IC3100, XAD4 and PVT) and two types of tissues (cardiac myxoma and adipose tissue), respectively. Optimized selection criteria for the positronium imaging allowed to obtain clear image of the annihilation points, reducing most of the scatterings from the data sample and preserving most of the pure data sample. The thesis is supplemented with Appendices, which present supplementary data on the results of the analysis described in this thesis.

Author's contribution:
Taking part in construction, commissioning, evaluation, investigations and maintenance of the J-PET detector and experimental setup construction. Taking part in design and development of the data and position reconstruction algorithms, Framework and J-PET Monte Carlo software. Taking part in measurement data collection and data curation.
Author of the thesis designed and developed the PALS Avalanche software (A,B), and use it to decompose positron lifetime spectra (C). In addition, author designed iterative position reconstruction algorithm for the reconstruction of the annihilation positions. Author also designed, implemented and performed the time, position and light velocity calibration for the J-PET detector (D,E). Author validated the analysis and simulation software used for the purposes of this thesis (F). It allowed the author also to generate and analyze the simulated data for the XAD4 measurement on the J-PET detector (F). Author also designed and implemented the data selection and scattering attenuation criteria and performed initial and final data analysis (F,G,H,I). Author estimated the background sources in the final data sample (F) and ortho-positronium decay rate. In addition, author designed the positronium imaging phantoms and implemented the positronium imaging algorithms (J).
Articles and patent in which the author of the thesis is the main or one of the main authors:

(A) K. Dulski, B. Zgardzińska, P. Białas et al., Analysis procedure of the positronium lifetime spectra for the J-PET detector. Acta Phys. Pol. A 132, 1637-1640 (2017)

(B) K. Dulski, PALS Avalanche - A New PAL Spectra Analysis Software. Acta Phys. Pol. A 137, 167-170 (2020)

(C) Z. Bura, K. Dulski, E. Kubicz, et al., Studies of the ortho-Positronium lifetime for cancer diagnostic. Acta Phys. Pol. B 51, 377-382 (2020)

(D) K. Dulski, P. Moskal, System i sposób kalibracji czasowej układu detekcyjnego tomografu ToF-PET, Polish patent number: PL434697

(E) K. Dulski, M. Silarski and P. Moskal, A method for time calibration of PET systems using fixed $\beta+$ radioactive source. Acta Phys. Pol. B 51, 195-200 (2020)

(F) K. Dulski, S.D. Bass, J. Chhokar et al., The J-PET detector - a tool for precision studies of ortho-positronium decays. Nucl. Instr. and Meth. A 1008, 165452 (2021)

(G) K. Dulski, C. Curceanu, E. Czerwiński et al., Commissioning of the J-PET detector in view of the positron annihilation lifetime spectroscopy. Hyperfine Interact. 239, 40-45 (2018)

(H) J. Raj, K. Dulski and E. Czerwiński, Towards time reversal symmetry test with o-Ps decays using the J-PET detector. Acta Phys. Pol. B 51, 149-152 (2020)

(I) E. Czerwiński, K. Dulski, P. Białas et al., Comissionning of the J-PET detector for studies of decays of positronium atoms. Acta Phys. Pol. B 47, 1961-1968 (2016)

(J) P. Moskal, K. Dulski, N. Chug et al., Positronium imaging with the novel multiphoton PET scanner Science Advances 7, eabh4394 (2021)

# Chapter 1

# Positronium and positronium imaging

## 1.1 Positron, positronium

The first confirmed discovery of a positron (antielectron) was in 1932 by Carl Anderson, while he was studying cosmic radiation [31]. Tracks on a lead plate with a curvature opposite to the electron allowed to identify antimatter for the first time. It opened a new chapter in particle physics, allowing to discover more antiparticles like antiproton and antineutron and to form new kind of the atoms - antiatoms. Antimatter provided a new insight in the studies of the fundamental physics, new elementary particles and interactions between them [32–34].

Experimentally, the three most common ways to create a positron are by radioactive decay, muon decay or by pair production. The type of radioactive decay that causes positron emission is the $\beta^+$ decay, in which one of the protons of the atomic nucleus turns into a neutron with emission of a positron and an electron neutrino ($\nu_e$). $\beta^+$ decay can occur when the number of protons is too high to maintain the stability of the nucleus. Examples of isotopes that can undergo a $\beta^+$ decay are: $^{18}$F, $^{22}$Na, $^{83}$Sr, $^{89}$Zr and $^{124}$I. A positron can also be formed during the decay of a antimuon (positive muon, $\mu^+$), which occurs as follows: $\mu^+ \rightarrow e^+ + \nu_e + \overline{\nu}_\mu$, where $e^+$ is positron, $\nu_e$ is electron neutrino and $\overline{\nu}_\mu$ is muon antineutrino. On the other hand, pair production can occur when an incoming high-energy photon interacts with matter. When the photon has energy greater than sum of the the rest masses of the resulting particles and is near a nucleus, a particle-antiparticle pair may be formed. The energy of 1022 keV is needed to generate the electron-positron pair, which can be obtained, for example, with high-energy lasers [35].

Positron as an antiparticle of an electron ($e^-$), shares the same mass ($m_e = 511\frac{\text{keV}}{c^2}$), spin ($s = 1/2$) and charge with it, differing only in the sign of the charge ($q_{e^+} = +e = -q_{e^-}$). Opposite charges allow the positron-electron pair to form an hydrogen-like bound state called Positronium (Ps), what was first experimentally confirmed by Martin Deutsch in 1951 [36]. It is worth noting that depending on the medium in which the positronium is formed, the positron energy range is determined for which the positronium creation is favored - the so-called Ore gap [37, 38]. Positronium as a two-body system has similar energy level structure to hydrogen with the Bohr radius twice as large as hydrogen, $r_b = 0.106$ nm. The combination of positron and electron spins allows for the formation of positronium in one of two states differing in the total spin ($S$). These two states can be distinguished as para-Positronium

(p-Ps, $S = 0$) and ortho-Positronium (o-Ps, $S = 1$). In theory, due to the spin statistic o-Ps is formed three times more often than p-Ps (Fig.1.1).

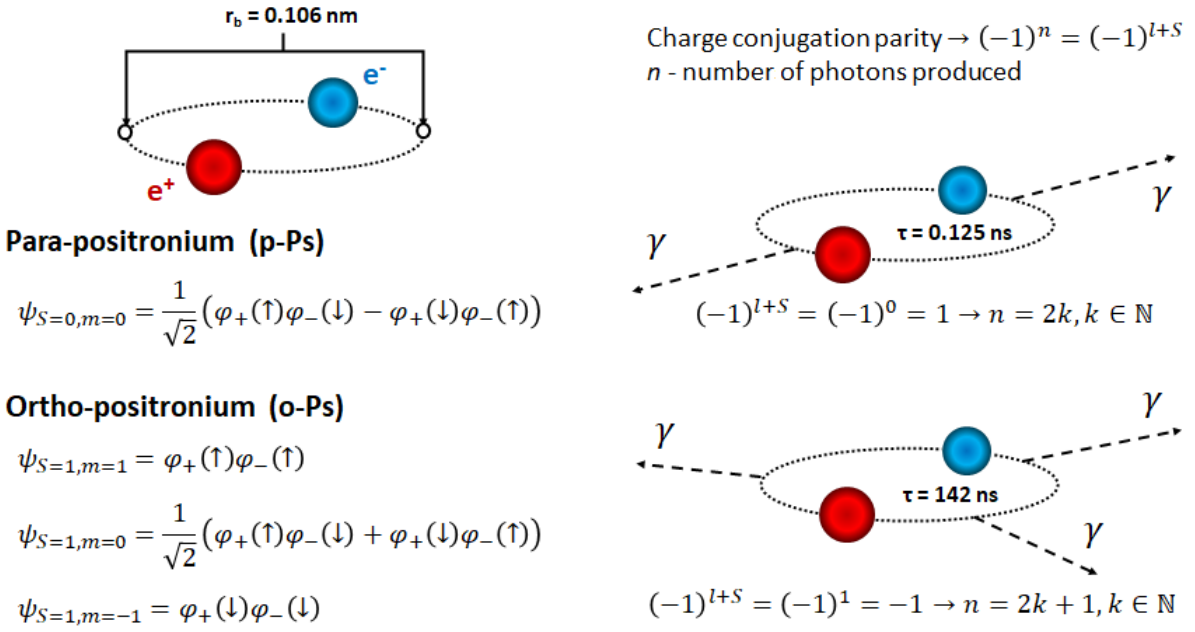


Figure 1.1: **Scheme of the positronium and its decay**. Positronium (Ps) composed of a positron ($e^+$) and an electron ($e^-$) can be formed in one of the two states - para-positronium (p-Ps) and ortho-positronium (o-Ps). P-Ps is formed when the total spin of the resulting positronium is equal to zero. This is true for one combination, expressed by $\psi_{S=0,m=0}$. In contrast, o-Ps has total spin equal to one, fulfilled for three wave functions $\psi_{S=1,m=1}$, $\psi_{S=1,m=0}$, $\psi_{S=1,m=-1}$. Due to the charge conjugation parity even number of photons ($\gamma$) are emitted when p-Ps annihilates and odd number of photons ($\gamma$) are emitted in case of o-Ps. In a vacuum mean lifetime of the ground states of p-Ps and o-Ps are equal to 0.125 ns and 142 ns, respectively.

Spin-spin interactions make para-positronium slightly lighter. Calculations of the cross-sections of the annihilation of free positrons with electrons [39, 40] lead to the estimation of the mean lifetime of the ground state p-Ps to 0.125 ns in vacuum, for slow positrons. On the other hand, based on the energy spectrum calculations for slow positrons , mean lifetime of the ground state of the o-Ps was estimated theoretically to 142 ns [41, 42]. From the charge conjugation symmetry conservation, it can be concluded that p-Ps annihilates with the emission of an even number of photons, while o-Ps annihilates with the emission of an odd number of photons. It is based on a fact, that on one side charge parity eigenvalue for positronium is given by $(-1)^{l+S}$, when on the other hand each photon contributes by a factor of $(-1)$. Therefore, comparing primary (positronium) and final (photons) states conjugation parity can be described as

$$(-1)^{l+S} = (-1)^n ,$$

where $l$ is the orbital angular momentum of positronium, $S$ is its total spin and $n$ is the number of photons emitted after the positronium annihilation. Properties of positronium are

summarized graphically in Fig. 1.1. In addition, rest mass of the positronium is equal to double mass of the electron ($m_{Ps} = 2m_e$) what determines the energy of the photon in case of the decay into two photons (both with energy of 511 keV) or the decays into more photons (that has the sum of the energies equal to the $m_{Ps}$). Positron-electron pair can also annihilate directly, without formation of the positronium. In case of direct annihilations, the ratio of three-quanta annihilation to two-quantum annihilation is equal to 1/378 [41, 43].

## 1.2 Positronium formation models

The positronium formation, as well as the positron-sample interaction itself, does not occur in the same way in every medium. In particular, three models can be distinguished for the description of the positronium formation - Ore, spur and blob. Historically, the first was the Ore model [37]. It is based on the simple consideration of ionization by a positron of a single molecule, creating a positronium with an electron detached from the atom. It is often expressed by process $e^{+,*} + X \rightarrow Ps + X^+$, where $e^{+,*}$ is positron with enough energy to ionize an atom X and form positronium (Ps) afterwards. This leads to the following definition of the energetic condition for the positronium to be formed: $E_{e^+} > I - E_b$, where $E_{e^+}$ is the energy of the positron, I is the ionization energy and $E_b$ is the binding energy of the positronium ($E_b = 6.8$ eV in vacuum). In addition, an upper bound on positron energy is also defined, below which it is possible (preferred) to form a positronium: $E_{ex} > E_{e^+}$, where $E_{ex}$ is the minimal energy of the electronic excitations. This is due to the fact that above the $E_{ex}$, ionization and excitations of the medium will dominate, which will reduce rapidly the chance of positronium creation. In this way, for each medium, it is possible to define the interval $(I - E_b, E_{ex})$ for which it will be possible (preferred) to form a positronium, the so-called Ore gap. This approach has been used successfully in the description of positronium formation in simple low-density gases [44, 45].

For other media, like especially condensed matter other models are proposed - spur [46, 47] and blob [48,49]. They are based on a similar assumption that a positron forms a positronium with one of the electrons at the end of the positron ionization track. In comparison to the Ore model, an additional effects from the denser presence of the molecules in condensed matter are contemplated. In particular, the repulsive interactions of atomic nuclei and the shielding of the Coulomb attraction by electrons increase the average separation between the electron and positron in the positronium [49]. As a result, the positronium binding energy ($E_b$) decreases, effectively reducing the width of the Ore gap and hence the efficiency of this mechanism in formation of positronium. Of course, this is the case when no strong external electric fields are used.

The general difference between spur and blob model is in the interpretation of the terminal state of positron. Spur model assumes some small spherical area with a couple of ion-electron pairs ($n_{e\text{-}I}$, usually $\lesssim 5$), where for blob it is several dozen of such pairs. The average positron energy loss in a given terminal structure is about 10-50 eV [46] and 500 eV [49] for the spur and blob model, respectively. In addition, the positron in the blob is considered more mobile than in the spur and can easily leave the blob, lifting the probability of positronium formation from the value of $n_{e\text{-}I}/(1 + n_{e\text{-}I})$, which is assumed for spur. However, in principle, depending

on the energy of the positron, either the spur model ($E_{e^+} > 500$ keV) or the blob model ($E_{e^+} < 500$ keV) can be applied [49] to describe the interactions of a positron in matter.

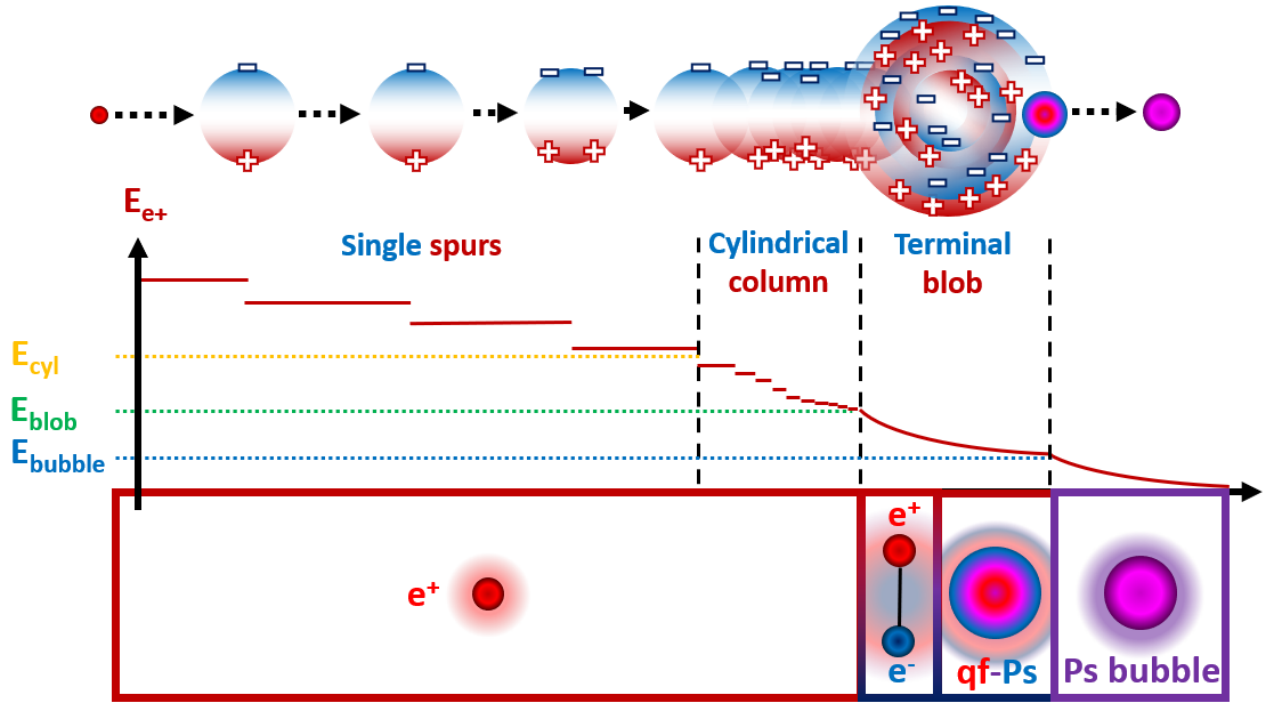


Figure 1.2: **Positronium formation by blob model**. High-energy positron, when entering condensed matter it ionizes molecules along its track. Depending on the energy of the positron ($E_{e^+}$, red line) ionization regions will form single separated spurs ($E_{e^+} > E_{cyl}$), multiple spurs in form of cylindrical columns ($E_{cyl} > E_{e^+} > E_{blob}$) and the terminal blob ($E_{blob} > E_{e^+} > E_{bubble}$). If a positron is located in the blob, it can form a positronium with one of the ionized electrons in the blob. The positronium formation process can be divided into three stages: initial losely bounded positron-electron pair ($e^+e^-$), intermediate quasi-free positronium (qf-Ps) and finally positronium bubble (Ps bubble) which can leave the terminal blob. The positronium formation for simplicity is shown in the linear scheme.

In both models, a positron can form a positronium with one of the electrons from the ion-electron pairs formed in the ionized region (terminal blob or spur). When a positron escapes from the terminal blob and does not return to it to catch one of the electrons from blob, this leads to annihilation of the positron with one of the electrons outside the terminal blob - the so-called direct annihilation of positron. However when it stays in the blob, then one can distinguish three main stages in formation of a positronium [50], which is schematically shown in Fig. 1.2:

- Loosely bound positron-electron pair. This is the initial precursor of the positronium, when positron picks up one of the electron from the terminal blob. Binding energy of such state is very small, around 0.1 eV. It proceeds to the next stage by releasing energy,

when exciting the vibrational states of the surrounding molecules, resulting in decrease of the distance between a positron and an electron;

- Quasi-free positronium (qf-Ps), which is formed after releasing enough energy to reach intermediate equilibrium in the terminal blob. It is the final state of positronium in condensed matter, that differs from its analogue in vacuum due to the presence of the other molecules. Binding energy of such state is about 1 eV;

- Bubble positronium state. The last stage, in which after some rearrangment of the molecules positronium is partially freed from interactions with ionized particles in the terminal blob. As a result of the repulsion of some of the molecules from the positronium's vicinity, the distance between the positron and the electron is further reduced. Such a positronium can diffuse in the matter further.

Interpreting the positronium formation that resulted in the Ps bubble helped explain many of the effects observed in condensed matter, completing the inaccuracies occuring from the application of the Ore model for such samples. In particular, it allowed to explain significant changes of the efficiency of the positronium formation in materials, where the Ore gap was practically the same [49]. In addition, unexpected long mean lifetime of o-Ps in liquid helium was also easily explained by strong repulsions of the electron from the positronium and electrons from surroundings, which was described as formation of a nano-bubble [51].

## 1.3 Positron Annihilation Lifetime Spectroscopy

Previous section covered the topic of the positronium formation. From the example of the formation process shown in Fig. 1.2 one can see that the positron does not form positronium on the first contact with the electron. This is especially true for positrons formed from radioactive decays, which are high-energy particles. When such positron is injected into some material, it interacts with the material molecules, creating the ionization track like in Fig. 1.3. The formation of ionization regions along the path by a positron is usually referred to as the thermalization process. Depending on the positron injection energy and temperature, the thermalization process can take from a few picoseconds to hundreds of picoseconds [52, 53]. After thermalization, a positronium can be formed by the injected positron and one of the ionized electron from the terminal blob if the energy condition is fulfilled (Ore gap). Positronium then can be trapped in area of lower or even zero electron density (free volumes), such as defects or in structural pores in material. In very dense materials, without or very small free volumes, like for example metals, no positronium will be formed and only direct annihilations of a positron and an electron will be observed.

When positronium is trapped in the free volume, its interaction with surrounding material can affect it, for example, reducing its mean lifetime. Shortening of the o-Ps mean lifetime is usually explained in literature by the partial overlapping of the wave functions of the positronium and the material electron density outside the free volume resulting in the possibility of occuring the so-called pick-off process [25, 26]. Pick-off process occurs when a positron from positronium annihilates directly with an electron from the material and not with an electron

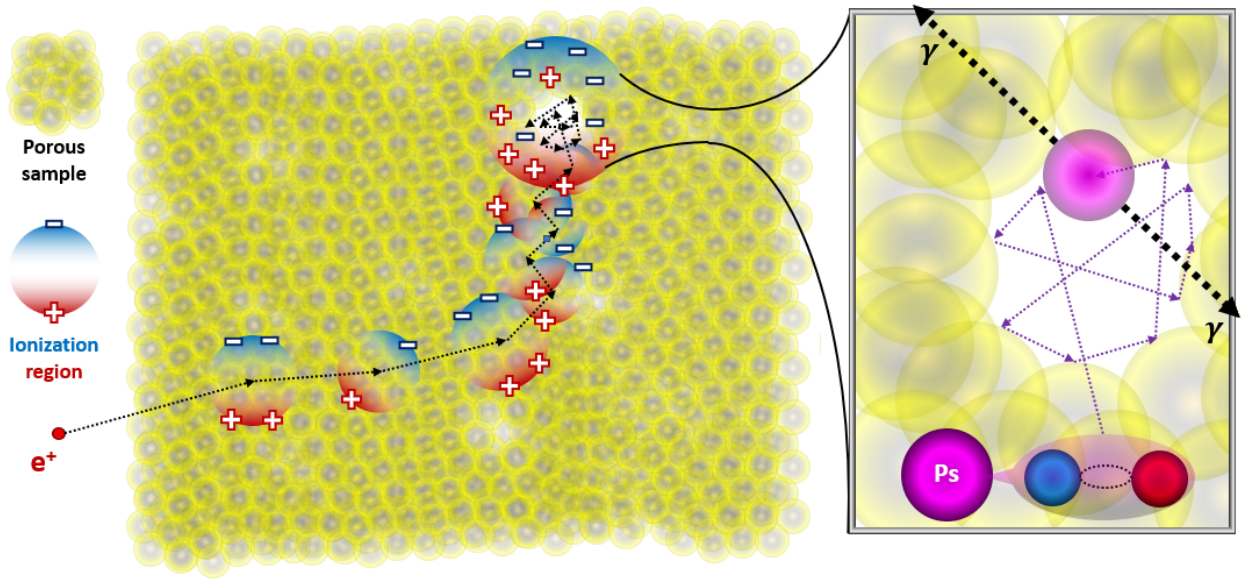


Figure 1.3: **Positron thermalization and positronium formation in porous matter**. After injecting positron ($e^+$) into a porous sample, ionization regions are formed in the area of interaction between positron and matter. Thermalized positron can either directly annihilate with the electron from the sample or form a positronium (Ps) with it, which then can be trapped in the low electron density areas, represented here by pores. Positronium trapped in a pore annihilates, resulting in emission of photons ($\gamma$).

forming positronium. Probability of such kind of the annihilation strictly depends on the size of the free volume. In fact, the smaller the free volume, the greater possibility of the pick-off process, the shorter for example the o-Ps mean lifetime will be. This effect is clearly visible for o-Ps due to its relatively long mean lifetime in vacuum compared to p-Ps. The relationship of the mean o-Ps lifetime and the radius of the free volume is well described by the Tao-Eldrup model (for small volumes, smaller than 1 nm in radius) [25,26] and its modification (for larger volumes even up to 100 nm) [27, 28]. It is also worth adding that the relationship described by the previously mentioned models is used to characterize free volumes in the size range 0.1-100 nm. Above 100 nm, o-Ps almost completely annihilates itself with the emission of three photons. The nowadays stabilized pick-off models will be discussed in more detail in section 1.4.

Assuming an exponential model of positronium decay, mean lifetime of o-Ps in matter ($\tau_{\text{o-Ps}}$) can be directly translated into the fraction o-Ps that self-annhilates with the emission of three photons to the total number of o-Ps annihilations ($f_{3\gamma}$) from the formula [29]:

$$f_{3\gamma} = \frac{\tau_{\text{o-Ps}}}{\tau_{\text{vacuum}}} = \frac{\tau_{\text{o-Ps}}}{142}. \tag{1.1}$$

One can distinguish an additional process that can shorten the mean lifetime of the o-Ps. Due to the spin interactions between positronium and molecules of the material, like for example paramagnetic oxygen, ortho-para conversion process can occur [54, 55]. After the conversion positronium will annihilate very shortly like p-Ps, which can additionally shorten o-Ps mean lifetime and decrease the number of the three-gamma decays [56].

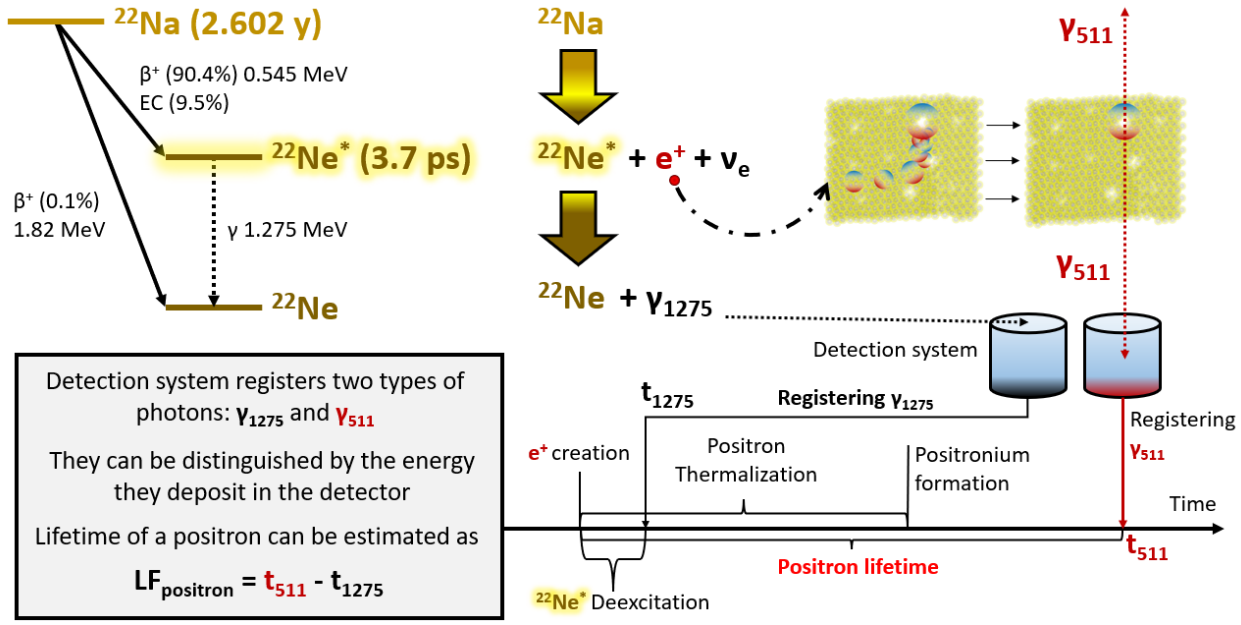


Figure 1.4: **$^{22}$Na decay, positronium formation and idea of positron lifetime measurement**. $^{22}$Na nucleus can undergo a $\beta^+$ decay (half-life of 2.602 years) with probability of 90.5% emitting positron ($e^+$) and electron neutrino ($\nu_e$) or electron capture may occur (9.5%). In most of the cases, after the $\beta^+$ decay $^{22}$Na transforms to the excited state of the neonium-22 ($^{22}$Ne*), which then deexcitates with emission of photon with energy of 1275 keV ($\gamma_{1274}$) after an average of 3.7 ps. Positron (red circle) from the $^{22}$Na decay is injected into the sample (yellow area) and thermalizes (red-blue areas), which then can create a positronium and eventually annihilate with the electron, emitting at least two photons, here each with an energy of 511 keV ($\gamma_{511}$). Emitted photons can be registered with a detection setup (represented by light blue cylinders) and distinguished based on the deposited energy in the detectors. Due to the low mean deexcitation time of $^{22}$Ne*, positron lifetime ($\mathrm{LF_{positron}}$) can be estimated as the time difference between annihilation ($\mathrm{t_{511}}$) and deexcitation ($\mathrm{t_{1274}}$) photons registration. The lengths on the timeline do not match the true distribution of the different stages in the positron's life.

Because of its sensitivity onto various conditions and chemical environment in the sample positron lifetime became a valid nanostructure indicator. A technique that deals with the correlation of positron lifetime with the nanostructure of a sample is the Positron Annihilation Lifetime Spectroscopy (PALS) technique. The application area of the PALS technique usually includes the study of metals [57], semiconductors [58], thin layers of dielectrics [59] and polymers [60]. Recently, even its potential applications in biology and medicine have been widely discussed [1–3, 30, 61–64]. Positron lifetime distribution allows to characterize nanostructure, defects and nanoporosity, while its changes to study thermal expansion of the material including phase transitions. The main challenge in determining the lifetime of a positron is finding markers that signal when the positron is formed. Therefore, PALS requires the use of a specific radioisotope or pulsed positron beam. Radioisotopes applicable for PALS technique

purposes (like widely used $^{22}$Na or $^{44}$Sc, $^{68}$Ge) are characterized by the emission of an additional photon in a short time interval from the emission of the positron. Example of the PALS measurement using $^{22}$Na source emitting additional photon with energy 1275 keV is shown in Fig 1.4. In order to collect the positron lifetime distribution from the sample and properly extract the mean lifetime of a positronium, the detection system should be characterized by very good timing properties and the ability to estimate the energy deposited by photons with an energy of about 1 MeV to distinguish deexcitation photons from the annihilation ones. The usual choice of the detectors is between inorganic scintillators like $BaF_2$, NaI or $LaBr_3$ and fast plastic scintillators. In case of a positron beam, estimating positron mean lifetime requires the detection of secondary electrons from collisions of the positron beam and the sample surface as a marker of positronium formation [65–67].

It is worth noting that the chemical environment of positrons in free volumes can be also successfully estimated from the measurements of the energy deposited by photons from positron-electron annihilation or by their angular correlations [68–70]. Momenta of the electrons from the sample may cause non-collinearity in the direction of the annihilation photons and change their energy. Energy broadening of the annihilation photons from the initial value of 511 keV (for two-gamma annihilations) is determined by precise measurements of the deposited energy, by superior in terms of the energy resolution detectors like HpGe, in Coincidence Doppler Broadening Spectroscopy (CDBS) [70]. It allows to distinguish contribution of positron annihilations with valence or free electrons (low electron momentum, characterized by the so-called S parameter) and with core electrons (higher electron momentum, characterized by the so-called W-parameter). On the other hand, the electron momentum distribution can also be extracted by measuring the angular correlation between annihilation photons in a technique called Angular Correlation of Annihilation Radiation (ACAR) [68–70]. Angle between photons can be successfully estimated measuring their tracks (position of interaction in the detector), which is usually achieved with position-sensitive detectors, such as multi wire proportional chambers or gamma cameras.

## 1.4 Pick-off models

Pick-off process is treated as a main factor contributing to the shortening of the mean lifetime of o-Ps in condensed matter. The probability of this process occurring will depend on the chance of the annihilation of the positron with an electron from the material, which is not forming positronium. In other words, it is the probability that the electron (positron) density of the positronium will intersect with the electron density of the material. If the formed positronium is localized in a free volume, a region with negligible or even zero electron density, then depending on its size, the probability of the pick-off process will also vary. The concept of this dependence is shown schematically in Fig. 1.5. The higher the probability for the pick-off process the lower the mean o-Ps lifetime, because in the pick-off regime the positronium will annihilate with the mean positronium lifetime in bulk ($\tau_{\text{bulk}} < \tau_{\text{o-Ps}}$). It is usually assumed that the $\tau_{\text{bulk}} = \frac{1}{\lambda_{\text{bulk}}} = \frac{1}{\frac{1}{4}\lambda_{\text{p-Ps}}+\frac{3}{4}\lambda_{\text{o-Ps}}} = 0.5$ ns. However, in various media, due to the different relative fraction of formation p-Ps to o-Ps value of $\tau_{\text{bulk}}$ can change [71].

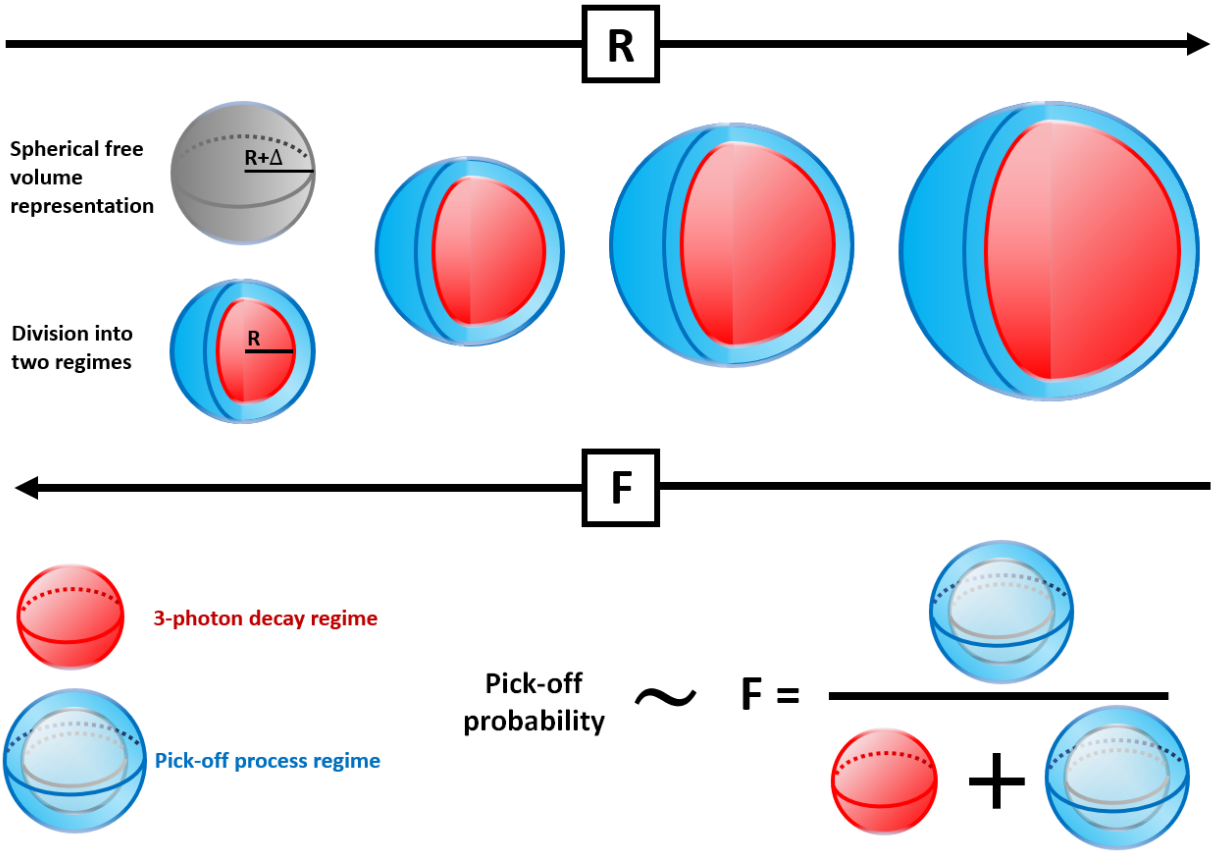


Figure 1.5: **Definition of extended free volume in pick-off models**. Free volume with radius R in the Tao-Eldrup model [25,26] can be represented by the extended free volume with radius R+Δ (grey ball). It can be then divided into two separate areas - ball with radius R where the three-photon decay dominates (3-photon decay regime, red ball) and spherical shell with thickness Δ where the pick-off process can occur (pick-off process regime, blue shell). As the radius of the free volume (R) increases, the pick-off regime fraction (F) will decrease, thereby reducing the probability of the pick-off process.

The description of the dependence of the size of the free volumes on the mean lifetime of o-Ps, the shortening of which is directly influenced by the rate of the pick-off process, was first introduced by Tao [25] and Eldrup [26]. In their approach, a positronium in a free volume of a given radius is expressed as a particle trapped in a rectangular infinitely deep potential well with spherical symmetry. For such well, spatial part of the wave function of the localized particle inside the well can be expressed as a linear combination of $\sin kx$ and $\cos kx$, where $x$ is the distance of the particle from the centre of the well, $k = \frac{2n\pi}{R}$ and $R$ is the radius of the well. However, only the ground level of the well is considered occupied. In addition, instead considering the positronium outside the potential well (pick-off regime), Tao and Eldrup considered expanded well with a parameter Δ and assumed that the pick-off can occur in a layer with a thickness of Δ, and the probability that the positronium will be outside is 0. Schematic overview of the division is shown in Fig. 1.5. This approach results in determining the probability of the pick-off process ($P_{\text{p-o}}$) on the radius of the free volume

(R) as

$$P_{p\text{-}o} = 1 - \frac{R}{R+\Delta} + \frac{1}{2\pi}\sin\left(\frac{2\pi R}{R+\Delta}\right). \tag{1.2}$$

The $\Delta$ parameter is correlated with the penetration depth of the positronium outside free volume. The most frequently used empirically determined value is 0.166 nm [72], but some variation of the $\Delta$ parameter depending on the type of material is also being considered [71].

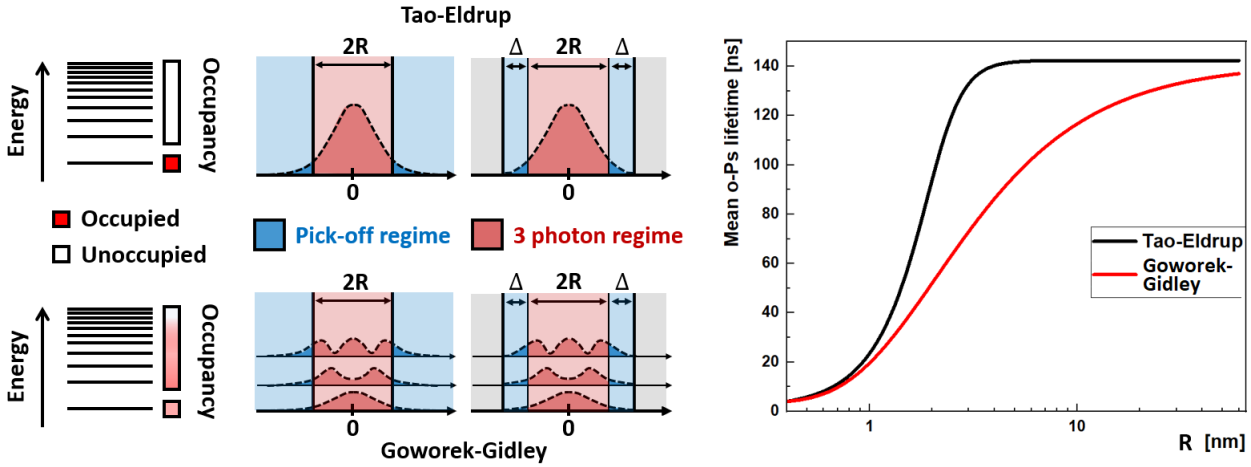


Figure 1.6: **Comparison of the pick-off models**. Two models, Tao-Eldrup and Goworek-Gidley, allow the mean lifetime of o-Ps to be correlated with the radius of free volume (R for spherical volumes). Both of them, instead of calculating the probability of the pick-off process outside the free volume, extend the free volume by the $\Delta$ parameter, and assume that the positronium wave function outside the enlarged free volume is zeroed. In the case of Tao-Eldrup, only the lowest energetic level is occupied by positronium located in a given free volume. In the Goworek-Gidley model, Boltzmann's distribution of occupancy of given energy states (depending on temperature) is assumed. The probability of the pick-off process in both models counts as the probability of positronium to be in the layer with thickness (R, R + $\Delta$) (pick-off regime). The greater the chance of the pick-off process, the shorter the mean lifetime of o-Ps, which is illustrated by the dependencies shown on the right, calculated for each model.

It was shown that the Tao-Eldrup model is applicable mostly for the smallest free volumes, with radius below 1 nm [73]. Accordingly, there was a need to develop other models that could correlate larger free volume sizes with the mean o-Ps lifetime. Extension of the Tao-Eldrup model was proposed by Goworek and Gidley [27, 28]. They used the same approach with the potential well, however the assumption that positronium occupies only the ground level of the potential well was lifted. Consequently, a Boltzmann distribution of the occupancy of the energy states of the well by the positronium was assumed. This allowed to enter the temperature directly as an additional parameter defining the pick-off model. In addition, Bessel functions was used as a solutions to the radial Schrödinger equation for the energy levels, which determine the distribution of the positronium presence inside the well. As

a result, depending on the energy level, the positronium will have a different probability of annihilation in the pick-off process. In particular, the probability of a pick-off annihilation by positronium at the $n, m$ energy level in a well with radius R will be given as

$$\mathrm{P}_{\text{p-o}}^{(n,m)} = \frac{\int_{x_n^{(m)} \frac{\mathrm{R}}{\mathrm{R}+\Delta}}^{x_n^{(m)}} J_n\left(r\right)^2 r\, dr}{\int_0^{x_n^{(m)}} J_n\left(r\right)^2 r\, dr}, \tag{1.3}$$

where $x_n^{(m)}$ is the $m$-th root of the Bessel function of the first kind $J_n$ for $m \in \mathbb{N}_+$ and $n \in \mathbb{N}$.

The relationships for both pick-off models described in this section, along with an schematic explanation of the main differences between them, can be found in Fig 1.6. Although the relationship between the mean o-Ps lifetime and the pore size, according to the Goworek-Gidley approach, can only be obtained numerically, it allows to quite accurately describe the changes in o-Ps lifetimes depending on temperature or structural changes [73]. Currently, it is one of the best models to assess the impact of the pick-off process on positronium decay and therefore characterize nanostructure of the sample from the PALS measurement.

## 1.5 Positron Emission Tomography

The way in which the positron-electron decays is also widely used in medical diagnostics through the technique of Positron Emission Tomography (PET), where the emphasis is on registering photons from two-photon annihilations [74]. Reconstructed distribution of annihilation positions allows for the determination of potential neoplastic lesions or metabolic changes [10]. Recently, the concept of enhancing positron diagnostic abilities through so-called positronium imaging has been proposed [2, 3, 11, 61], what will be described in more detail in the next section. Schematic view of the PET scan is shown in Fig. 1.7.

Positrons for PET are delivered to the patient by administering a suitable radiopharmaceutical (radioisotope-labeled molecule). Positron from the decay of the radioisotope travels nearby and annihilates with one of the electrons from the patient's body. The basic assumption of PET diagnostics is that radiopharmaceuticals should accumulate in greater amounts in the areas of potential health or life threat to the patient. Commonly used molecules, based on fluorine-18, like $^{18}$F-Fludeoxyglucose ($^{18}$F-FDG), $^{18}$F-Fluoro-L-dihydroxyphenylamine ($^{18}$F-fluoro-L-DOPA) and Fluorine-18-Fluoride allows to identify tumor cells with higher glucose consumption, Parkinson disease and study both bone formation and blood flow, respectively [12]. However, the most frequently used application of PET so far is to mark areas with potential neoplastic lesions. Such molecules as $^{18}$F-FDG (lung and breast cancers, sarcoidosis), $^{18}$F-fluoro-L-DOPA (neuroendocrine tumours) and $^{18}$F-16 $\beta$-Fluoro-5$\alpha$-dyhidrotestosterone (prostate cancer) can be distinguished in particular. It is worth mentioning that other labeling radioisotopes are also used, such as carbon-11 ($^{11}$C), nitrogen-13 ($^{13}$N) and oxygen-15 ($^{15}$O) in combination with glucose or oxygen [12].

In PET, photons from positron and electron annihilation are observed by scintillating detectors arranged into the detection ring. For the image reconstruction in the commercial PET scanners only annihilation photons are selected, which deposited energy through the

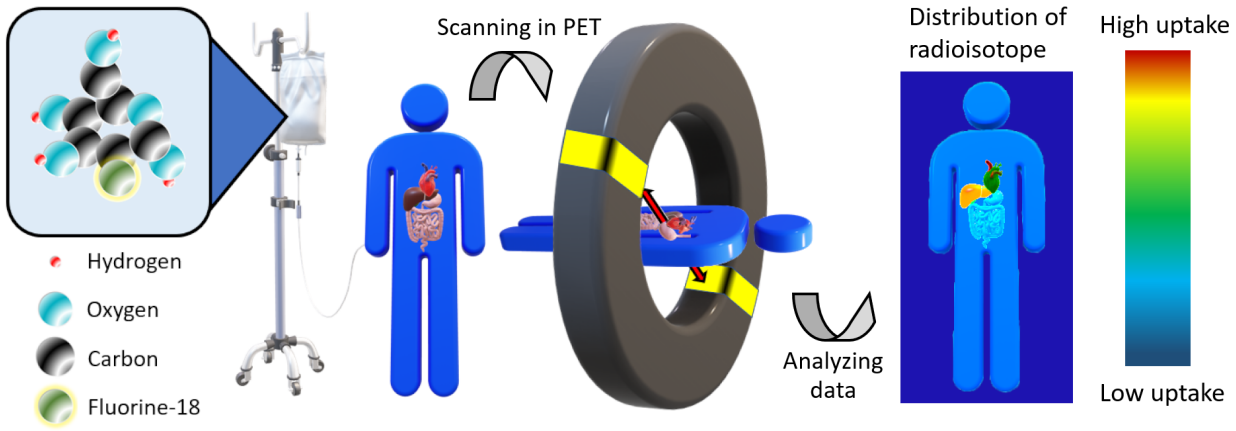


Figure 1.7: **Scheme of the PET scan.** Radioisotope ($^{18}$F) contained in an appropriate radiopharmaceutical (glucose, molecule in light blue area) is given to the patient (blue human shape). Next, patient is inserted into the PET scanner, represented here as a detection ring (grey). Positron-electron annihilations occurring in the patient's body that results in emission of two back-to-back photons (red arrows), can be registered by the tomograph. Registration of the annihilations photons allows to reconstruct distribution of the radioisotope in the patient's body. For example, some organs such as the liver, may take up more radiopharmaceutical, which leads to a higher uptake value (yellow) in contrast to other organs like stomach and intestines (blue). Changes in the biodistribution of the radioisotope can be translated into metabolic changes useful in the diagnosis of certain neoplastic changes, such as lung cancer or sarcoidosis [12].

photoelectric effect in the scintillators [10]. Using photoelectric effect for selection allows to reduce an effect of the scatterings in the final data sample. Image reconstruction itself can be performed in two ways: solely on the basis of the detection position (standard PET) or with the addition of the detection time (Time-of-Flight PET). In standard PET, points on the Line-of-Response (LOR), which is a line connecting two detectors in which annihilation photons have been registered, are treated equally as a potential annihilation position. Therefore, higher intensity will be in voxels where more LORs have crossed. It is worth nothing that the registration of one of the annihilation photons will occur earlier in the detector closer to the place where the annihilation took place. Hence, the time difference between the registration of annihilation photons should allow to limit the area of potential annihilation positions. The TOF-PET approach weights the points on the LOR based on the time difference between the photon registration. This results in much better selection properties of TOF-PET compared to standard PET. Principles of both ways of detection are compared in Fig.1.8.

Precise determination of the radioisotope distribution in the patient's body is based on the ability to detect annihilation photons. The smaller the detectors, the more precisely the position of energy deposition by annihilation photons is known, and thus the position of annihilation is better estimated. Therefore, the image quality of standard PET systems is limited by the number of detection modules in a single detection ring. The typical dimensions

of a single scintillation crystal are equal to $4 \times 4 \times 20$ mm$^3$ allowing tens of thousands of scintillators to be packed in a detection ring with a radius of ~40 cm [8]. Currently, TOF-PET scanners commercially available achieve spatial resolution 4-5 mm in Full Width at Half Maximum (FWHM) [10]. It is worth noting that even though the fundamental limit of spatial resolution of the current clinical solutions in PET scanners is 1-2 mm (in FWHM) [8], further improvements should reduce this value below 1 mm [9].

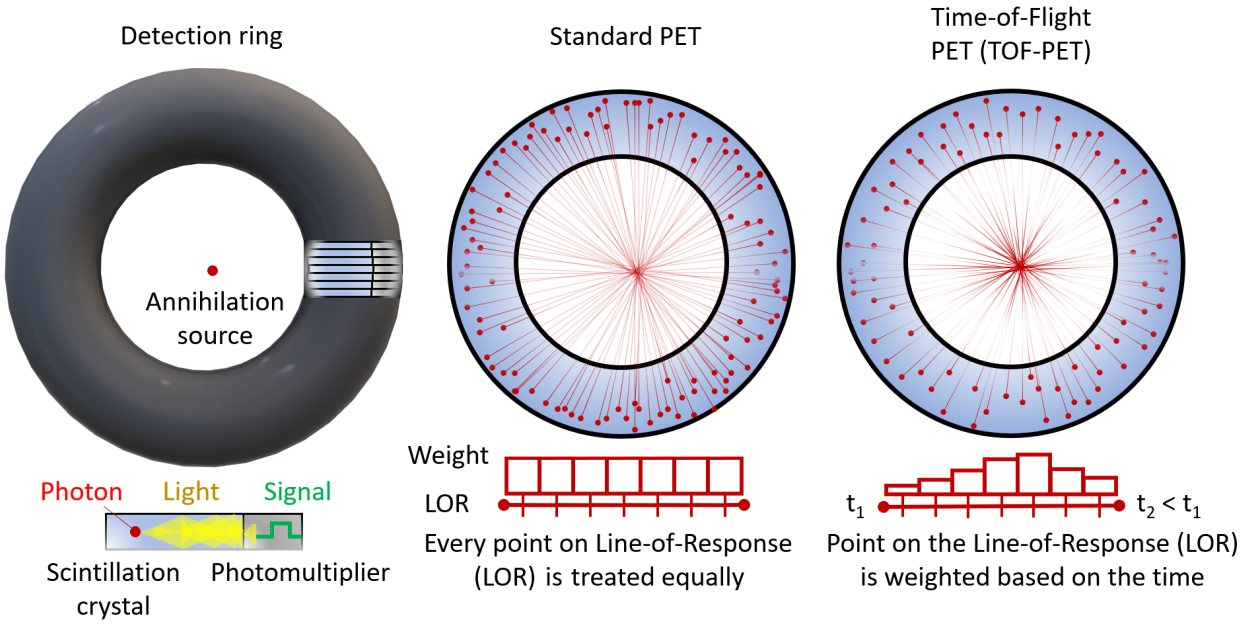


Figure 1.8: **PET and TOF-PET comparison.** PET scanner detection area is limited to a ring of individual detection modules. Each module can be represented by photon sensitive part (scintillation crystal), in which the deposited photon energy can be further transferred, and an energy collector (photomultiplier), which converts the deposited energy from the sensitive part to an electrical signal. The operation of the detection module can be described as follows: the photon deposits energy in a scintillator (red circle), which is converted into light (yellow), which goes to a photomultiplier, where it is converted into an electrical signal (green pulse). Detection modules in the ring can be positioned close together as shown in the small cross-section on the right side of the grey detection ring. The standard approach of PET focuses on collecting single lines connecting the two modules that have registered annihilation photons (Line-of-Response LOR, red line), on which the points are weighted equally. In the Time-of-Flight PET (TOF-PET) points on the LOR are weighted based on this time difference between signals.

Due to the need to register both annihilation photons in order to reconstruct the positron-electron annihilation position, only a small part of the body can be scanned at a time in one scan (limited to the width of the scintillation crystals). This creates problems in imaging the full metabolism of the patient, allowing the search for metabolic changes and potential neoplastic metastases. The answer to this challenge was proposed by the extension of the detection area by additional rings or changes in the scanner geometry in the promising concept

of Total-Body PET. Total-Body PET may allow for increasing the diagnostic possibilities of positron tomography in the future [10, 11, 75, 76].

## 1.6 Positronium imaging

The development in the field of detection elements and their geometry for positron emission tomography allows obtaining more and more accurate images. This translates into a more precise determination of the place of metabolic changes in the patient's body and the possibility of imaging smaller and smaller neoplastic changes. However, further development of the PET technique can be achieved also by introducing new markers, such as mean positronium lifetime, which is an effective marker for nanostructural changes occurring, for example, in cancer. A proposal for a new type of imaging - positronium imaging, that is based on the lifetime of the positronium was introduced by Moskal [2,3,77,78] and recently experimentally confirmed by means of the J-PET detector [1]. Combination of radioisotope distribution with structural information could bring new contrast in positron tomography and possibly allow the diagnosis of more types of neoplastic lesions or even the identification of different stages of cancer [63,64,79–91]. To obtain structural information in a given voxel, a way to estimate the mean positron lifetime must be found, for example by using additional photons as described in Section 1.3. Unfortunately, there are not many radiopharmaceuticals used for PET scans that emit an extra photon, such as $^{68}$Ga, for example. However, recent development in designing new radiopharmaceuticals that are characterized by emission of additional deexcitation photons like $^{44}$Sc, $^{66}$Ga and $^{94}$Tc [13–15] can answer these demand.

Concept of the positronium imaging, using exemplary radiopharmaceutical $^{44}$Sc is schematically depicted in Fig. 1.9. Position of the annihilation is estimated based on the time and position of registration of photons from the positron-electron annihilation, like in TOF-PET. Time difference between registration of additional photon, coming from the deexcitation of the radioisotope and annihilation photons allows to estimate lifetime of the positron, following the formula in Fig. 1.9. Collected positron lifetime spectra in each voxel, can be decomposed to estimate mean positronium lifetime. Exemplary procedure for decomposing positron lifetime spectrum is described in Section 4.2. Changes in the mean positronium lifetime in different part of the patient's organs may indicate potential threat to health and life. Additionally, if the lesions do not have a higher radiopharmaceutical uptake, which is visible on PET, positronium imaging may increase the number of neoplastic lesions that can be diagnosed by positron tomography. The first positronium images obtained for two phantoms by the J-PET detector will be shown in Chapter 6. Assessment of the J-PET detector, in view of the positronium imaging, based on the simulations was shown before in [77, 78].

It is worth noting that the applications of positronium imaging are not limited to medical imaging only. Collection of the positron lifetime distribution in different part of the sample can be transformed into a 3D structural imaging technique that can find application in materials science (porosity images), chemistry (uniformity of the solution or compound) or biophysical studies (imaging inside of the biological systems).

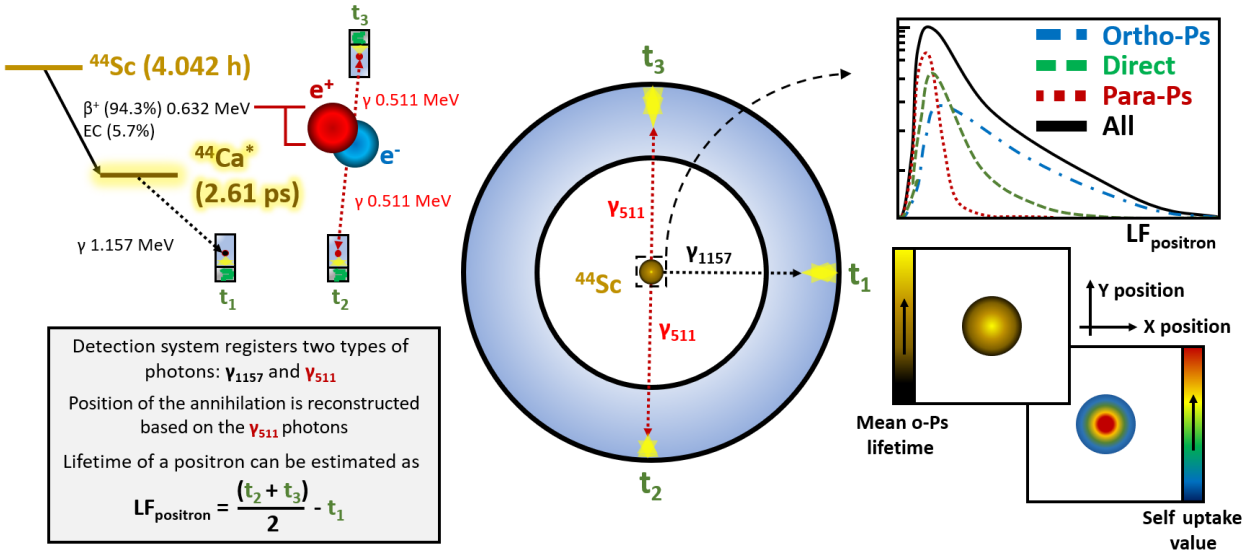


Figure 1.9: **Concept of the positronium imaging with $^{44}$Sc.** Scandium-44 ($^{44}$Sc with half-life of 4.402 h) nucleus undergoes a $\beta^+$ decay emitting positron with energy of 0.632 MeV in 90.4% of cases. After emitting positron (red circle) $^{44}$Sc nucleus transforms to the excited state of calcium $^{44}$Ca$^*$, which then deexcitates with emission of photon with energy of 1.157 MeV ($\gamma_{1157}$) after an average of 2.61 ns. Positron from the $\beta^+$ decay can annihilate with an electron (blue circle) with emission of two photons with energy of 0.511 MeV ($\gamma_{511}$). $^{44}$Sc radioactive source can contribute to the emission of three photons (1 deexcitation and 2 annihilation photons) in relatively small time window (mean o-Ps lifetime), which then can be registered by the detection ring. Position of the annihilation in a single event can be reconstructed based on the time and position of registration of the annihilation photons. Lifetime of the positron ($LF_{positron}$) can be calculated as time difference between registration of annihilation and deexcitation photons. In each voxel of the image positron lifetime distribution can be collected and contribution of each type of annihilation can be estimated - from ortho-positronium (Ortho-Ps), direct $e^+e^-$ annihilation (Direct) and para-positronium (Para-Ps). Because mean o-Ps lifetime is a structural indicator, it is possible to create an image characterizing nanostructure in every voxel. It is an image complementary to the standard imaging obtained in a PET scan, which shows the distribution of the radioisotope inside the detection ring.

# Chapter 2

# J-PET detector

Proof of concept of the positronium imaging shown in this dissertation was obtained using a new type of the PET tomograph - the Jagiellonian Positron Emission Tomograph (J-PET) [4–6]. The construction and characteristics of the J-PET detector along with the detailed analysis procedures will be the subject of this chapter.

## 2.1 Construction

The J-PET detector uses polymer-based long scintillating strips EJ-230 [92, 93] to detect radiation with energy around 1 MeV. The scintillators used in the system are characterized by very good time properties - rise time 0.9 ns and decay time 2.1 ns. Strips (192 scintillators) are arranged in three concentric layers (with radius of 42.5, 46.75 and 57.5 cm), forming large cylindrical detection chamber like in Fig. 2.1, 2.2. Each scintillation strip (with dimensions $19\times7\times500$ mm$^3$) is connected on both sides with vacuum photomultipliers Hamamatsu R9800 [94]. Two photomultipliers are used to collect light resulting from energy deposition by high-energy photons and reconstruct its position along the longest axis. Electrical signals converted from light by photomultipliers are transmitted to the data acquisition system (DAQ). First, the signals are probed at four predefined thresholds by dedicated front-end electronics [17]. Next, data are transformed to binary data by a novel trigger-less acquisition system, based on field programmable gate array (FPGA) platform [18]. It allows to obtain high data flux and good time resolution for a signle signal, even up to 150 ps [6]. Better time properties corresponds to the better spatial resolution of the reconstructed annihilation points.

Plastic scintillators are characterized by very good time properties that allow their use in TOF-PET tomographs. However, the dominant process that allows the detection of high-energy photons for these types of detectors is the Compton effect [4, 5]. In commercial PET scanners, the basis for the correct selection of coincidences and reduction of scattering is the observation of photons reacting by the photoelectic effect [10]. Therefore, a specific set of selection criteria for the J-PET detector will be introduced in section 2.4, which allowed to cover proper selection of the annihilation photons based on the geometry of the decay and proper scatterings reduction. Further development of the J-PET detector detection systems and analysis procedures may allow to push the limits of the measurement of the basic opera-

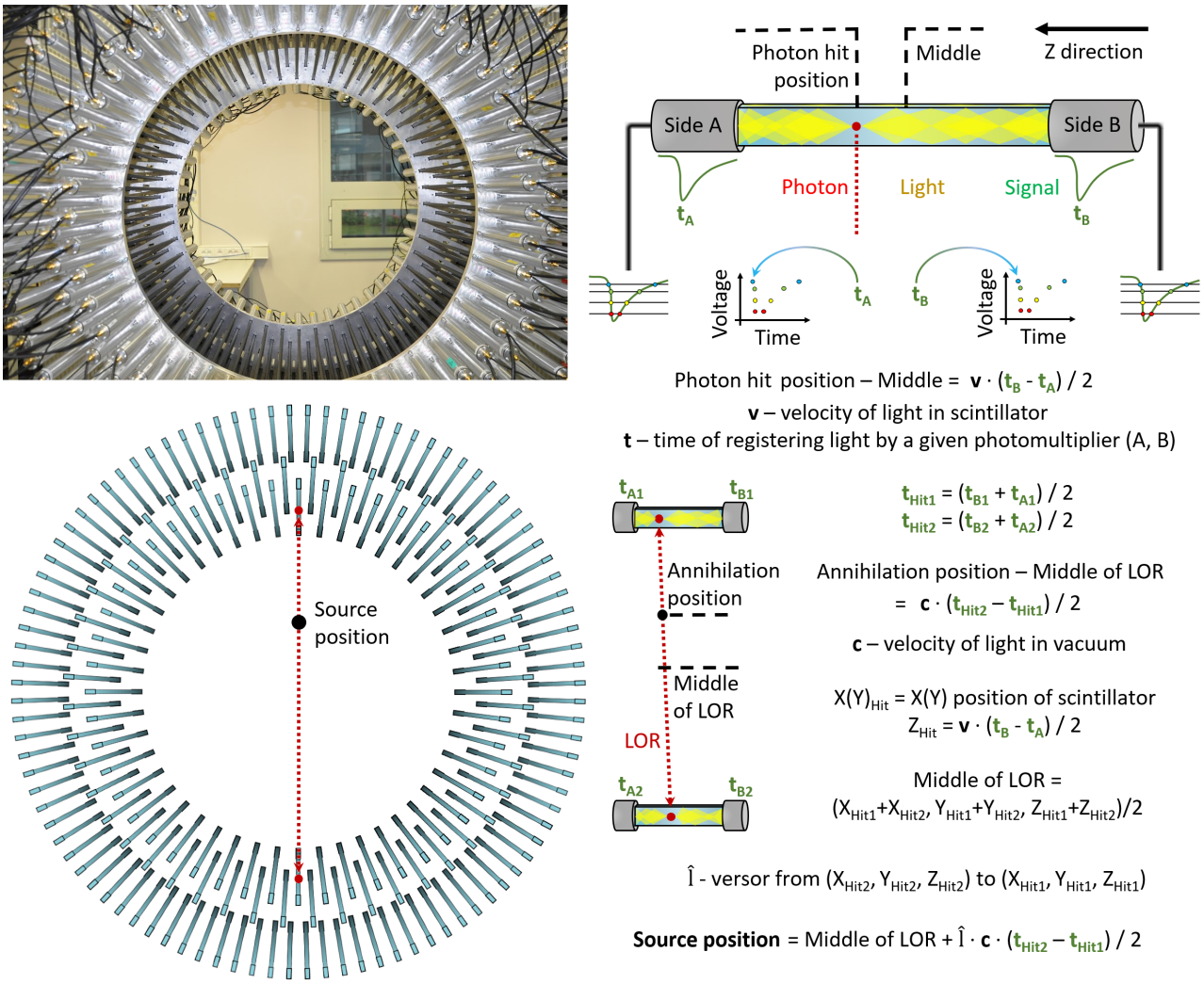


Figure 2.1: **The J-PET detector and basic position reconstruction.** (left, top) Photo of the J-PET detector. (left, bottom) Schematic view of the J-PET detector limited to scintillators arranged in three concentric layers. Position of the positron source (black dot) can be reconstructed when resulting photons (red dashed lines) coming from the positron-electron annihilation are registered in opposing scintillators. For reconstruction, one needs to determine the time and position where the photons were detected. (right, top) Photon deposited energy can be converted into light. It can then be collected by photomultipliers attached to both sides (A, B) of the scintillator and transformed into signals (green pulses). Position of the photon detection along the strip (Z position) can be calculated based on the time difference between the signals ($t_A$, $t_B$). Since the signals are probed on four thresholds in the J-PET detector, the time of the signal is estimated as the time on the threshold closest to the signal pedestal (blue dot). Time of the photon detection ($t_{Hit}$) is calculated as an average of the signals on both sides. (right, bottom) X and Y coordinate of the position where photon deposited energy are assumed as a middles of a scintillator in a proper direction. Similar to the Z position reconstruction, position along the Line-of-Response (LOR) can be calculated based on the time of the hits ($t_{Hit}$) in two scintillators.

tors allowing to study physics of some of the fundamental processes [19–24] and specific positronium physics [95, 96].

## 2.2 Experimental setup description

In order to study some of the basic properties of the positronium decay, like annihilation geometry and its mean lifetime following detection system configuration was used. Porous material (XAD4 [98]) surrounding $^{22}$Na positron source was placed in an aluminium annihilation chamber and connected to rotary vacuum pump, like in Fig. 2.2. It allowed to maintain stable conditions during the measurement (1 Pa pressure, room temperature). In order to get relatively large fraction of positrons that were implanted into XAD4 material, $^{22}$Na (1 MBq) was encapsulated between very thin layers of Kapton foil ($\approx$7 $\mu$m). Measurement in such configuration lasted 27 days. XAD4 allowed to obtain very high fraction of the o-Ps that annihilated with emission of the three photons (40% [29]) with relatively high mean lifetime (90 ns [29]). Photo of the chamber with the XAD4 nanoporous material used in the measurement is shown in Fig. 2.2. In the next sections, whole analysis chain will be described in detail. Measurement with XAD4 allowed to fully calibrate the J-PET detector in the time domain, as will be shown in Chapter 3. Final results of the positronium properties will come later in the Chapter 5.

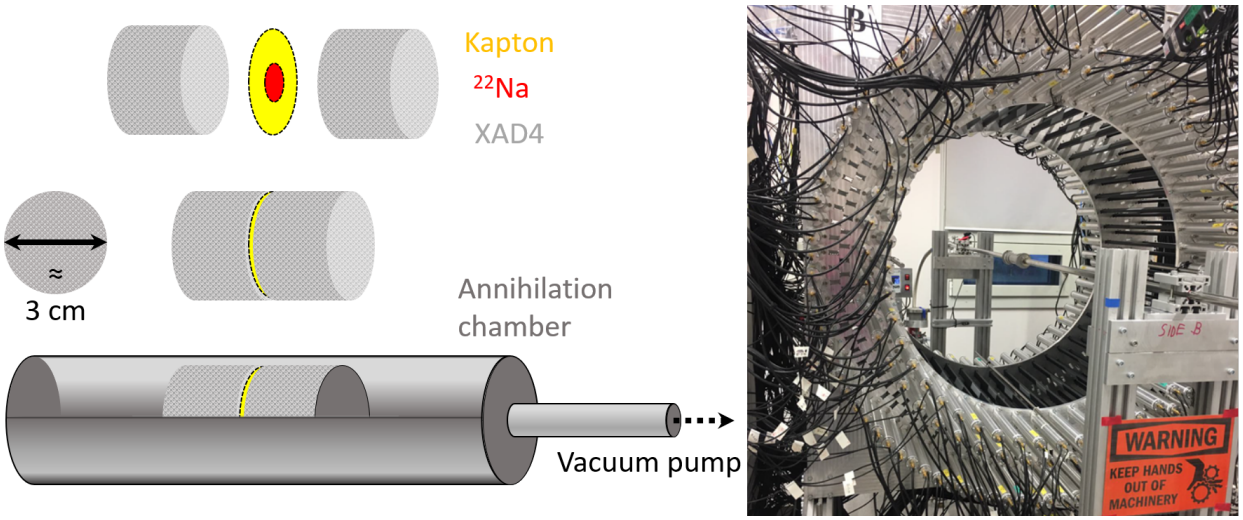


Figure 2.2: **Scheme of the annihilation chamber with XAD4.** Positron source $^{22}$Na encapsulated in a thin Kapton foil was surrounded by the XAD4 material. All elements were placed in a aluminium annihilation chamber [97]. Cross-section of the annihilation chamber with the sample inside is shown on the left. Chamber was connected to a rotary vacuum pump and inserted inside the J-PET detector like in a photo on the right.

## 2.3 Data reconstruction

The data collected during the measurement was analysed in the J-PET Framework [99] architecture. It is based on the C++ programming language and ROOT libraries [100]. The J-PET Framework software allows to recover full events from the trigger-less data acquisition system. Exemplary signal collected from a single photomultiplier of the J-PET detector is shown in Fig. 2.3. The J-PET detector measurement data is in the form of individual times when the signal exceeds a given threshold. Additionally, information is recorded whether the signal has exceeded the threshold when the light in photomultiplier is accumulating (leading edge) or deexciting (trailing edge). For this reason the basic challenge of the analysis software is at first to reconstruct signal from a single photomultiplier, then to join signals created from the same scintillator to form a hit. At the end hits are wrapped into events for further analysis. In order to reconstruct data structures: signals, hits and events, separate time windows are used, like it is shown in Fig. 2.3. The following time windows were used during the analysis: Signal Time Window - 3 ns; Hit Time Window - 5 ns; Event Time Window - 600 ns. Values of specific windows comes from the characteristics of scintillators (rise time 0.9 ns and decay time 2.1 ns); velocity of light in the plastic scintillator (around 12 cm/ns) and its length (50 cm); mean lifetime of o-Ps in XAD4 (90 ns), respectively for signals, hits and events.

After the data reconstruction, every event is analysed separately which will be discussed in more detail in the next section. However during the reconstruction there is an additional analysis procedure, that allows to estimate the position of the hits and the energy-equivalent Time-over-Threshold (TOT) value. Position of the hit is estimated based on the time difference between the signals collected by two photomultipliers connected to the same scintillator. It is worth noting, that the time of the single signal is estimated as the time on the lowest threshold (-30 mV) like it is shown in Fig. 2.1. TOT value can be calculated for three structures: threshold, signal and hit, and it is depicted in Fig. 2.4.

## 2.4 Analysis procedure

The final analysis of the reconstructed events requires first selecting a representative part of the data sample. In the selection process, a set of criteria will be introduced based on the time, geometry and energy deposition of the registered photons. In the first stage of selection, hits are distributed based on their origin. The origin is checked on the basis of information about the energy deposition coming from the $\mathrm{TOT_{hit}}$ value. Due to the presence of two types of photons ($^{22}$Na as a positron source), three main types of origin can be distinguished: annihilation, deexcitation and inconclusive origin. The $\mathrm{TOT_{hit}}$ spectrum collected during the measurement along with the ranges for each type, defined as in Fig. 2.4, can be seen in Fig. 2.5 a). It should be emphasized that the average energy deposited by photons from the two-photon decay is higher than in the case of the three-photon decay. Therefore, the TOT range for the three-photon decays is wider than for the two-photon decays for the analysis. After the categorization of the hits, only annihilation and deexcitation hits will be considered in the next step of the analysis.

For the annihilation hits one can introduce additional selection criteria that will help to

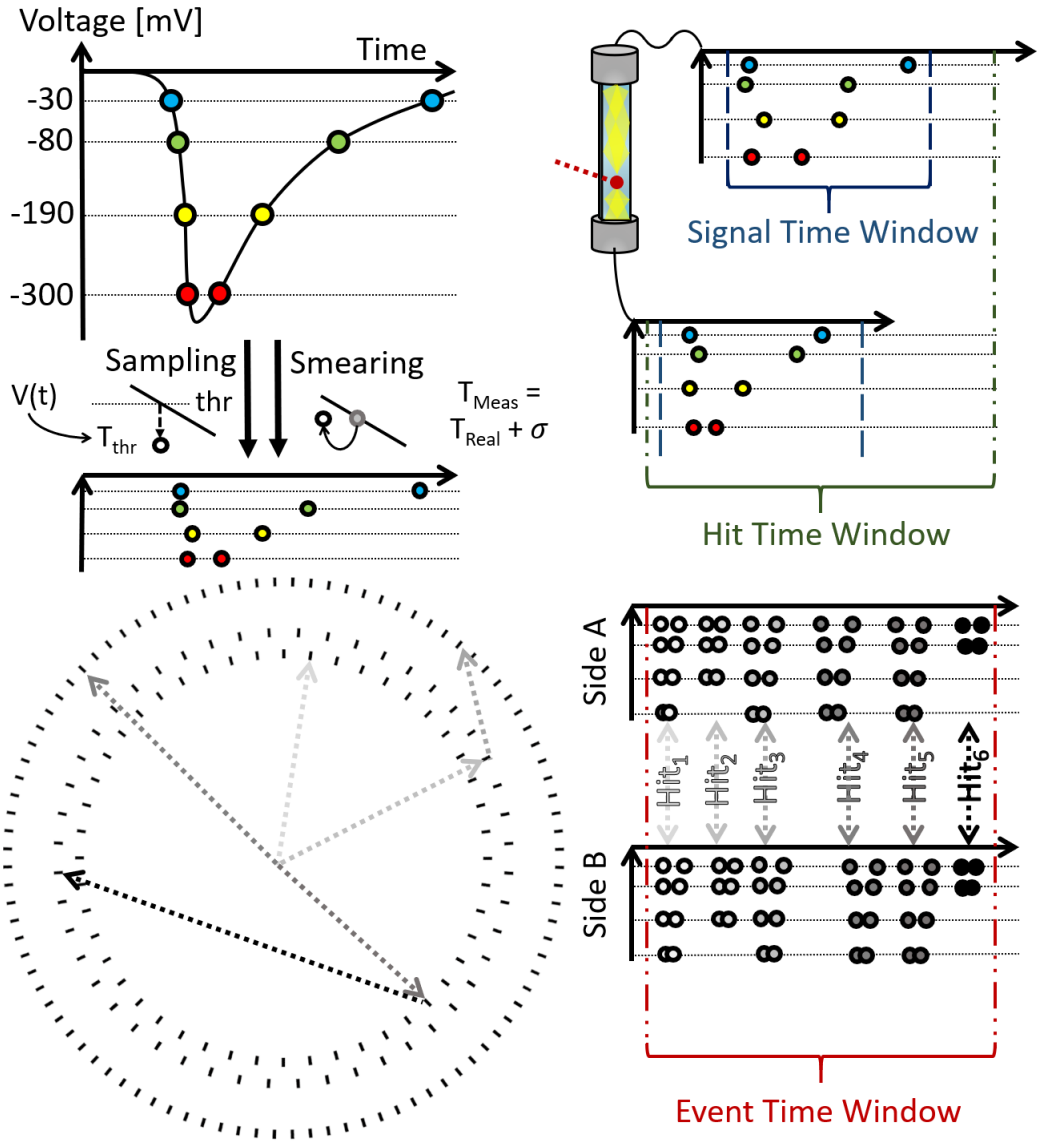


Figure 2.3: **Scheme of the data reconstruction procedure.** (left, top) The light collected by the photomultiplier is converted into an electrical signal - voltage dependence over time V(t). Signal is probed on four thresholds with nominal values: -30, -80, -190 and -300 mV. Due to the smearing, measured times on individual thresholds can be slightly shifted from the real values, which can complicate the reconstruction process. (right, top) For a given photomultiplier signal is reconstructed if the measured times on different thresholds are in some Signal Time Window. Signals from two photomultipliers connected to the same scintillator can create a hit if they are separated by no more than the value of the Hit Time Window. (left, bottom) The J-PET detector, represented by the black rectangles, can register multiple photons (grey arrows) during the measurement, which can be reconstructed as hits. (right, bottom) Events are reconstructed as a set of hits within an Event Time Window.

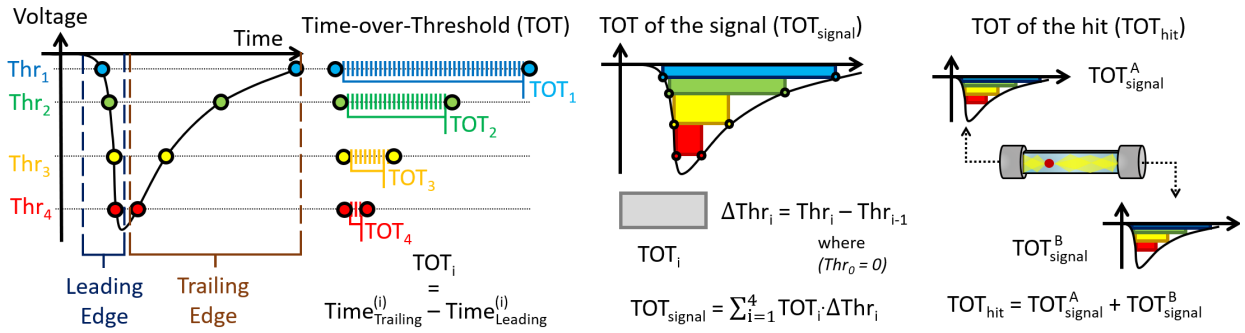


Figure 2.4: **Time-over-Threshold calculations.** Time-over-Threshold (TOT) can be a valid energy estimate of the electric signal [16]. The J-PET detector data acquisition system probes signal on four thresholds ($\mathrm{Thr}_i$). In addition it distinguish two range of the signal, where the amount of light collected by the photomultiplier is increasing (Leading) or decreasing (Trailing). Time-over-Threshold for a single threshold is then calculated as a time difference between the Trailing and Leading edges. In order to incorporate information coming from the threshold values, TOT of the signal ($\mathrm{TOT_{signal}}$) is estimated as a sum of the TOTs multiplied by threshold nominal value. Finally, TOT of the hit ($\mathrm{TOT_{hit}}$) is calculated as a sum of the $\mathrm{TOT_{signal}}$ from photomultipliers (A, B) from both sides of the scintillator. $\mathrm{TOT_{hit}}$ is the estimation of the amount of light that was created in the scintillator and therefore the deposited energy.

purify the data sample. They are based on the geometry and timing of the registered hits. The momentum conservation law for electron positron annihilation defines its decay geometry. When two or three annihilation photons are created in the act of annihilation, the photons will be emitted in one line or decay plane, respectively. It holds only for low energies of a positron and an electron, which is the most common case when they annihilate. Therefore, if two or more reconstructed annihilation hits occur in an event, the decay plane (line) can be constructed from the positions at which the photons deposited energy like in Fig. 2.5 b). When the position at which the annihilation is approximately known, the distance of the decay plane from that position may be the criterion for selecting suitable candidates for electron and positron annihilation studies. The distribution of distances of the decay planes ($\mathrm{D_{decay}}$) for events with two or more annihilation hits from the measurement with the XAD4 can be seen in Fig. 2.5 b). The cut-off for this measure was selected on the basis of the assumed location of the chamber during the measurement - approximately 5 cm from the centre.

When the position of the annihilation is calculated like in Fig. 2.1 it is possible to select events for which the annihilation position would be inside the detection chamber and to reject potential scatterings. Selection of the annihilation time difference ($\Delta \mathrm{t_{anni}} = |t_{\mathrm{AnniHit1}} - t_{\mathrm{AnniHit2}}|$) acceptance range to $[0,\ 0.5]$ ns, corresponds to 15 cm maximal distance of the annihilation point from the centre, which is the length of the aluminium chamber. Distribution of the $\Delta \mathrm{t_{anni}}$ for the measurement is shown in Fig. 2.5 c). The last criterion, that is based on geometry and timing allows to reject additional scatterings from the analysis that survived previous conditions. Probability that the two hits ($\mathrm{hit_1}$, $\mathrm{hit_2}$) are coming from the same

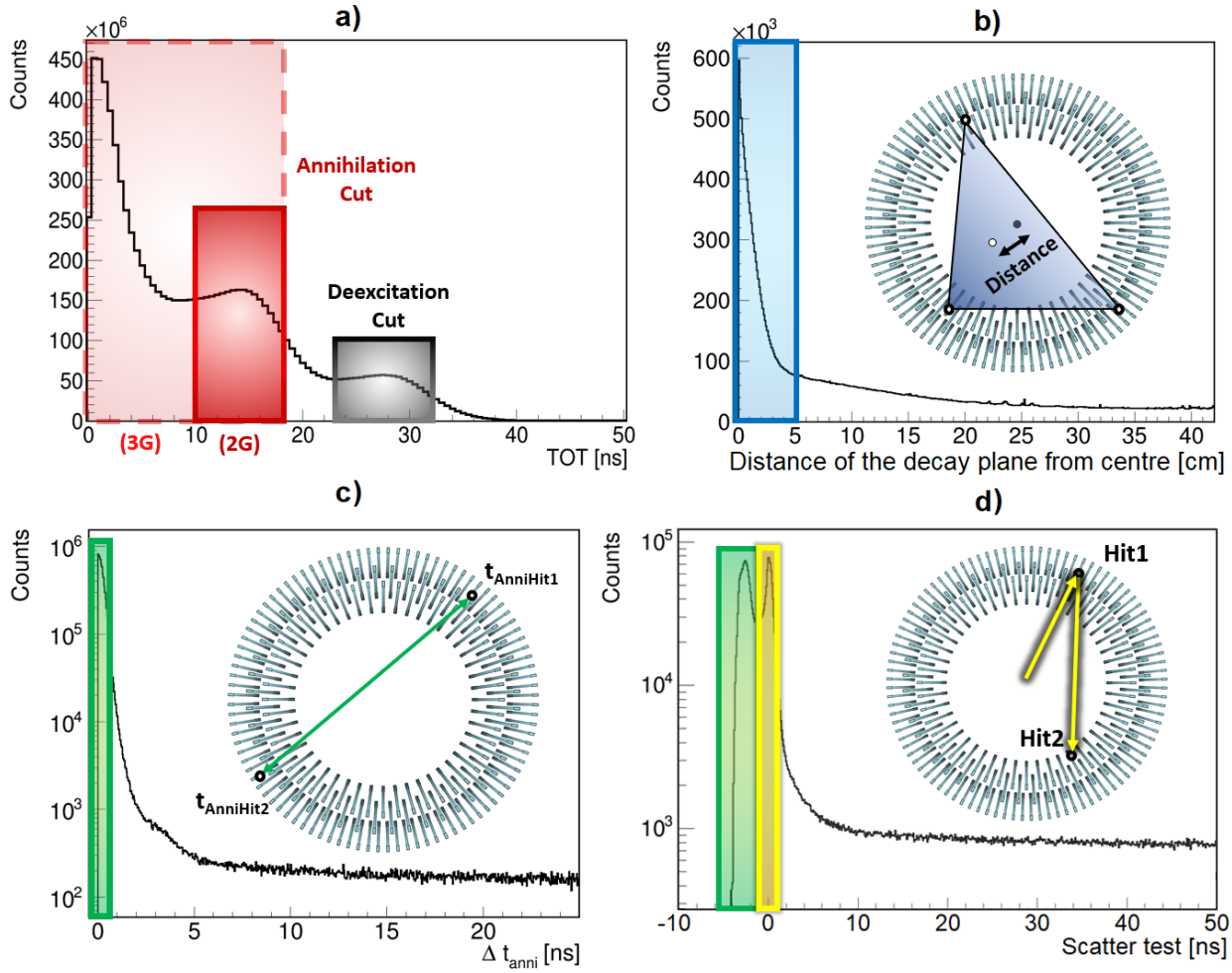


Figure 2.5: **Selection criteria.** Experimental data. a) Distribution of the Time-over-Threshold (TOT) values from the measurement with the XAD4. One can distinguish two ranges of hits that consists of hits which with high probability comes from annihilation photons (red, from 10 to 18 ns - decay into two photons (2G) and 1 to 18 ns - decay into three photons (3G)) and deexcitation photons (black, from 23 to 32 ns). b) Distribution of the distances of the decay plane from the centre of the detector. Decay plane can be constructed from the positions, where the photons deposited energy. Blue range (less than 5 cm) indicate selected events for the final analysis. c) Distribution of the annihilation time difference ($\Delta t_{anni}$) from the aforementioned measurement. Events that produces annihilation positions close to the centre (green area, less than 1 ns) are selected for the final analysis. d) Distribution of the scatter test defined by Eq. 2.1. One can distinguish three areas coming from different type of pair of hits: (green) annihilation hits coming from the same decay, (yellow) hits that are coming from the same photon and the photons coming from different decays (accidental coincidences).

photon will grow when the $\mathrm{ST}\left(\mathrm{hit}_1, \mathrm{hit}_2\right)$ function defined as below, will go to zero.

$$\mathrm{ST}\left(\mathrm{hit}_1, \mathrm{hit}_2\right) = \Delta \mathrm{t}\left(\mathrm{hit}_1, \mathrm{hit}_2\right) - \frac{\mathrm{Distance}\left(\mathrm{hit}_1, \mathrm{hit}_2\right)}{c}, \tag{2.1}$$

where $c$ is the speed of light in vacuum ($c = 29.98\ \frac{\text{cm}}{\text{ns}}$), $\Delta t\,(\text{hit}_1, \text{hit}_2)$ is a time difference between two hits and Distance $(\text{hit}_1, \text{hit}_2)$ is a distance from the reconstructed positions of hits. Potential scatterings will be included in the $[-0.5, 0.5]$ ns, shown in Fig. 2.5 d) as the yellow range. Therefore, annihilation hits coming from the same decay will contribute to the ST value lower than -0.5 ns, because of a very low time difference ($\Delta$t) between them, shown in Fig. 2.5 d) as the green range. For the reasons which will be shown in Chapter 5, the scatter test will only be used between the annihilation hits so as not to distort the results obtained, for example, when such a test would be used between annihilation and deexcitation hits. Presented criteria allowed to select proper data sample for the analysis of the positronium properties, widely discussed in Chapter 5.

## 2.5 J-PET Monte Carlo Geant4 software

In order to estimate the fraction of various types of background in the final sample of the data, appropriate Monte Carlo simulations were performed and analyzed. Simulation software is based on the Geant4 libraries, and it is dedicated for the J-PET detector, allowing to simulate its geometry with different annihilation chambers and positron sources [101]. Positron generation is limited to the simulation of the annihilation position. Position of the positron annihilation is simulated based on the effective positron radius in different materials. After drawing the position, the appropriate decay channel (p-Ps, o-Ps and direct annihilation) of the positron-electron annihilation is chosen, according to their distribution in the material in which position of the annihilation was drawn in. The main fraction of annihilations was simulated in the target material - XAD4, for which mean lifetime distribution was shown elsewhere [29].

Each decay channel is characterized with different mean lifetime and the probability to annihilate with emission of three photons ($f_{3\gamma}$). The fraction of simulated events for a given channel that resulted in emission of two photons for a given channel is equal to $1 - f_{3\gamma}$. From the theory $f_{3\gamma}$ is constant for p-Ps and direct annihilation and it is equal to 0 and 1/378 respectively. For the o-Ps, fraction of the annihilation into three photons is calculated as in Eq. 1.1. The path and interaction of generated photons are simulated according to the Livermore Polarized electromagnetic model introduced in the Geant4. During the generation, when the photons deposits energy in the scintillators, a new hit structure is created from the position of the deposition and its energy. Simulated hits from each generated decay are packed into events and saved for the analysis by the J-PET Framework software.

$10^9$ events were generated for the aluminium chamber with the XAD4 inside, which surrounded the Kapton foil with $^{22}$Na source. Simulated events are analyzed according to the analysis chain shown in Fig. 2.6. At first each simulated hits' time, position and energy is smeared by the appropriate resolution functions, shown in Fig. 2.6. Next, events are distributed in time, according to the assumed activity of the source (1 MBq). At the end, event selection based on the criteria described above is performed. The only difference is in the energy selection of the annihilation and deexcitation hits, that is done based on the energy and not on the energy-equivalent TOT value, as shown in Fig. 2.6.

An additional information that can be retrieved from the simulations, comparing to the

data, is the type of the hit (annihilation, deexcitation) and its order in time (primary, secondary and higher photons). It allows to estimate contribution of each type of background (scatterings, secondary particles, mixed two and three gamma decays) and retrieve pure components for each decay channel in the final data sample. In addition, simulations of the measured setup help to test selection criteria described in the previous section. Proper evaluation of the simulation software will be done later in Sec. 4.4

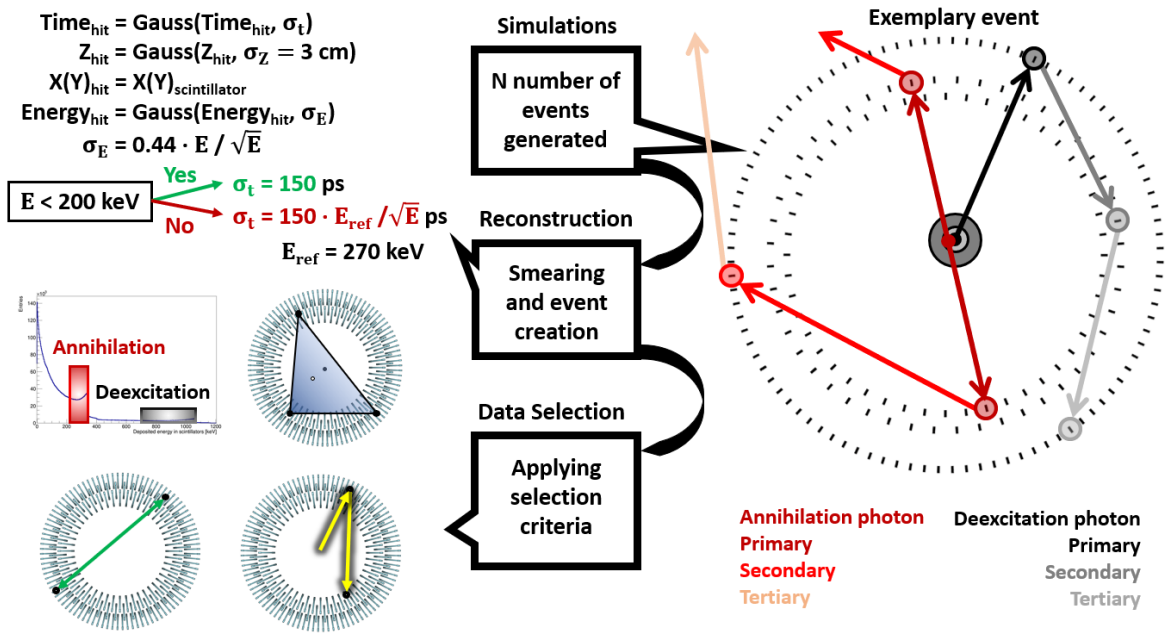


Figure 2.6: **Analysis chain for the simulated events.** Analysis procedure of the generated data by Monte Carlo simulation package for the J-PET detector. After generating N events (exemplary event on the right), each consisting of annihilation and deexcitation photons, hits are constructed when those photons deposits energy in the scintillators (black, and red circles). One can distinguish different order of the hit, based on the amount of primary photon scattering that occurred prior to energy deposition. (left, top) After generation, each hit property (time, position and energy) is smeared according to the respective function [4] and the resolution of that parameter ($\sigma_t, \sigma_E, \sigma_Z$), creating reconstructed hits. These then, after applying the appropriate distribution of hits over time, based on the assumed activity of the source, created new reconstructed events. (left, bottom) Finally, events are selected by the same criteria that were used on the measurement data.

# Chapter 3

# Calibration of the J-PET detector

Calibration of the detection modules in the J-PET detector was performed based on the data collected with the point-like source surrounded with XAD4 inside the annihilation chamber, like it was described in Sec. 2.2. Calibration methods for time, position and the effective length of the scintillator will be presented in this chapter.

## 3.1 Calibration of the position along the strip

Time synchronization procedure starts from the consideration of all of the scintillators separately. Each scintillator is connected to two photomultipliers, allowing to determine the position of the photon interaction based on the time difference between signals on them. Therefore, for an accurate estimation of the position along the scintillating strip both photomultipliers must have the same reference time, from which they work on.

At first one needs to reconstruct hits which allow to obtain $t_{BA}$ distributions for each scintillator and threshold. Hits are reconstructed based on the time windows given in Sec. 2.3. Procedure that will be shown was applied for every scintillator and threshold in the J-PET detector. However, it is worth to notice, that the Z position along the strip will be calculated only based on the lowest threshold. Such convention allows to reconstruct the Z position of every hit that crossed at least one threshold on both photomultipliers. It helps to reconstruct even very small signals, what maximizes number of the reconstructed hits.

For the next step, in order to properly understand the offset of the $t_{BA}$ distribution, one can start with its decomposition. When the strip is irradiated uniformly, and the times are measured with the perfect resolution, then $t_{BA}$ will form a rectangular shape, like in Fig. 3.1 a). It is also assumed that every position of the scintillating strip has the same probability to create signals at both photomultipliers. In other words, this means that light is not attenuated as much as it passes through the strip, which is true of the selected EJ-230 scintillators (Light Attenuation Length $\approx$ 52 cm) [92,93]. When the source inserted into the detection chamber is point-like, then the irradiation of the scintillating strip will be cosine like, from the Lambert's cosine law, schematically shown in Fig. 3.1 b). If one adds the smearing derived from non-zero time resolution the final distribution will look like in Fig. 3.1 c). In addition, if the photomultipliers connected to both ends of the same scintillating strip will not be calibrated

then the $t_{BA}$ distribution will be shifted like in Fig. 3.1 d).

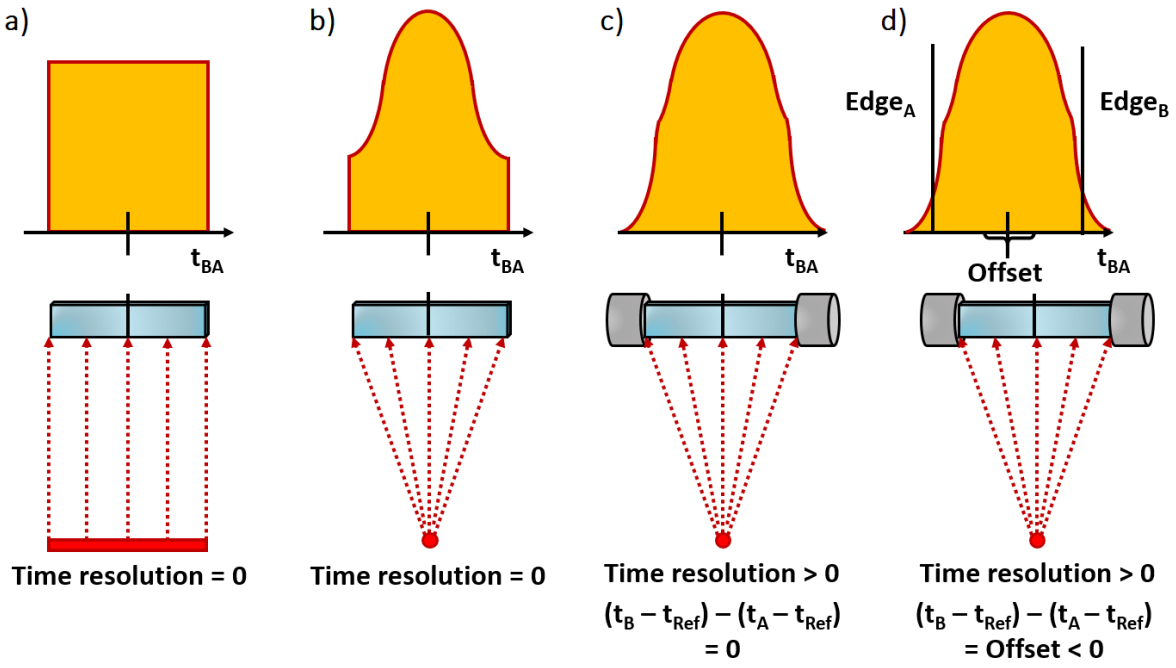


Figure 3.1: **Scheme of the influence of resolution and offset on the $t_{BA}$ distribution.** $t_{BA}$ distribution for the perfect time resolution with a) uniform and b) point-like irradiation. $t_{BA}$ distribution with some non-zero time resolution and c) without and d) with some offset between photomultipliers connected to both ends of the scintillator.

Centre of the $t_{BA}$ distribution will be affected by both non-uniform irradiation and time resolution, making it difficult to estimate its center and thus the offset, especially when the time resolutions are different for the two photomultipliers. However, the edges of the aforementioned distribution will be only disturbed by the timing properties, lowering an uncertainty of the determined offset. If the middle of the edges of the $t_{BA}$ distribution will be estimated as $Edge_A$ and $Edge_B$, then the offset can be calculated as the sum of them ($Offset^{AB} = Edge_A + Edge_B$). Single edge of the distribution was estimated by the analysis of the informations carried out by the first and the second derivative. It was assumed that the invariant point of the edge is the inflection point.

The first derivative is used for the restriction of the fitting range near maximum or minimum for $Edge_A$ and $Edge_B$, respectively. The fitting range is adapted to the second derivative, and more precisely to the estimation of the zero point in this range. Linear fit $\rightarrow a \cdot t_{BA} + b$ is performed in restricted range and a zero points is estimated as $-\frac{b}{a}$. An example of the $t_{BA}$ distribution for different thresholds with the results of edge determination is shown in Fig. 3.2 and 3.4.

For the calibration purposes one side of the scintillator (side A) is chosen as a reference side, when the other side (side B) is corrected by $Offset^{AB}/2$ such that $t_B^{corrected} = t_B - Offset^{AB}/2$. The initial and resulting from the calibration $t_{BA}$ for every scintillator and for each threshold can be seen in Fig. 3.4. Calibration of a single detection module allows for a proper estimation

of the position and time of the hit, resulting in a better quality of the reconstructed hits. Next part will focus on the synchronization between modules to obtain the best spatial resolution on the reconstructed images, that is based on the time difference between two hits, like in Fig. 2.1.

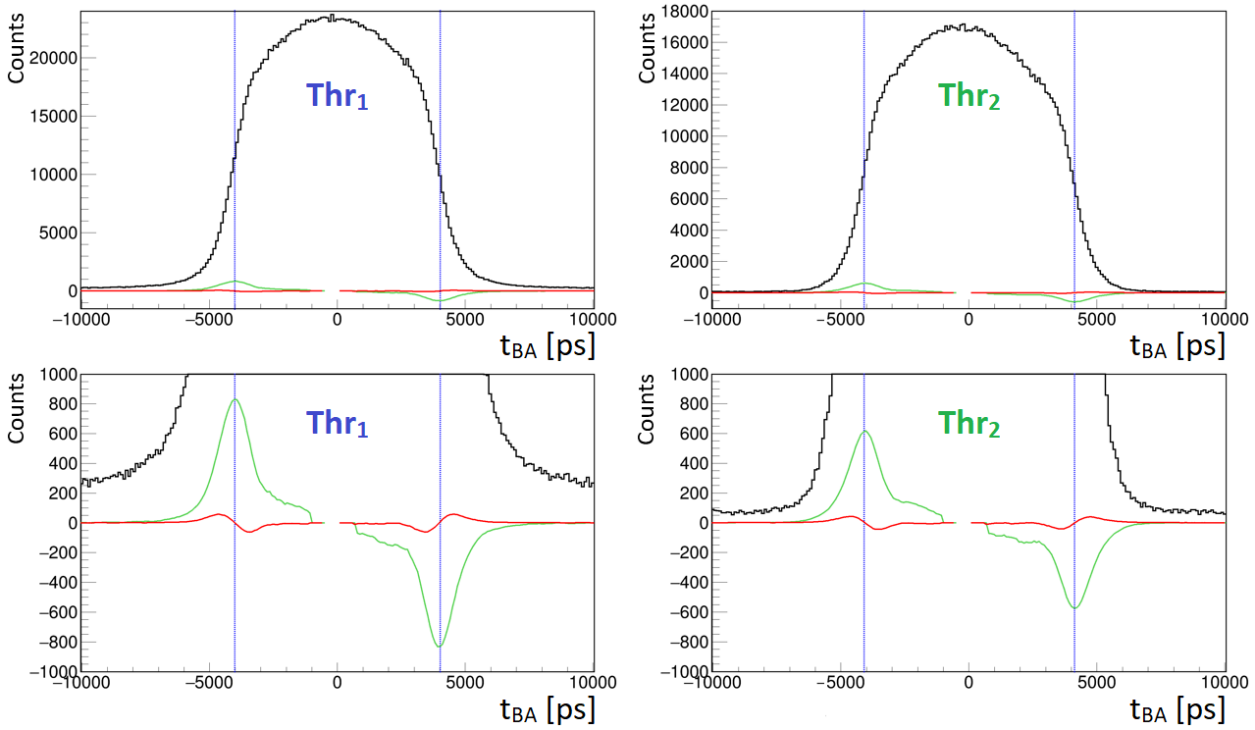


Figure 3.2: **Determination of the $t_{BA}$ edges for the first ($Thr_1$) and the second threshold ($Thr_2$).** Experimental data. Example of the estimation of the edges of the $t_{BA}$ distribution by means of its derivatives for scintillator with ID equal to 1. For every $t_{BA}$ distribution (black, solid line) one can calculate the first (green, solid line) and the second (red, solid line) derivative. A blue vertical dashed line indicates the estimated inflection point. For convenience, the charts at the bottom are the charts at the top in a narrower vertical range.

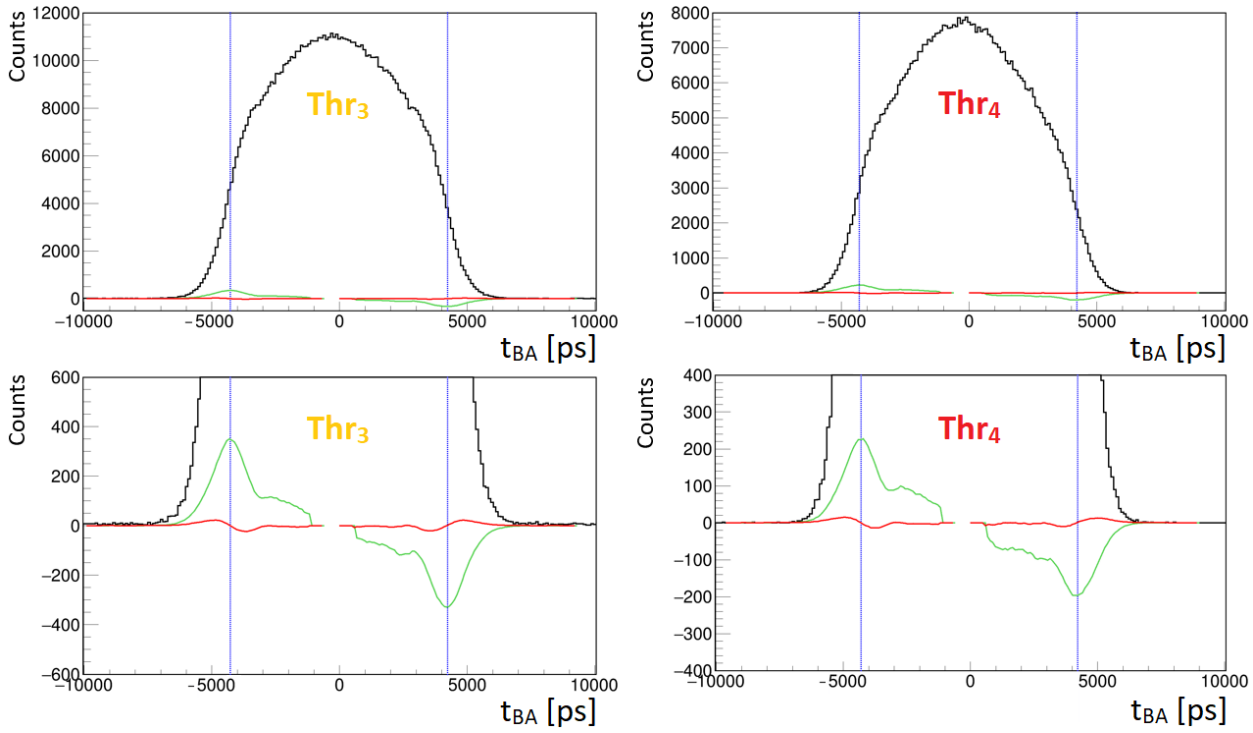


Figure 3.3: **Determination of the $t_{BA}$ edges for the third ($Thr_3$) and the fourth threshold ($Thr_4$).** Experimental data. Example of the estimation of the edges of the $t_{BA}$ distribution by means of its derivatives for scintillator with ID equal to 1. For every $t_{BA}$ distribution (black, solid line) one can calculate the first (green, solid line) and the second (red, solid line) derivative. A blue vertical dashed line indicates the estimated inflection point. For convenience, the charts at the bottom are the charts at the top in a narrower vertical range.

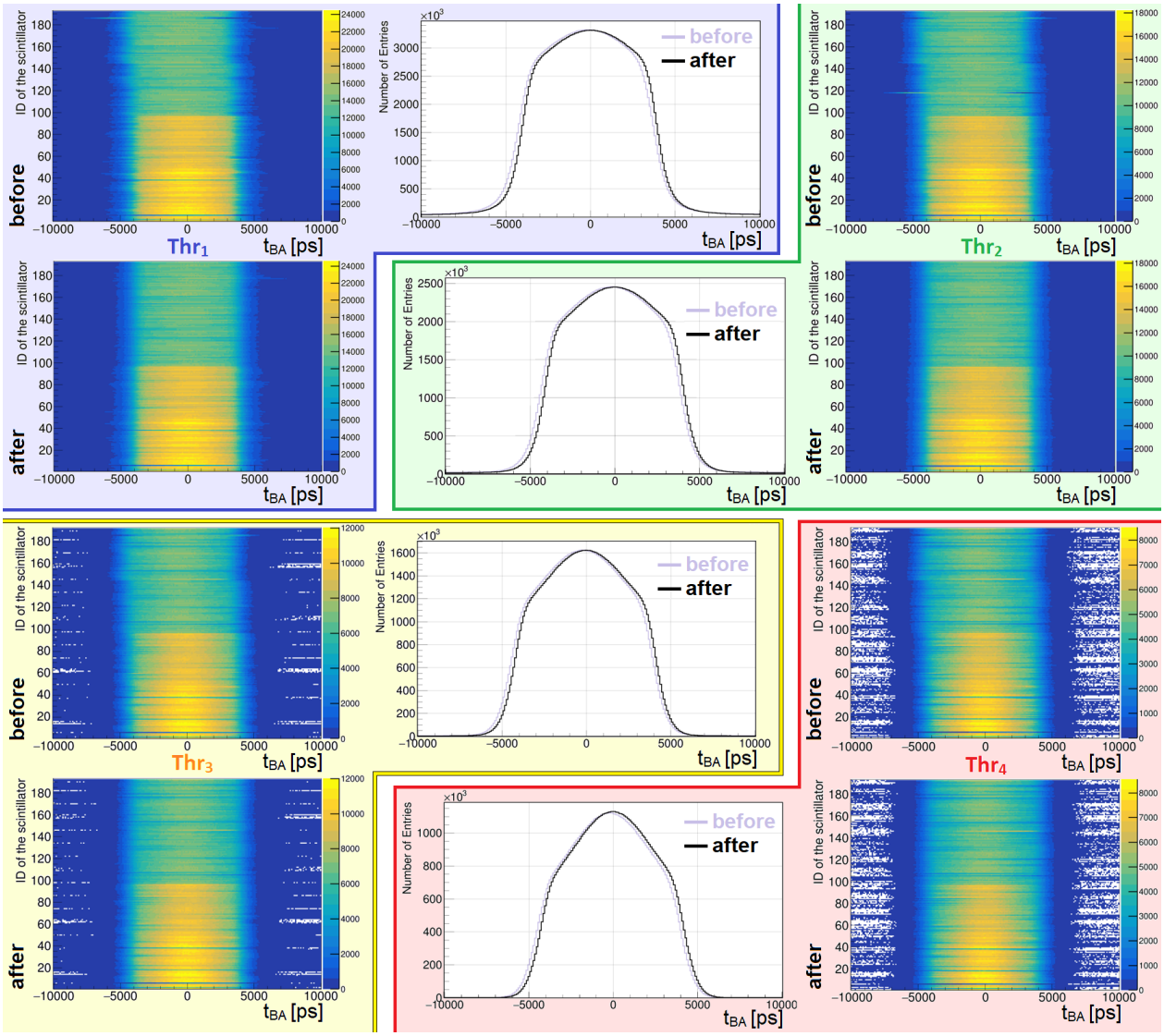


Figure 3.4: **Results from the calibration of a single module.** Experimental data. Comparison of the $t_{BA}$ distributions for each scintillator and for each threshold **before** and **after** applying calibration. Each threshold is marked with different area: first (blue), second (green), third (yellow) and fourth (red). In addition projection of $t_{BA}$ over all scintillators for each threshold separately are shown before (light violet) and after calibration (black) in the middle. Slight differences between the distributions before and after calibration indicate that the detectors have been stable since the previous calibration performed about two years earlier.

## 3.2 Time calibration by positron lifetime distribution

There is a couple of established methods that can be used to calibrate detection modules of the PET scanners. One can especially highlight two main methods: with large phantom or with rotating reference detector. These are described in more detail in the Appendix A.

Both methods require additional setup inserted inside the detection chamber, and its precise location in order to properly calibrate the detection system. Here, a new method of time calibration, based on the measurement with a single point-like source and positron lifetime distribution will be described. In addition, its application and results from the calibration of the J-PET detector will be shown in the next section. That method was briefly described in [102], and its enhancement based on the decomposition of the lifetime spectrum and extracting p-Ps component was proposed in [103]

First, one can focus on a single positron lifetime spectrum, created for pair of detectors like in Fig. 1.4. The idea of calibration that will be described later is shown in Fig. 3.7 (top). To collect lifetime spectrum one detector ($\mathrm{detector_1}$) should register photons coming from the deexcitation of the positron-emitter isotope ($\mathrm{t_{1275}}$) when the second detector ($\mathrm{detector_2}$) registers single photons from the annihilation of positron-electron pair ($\mathrm{t_{511}}$). When both detectors registered desired photons, a lifetime of a single positron can be estimated as time difference between those signals ($\mathrm{LF_{positron}} = \mathrm{t_{511}}$ - $\mathrm{t_{1275}}$). The distinction between annihilation and deexcitation photons can be obtained based on the $\mathrm{TOT_{hit}}$ value, shown in Fig. 2.5 a). If the positions of the isotope emitting positrons and the positron annihilation are very close (at position $\mathrm{r_0}$, $\mathrm{LF_{positron}}$ for given pair of detectors $(\mathrm{detector_1}, \mathrm{detector_2})$ can be defined like

$$\begin{aligned}\mathrm{LF_{positron}}\left(\mathrm{detector_1}, \mathrm{detector_2}\right) = \mathrm{t_{511}} - \mathrm{t_{1275}} = \left(\mathrm{t_{detector_2}} + \mathrm{TOF}_{\mathrm{r_0}}^{\mathrm{detector_2}}\right) - \\ - \left(\mathrm{t_{detector_1}} + \mathrm{TOF}_{\mathrm{r_0}}^{\mathrm{detector_1}}\right) = \mathrm{t_{detector_2}} - \mathrm{t_{detector_1}} + \Delta\mathrm{TOF}_{\mathrm{r_0}}\left(\mathrm{detector_2}, \mathrm{detector_1}\right),\end{aligned} \tag{3.1}$$

where $\mathrm{t}_i$ is the time of registering signal at $i^{th}$ detector, $\mathrm{TOF}_{\mathrm{r_0}}^{i}$ is the time that photons needs to travel (Time of Flight) from $\mathrm{r_0}$ to the position of the $i^{th}$ detector and finally $\Delta\mathrm{TOF}_{\mathrm{r_0}}\left(\mathrm{detector}_i, \mathrm{detector}_j\right)$ is the time difference between $\mathrm{TOF}_{\mathrm{r_0}}^{i}$ and $\mathrm{TOF}_{\mathrm{r_0}}^{j}$. If the $\mathrm{r_0}$ is equidistant from both detectors then $\Delta\mathrm{TOF}_{\mathrm{r_0}}\left(\mathrm{detector_2}, \mathrm{detector_1}\right) = 0$. However, in different situation when the $\mathrm{r_0}$ is known, $\mathrm{LF_{positron}}$ can be corrected by constant for a given pair of detectors value of $\Delta\mathrm{TOF}_{\mathrm{r_0}}\left(\mathrm{detector_2}, \mathrm{detector_1}\right)$. Times of the signals for $i^{th}$ detector, that was corrected on TOF will be given as $\mathrm{t}_i^{\mathrm{emission}} = \mathrm{t}_i - \mathrm{TOF}_{\mathrm{r_0}}^{i}$.

In the above considerations there was no influence of the miscalibration of two given detectors. If there is some offset, the measured times $\mathrm{t}_i^{\mathrm{emission}}$ can be rewritten as

$$\mathrm{t}_i^{\mathrm{emission}} = \mathrm{t}_i^{\mathrm{real}} + \mathrm{Offset}_i$$

for a given $i^{th}$ detector, where $\mathrm{t}_i^{\mathrm{real}}$ is the time of registering given photon by $i^{th}$ detector for perfectly calibrated detector, corrected on TOF. The $\mathrm{LF_{positron}}$ corrected on TOF will be equal to

$$\begin{aligned}\mathrm{LF_{positron}}\left(\mathrm{detector_1}, \mathrm{detector_2}\right) = \mathrm{t_{511}} - \mathrm{t_{1275}} = \mathrm{t}_{\mathrm{detector_2}}^{\mathrm{emission}} - \mathrm{t}_{\mathrm{detector_1}}^{\mathrm{emission}} = \\ \left(\mathrm{t}_{\mathrm{detector_2}}^{\mathrm{real}} + \mathrm{Offset_{detector_2}}\right) - \left(\mathrm{t}_{\mathrm{detector_1}}^{\mathrm{real}} + \mathrm{Offset_{detector_1}}\right) = \\ \mathrm{t}_{\mathrm{detector_2}}^{\mathrm{real}} - \mathrm{t}_{\mathrm{detector_1}}^{\mathrm{real}} + \left(\mathrm{Offset_{detector_2}} - \mathrm{Offset_{detector_1}}\right).\end{aligned} \tag{3.2}$$

Such situation cause that the $\mathrm{LF}_{\mathrm{positron}}$ distribution will be shifted by $\mathrm{Offset}_2^{(1)} = \mathrm{Offset}_{\mathrm{detector}_2}$ - $\mathrm{Offset}_{\mathrm{detector}_1}$. $\mathrm{Offset}_2^{(1)}$ is usually not so easy to calculate as it requires knowledge of a non-shifted distribution. On the other hand, if one would change the role of the detectors in a sense that now the $\mathrm{detector}_1$ registers annihilation and the $\mathrm{detector}_2$ deexcitation photons then

$$\mathrm{LF}_{\mathrm{positron}}^{\mathrm{reversed}}\left(\mathrm{detector}_1, \mathrm{detector}_2\right) = \mathrm{t}_{511} - \mathrm{t}_{1275} = \mathrm{t}_{\mathrm{detector}_1}^{\mathrm{real}} - \mathrm{t}_{\mathrm{detector}_2}^{\mathrm{real}} + \left(\mathrm{Offset}_{\mathrm{detector}_1} - \mathrm{Offset}_{\mathrm{detector}_2}\right). \tag{3.3}$$

In that configuration the $\mathrm{LF}_{\mathrm{positron}}^{\mathrm{reversed}}$ distribution will be shifted by $\mathrm{Offset}_{\mathrm{detector}_1}$ - $\mathrm{Offset}_{\mathrm{detector}_2}$ = -$\mathrm{Offset}_2^{(1)}$. Therefore, comparing two distributions $\mathrm{LF}_{\mathrm{positron}}$ and $\mathrm{LF}_{\mathrm{positron}}^{\mathrm{reversed}}$ for $\mathrm{detector}_2$ the shift between them ($\Delta$LF) will be equal to

$$\Delta\mathrm{LF} = \mathrm{LF}_{\mathrm{positron}}\left(\mathrm{detector}_1, \mathrm{detector}_2\right) - \mathrm{LF}_{\mathrm{positron}}^{\mathrm{reversed}}\left(\mathrm{detector}_1, \mathrm{detector}_2\right) \overset{3.2,3.3}{=} 2 \cdot \mathrm{Offset}_2^{(1)} = 2 \cdot \mathrm{Correction}_2^{(1)}. \tag{3.4}$$

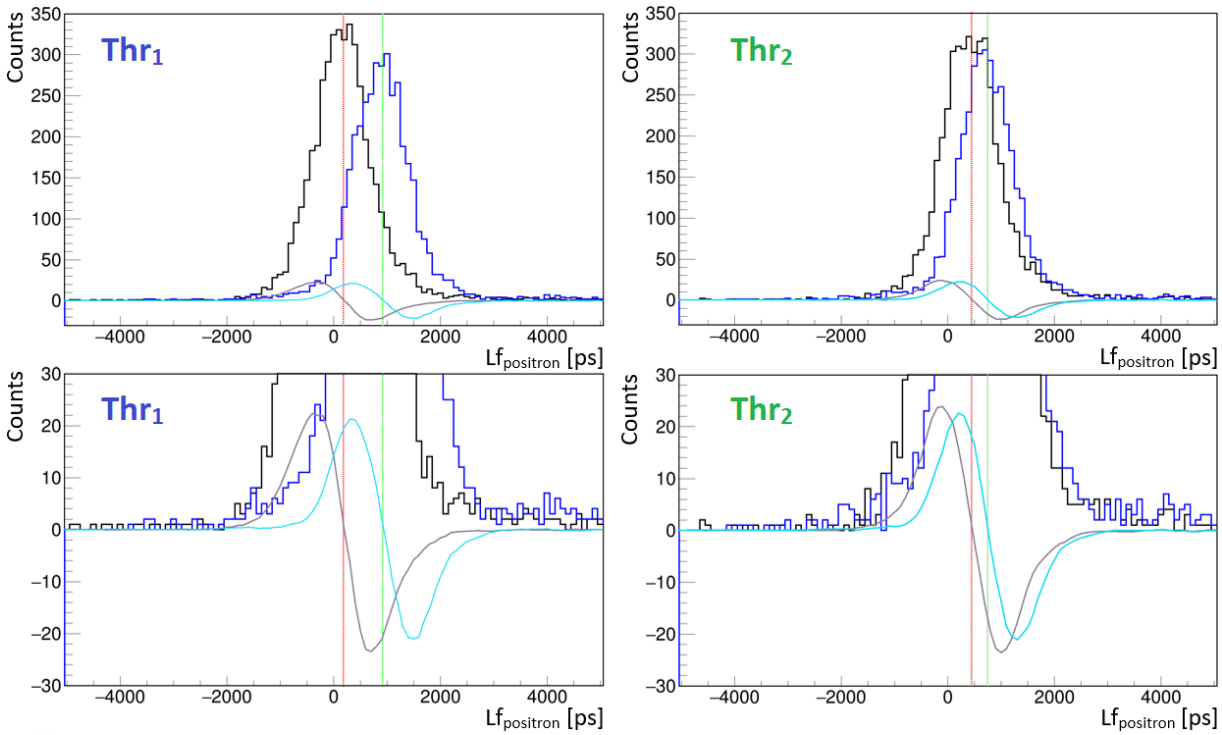


Figure 3.5: **Determination of the $\mathrm{LF}_{\mathrm{positron}}$ and $\mathrm{LF}_{\mathrm{positron}}^{\mathrm{reversed}}$ maxima for the first ($\mathrm{Thr}_1$) and the second ($\mathrm{Thr}_2$) threshold.** Experimental data. Example of the estimation of the maxima of the $\mathrm{LF}_{\mathrm{positron}}$ and $\mathrm{LF}_{\mathrm{positron}}^{\mathrm{reversed}}$ distributions by means of its derivative for scintillator with ID equal to 1. For every $\mathrm{LF}_{\mathrm{positron}}$ (black) and $\mathrm{LF}_{\mathrm{positron}}^{\mathrm{reversed}}$ (blue) distributions one can calculate the first derivatives marked by grey and light blue, respectively. A red and green vertical dashed lines indicates the estimated maxima point for grey and light blue derivatives. For convenience, the charts at the bottom are the charts at the top in a narrower vertical range.

So in theory for a pair of detectors one can calibrate one with another just by matching the positron lifetime spectra. Shift of the distribution can be estimated based on the values of argmax ($\mathrm{LF}_{\mathrm{positron}}$) and argmax ($\mathrm{LF}^{\mathrm{reversed}}_{\mathrm{positron}}$), where argmax is the function that finds the most probable value of the distribution. Therefore, $\mathrm{Correction}_2^{(1)}$ will be equal to half of the shift between distributions, following Eq. 3.4. Argmax of the $\mathrm{LF}_{\mathrm{positron}}$ and $\mathrm{LF}^{\mathrm{reversed}}_{\mathrm{positron}}$ distributions was determined as a zero of the first derivative. Linear fit is performed in close range of the maximum bin of the origin distribution $\rightarrow a \cdot \mathrm{t_{BA}} + b$ and a zero points is estimated as $-\frac{b}{a}$. Example of how to calculate argmax for different thresholds is shown in Fig. 3.5 and 3.6

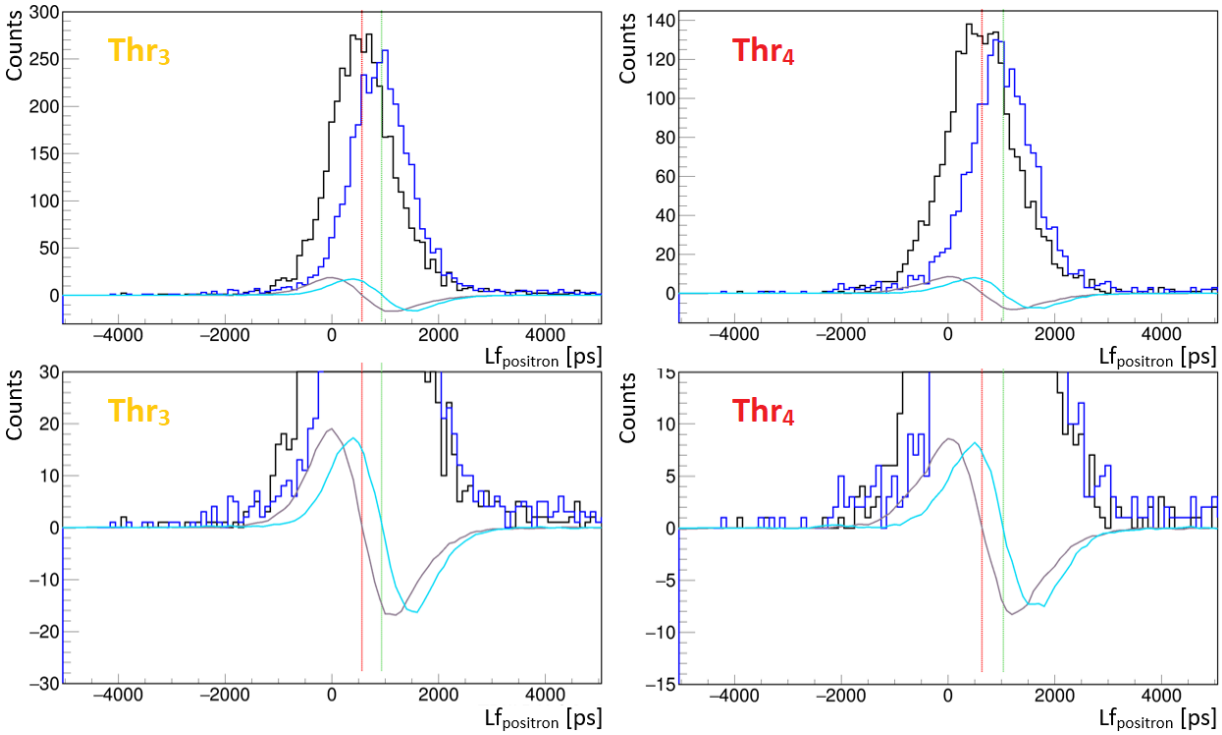


Figure 3.6: **Determination of the $\mathbf{LF_{positron}}$ and $\mathbf{LF^{reversed}_{positron}}$ maxima for the third ($\mathbf{Thr_3}$) and the fourth ($\mathbf{Thr_4}$) threshold.** Experimental data. Example of the estimation of the maxima of the $\mathrm{LF}_{\mathrm{positron}}$ and $\mathrm{LF}^{\mathrm{reversed}}_{\mathrm{positron}}$ distributions by means of its derivative for scintillator with ID equal to 1. For every $\mathrm{LF}_{\mathrm{positron}}$ (black) and $\mathrm{LF}^{\mathrm{reversed}}_{\mathrm{positron}}$ (blue) distributions one can calculate the first derivatives marked by grey and light blue, respectively. A red and green vertical dashed lines indicates the estimated maxima point for grey and light blue derivatives. For convenience, the charts at the bottom are the charts at the top in a narrower vertical range.

## 3.3 Time calibration of the J-PET detector

Based on the previous section, in order to calibrate all modules one could assume one detector as a reference and calibrate the rest to it. However it can be achieved also in simpler and more efficient way for such configurations, what will be discussed after the description of the method. Idea is to calibrate each module separately to some virtual reference detector that

will be represented as a mean detector. Idea of that approach is shown in Fig. 3.7 (middle). At the beginning one needs first to select proper data sample for calibration. On this level of analysis it is assumed that hits are already reconstructed based on the time windows given in Sec. 2.3 and each scintillator is calibrated by sides. In addition for simplicity the Z position is reconstructed as in Fig. 2.1 with the velocity of light in scintillator equal to 12 cm/ns. More sophisticated method of estimating velocity of light in each scintillator separately will be described in the next section, by means of the effective length determination. Each hit was corrected on TOF, following Eg. 3.1, based on the assumed position of the source - (0, 0, 0).

To calculate the positron lifetime in each event there should be at least one annihilation hit and only one deexcitation hit in event. However, only events with only one annihilation hit will be selected to avoid ambiguity. For the same reason and to reduce the influence of the additional coincidences requirement of having only one deexcitation hit is introduced. Selection of each type of hit is based on the TOT value with cuts shown in Fig. 2.5. For each threshold and scintillator two distributions will be considered, similar to those described in the previous section. For a given scintillator with ID equal to $k$, $\mathrm{LF}_{\mathrm{positron}}$ and $\mathrm{LF}^{\mathrm{reversed}}_{\mathrm{positron}}$ distributions will be defined as

$$\mathrm{LF}_{\mathrm{positron}}\left(\mathrm{detector}_k\right) = \sum_{\substack{j\in[1,192]\\ j\neq k}} \mathrm{LF}_{\mathrm{positron}}\left(\mathrm{detector}_k, \mathrm{detector}_j\right), \tag{3.5}$$

$$\mathrm{LF}^{\mathrm{reversed}}_{\mathrm{positron}}\left(\mathrm{detector}_k\right) = \sum_{\substack{j\in[1,192]\\ j\neq k}} \mathrm{LF}^{\mathrm{reversed}}_{\mathrm{positron}}\left(\mathrm{detector}_k, \mathrm{detector}_j\right). \tag{3.6}$$

Calculation of the offset can be derived from either Eq. 3.5 or Eq. 3.6, following logic from Eq. 3.2, 3.3. Expanding Eq. 3.5 will lead to

$$\mathrm{LF}_{\mathrm{positron}}\left(\mathrm{detector}_k\right) = \sum_{\substack{j\in[1,192]\\ j\neq k}} \left(\mathrm{t}^{\mathrm{real}}_{\mathrm{detector}_k} + \mathrm{Offset}_{\mathrm{detector}_k}\right) - \left(\mathrm{t}^{\mathrm{real}}_{\mathrm{detector}_j} + \mathrm{Offset}_{\mathrm{detector}_j}\right) =$$

$$\sum_{\substack{j\in[1,192]\\ j\neq k}} \left(\mathrm{t}^{\mathrm{real}}_{\mathrm{detector}_k} - \mathrm{t}^{\mathrm{real}}_{\mathrm{detector}_j}\right) + \sum_{\substack{j\in[1,192]\\ j\neq k}} \left(\mathrm{Offset}_{\mathrm{detector}_k} - \mathrm{Offset}_{\mathrm{detector}_j}\right) = \ldots$$

putting the mean offset as

$$\mathrm{Offset}_{\mathrm{G}}(k) = \mathbb{E}\mathrm{Offset} = \frac{1}{191} \sum_{\substack{j\in[1,192]\\ j\neq k}} \mathrm{Offset}_{\mathrm{detector}_j} \tag{3.7}$$

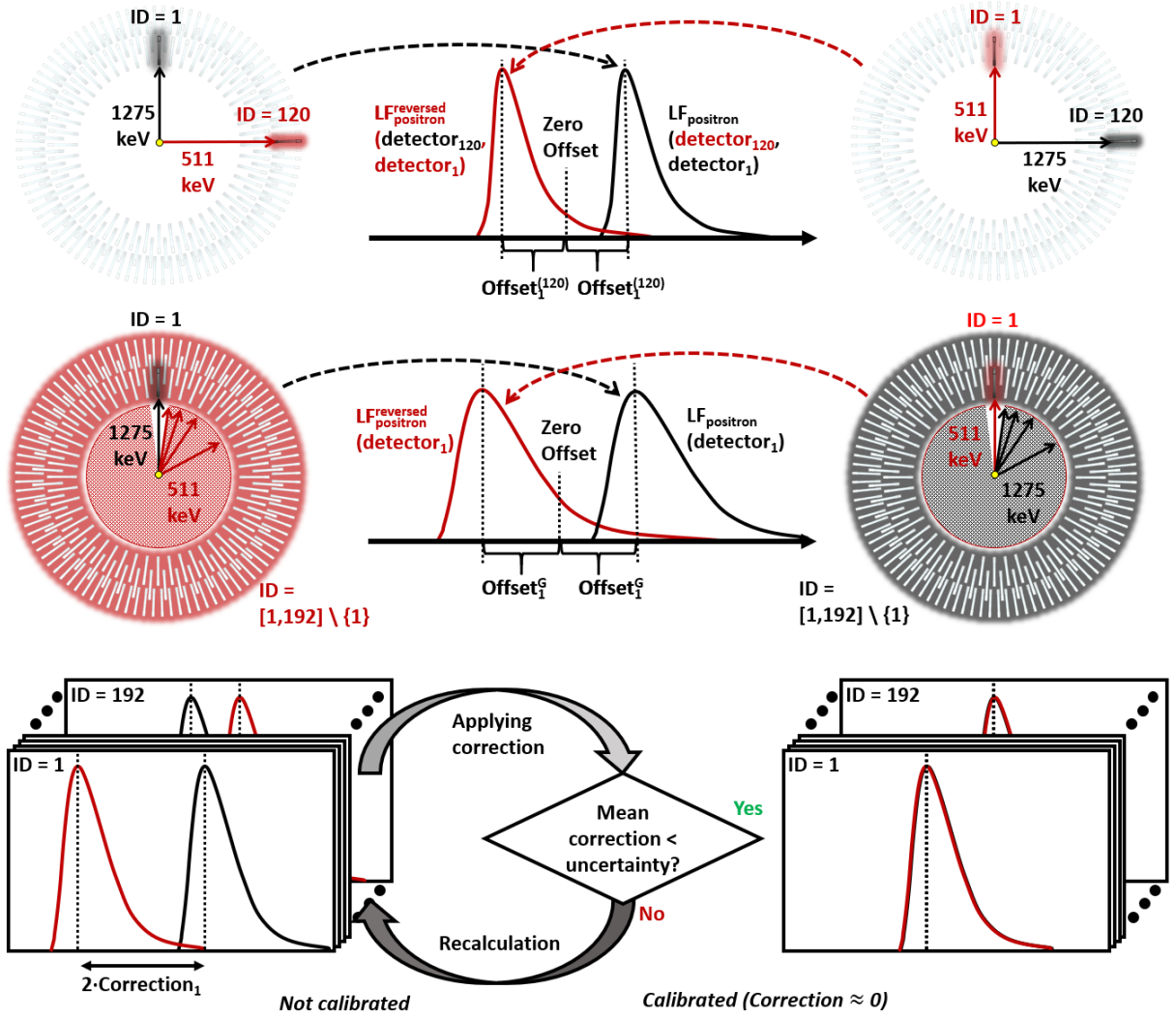


Figure 3.7: **Scheme of the calibration procedure of the J-PET detector.** (top) Time calibration of the detector with ID equal to 1 in reference to detector with ID equal to 120 can be performed based on the creation of the positron lifetime distributions between them defined as in Eq. 3.2 and 3.3. Both distributions will be shifted by $\mathrm{Offset}_1^{(120)}$ in opposite direction if there will be some miscalibration between detectors. Detector with ID equal to 1 can be calibrated by calculating value of the shift between $\mathrm{LF}_{\mathrm{positron}}$ and $\mathrm{LF}^{\mathrm{reversed}}_{\mathrm{positron}}$ and dividing it by two. (middle) Similar approach may be used without chosing one reference detector. Scintillator with ID equal to 1 can be calibrated to some virtual reference detector that will be created by summing over all other detectors. Correction for a scintillator can be calculated as half of the shift between $\mathrm{LF}_{\mathrm{positron}}$ and $\mathrm{LF}^{\mathrm{reversed}}_{\mathrm{positron}}$ distributions. These are created for coincidences between the first and the rest of the detection modules. (bottom) Calibration procedure can be performed iteratively. In each iteration correction is calculated (like in middle part) and applied to each detector. Calibration is done until mean correction are lower than uncertainty of its determining. After calibration the difference between $\mathrm{LF}_{\mathrm{positron}}$ and $\mathrm{LF}^{\mathrm{reversed}}_{\mathrm{positron}}$ for each scintillator should be negligible.

one can continue that

$$\ldots = \sum_{\substack{j\in[1,192]\\ j\neq k}} \left(\mathrm{t}^{\mathrm{real}}_{\mathrm{detector}_k} - \mathrm{t}^{\mathrm{real}}_{\mathrm{detector}_j}\right) + \sum_{\substack{j\in[1,192]\\ j\neq k}} \left(\mathrm{Offset}_{\mathrm{detector}_k} - \mathrm{Offset}_{\mathrm{G}}(k)\right) =$$

$$\sum_{\substack{j\in[1,192]\\ j\neq k}} \left(\mathrm{t}^{\mathrm{real}}_{\mathrm{detector}_k} - \mathrm{t}^{\mathrm{real}}_{\mathrm{detector}_j} + \mathrm{Offset}_{\mathrm{detector}_k} - \mathrm{Offset}_{\mathrm{G}}(k)\right) =$$

$$\sum_{\substack{j\in[1,192]\\ j\neq k}} \left(\mathrm{t}^{\mathrm{real}}_{\mathrm{detector}_k} - \mathrm{t}^{\mathrm{real}}_{\mathrm{detector}_j} + \mathrm{Offset}^{\mathrm{G}}_{k}\right), \tag{3.8}$$

where $\mathrm{Offset}^{\mathrm{G}}_{k} = \mathrm{Offset}_{\mathrm{detector}_k} - \mathrm{Offset}_{\mathrm{G}}$. It is also worth to noting, that $\mathrm{Offset}_{\mathrm{G}}$ depends very little on index of the scintillator $k \in [1, 192] \cap \mathbb{N}$. When looking at difference of the $\mathrm{Offset}_{\mathrm{G}}(k)$ for some $k_1$ and $k_2$ one can show that

$$\Delta\mathrm{Offset}_{\mathrm{G}}\left(k_1, k_2\right) = \mathrm{Offset}_{\mathrm{G}}\left(k_1\right) - \mathrm{Offset}_{\mathrm{G}}\left(k_2\right) \overset{3.7}{=} \frac{\mathrm{Offset}_{\mathrm{detector}_{k_1}} - \mathrm{Offset}_{\mathrm{detector}_{k_2}}}{191}. \tag{3.9}$$

Assuming that $\mathrm{Offset}_{\mathrm{G}}(k) \sim \mathcal{U}\left(0, \mathrm{TW}_{\mathrm{Off}}\right)$, where

$$\mathrm{TW}_{\mathrm{Off}} = \max_{k_i, k_j \in [1,192]\cap\mathbb{N}} |\mathrm{Offset}_{\mathrm{detector}_{k_i}} - \mathrm{Offset}_{\mathrm{detector}_{k_j}}|,$$

and $\mathcal{U}$ denotes uniform distribution one can show that $\Delta\mathrm{Offset}_{\mathrm{G}}\left(k_1, k_2\right)$ will follow triangular distribution with full width at half maximum (FWHM) equal to $\frac{\mathrm{TW}_{\mathrm{Off}}}{191}$. When calibrating to some perfect virtual reference detector with some mean offset equal to

$$\mathrm{Offset}_{\mathrm{virtual}} = \min_{k\in[1,192]\cap\mathbb{N}} \left(\mathrm{Offset}_{\mathrm{detector}_k}\right) + \frac{\mathrm{TW}_{\mathrm{Off}}}{2}$$

maximal correction that can be applied, will be equal to $\frac{\mathrm{TW}_{\mathrm{Off}}}{2}$. This is two orders greater than the FWHM of the $\Delta\mathrm{Offset}_{\mathrm{G}}\left(k_1, k_2\right)$ distribution that represents possible uncertainties in determining correction for a given scintillator, with method described by using Eq. 3.7 and 3.8. In fact, if offsets for different scintillators were spread over a narrower range, the calibration uncertainty would also decrease. To obtain the highest accuracy of the calibration method described here, calibration can be performed iteratively, until mean correction in given iteration is lower than uncertainty of determining position of the maximum of the $\mathrm{LF}_{\mathrm{positron}}$ and $\mathrm{LF}^{\mathrm{reversed}}_{\mathrm{positron}}$. Iterative approach is depicted in Fig. 3.7 (bottom).

In addition, $\mathrm{Offset}^{\mathrm{G}}_{k}$ represents offset of the $\mathrm{LF}_{\mathrm{positron}}$ for all of the coincidences between $\mathrm{detector}_k$ and every other detector, in which annihilation photon was registered in the $\mathrm{detector}_k$. In mirror situation with $\mathrm{LF}^{\mathrm{reversed}}_{\mathrm{positron}}$ an offset will be equal to $-\mathrm{Offset}^{\mathrm{G}}_{k}$, and it covers all situations in which deexcitation photon was registered in the $\mathrm{detector}_k$. To sum up, correction for a given scintillator can be derived in similar manner that it was shown by Eq. 3.4

$$\Delta\mathrm{LF} = \mathrm{LF}_{\mathrm{positron}}\left(\mathrm{detector}_k\right) - \mathrm{LF}^{\mathrm{reversed}}_{\mathrm{positron}}\left(\mathrm{detector}_k\right) \overset{3.4,3.8}{=} 2\cdot\mathrm{Offset}^{\mathrm{G}}_{k} = 2\cdot\mathrm{Correction}_k, \tag{3.10}$$

for which Correction$_k$ is calculated when the reference detector was chosen as a virtual detector shifted in time by Offset$_G$.

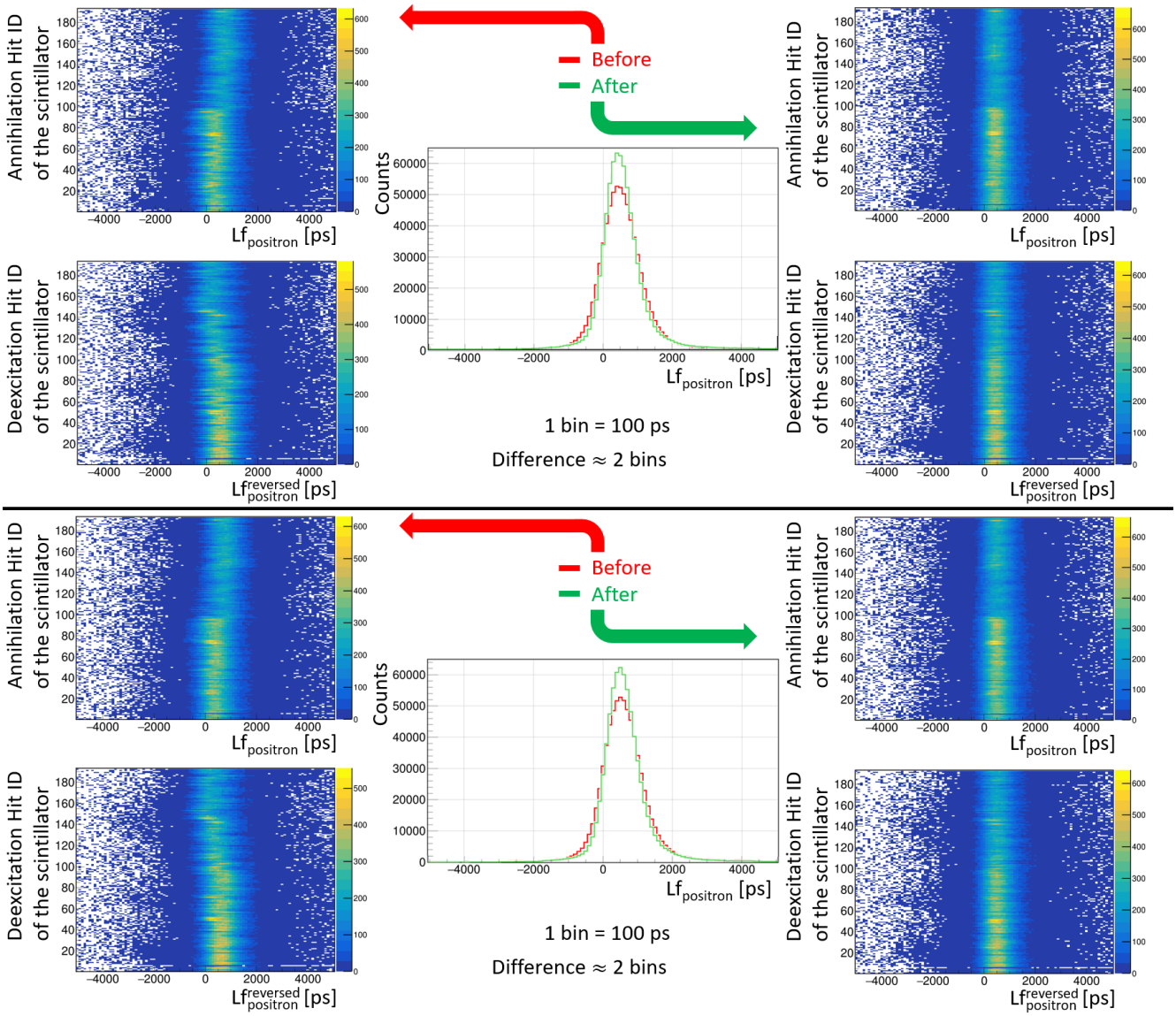


Figure 3.8: **Results from the time calibration of the J-PET detector for the first an the second threshold.** Experimental data. Comparison of the LF$_{positron}$ and LF$^{reversed}_{positron}$ distributions for each scintillator and for the first (above black line) and the second (below black line) threshold before(left) and after (right) applying calibration. In addition, projection of LF$_{positron}$ over all scintillators for each threshold separately are shown before (green) and after (red) calibration. The time resolution was improved by approximately 200 ps.

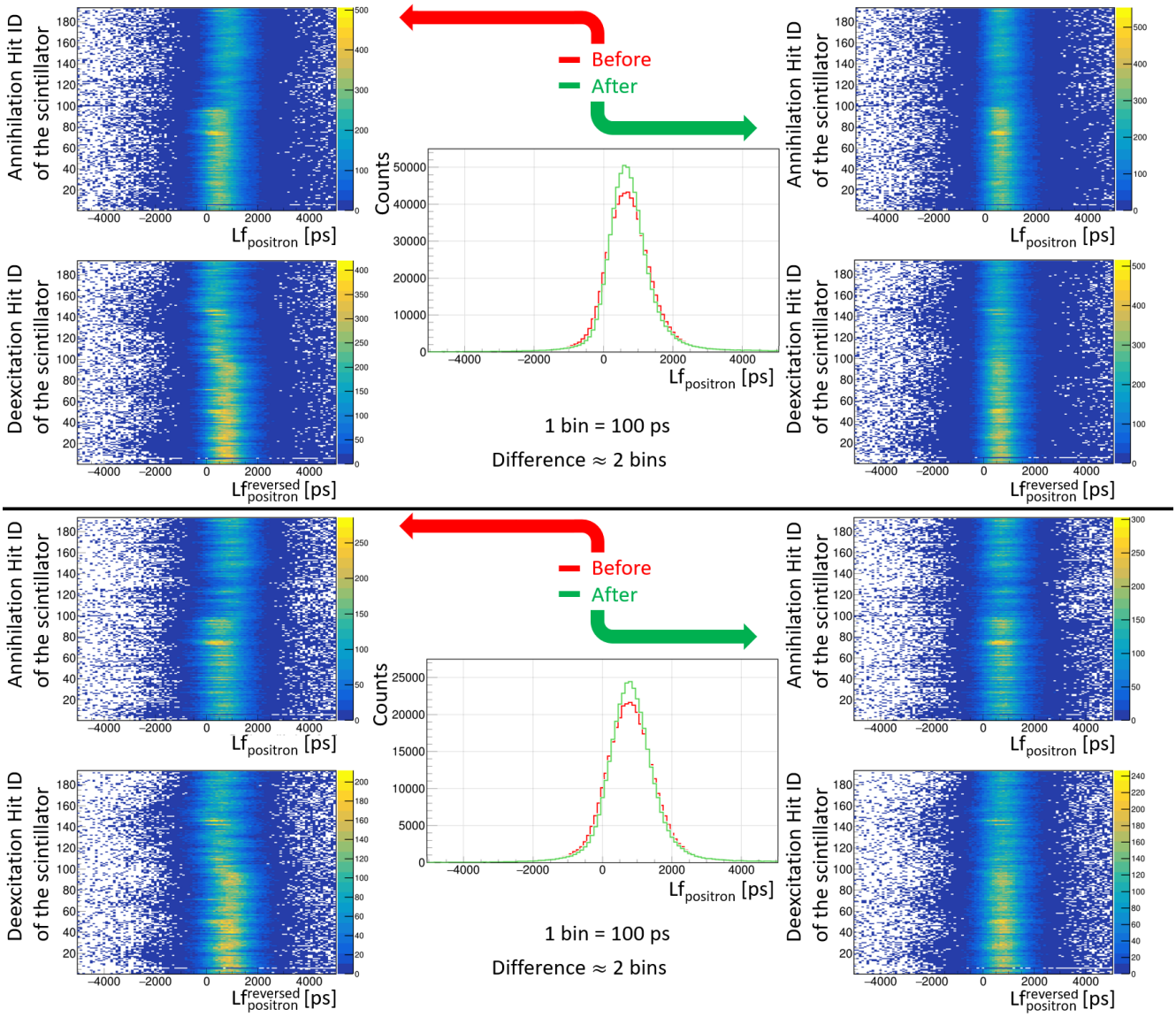


Figure 3.9: **Results from the time calibration of the J-PET detector for the third an the fourth threshold.** Experimental data. Comparison of the $\mathrm{LF}_{\mathrm{positron}}$ and $\mathrm{LF}^{\mathrm{reversed}}_{\mathrm{positron}}$ distributions for each scintillator and for the third (above black line) and the fourth (below black line) threshold before(left) and after (right) applying calibration. In addition, projection of $\mathrm{LF}_{\mathrm{positron}}$ over all scintillators for each threshold separately are shown before (green) and after (red) calibration. The time resolution was improved by approximately 200 ps.

The main advantage of the presented approach is in the amount of data that needs to be collected for calibration, comparing to the calibration to one chosen detector. For a single scintillator, considering all coincidences like in Eq. 3.10, instead of one represented by Eq. 3.4 increases total number of counts of considered distributions by 190. Thus, it reduces the time needed for measurement by the same fraction making it more efficient. Distributions $\mathrm{LF}_{\mathrm{positron}}\,(\mathrm{detector}_k)$ and $\mathrm{LF}^{\mathrm{reversed}}_{\mathrm{positron}}\,(\mathrm{detector}_k)$ for the measurement with XAD4 before and

after calibration can be seen in Fig. 3.8 and 3.9. Correction as a function of the scintillator ID for different thresholds for the first and the last iteration (seventh) is shown in Appendix in Fig. B.1 to B.5. In order not to change the calibration between side A and B, final correction for each photomultiplier connected to $k^{th}$ scintillator will be equal to $\text{Correction}_k/2$.

## 3.4 Effective length determination

As the last calibration procedure determination of the effective length will be described. It will be shown later that the effective length is a function of the velocity of light in the scintillator, what would be helpful in the finding of a proper calibration measure. It's best to start by focusing on the speed of light signal in the scintillator material. In Sec. 3.3, an assumption was made about the speed of light signal in the scintillator (v), which was used to calculate the position along the scintillator (Z position) and therefore to enable correction hits on TOF. Correctly estimating value of v can improve the accuracy of the calibration. Here, specific numerical procedure will be shown that describes how to estimate v for every scintillator separately. It will be achieved by introducing conception of the effective length of the scintillator, which will be defined later.

At first, it would be useful to look at the $\text{t}_{\text{BA}}$ distribution defined in Sec. 3.1. Hits with $\text{t}_{\text{BA}}$ in the nearby of its edges will be consisted of two signals - $\text{Signal}_{\text{A}}$ and $\text{Signal}_{\text{B}}$, that have some interesting feature. Namely, exactly one of the signals will be created from the light that traveled through almost all of the scintillator length ($\text{Signal}_{\text{length}}$). Therefore, $\text{Signal}_{\text{length}}$ will carry information about its velocity in the material of the scintillating strip.

The time it takes for light to travel along the entire scintillator, ultimately creating $\text{Signal}_{\text{length}}$, will be equal to the maximum time difference ($\text{t}_{\text{BA}}^{\text{max}}$) between signals A and B. This time can be estimated from the edges of the $\text{t}_{\text{BA}}$ distribution, determined in Sec. 3.1, and will be equal to $\text{t}_{\text{BA}}^{\text{max}} = \frac{\text{Edge}_{\text{B}} - \text{Edge}_{\text{A}}}{2}$. Division by two comes from the fact, that the time equal either to $\text{Edge}_{\text{A}}$ or $\text{Edge}_{\text{B}}$ will correspond to the $\text{Signal}_{\text{length}}$ that was reconstructed in the photomultiplier A ($\text{Signal}_{\text{length}}^{\text{A}}$) or B ($\text{Signal}_{\text{length}}^{\text{B}}$). $\text{Signal}_{\text{length}}^{\text{A}}$ will come from the light that passed from side B to side A, where $\text{Signal}_{\text{length}}^{\text{B}}$ will travel inversely from side A to side B. Therefore, the difference between the edges will cover the entire length of the scintillator traveled twice in two different directions.

To conclude, knowing for some $i^{th}$ scintillator, that the light will need time $\text{t}_{\text{BA}}^{\text{max}}$ to travel with some velocity $\text{v}_i$ one can define the effective length of the scintillator ($\text{L}_i^{\text{effective}}$) as

$$\text{L}_i^{\text{effective}} = \text{v}_i \cdot \text{t}_{\text{BA}}^{\text{max}(i)}. \tag{3.11}$$

Effective length is corresponding to the length of the scintillator which is sensitive to photons registration. To be more precise, this is the length the light in the strip can travel to reconstruct the signal from it. There are several factors that can affect the value of $\text{L}_i^{\text{effective}}$, with two major ones being mechanical shields or light attenuation in a scintillator. Mechanical shields do not affect the effective length so much, due to the high penetration of photons with energies of several hundred keV. Additionally, the only mechanical targets were aluminium holders in which the ends of the scintillation strip were placed, up to 1 cm per side.

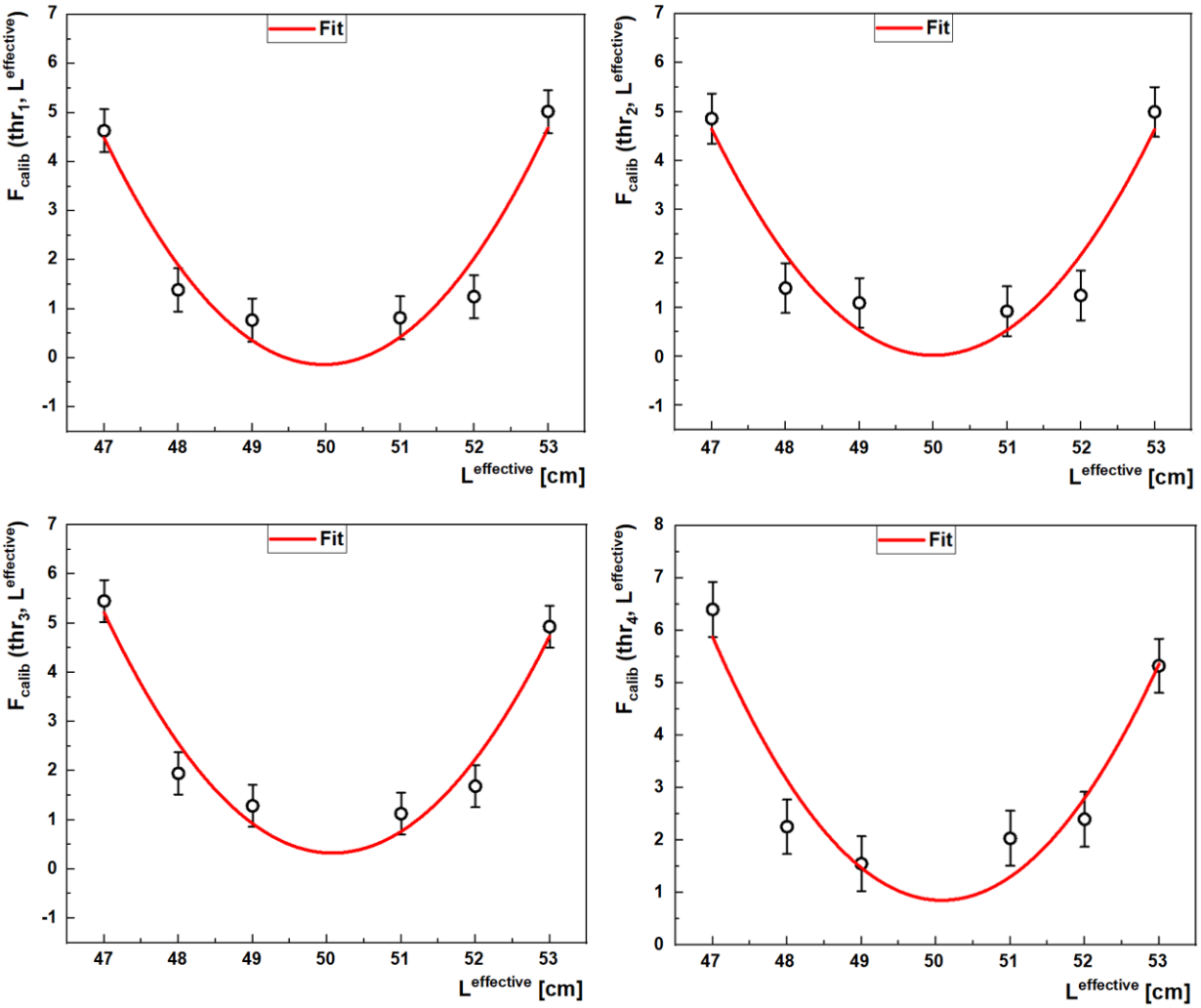


Figure 3.10: **Mean difference of the calibration constants from the reference.** Experimental data. Dependence of the inaccuracy of the calibration ($F_{calib}$) as a function of assumed value of the effective length ($L^{effective}$) for four different thresholds $thr_1$ (left, top), $thr_2$ (right, top), $thr_3$ (left, bottom) and $thr_4$ (right bottom). To estimate optimal value of the effective length $L^{optimal}$ quadratic function $f\left(L^{effective}\right) = A\left(L^{effective} - L^{optimal}\right)^2 + f_0$ has been fitted to each plot.

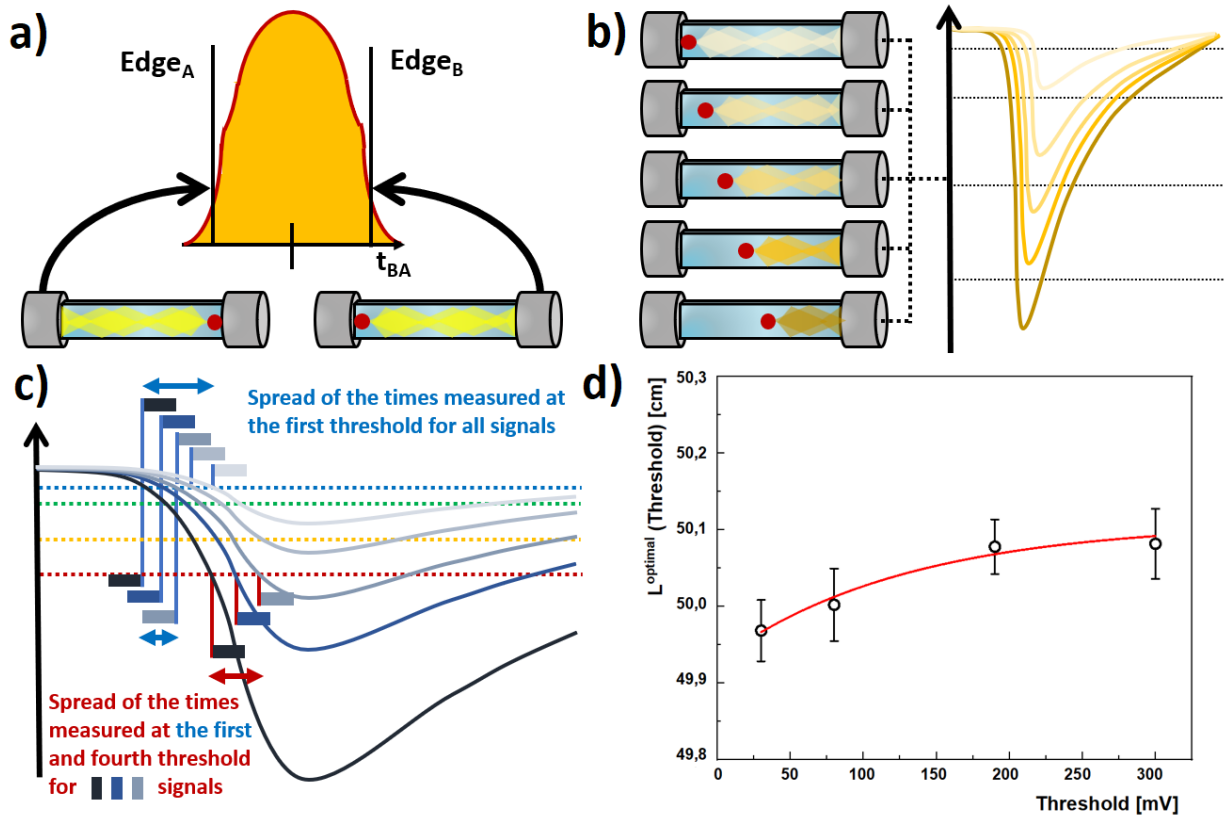


Figure 3.11: **Optimal effective length origin and estimation.** Experimental data. Optimal effective length, which allows to calculate velocity of light in the scintillator, can be estimated based on the $t_{BA}$ distribution. a) Values of the edges of the $t_{BA}$ distribution correspond to the situations where the light passes through the entire length of the scintillator in both directions. Therefore, the difference of the edges ($Edge_A$ and $Edge_B$) will be the time for which the light will travel two scintillator lengths. There are two counteracting main effects b), c) that can influence determination of the optimal effective length for a given threshold. b) During the travel, the light can be attenuated, thereby reducing the resulting signal in one of the photomultipliers, which then may not pass a given threshold. This can reduce the effective scintillator length for the higher thresholds. c) Time of the signal can be probed differently on a given threshold, when the energy of the signal is changing. It results in smearing of the measured time of the signal. This effect, the so-called time-walk, is greater for higher thresholds (blue arrow) than it is for lower threshold (red arrow) when compared for the same signals. However, as a wider spectrum of signals is registered at the lower thresholds, the overall time spread may be greater with the lower thresholds. d) $L^{optimal}$ for different thresholds estimated by fits from Fig. 3.10.

The second factor related to attenuation of light along the strip will reduce the amount of light that will go to the photomultiplier. The light attenuation length for the EJ-230 scintillation strips used is ≈52 cm [92, 93], so the attenuation should also not have a major impact on the effective length. However, if the lowest threshold of the data acquisition system were too high, the light attenuation effect would also increase. As different thresholds have

been used, it will be possible to check how the threshold value affects the effective length.

The method of determining the effective length will be based on Eq. 3.11. One can conclude, that for a given scintillator v and $L^{\text{effective}}$ are proportional to each other by the value of $t_{BA}^{\max(i)}$, which in principal can be estimated from the edges of the $t_{BA}$ distribution. The relationship between the above variables will be used to compute both of them by the following method consisting of several points:

1. Assumption of several values of the $L^{\text{effective}}$ - 47, 48, 49, 50, 51, 52, 53 cm. The same for each scintillator;

2. Calculation of the $v_i$ based on the assumed value of $L^{\text{effective}}$ and Eq. 3.11. It will be different for each scintillator, because of different value of $t_{BA}^{\max(i)}$;

3. Calculation of the position along the strip (Z) for each hit, based on the newly estimated value of $v_i$;

4. Performing calibration, that was described in Sec. 3.3. Different values of $L^{\text{effective}}$ will influence correction on TOF. The closer to the true $L^{\text{effective}}$ value, the more stable the correction constants determined in the calibration process will be;

5. Inaccuracy of the calibration as a function of the $L^{\text{effective}}$ allow to estimate an optimal value of $L^{\text{effective}}$.

As for the second point of the list above, it is worth noting that even if $L^{\text{effective}}$ will change depending on the scintillator, this variability will be compensated by the variable value of $v_i$. The basis of the fourth point is that as value of the $L^{\text{effective}}$ is farther from its true value, the calibration results will be smeared greater reducing accuracy of the calibration. Calculations of the inaccuracy of the calibration, mentioned in the fifth point, will be based on the time calibration constants, that are determined for each scintillator and threshold separately. For a given threshold thr and value of $L^{\text{effective}}$ inaccuracy of the calibration $F_{\text{calib}}$ will be defined as

$$F_{\text{calib}}\left(\text{thr}, L^{\text{effective}}\right) = \frac{1}{192}\sum_{i=1}^{192}|\text{CalibConst}_{\text{thr}}^{L^{\text{effective}}}\left(\text{scintillator}_i\right) - \text{CalibConst}_{\text{thr}}^{\text{Ref}}\left(\text{scintillator}_i\right)|, \tag{3.12}$$

where CalibConst is a total time correction (summed over all iterations) for a given scintillator, that is calculated by procedure described in Sec. 3.3. $\text{CalibConst}_{\text{thr}}^{\text{Ref}}$ is a calibration constant for some reference effective length, here values for 50 cm was chosen to be treated as a reference for all thresholds, which is nominal length of the scintillator. It is worth noting that the choice of the reference value has no significant impact on the determination of the optimal value of the effective length. Indeed, if the calibration constants for a certain reference value ($L_{\text{ref}}$) will deviate from the constants for the optimal effective length by $\sigma_{\text{ref}}$ then the differences of the calibration constants for some other length $L_C$ will be deviated by $\sqrt{\sigma_{\text{ref}}^2 + \sigma_C^2}$. Therefore, minimal deviation can be estimated by minimizing $\sigma_C$ value, which is in general independent of $L_{\text{ref}}$. To test this approach, estimation of the effective length was also carried out for a

reference length of 49 cm. The results were consistent with the value determined for 50 cm which can be found in Appendix C.

For a given threshold, the dependence of $F_{calib}$ on the effective length can be plotted like it is shown in Fig. 3.10. Uncertainty of the $F_{calib}$ was calculated as a mean uncertainty of correction difference for a given threshold. Uncertainty of correction difference ($\sigma_{correction}$) for some effective length $L_i$ was calculated including uncertainty of the reference correction as $\sigma^2_{correction} = \left(\sigma^{L_i}_{correction}\right)^2 + \left(\sigma^{L_{reference}}_{correction}\right)^2$. Uncertainty of a single correction was estimated as an uncertainty of the linear fit to the second derivative of the $t_{BA}$ distribution. One can find an optimal value of $L^{effective}$ for different thresholds ($L^{optimal}$(thr)), by fitting some peak model. For simplicity quadratic function was chosen as a model to find an optimal value of the effective length. Values of $L^{optimal}$ for different thresholds from fitting: 49.97 (12) cm with adjusted $R^2$ = 0.885 - $thr_1$, 50.00 (14) cm with adjusted $R^2$ = 0.843 - $thr_2$, 50.08 (11) cm with adjusted $R^2$ = 0.909 - $thr_3$ and 50.08 (14) cm with adjusted $R^2$ = 0.854 - $thr_4$. For the sake of completeness: fits of other functions derived from the Gaussian distribution gave the same results of $L^{optimal}$. Even though the fits are not perfect and probably other function could give more accurate fits, the main feature of the $F_{calib}$ dependence that allows to estimate $L^{optimal}$ is the comparison of the $F_{calib}$ values for the 47 and 53 cm. Indeed, one can see that, if the $F_{calib}(thr, 53) > (<) F_{calib}(thr, 47)$, the $L^{optimal}$ should be smaller(greater) than 50 cm. Selected function has the same feature, and therefore it should be sensitive to the changes of the $L^{optimal}$.

$L^{optimal}$(thr) can be used for calculation of the velocities of light signal in each scintillator separately by using Eq. 3.11, what allows to find both an optimal value of the effective length and a velocity of light in each scintillator by one simple procedure. In addition, dependence of the $L^{optimal}$(thr) for different threshold is shown in Fig. 3.11. One can see, that the higher the threshold value, the slightly greater the optimal effective length. It is a reverse effect that can come from the influence of the light attenuation inside the scintillator. It is worth noting that the attenuation length of the scintillators used is around 52 cm [92, 93], so for the light flying through all of the scintillator strip length it will be reduced by ≈62%. The dependence of optimal effective length on the threshold value mainly results from the uncertainty of determining time at a given threshold which is optimized in the process of the time calibration, the so-called time-walk effect. However, the value of the optimal effective length, with reduction of the time-walk effect can be obtained by fitting exponential decay model

$$f(\text{threshold}) = f_0 + A \exp\left(-\lambda * \text{threshold}\right), \tag{3.13}$$

and taking value of the $f_0$ parameter. This value will be an estimate of the optimal effective length minimizing the time-walk effect. Exponential decay model (Eq. 3.13) was fitted to the plot in Fig. 3.11, resulting in $f_0$ = 50.108(11) cm with adjusted $R^2$ = 0.955, which can be used as an estimate of the real $L^{optimal}$ value for scintillators used in the detection modules.

Finally, from the value of the optimal effective length one can estimate value of the velocity of light in each scintillator separately. Values of the velocity for each scintillator is shown in Fig. 3.12. Mean value of the velocity of light in scintillators used in the 192-strip J-PET detector were estimated to value of 12.49 (14) cm/ns. This value is in agreement with the measurement of the same scintillating strips done by means of the oscilloscope and the small

barrel J-PET setup described in [4], and close to literature values for other plastic scintillators obtained by other groups [104–106]. With the values of the velocity of light in each scintillator, Z position can be reconstructed as shown in Fig. 2.1. In addition Z resolution can be estimated based on the similar approach as it was shown in Sec. 3.1 with using the derivatives of the $t_{BA}$ distribution. It is described in more detail in Appendix D, with the resulting value of $\sigma_Z = 3.029(75)$ cm, resolution of the position along the strip.

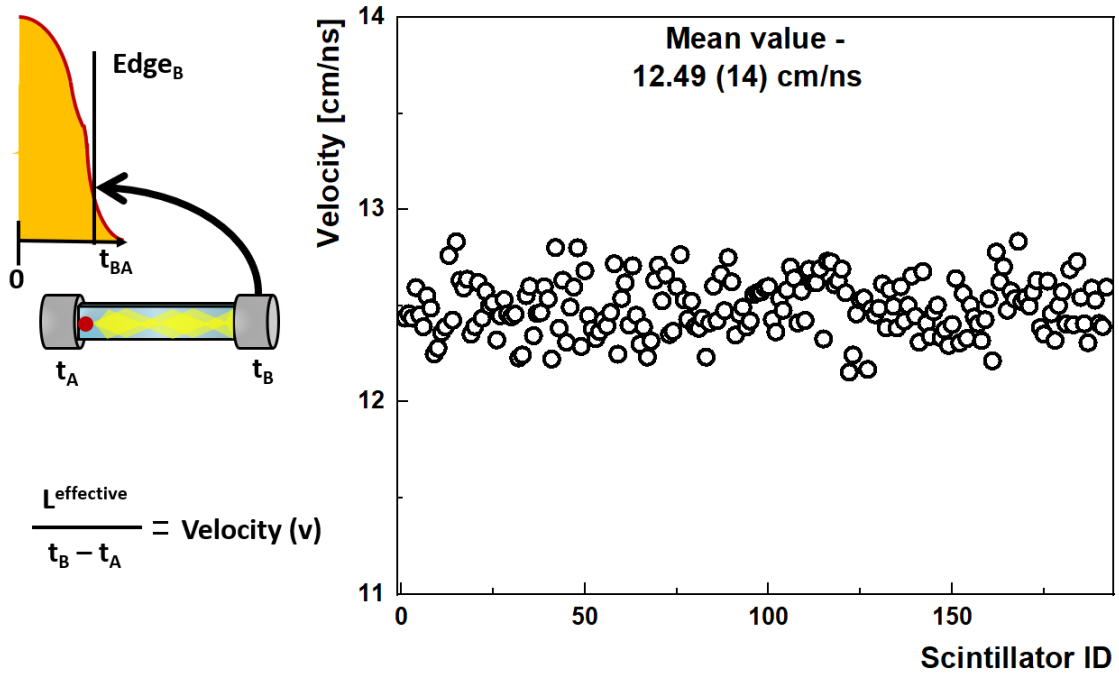


Figure 3.12: **Velocity of light as a function of a scintillator ID.** Experimental data. Velocity of light allows to calculate position along the scintillating strip, from the time difference from two sides A and B. Velocity was calculated based on the effective length value and the width of the $t_{BA}$ distribution. Resulting velocities of light in the scintillator for the determined value of the effective length - 50 cm, as a function of the scintillator ID.

After calibration procedures that were described in this chapter, one can properly reconstruct signals and hits with the best timing and spatial resolutions. This is especially important for final data analysis. However, one thing is still left to do before showing the results from the analysis. Next chapter will focus on the evaluation of the analysis software. It will allow to estimate uncertainty of the fitting, reconstruction and the selection criteria shown in Sec. 2.4. After estimation of the different sources of background, that can survive the data selection final results from the analysis will be shown.

# Chapter 4

# Analysis software evaluation

In order to properly process, select and analyse the data sample collected by the J-PET detector specific algorithms and software were developed. Data reconstruction algorithms were already described in Sec. 2.3 followed by the data selection in Sec. 2.4. Moreover, to check how different positronium decay channels affect the reconstructed data, dedicated simulation software was also designed, what was described in Sec. 2.5. Part of the analysis of the mean positronium lifetime distribution will be described in the next section. It was separated from the analysis software chapter, as it is used at the last stage of the analysis and it is closer to the final analysis then to data reconstruction or selection.

## 4.1 Position reconstruction for higher order decays

The main application of PET systems is the reconstruction of the positron-electron pair annihilation image. Two approaches using only the position and with the addition of the photon registration time in the detector are shown schematically in Fig. 1.8 and computationally Fig. 2.1. Both methods are oriented towards reconstruction of the position of the decay into two collinear photons. For higher order decays, that is, into more than two photons, the assumption of collinearity is no longer met, requiring the design of a separate method of position reconstruction.

The first type of decay that will be discussed in the context of the reconstruction algorithm will be three-photon decay. Due to the conservation of momentum, the three photons produced in this act must be emitted in the same plane. Therefore, the problem of the reconstruction of the annihilation position from the three points in space can be reduced to the reconstruction on the plane - the annihilation (decay) plane. It is also worth adding that method of reconstruction from multiple points is used in the Global Positioning System (GPS). Recently, the application of this method in nuclear physics was demonstrated with the example of the J-PET detector [107] - by the so-called trilateration method. This is a strict method that consists in finding the intersection of the three circles in the plane of annihilation. The radii of these circles depend strictly on the times in which the photons were registered by the detection modules.

Various conditions can affect the precision of the location of a given annihilation point. The

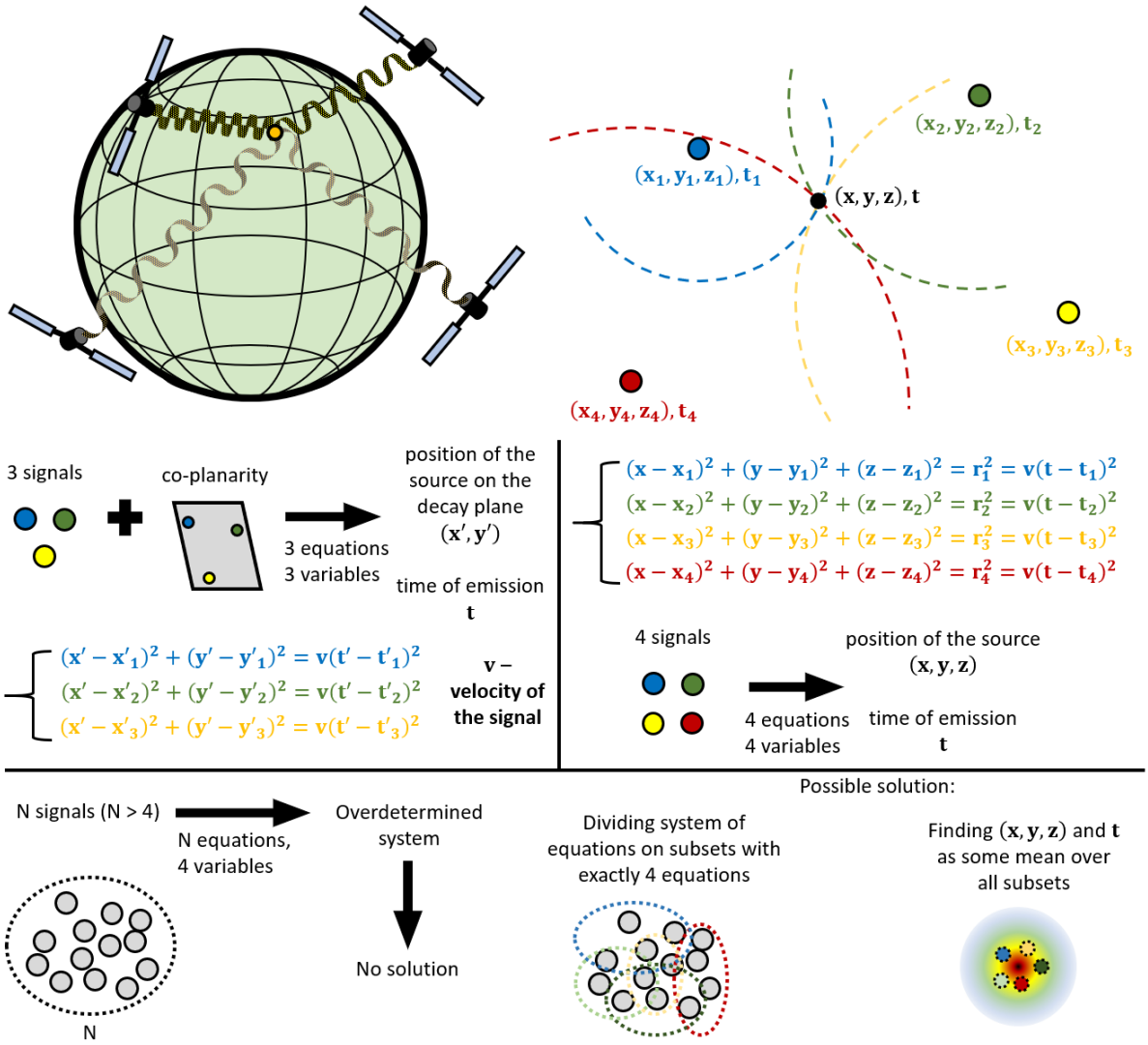


Figure 4.1: **Source position reconstruction in GPS.** Position of the source emitting multiple signals can be estimated based on the method introduced in the Global Positioning System (GPS). Once the signals have been registered in the detectors, a possible source position can be calculated by looking at the intersection of spheres centred at the detector positions $(x_i, y_i, z_i)$. Radii $(r_i)$ of the spheres are proportional to the time of registration the signals by the velocity of the signal. For different number of signals registered position can be estimated directly (4 signal), with assumption of co-planarity (3 signals) or by decomposing the system of equations into smaller ones (N signals, when N $>$ 4).

main influence is the uncertainty of determining the time and position in the detection module in which the photons deposit energy. This is because these are the crucial variables used in the reconstruction algorithm. Moreover, it is not so easy to extend this method to higher order decays due to the lack of determination of the system of equations, shown in Fig. 4.1, which describe the position of annihilation. Here the proposition of the iterative version of the trilateration-like method and its extension to higher order decays will be described.

Trilateration method requires that the spheres used in the reconstruction process intersects in the same position. However, due to the smearing of the signals times and positions, it may be difficult to determine the true position of the source of these signals. Therefore, a new method will be presented to minimize the area created by the intersection of pairs of spheres or circles in the case of o-Ps decay into three photons. Principle of the method is shown in Fig. 4.2 for situation of the annihilation of o-Ps into three photons. For the J-PET detector with three annihilation hits in an event, characterized by positions $\mathrm{Pos}_1$, $\mathrm{Pos}_2$ and $\mathrm{Pos}_3$ one can create an annihilation plane by calculating

$$\overrightarrow{p} = \overrightarrow{\mathrm{Pos}_1, \mathrm{Pos}_2} \times \overrightarrow{\mathrm{Pos}_2, \mathrm{Pos}_3}. \tag{4.1}$$

In the above equation $\overrightarrow{p}$ is the vector perpendicular to the annihialtion plane, $\overrightarrow{\mathrm{Pos}_i, \mathrm{Pos}_j}$ is the vector connecting positions of i$^{th}$ and j$^{th}$ hit and $\times$ is the vector product. After creating such plane, one can follow the procedure shown in Fig. 4.2. Presented method will find an application in reconstruction of the annihilation position of the three photon decays in Sec. 5.5. An extension of the presented method to higher orders of decays is included in the Appendix E and consists in generalizing it to N hits. The comparison between the proposed method and the trilateration method is shown in Appendix Sec. F.

## 4.2 Positronium lifetime

Knowing how to estimate the positronium annihilation site, one can focus on how to obtain its mean lifetime. It was accomplished by the iterative algorithm based on the exponential model describing positron lifetime distribution [110]

$$f(t) = y_0 + \mathrm{A} \sum_{i=1}^{n_\sigma} \sum_{j=1}^{n_\tau} I_i^g I_j^e \cdot \mathrm{Gauss}\left(t, t_0^{(i)}, \sigma_i\right) * \mathrm{Exp}\left(t, \tau_j\right) = y_0 +$$

$$\mathrm{A} \sum_{i=1}^{n_\sigma} \sum_{j=1}^{n_\tau} \frac{I_i^g I_j^e}{2 \cdot \tau_j} \exp\left(\frac{\sigma_i^2}{2 \cdot \tau_j^2} - \frac{t - t_0^{(i)}}{\tau_j}\right) \left(\mathrm{erf}\left(\frac{t - t_0^{(i)} - \frac{\sigma_i^2}{\tau_j}}{\sqrt{2} \cdot \sigma_i}\right) - \mathrm{erf}\left(\frac{-t_0^{(i)} - \frac{\sigma_i^2}{\tau_j}}{\sqrt{2} \cdot \sigma_i}\right)\right). \tag{4.2}$$

In the above equation $y_0$ stands for the background level, A is the area under the curve of the model, $*$ is a convolution operation and $\mathrm{Gauss}\left(t, t_0^{(i)}, \sigma_i\right)$ is a Gaussian distribution with mean $t_0^{(i)}$ and standard deviation $\sigma_i$. $\sum_{i=1}^{n_\sigma} \mathrm{Gauss}\left(t, t_0^{(i)}, \sigma_i\right)$ determines the resolution function of the apparatus, estimated as a sum of Gaussians. $\mathrm{Exp}\ (t, \tau_j)$ is an exponential distribution with mean $\tau_j$, and for given $j$ it models the positron lifetime of a $j^{th}$ component. $I_i^g$ and $I_j^e$ are the intensities for a given Gaussian or exponential component respectively, and they are in the range $[0, 1]$. In addition, both intensities sums up to one: $\sum_{i=1}^{n_\sigma} I_i = 1$ and $\sum_{j=1}^{n_\tau} I_j = 1$. $n_\sigma$ and $n_\tau$ were similarly defined as a number of Gaussian and exponential components that are expected for the analyzed positron lifetime distribution. Finally, erf is an error function defined as

$$\mathrm{erf}\,(x) = \frac{2}{\sqrt{\pi}} \int_0^x e^{-t^2} dt.$$

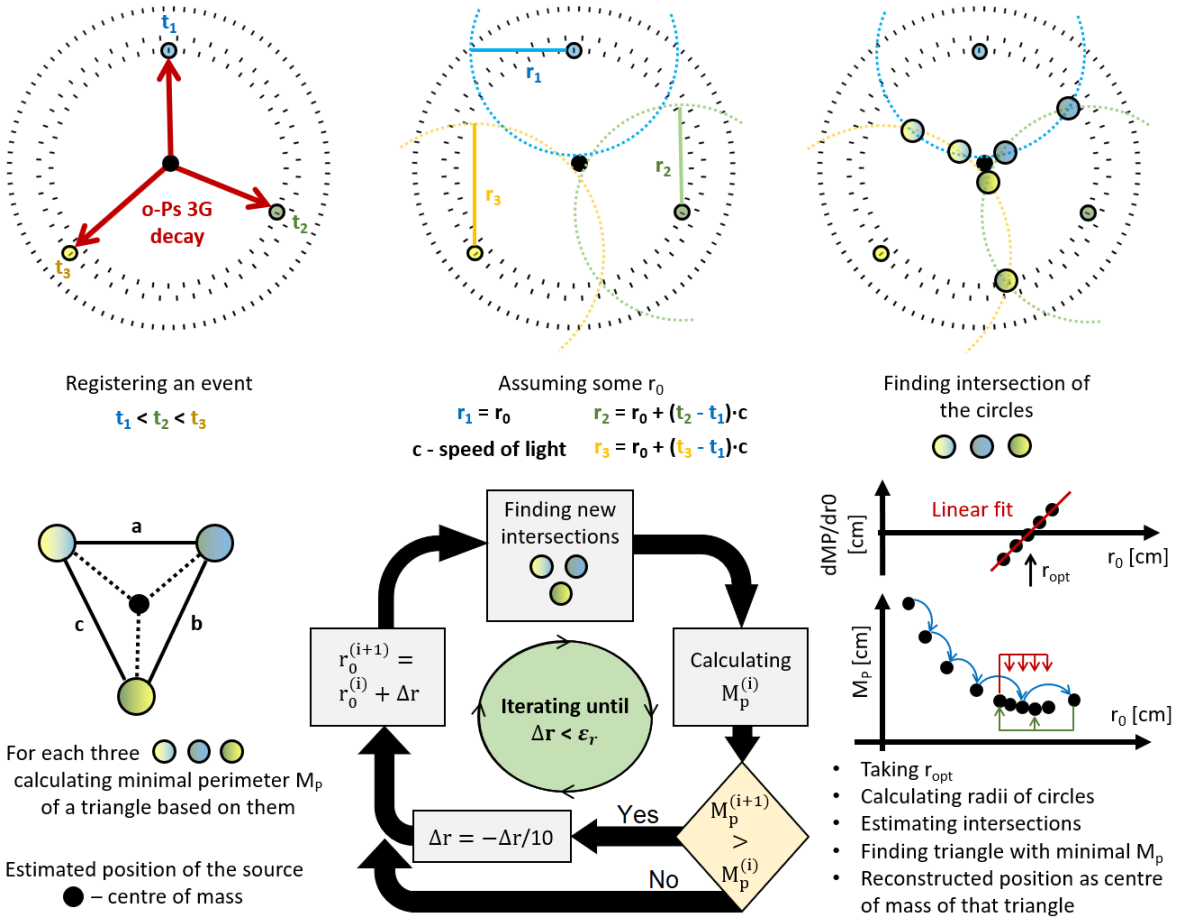


Figure 4.2: **Position reconstruction procedure for o-Ps decay into three photons.** After recording and selecting photons from the ortho-positronium decay into three photons, it is possible to reconstruct the position from which the photons were emitted. Due to the law of conservation of momentum, the problem of reconstruction in space can be simplified to an in-plane problem. From each place where a photon was recorded, a circle can be created corresponding to all possible annihilation positions $r_i = r_0 + (t_i - t_1) \cdot c$ away, where i = 1, 2 and 3. Then, the places of intersection of these circles are determined, from which it is possible to determine such three positions from various intersections, which will form a triangle with a minimum perimeter. The optimal value of $r_0$ ($r_{opt}$) can be found by minimizing the triangle between intersections to have the smallest perimeter $M_p$. This can be achieved by linear fit to the derivative of $M_p$ over $r_0$ and estimating zero point. The position of the annihilation can then be estimated as the triangle's center of mass for $r_0 = r_{opt}$.

Model described in Eq. 4.2 is in principal a convolution of the Gaussian and exponential distributions. Number of Gaussian components $n_\sigma$ and theirs standard deviation $\sigma_i$, that describes the resolution function, can be obtained experimentally by measuring material with known positron lifetime distribution. Metals that have the simplest positron lifetime distributions, usually composed of one or two components with a low lifetime ($\sim$ 200ps), are a good candidate for such measurements. As for the distribution of positron lifetime, the appropri-

ate distribution of an unknown material and mainly the number of components ($n_\tau$) can be obtained by minimizing the goodness of fit - $\chi^2$ for different values of $n_\tau$.

In addition, Eq. 4.2 assumes discrete positron lifetime distribution estimating the mean lifetimes more than the exact positron lifetime distribution in a given material. Fitting model can be expanded to more continuous case with some finite sum of the lifetime components with fixed lifetimes that are distributed in some range. The fitting procedure was also widely described elsewhere [110]. However, this approach requires high statistic of the PAL spectrum ($\sim$ 5 mln counts). It usually entails the need for a very long measurement, rather unattainable for biological measurements, especially with living tissues susceptible to all kinds of fluctuations in the measurement conditions, like temperature, pressure and others. As the thesis focuses on potential applications in medical diagnosis, this procedure will not be considered in the analysis.

The developed software written in C++ and based on the ROOT [100] libraries was given the name PALS Avalanche [95, 108, 109]. The main feature of the software is that it fits the model several times in order to stabilize the results and obtain more accurate values. The new functionality that was added is the parametrization of the intensity parameter ($I_i^g, I_j^e$) such that it reduces the number of the degrees of freedom, therefore stabilizing the fitting results. Previously, intensities were a free parameters that could vary between 0 and 1, and during each iteration intensities were renormalized such that $\sum_{i=1}^{n_\sigma} I_i = 1$ and $\sum_{j=1}^{n_\tau} I_j = 1$.

The new approach is based on the use of the probability simplex definition such that k intensities will be defined as elements of k-simplex defined as a set

$$\Delta_k = \{x \in \mathbb{R}^k | \sum_{i=1}^{k} x_i = 1 \text{ and } \forall_{i=1\ldots k} x_i > 0\}. \tag{4.3}$$

Such sets can be presented graphically as in Fig. 4.3. Note that for the k intensity parameters, only k-1 needs to be adjusted, since the $k^{th}$ parameter will be equal by definition to $x_k = \sum_{i=1}^{k-1} x_i$. In effect, this reduces the number of degrees of freedom by one for each set of intensity parameters. Therefore, when fitting the PALS spectra, this reduces the number of degrees of freedom by two ($I_i^g, I_j^e$) compared to the standard fitting without such parametrization.

Performance of the PALS Avalanche was compared to other well-known and widely used analysis software in PALS - LT [95, 108]. The results for both programs of the fitting on the basis of hexane measurements were shown to be comparable. The next section will focus on the evaluation of the fitting software in view of the positronium imaging and more specifically, to estimate the uncertainty of the obtained distribution parameters for various analysis conditions.

## 4.3 PALS Avalanche evaluation

At first, in order to produce spectra for uncertainty estimation simple simulation script was created. Spectrum consisting of four lifetime components ($n_\tau = 3$) and one resolution component ($n_\sigma = 1$) were considered for the simulations. Positron lifetime of a given component was

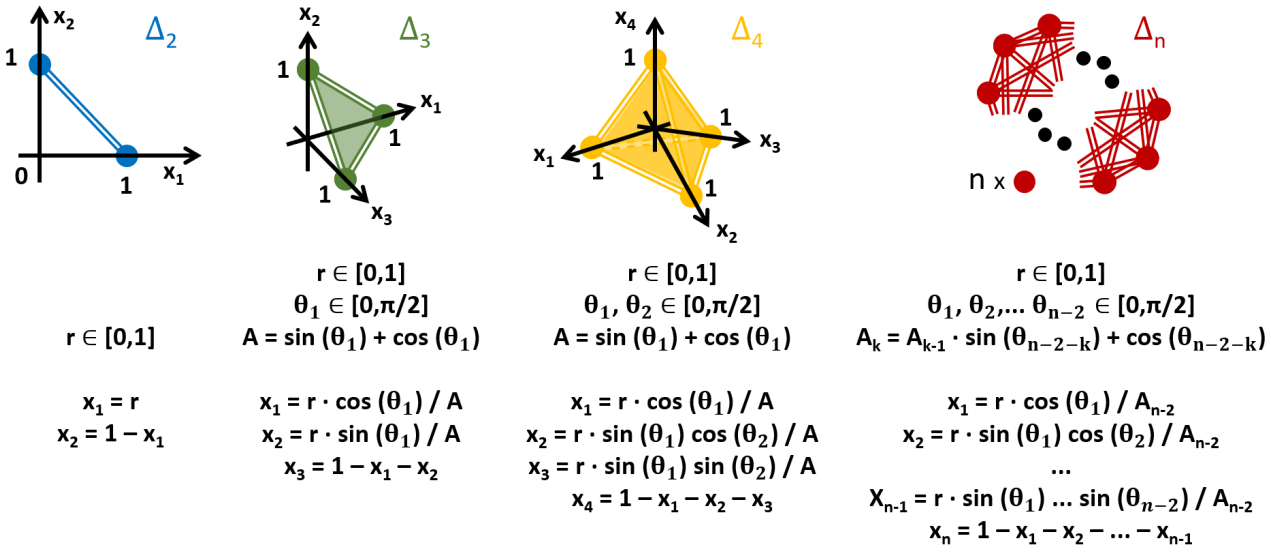


Figure 4.3: **Definition and implementation of the simplex set.** Graphic representation of simplex sets $\Delta_2, \Delta_3, \Delta_4$ and $\Delta_n$ defined in Eq. 4.3. In $\mathbb{R}^2$ 2-simplex set is defined as a line connecting two points (1,0) and (0,1). Having one coordinate $x_1$ one can get the second coordinate from the definition of the simplex set. $\Delta_3$ is a triangle in $\mathbb{R}^3$ space, in which one needs only knowledge of the r and $\theta_1$ parameters to calculate all points on the triangle. Parameter A is a normalization factor, which provides the correct definition on the simplex. For $\Delta_4$ one needs to add only one parameter $\theta_2$ that covers all points on the tetrahedron. Knowing the previous cases, the representation of $\Delta_n$ can be extended by defining r plus n-2 ($\theta_k$) other parameters. This allows to obtain representation for any dimension.

simulated according to the exponential distribution with mean $\tau_i$. Probability of simulating $j^{th}$ component was calculated as $I_j$, according to the definition of intensity as a number from $[0, 1]$. Gaussian distribution was simulated according to the Box-Muller algorithm. To simulate accidental coincidences uniform distribution was added to the simulated distribution. Parameters of the lifetime distribution generation are given in Tab. 4.1. The resolution function was chosen to be shifted from zero to bypass potential calculation errors in zero and to have a standard deviation close to the desired time resolution for future J-PET detector designs. The simulated mean lifetimes correspond to the components derived from p-Ps (0.125 ns), direct annihilation (0.5 ns), and o-Ps (5 ns). The values were chosen so that they were similar or at least the same order to those observed during the patient scan.

There is a couple of different parameters of the fit that can be compared to the theoretical values coming from the simulations, like mean lifetime, intensity standard deviation and offset. In order to estimate error of the fitted model to a given spectrum, that will combine error of every possible parameter, following measure of the error will be introduced

$$\mu_{\text{fit}}\left(\mathrm{p}^{\text{fit}}, \mathrm{p}^{\text{theory}}\right) = \sum_i \left|\frac{\mathrm{p}_i^{\text{fit}} - \mathrm{p}_i^{\text{theory}}}{\mathrm{p}_i^{\text{theory}}}\right|^2 \Big/ \sum_i \left|\frac{\mathrm{p}_i^{\text{fit}} - \mathrm{p}_i^{\text{theory}}}{\mathrm{p}_i^{\text{theory}}}\right|. \tag{4.4}$$

Table 4.1: **Simulated positron lifetime distribution parameters.** List of parameters on the basis of which positron lifetime distributions were simulated [109]. At first, (left) positron lifetime was simulated as an exponential decay with a mean equal to Mean Lifetime with probability equal to Intensity. As the second step each simulated lifetime was smeared according to the (right) resolution function with Standard Deviation and Offset.

| **Lifetime distribution** | | |
|---|---|---|
| Component number | Mean Lifetime [ns] | Intensity [%] |
| 1. | 0.125 | 15 |
| 2. | 0.5 | 50 |
| 3. | 5 | 35 |

| **Resolution function** | |
|---|---|
| Standard deviation [ns] | Offset [ns] |
| 0.1 | 6 |

In the above equation p stands for a set of parameters $(\tau_1, \tau_2, \tau_3, I_1, I_2, I_3, \sigma, \mathrm{t}_0)$ for the fitted model ($\mathrm{p}^{\mathrm{fit}}$) and for the theoretical values during the generation ($\mathrm{p}^{\mathrm{theory}}$). $\mu_{\mathrm{fit}}$ can be treated as a weighted average, where the differences between the fit and the theory are weighted by themselves. Introduced weights allows to decrease an impact of fitted parameters that by accident are very close to the simulated value. To compare parameters with different types fractional error was calculated for every parameter.

To fit a model given by Eq. 4.2 to some spectrum one needs to assume several fitting options that can influence goodness of the fit like width of the bin of the spectrum, the range of the fitting and the initial parameters. The smaller the bin the more accurate distribution one can obtain, but it also increase number of degrees of freedom and an impact of the fluctuations. Similar for the range of the fit, the wider it is the higher impact of the fluctuations and number of degrees of freedom. In addition PALS Avalanche works iteratively, reducing an impact of the bad estimation of the initial values of the fitting parameters. An additional factor that was tested in estimation of an error of the fit is the total number of counts. It is well established fact, that the higher the total number of counts of the distribution, the more accurate it is to estimate its lifetime parameters.

Estimating uncertainty for different conditions of the fitting options, required to conduct several simulations with different spectrum conditions. In addition, to reduce statistical error simulations for each set of condition ($\mathrm{C_S}$) was performed ten times, creating $\{\mathrm{p}^{\mathrm{fit}}_{\mathrm{C_S}}(i)\}_{i=1}^{10}$ after fitting. Thus, an average fit parameter was taken, for comparison with the theoretical value

$$\mathrm{p}^{\mathrm{fit}}_{\mathrm{C_S}} = \frac{1}{10}\sum_i \mathrm{p}^{\mathrm{fit}}_{\mathrm{C_S}}(i).$$

The simulations were conducted for a different total number of counts that varied within a $[6.75 \cdot 10^4, 2 \cdot 10^6]$. Fitting itself was performed for simulated distributions with total number of counts equal to $2 \cdot 10^6$ and for bin widths within $[0.01, 0.1]$ ns and fitting range ends within $[6, 40]$ ns. In addition, the effect of the initial conditions of the lifetime parameters was tested for simulations with total number of counts equal to $2 \cdot 10^6$, bin width equal to 0.02 ns and 40 ns as an end of the fitting range. Relative differences of the initial parameters from the the-

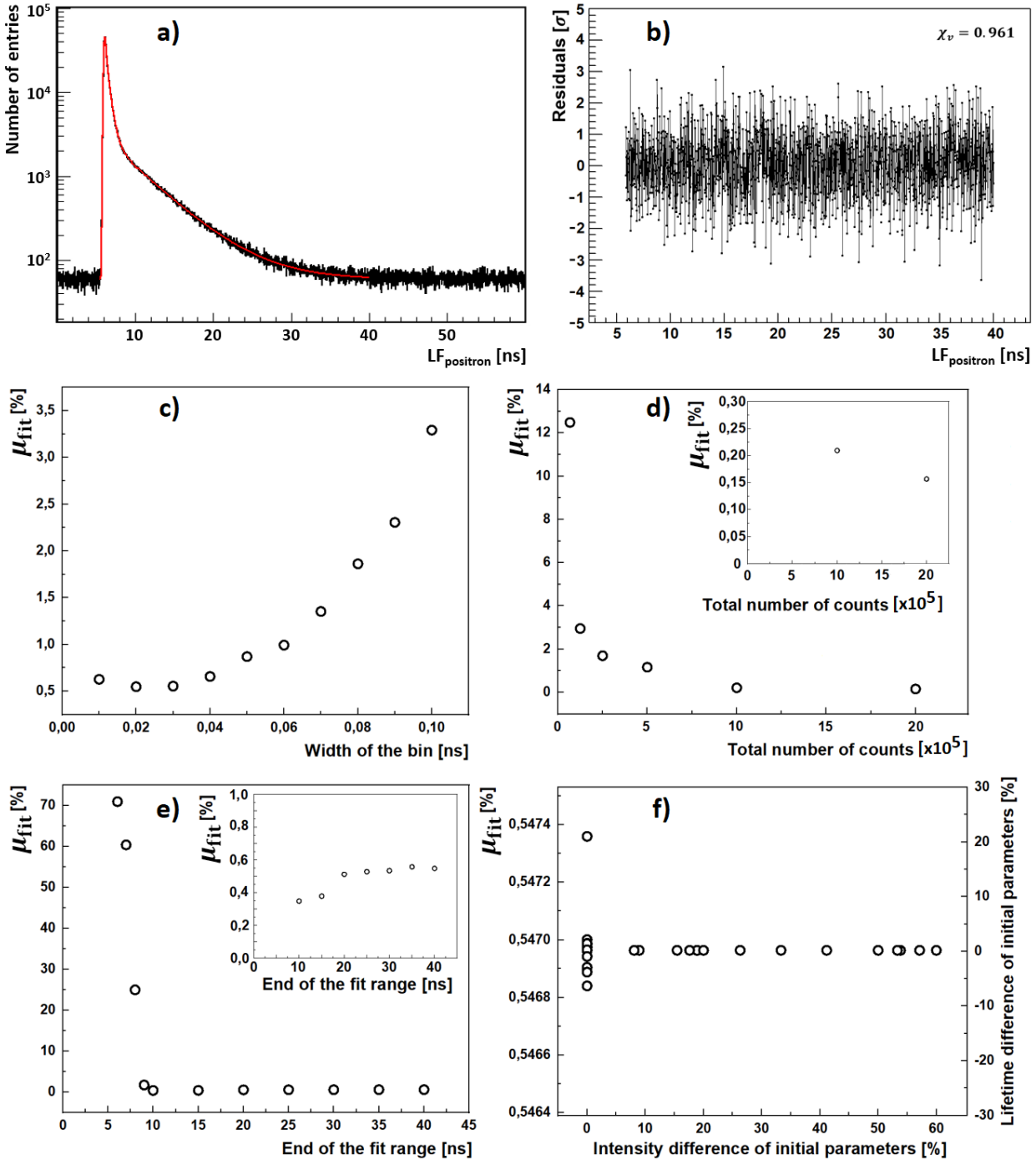


Figure 4.4: **Results from fitting simulated PAL spectra [109].** Simulated data. a) Exemplary simulated distribution for $2 \cdot 10^6$ total number of counts and width of the bin equal to 0.02 ns, with fit (red line). b) Residuals from the fit to the distribution from a) where the goodness of the fit was measured by the chi squared value divided by degrees of freedom $\chi^2_v$. Dependence of measure of error ($\mu_{\text{fit}}$) of the fitted parameters from the theoretical values for different: c) width of the bin and d) total number of counts, e) range of the fit expressed as end of the fit range parameter and f) impact of different initial values of the fitted parameters: lifetime ($\tau$) and intensity (I).

oretical values were tested up to 30% and 60% for the mean lifetime and intensity, respectively. Dependence of $\mu_{\text{fit}}$ for different fitting conditions is shown in Fig. 4.4. Exemplary fit results for two spectra with different total number of counts can be seen in Tab. 4.2.

Table 4.2: **Exemplary fit results for two spectra differing in total number of counts.** List of the fitted parameters to the spectra with total number of counts equal to $6.75 \cdot 10^4$ and $2 \cdot 10^6$ [109].

| **Parameter** | **Simulated value** | **Value for $6.75 \cdot 10^4$ total number of counts** | **Value for $2 \cdot 10^6$ total number of counts** |
|---|---|---|---|
| $\sigma_1$ [ns] | 0.1 | 0.102 | 0.100 |
| $t_0^{(1)}$ [ns] | 6 | 6.00 | 6.00 |
| $\tau_1$ [ns] | 0.125 | 0.105 | 0.124 |
| $I_1^e$ [%] | 15 | 14.3 | 14.9 |
| $\tau_2$ [ns] | 0.5 | 0.489 | 0.499 |
| $I_2^e$ [%] | 50 | 50.9 | 50.1 |
| $\tau_3$ [ns] | 5 | 4.90 | 5.00 |
| $I_3^e$ [%] | 35 | 34.8 | 35.0 |

Summarizing the results of fitting model to simulated distributions, one can see that:

- The mean parameter error is hyperbolically-like dependent on the total number of counts;
- It is enough to have $5 \cdot 10^5$ total number of counts to ensure the accuracy of the parameters obtained up to 1%;
- For a total number of counts of one hundred thousand, the average error of fit increases even to 20%;
- Shape of the distribution for different bin widths shown in Fig. 4.4 indicates the existence of an optimal value of the bin width for which the smallest fitting error will be obtained;
- Optimal value of the bin width of the distribution can be obtained based on the quadratic fit to the $\mu_{\text{fit}}$ over the bin width for a given lifetime distribution;
- It is important that the fit range is chosen to cover the value of the highest mean lifetime for a given distribution (offset is equal to 6 ns);
- There is a certain fit range value for which an error is minimized - close to the range encompassing one highest mean lifetime
- Initial intensity for a given lifetime component is not so sensitive for fitting parameters;
- The differences of the initial value of the mean lifetime do not exceed the error of 0.1% even for high differences;

- Iterative algorithm in PALS Avalanche allows to minimize an effect of the wrongly assumed values of the lifetime distribution component.

## 4.4 Validation of the simulation software

One of the main advantages of the simulations carried out is the knowledge not only about the real time, location and deposition energy of a given photon that has been registered, but also about what kind of photon it is - primary, secondary and further, or derived from deexcitation or annihilation on 2 or 3 photons.

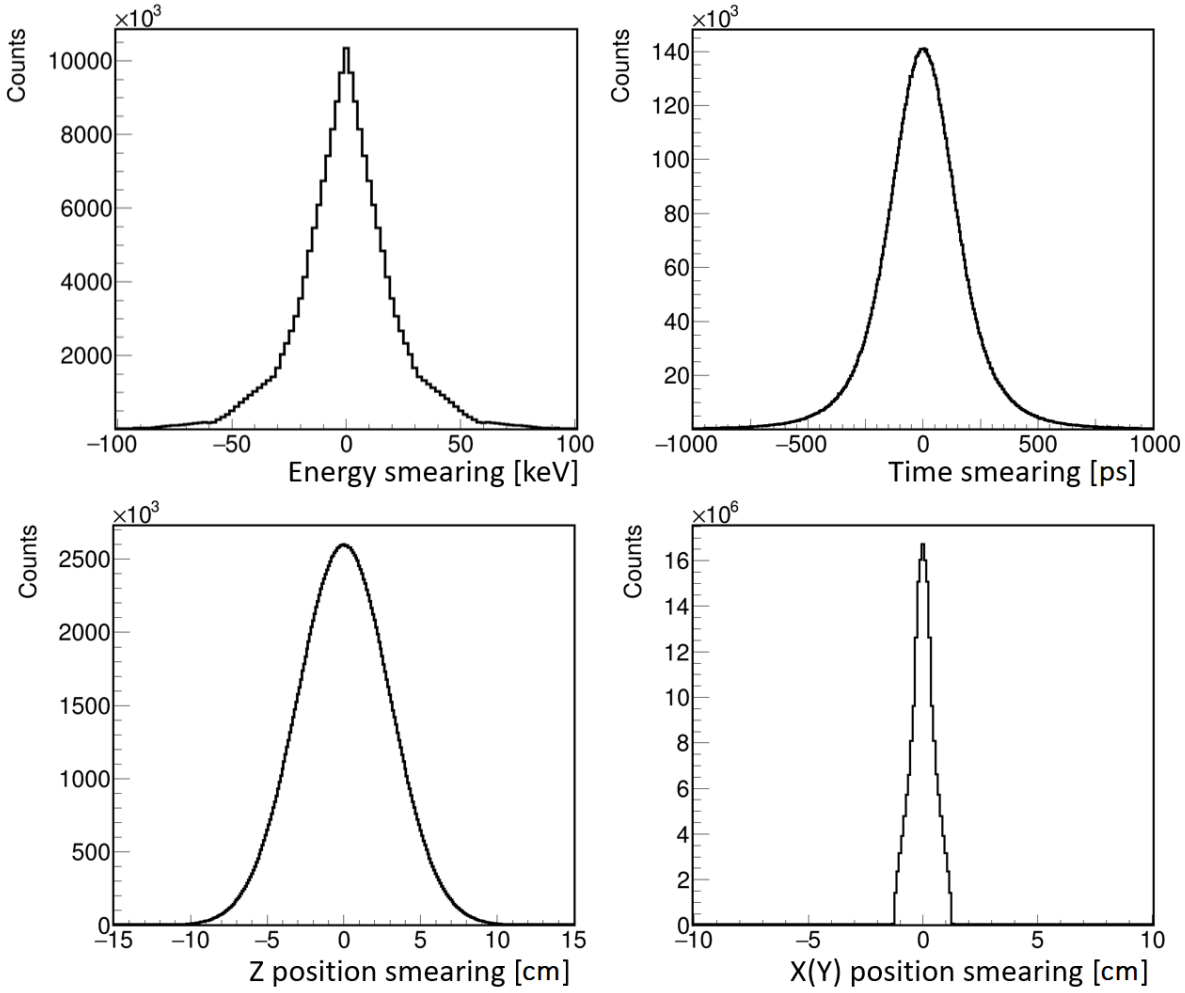


Figure 4.5: **Smearing functions for different hit properties.** Simulated data. The distribution of the smearing functions for the energy deposition, time of the hit, and position in each dimension is shown. Note that, the smearing for the X and Y position is the same, as it comes from the assumption that the X and Y position is the centre of the scintillator.

Simulated data for the aluminium chamber shown schematically in Fig. 2.2 was simulated with a $^{22}$Na positron source in a Kapton foil and XAD4 material around the source. Simulated

hits were transformed to reconstructed hit by applying appropriate smearing. Formulas for smearing function were shown in Fig. 2.6 and their shape are shown in Fig. 4.5 as a difference between the simulated and reconstructed hit parameters like position, energy and time.

As a next step, simulation and reconstruction of the simulated hits will be evaluated in view of the selection criteria described in Sec. 2.4. Time, Z position and energy resolutions expressed as $\sigma_t$, $\sigma_Z$ and $\sigma_E$ respectively were assumed as in Fig. 2.6. For the experiment some threshold was set in the data acquisition system, in order to distinguish electronic noises from the real signals resulting from the energy deposition in the scintillators. However, the use of the threshold limits or even prevents the detection of very low energy signals. To achieve this for the simulation, the energy threshold ($E_{thr}$) was set to 50 keV and all hits with energy less than $E_{thr}$ were discarded from further analysis. Any discrepancies resulting from the assumption of too low or too high threshold will not have a major impact on the results, as the energy cut is quite large for both the measurement data and the simulation. Comparison with the distributions from the analysis of the measurement data is shown in Fig. 4.6. Possible discrepancies can come from the cosmic radiation that were registered by the J-PET detector, and which were not taken under account during the simulations.

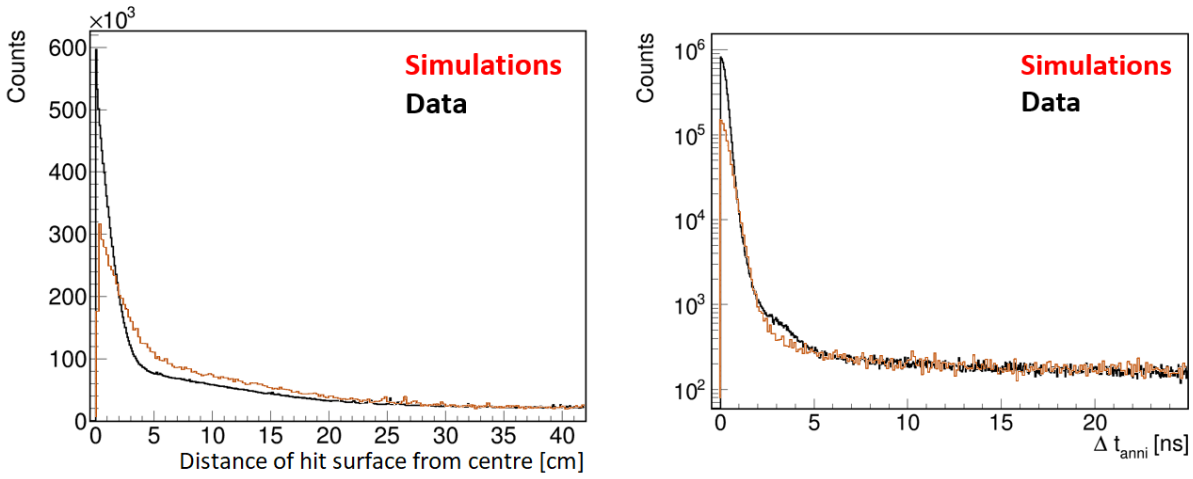


Figure 4.6: **Comparison of the selection criteria distribution between simulations and experiment.** Distributions of the annihilation plane distance from centre and the time difference between annihilation hits in event, for simulations (red) and the data (black).

The presented comparison allows the validation of the simulation software. This validates using data from Monte Carlo simulations to check the effectiveness of the criteria used and to estimate the possible uncertainties of the analysis itself. Next section will focus on the estimation of the J-PET detector sensitivity to observe positron-electron annihilations into 2 and 3 photons based on the analysis of the simulation data.

## 4.5 Sensitivity of the J-PET detector

For the analysis of positronium properties, particular emphasis will be placed on the identification of appropriate decays. The most probable positronium decays are those into two and

three gamma quanta. Here the estimation of the sensitivity of the J-PET detector to register events containing those decays, based on the simulations will be described. Furthermore, the accuracy of each selection criteria in terms of filtering the desired events will be shown.

One can start from the definition of the sensitivity. Sensitivity will be defined as a fraction of true events that passed all the selection process to all true events that were generated. It covers not only the probability to observe given type of the event but also the ability of the software to properly reconstruct it and selection criteria to select them. Sensitivity will be calculated at each stage of the selection process.

Next, the definition of the (2G) and (3G) events will be introduced. Because interest of the thesis is to develop positronium imaging, which is based on the estimation of positron lifetime following definition will be applied:

(2G) Event containing two annihilation hits originating from two gamma decay and one deexcitation hit from the same generated event;

(3G) Event containing three annihilation hits originating from three gamma decay and one deexcitation hit from the same generated event.

The requirement to have a deexcitation hit gives the opportunity to recover the positron lifetime from the selected event. Annihilation hits provide an option to reconstruct the position of annihilation. Combining this information allows (2G) and (3G) to be treated as applicable events for the positronium imaging. For this reason, these definitions are central to further positronium imaging considerations.

Given the appropriate definition, simulated data can be used to calculate the sensitivity at different stages of the analysis and set of selection criteria. During generation, one can extract the number of events that were generated and registered by the detector. Sensitivity calculated as number of events selected by a given selection criterion divided by total number of events generated is shown in Tab. 4.3 and 4.4. The final sensitivities for the analysis of the (2G) and (3G) are equal to $1.17 \cdot 10^{-6}$ and $0.41 \cdot 10^{-6}$, respectively. This values covers the probability of the photon hitting the detector, the probability of a single photon being registered by the detectors (approximately 10%) and the chance that the photon will deposit enough energy to be properly reconstructed. The main difference between the (2G) and (3G) events, directly affecting the sensitivity, is the requirement to register an additional annihilation photon.

Indeed, the effect of the probability of a photon hitting the detector is reduced by the collinearity for (2G) and the coplanarness for (3G). This allows to assume that if the decay plane intersects with the detectors, then all photons have a high chance of hitting the detector. In such a situation, the total probability of several photons to hit a detection module is reduced to a single probability of the intersection of the decay plane (line) with the detectors. In addition, extending the cut to TOT for three-photon decays also reduced the impact of the energy threshold, detectors, which defined the minimum energy that a photon must deposit to be correctly reconstructed as a hit.

Additional information that can be obtained from the simulation is the purity of a given selection criterion. Purity will be defined as number of true events (2G) or (3G) divided by total number of events that passed given selection criterion. Purity for each selection criterion

is shown in Tab. 4.3 and 4.4. One can notice the high purity in the analysis of the (2G) events (94.71%) comparing to (3G) events (56.27%). This is mainly due to a less rigorous selection of annihilation hits based on the TOT value. On the other hand, it allows to maintain quite high sensitivity to (3G) events.

In particular, the Tab. 4.3 and 4.4 also includes the values for the last stage of the analysis, which will be shown in the next chapter. There will also be an additional selection criterion introduced in the next chapter, that will allow to distinguish between decay types and further reduce scattering.

The last section of this chapter describes the division of the different background sources in the final data sample selected. It will especially help to show how different type of the background affects the final results.

## 4.6 Background estimation

There is a several types of the events that can constitute a background to previously defined (2G) and (3G) events. Special attention can be paid to those with scatterings and their erroneous assignment as hits originating from the original interaction of a given photon - annihilation or deexcitation. This can happen when in a given event one of the primary photons has not been registered and the remaining photons have been scattered more than once in the sensitive part of the detector - scintillators. However, it only applies to confusing the hit from the deexcitation photon as an annihilation hit, due to the fact that the deexcitation photon has more than twice the energy of the annihilation photon. In fact it causes problems in selection, especially for the low energies of deposition by the deexcitation photon. The above cases shown schematically in Fig. 4.7, present the types of backgrounds, the fraction of which can be estimated on the basis of simulation. In addition, different types of events can be reconstructed as a single event, increasing the impact of random coincidences.

There is also one type of background-event due to the cosmic rays. They are events, in which muons coming from the showers produced by the cosmic rays reaching the surface of the earth. Muons hitting scintillator of the J-PET detector can deposit energy around 1 MeV, which can be mistaken with the deexcitation or annihilation photons. The number of cosmic events that can pass a given stage of the selection process can be estimated from the separate measurement without any radioactive source inside the detection chamber. It is worth noting, that it covers also some part of the radiation that can come from background radiation, not coming from cosmic rays.

Besides (2G) and (3G) defined in the previous section one can introduce additional categories of events:

(DeexScat) Event containing one true annihilation hit originating from two gamma decay or less than three true annhilation hits originating from three gamma decay and one true deexcitation hit from the same generated event. In addition there is one hit or more coming from the scattering of the deexcitation photon, that was wrongly assigned as annihilation hit. This category also includes a situation where all hits come from the scattering of the deexcitation photon.

Table 4.3: **Sensitivity and purity of the data sample on each stage of the analysis for the (2G) events.** It should be emphasized that each criterion of data selection was tested independently. This made it possible to select suitable candidates for the application of a given selection criterion. The after selection stage represents a sample of data that has been selected for the final analysis, i.e. lifetime analysis. Random coincidences were not distinguished if they came from the same type of decays. In this table type (3G) means incorrectly marked (3G) event as (2G) and is considered as an additional background contributor. (DeexScat), (AnniScat) and (AnniMix) are types of events schematically shown in Fig. 4.7.

| **Stage of the analysis** | | **(2G)** | | | | | |
|---|---|---|---|---|---|---|---|
| | | Sensitivity [$\cdot 10^{-6}$] | Purity [%] | (DeexScat) [%] | (AnniScat) [%] | (AnniMix) [%] | (3G) [%] |
| Hit selection | TOT cut | 15.59 | 34.62 | 7.89 | 13.63 | 41.80 | 2.06 |
| Data selection | Distance | 7.21 | 61.73 | 3.90 | 7.11 | 23.44 | 3.82 |
| | Time difference | 4.76 | 54.28 | 7.04 | 7.17 | 27.02 | 4.50 |
| | Scater test | 5.40 | 55.13 | 5.44 | 11.38 | 27.82 | 0.22 |
| After selection | | **1.17** | **94.71** | 0.44 | 1.84 | 2.10 | 0.90 |

(AnniScat) Event containing at least one but not all of the true annihilation hits originating from two or three gamma decay and one deexcitation hit from the same generated event. In addition there is one hit or more coming from the scattering of the annihilation photon, that was wrongly assigned as primary annihilation hit.

(AnniMix) Event containing at least two annihilation hits from the same generated event. In addition there is an deexcitation hit that comes from the different event.

All situations are shown schematically in Fig. 4.7. It is worth noting that the above mentioned situations were not distinguished when the annihilation and deexcitation hits come from various events - the so-called random coincidences. Such situations can be distinguished in the simulation, but in principal they are not correlated in time and space, so they will not be considered as a separate case.

Relative fractions of events introduced here at each stage of the analysis is shown in Tab. 4.3 and 4.4. One can see, that the (2G) data sample is very pure after the analysis with the highest impact of the coincidences of two- and three-photon decay as a background. However, they will be clustered for the low time differences, considering the criterion of the difference in time of annihilation hits and two different decays coincidences. It is worth noting, that the (AnniScat) events will follow the same distribution as the (2G), so it will

Table 4.4: **Sensitivity and purity of the data sample on each stage of the analysis for the (3G) events.** It should be emphasized that each criterion of data selection was tested independently. This made it possible to select suitable candidates for the application of a given selection criterion. The after selection stage represents a sample of data that has been selected for the final analysis, i.e. lifetime analysis. Random coincidences were not distinguished if they came from the same type of decays. In this table type (2G) means incorrectly marked (2G) event as (3G) and is considered as an additional background contributor. (DeexScat), (AnniScat) and (AnniMix) are types of events schematically shown in Fig. 4.7.

| **Stage of the analysis** | | **(3G)** | | | | | |
|---|---|---|---|---|---|---|---|
| | | Sensitivity [$\cdot 10^{-6}$] | Purity [%] | (DeexScat) [%] | (AnniScat) [%] | (AnniMix) [%] | (2G) [%] |
| Hit selection | TOT cut | 12.36 | 21.04 | 11.99 | 6.74 | 34.02 | 26.22 |
| Data selection | Distance | 3.26 | 33.20 | 5.29 | 5.44 | 32.90 | 23.17 |
| | Time difference | 4.08 | 17.73 | 10.00 | 18.02 | 22.20 | 32.08 |
| | Scater test | 3.26 | 11.53 | 10.14 | 2.11 | 39.06 | 37.15 |
| After selection | | **0.41** | **56.27** | 4.73 | 14.46 | 10.88 | 13.66 |

not change much the obtained results of the lifetime components. The same applies in the situation of (3G) and corresponding (AnniScat) events. However in case of (3G) the purity is on the level of about 56% with the highest impact of misidentification of the three-photon decay annihilation hits with those coming from the two-photon decay. Since this requires the presence of three annihilation hits in some time window, event (2G) can be confused with (3G) if this event is accompanied by a scattering of either a deexcitation photon or one of the annihilation photons. Unfortunately, these events could not be separated by any of the selection criteria used. This may be due to scatterings in the detector construction or the annihilation chamber, that cannot be distinguished based on the reconstructed hits. However, thanks to simulations, it is possible to successfully estimate each background source and distinguish its influence, e.g. on the lifetime spectrum and it is possible to separate the shape of the background from the shape of the analyzed decays. The decomposition of the lifetime spectra onto different components and distinguishing between true signal and background will be shown in the next chapter. It can especially help in explanation of the shape of the (3G) lifetime distribution, which is characterized by relatively low purity.

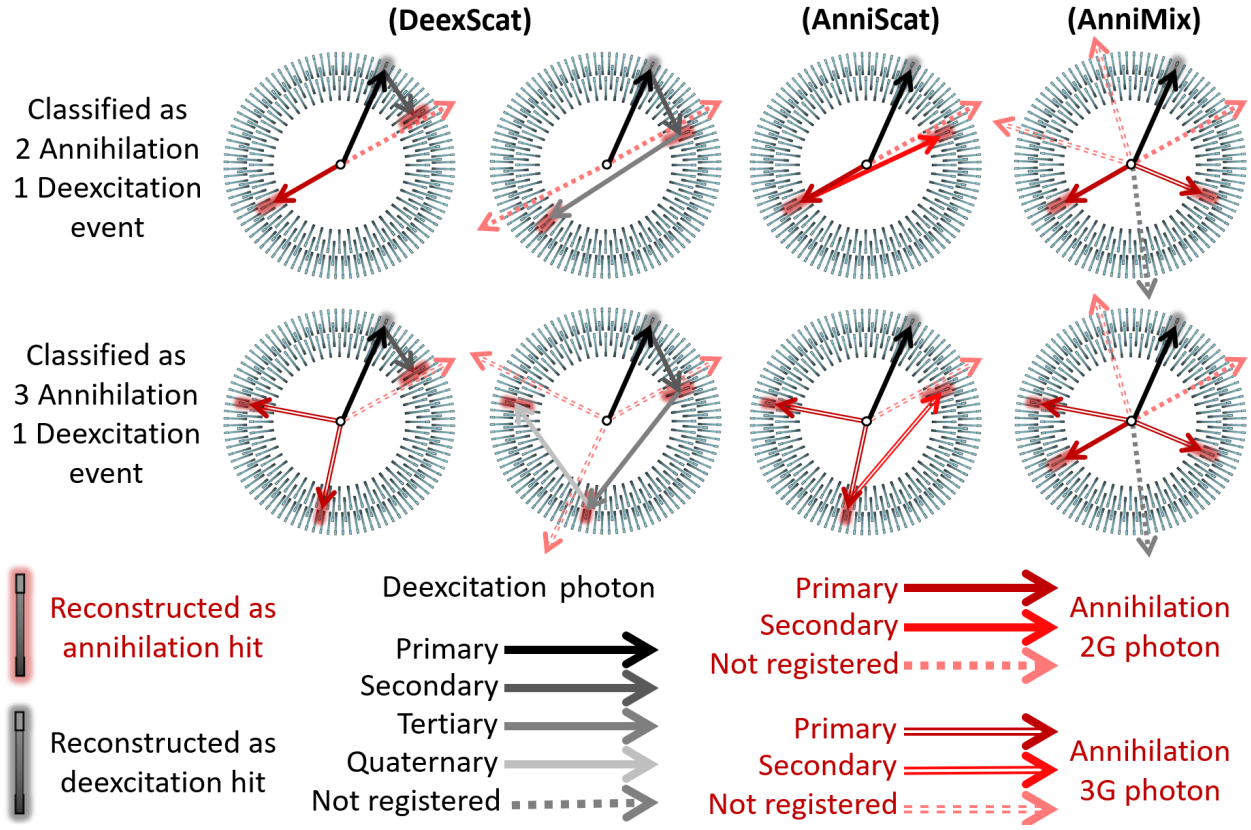


Figure 4.7: **Different types of background events.** When deexcitation photon and its scatterings is registered by the detector, and one of the annihilation photons was not registered (DeexScat) event is collected. There is also a chance that none of the annihilation photons will be registered, but the deexcitation photon will scatter more than two times in the scintillators. This situation is also included in the (DeexScat) category. On the other hand, when the scattering from the annihilation photon is registered and one of the annihilation photons is not, (AnniScat) is collected. The last type is the coincidence of two types of the decay, when at least one annihilation photons is registered from two or more positron-electron annihilations.

# Chapter 5

# Analysis of the positronium properties with the J-PET detector

Positronium can bring a new perspective in many fields like fundamental studies as rare and forbidden decays, due to its simplicity as a two-body system [19–24]. It can even lead to the development of imaging techniques benefiting from its specific properties and especially its ability to characterize nanoporosity [2, 3, 11, 61]. In this chapter, positronium in view of its lifetime and the geometries of the two- and three-gamma decays will be described. This is possible based on the estimates made in the previous chapter.

Chapter will start with the evaluation of the J-PET detector in view of the determination of the positron lifetime spectrum. Additional specific selection criteria will be described allowing to distinguish different types of the decay represented by (2G) and (3G) and also to reduce scatterings [96]. Also besides analysis of the positronium properties, last source of the background will be estimated based on the analysis of the measurement with cosmic radiation only. At the end, determination of the decay constant will be obtained based on the comparison between (2G) and (3G) in view of the positron lifetime spectra.

## 5.1 Photon scattering suppression

The first part of the analysis focuses on the positron lifetime distribution estimation in XAD4, the measurement details of which are described in Sec. 2.2. The simplest type of the event that can be used for the estimation of the lifetime of positron is when there is only one annihilation and only one deexcitation hit reconstructed in a given event. This type of event was already used in the time calibration process based on the lifetime distribution. The requirement for single hits in an event reduces ambiguity in the selection process. It is worth noting, that pair of hits registered in such events mimics the standard PALS apparatus [110].

Unfortunately, this limits the amount of information that can be obtained from this type of event in the data selection process. The selection criteria introduced in Sec. 2.4 without cut on the TOT, cannot be used here and therefore it can increase the effect of scatterings in the obtained results. However, it is possible to reduce the scatterings by assuming that there

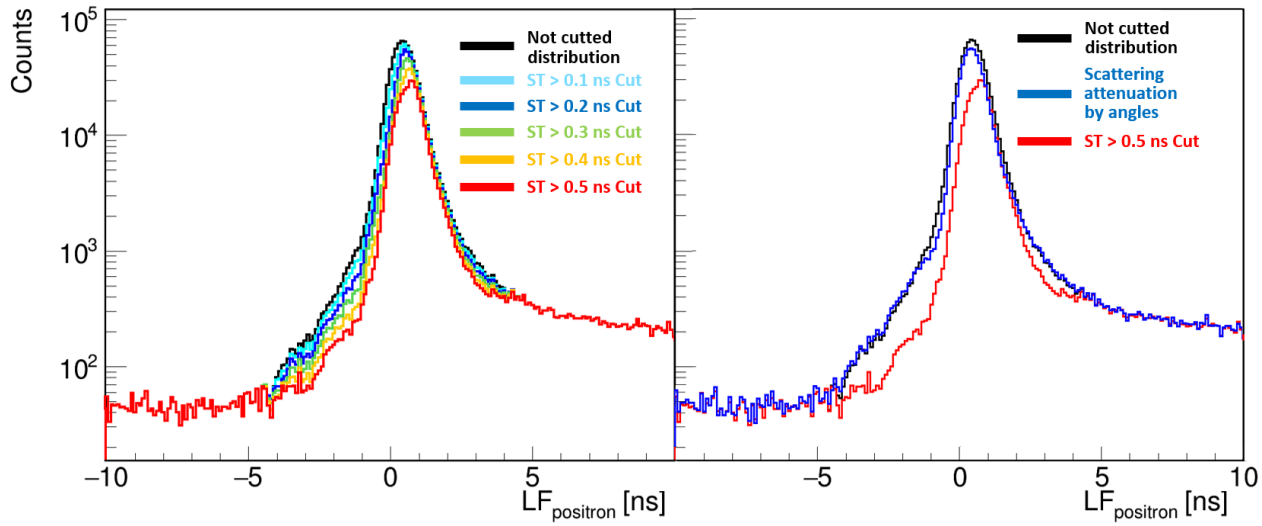


Figure 5.1: **Scattering reduction and its impact on the lifetime spectrum.** Experimental data. Scatter test defined in Eq. 2.1 can reduce scatterings in the data sample. However, when calculating scatter test between annihilation-deexcitation hits pair some real coincidences can be accidentally rejected. It can disturb lifetime distribution in the range of the time differences that corresponds to the maximal distance between two detectors. It is shown for different values of the cut-off on the scatter test on the top. Other method of reducing scatterings is the angular cut on the angles for which the scattering is at most probable. (bottom) The comparison between cut on the scatter test and by angle cut described in this section is shown on the bottom. Distribution with the scattering suppression by angles is normalized to the background level. One can see that, reducing scattering by angles does not disturb the $\mathrm{LF}_{\mathrm{positron}}$ distribution, but it reduces some scatterings near the peak.

are some relative positions of a pair of detectors which have an increased probability of observing consecutive scatterings of a single photon. To show this, scatter test defined in Eq. 2.1 will be used, however not directly.

At the beginning, it is worth explaining why the scatter test cannot be used directly as a selection criterion on events of this type. This is because this test can affect the positron lifetime distribution. One can imagine what is the highest time difference that can be registered between two consecutive scatterings of a single photon. It will come from the longest distance between two scintillators in the J-PET detector, which corresponds to a pair of scintillators from the last, third layer that lie opposite in respect to the center of the detector. Considering only XY plane, the radius of the third layer is equal to 57.5 cm, then the longest distance $\left(\mathrm{d}^{\mathrm{XY}}_{\mathrm{max}}\right)$ will be equal to 115 cm. When one adds the maximal difference of the Z positions $\left(\mathrm{d}^{\mathrm{Z}}_{\mathrm{max}}\right)$ of the reconstructed hits equal to the length of the scintillator equal to 50 cm, then the maximal distance $(\mathrm{d}_{\mathrm{max}})$ between any two hits will be

$$\mathrm{d}_{\mathrm{max}} = \sqrt{\left(\mathrm{d}^{\mathrm{XY}}_{\mathrm{max}}\right)^2 + \left(\mathrm{d}^{\mathrm{Z}}_{\mathrm{max}}\right)^2} = 125.4 \text{ cm}.$$

According to Eq. 2.1, $\mathrm{d}_{\mathrm{max}}$ corresponds to a maximum time difference of 4.18 ns. This

results in an increased chance of accidentally classifying a real event as a scattering event, in the range $[-4.18, 4.18]$ ns. Therefore, lifetime distribution based on the time difference between two hits can be artificially reduced in this range, complicating process of estimation of the mean lifetime, especially when the mean lifetime is lower or in the range of 2 ns. The issue for different cuts on the scatter test is shown in Fig. 5.1.

To overcome this problem, the scatter test will find application in a different way, to find pairs of hit that have the highest probability to origin from the scattering of a single photon. In the J-PET detector there is some scatterings that are more preferable to detect. To visualize that, it will be helpful to define scattering angle, as angle between direction of the primary photon and the direction of the scattered photon. There are two exemplary situations of scatterings shown in Fig. 5.2. In the first situation, when the primary photon scatters at the $\alpha_1$ angle, the scattered photon can only be detected in one scintillator in the third layer. Probability of observing such scattering angle ($P_1$) is proportional to the distance that the scattered photon travels through the active part of the detector, which is the scintillating area. Therefore, it is proportional to the size of single scintillating strip. In the second situation primary photon scatters at angle $\alpha_2$, but in contrast scattered photon on its way to the scintillator in the third layer it can pass through three other scintillators. Distance in the active part of the detector will be then approximately four times greater compared to the first situation. One can conclude, that the probability of observing such scattering angle ($P_2$) is four times greater than it is for angle $\alpha_1$.

As a geometric indicator to classify potential scattering, the scattering angle will be calculated between the pair of hits ($hit_1$, $hit_2$) which are ordered in time, as in Fig. 5.2. One can start by selecting events where exactly two hits are reconstructed - one annihilation and one deexcitation categorized by the TOT selection shown in Fig. 2.5. As a next step ST (Eq. 2.1) is calculated for such events. If the ST value will be in the yellow range from Fig. 2.5, defined on range $[-0.5, 0.5]$ ns such event is categorized as potential scattering.

The 0.5 ns cut-off was chosen to cover the differences due to the assumed time resolution ($\sigma_t \approx 160$ ns) as well as the accuracy of the hit position determination ($\sigma_Z \approx 3$ cm, $\sigma_{X,Y} \approx 0.72$ cm). $\sigma_t$ can be estimated based on the lifetime spectrum, what will be shown later in the next section. One can show that, when the Z position is determined based on the time difference between two signals, then each signal time is smeared with $\sigma_t$ then $\sigma_Z = \frac{\sqrt{2}\cdot\sigma_t}{v}$, where v is the mean velocity of light in scintillator equal to 12 cm/ns. When it comes to X(Y) position, its uncertainty comes from the assumption that hit position was always in the centre of the scintillator in X(Y) plane and it is connected to the dimension of the scintillator. Uncertainty of determining position can influence uncertainty of the calculations of the ST, therefore $\sigma_{ST}$ it can be calculated as

$$\sigma_{ST} \overset{2.1}{=} \sqrt{\left(\sqrt{2}\sigma_t\right)^2 + \left(\frac{\sigma_{pos}}{c}\right)^2} = 0.238 \text{ ns},$$

where c is the speed of light in vacuum and $\sigma_{pos} = \sqrt{(\sigma_{XY})^2 + (\sigma_Z)^2}$ is the total uncertainty of the hits' position and $\sigma_{XY} = \sqrt{(\sigma_X)^2 + (\sigma_Y)^2} = \sqrt{\left(\frac{\text{width=0.7 cm}}{\sqrt{2}}\right)^2 + \left(\frac{\text{height=1.9 cm}}{\sqrt{2}}\right)^2}$. To cover all potential scatterings value of $2\sigma_{ST}$ was chosen as cut-off.

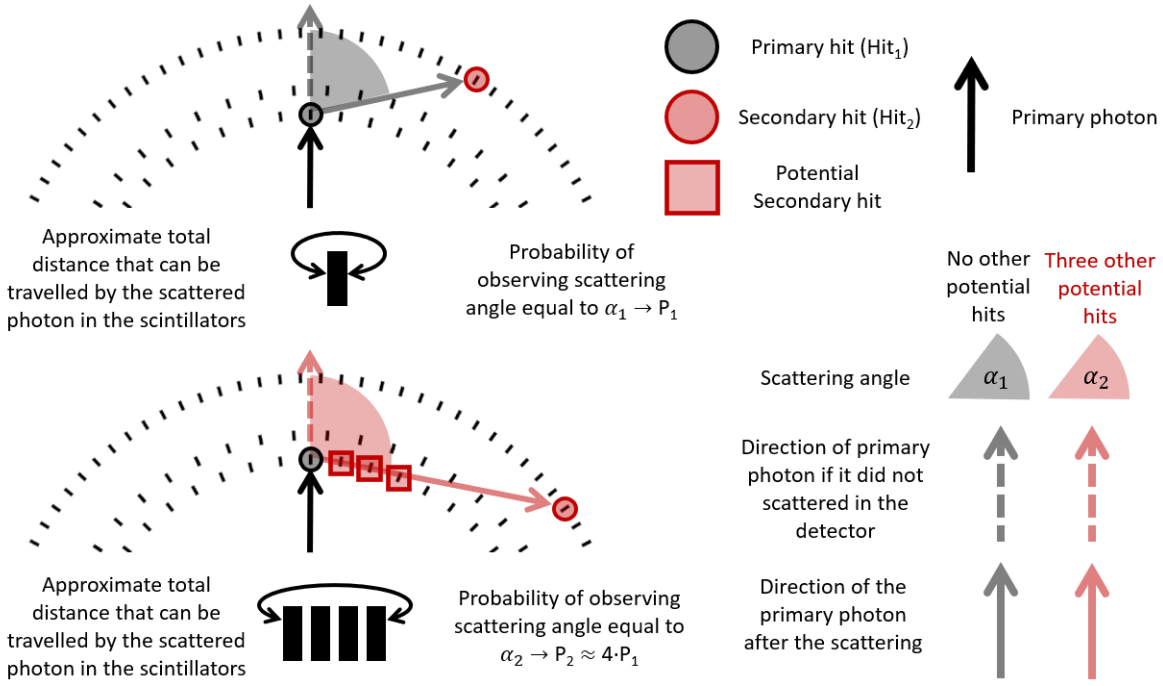


Figure 5.2: **Scattering angle definition for the J-PET detector.** Two exemplary scatterings that can be observed by the 192-strip J-PET detector. Primary photon (black solid arrow) interacts in the scintillator from the first layer (black circle) and then interacts once again in the scintillator in the third layer (red circle). Depending on the scattering angle, a different number of other scintillators may stand on the path between the first scintillator and the second scintillator, thereby increasing the probability of observing scattering from a given angle $\alpha_1$ or $\alpha_2$.

Next for potential scattering events scattering angle is calculated, when the second hit in time is treated as a primary scattering. Distribution for such events is shown in Fig. 5.3. One can see there is some increased probability of observing certain scattering angles, that is coming from the geometry of the J-PET detector. Indeed, there are three ranges of scattering angles that can be distinguished - in Fig. 5.3 marked by blue, yellow and red. Blue range indicates situation in which scattered photon can deposit energy in two potential detector on its way - in the second and then in the third layer. Therefore, such scattering angles can be obtained for two different pairs of detectors - primary hit in the first layer with secondary hit either in second or third layer. It increases chance of observing blue angles by two, comparing to angles where scattered photons can be registered in only one detector. In the yellow range, this effect is even greater, because for some angles there is a chance for multiple scintillators to pass, even a few strips in the first layer itself. Multiple scintillators in a single layer on the path of the photon increases the probability of observing such photon even 4 or 5 times, what can be deduced from the scattering angle distribution. The last red range differs from the yellow one in that it has no chance of passing through several modules in one layer. However, there is still a chance of passing single detectors from all three layers, in contrast to the blue range.

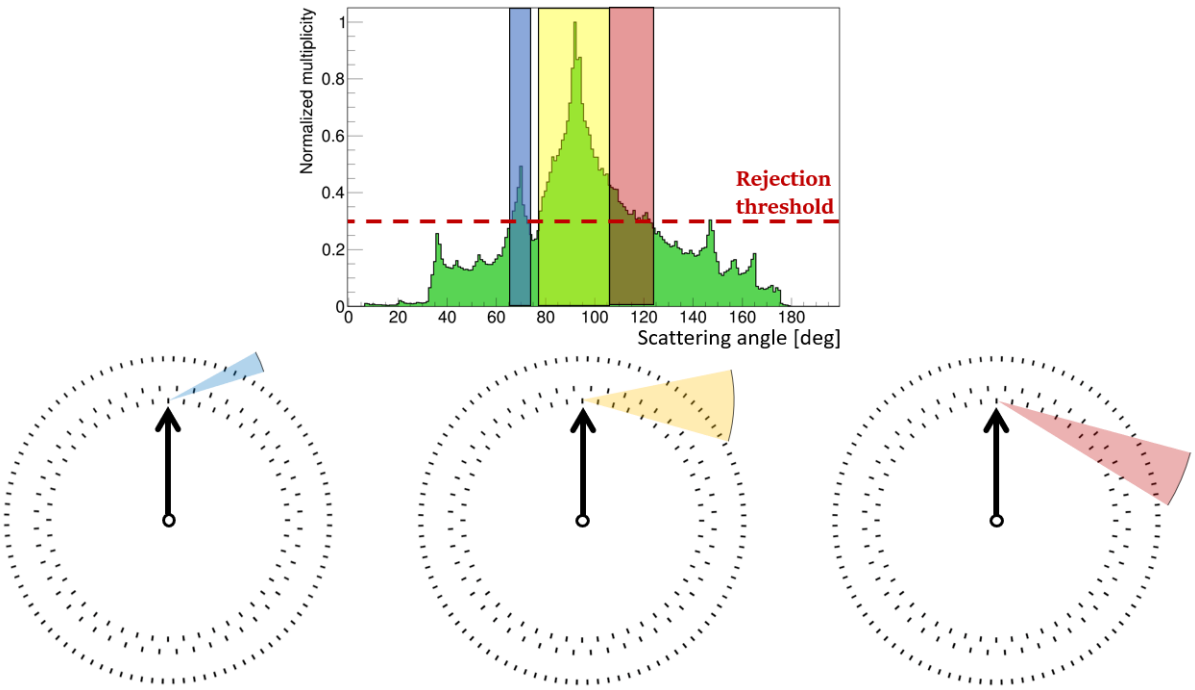


Figure 5.3: **Scattering angle distribution for the J-PET detector.** Experimental data. Scattering angle distribution for events with one deexcitation and one annihilation hits in event, where primary hit, defined in Fig. 5.2 is the first hit in time. Distribution is normalized to the maximum. The areas marked in red, yellow and green represent the scattering angles for which there is an increased chance of observation.

## 5.2 Positronium lifetime in XAD4

Lifetime spectrum can be collected for events mentioned in the previous section - events with exactly one annihilation and one deexcitation hit. In order to reduce the amount of scatterings from selected events, a criterion based on the previous section consideration will be formulated. As it was described briefly, hard cutting based on the scatter test can disturb lifetime spectrum. Therefore, a different approach will be taken which is not based on time. Events with geometrical configurations most likely to arise from single photon scattering will be rejected.

For every event selected for estimating lifetime of positronium (1 annihilation + 1 deexcitation) scattering angle will be calculated, according to the convention shown in Fig. 5.2. The $\mathrm{Hit}_1$ is the first hit in time reconstructed, no matter if it is categorized as annihilation or deexcitation. When the calculated scattering angle belongs to the range marked in blue, yellow or red in Fig. 5.3 it will be rejected. Positron lifetime in an event will be estimated as:

$$\mathrm{LF}_{\mathrm{positron}}\left(\mathrm{Hit}_{\mathrm{Anni}}, \mathrm{Hit}_{\mathrm{Deex}}\right) = \mathrm{t}^{\mathrm{emission}}_{\mathrm{AnniHit}} - \mathrm{t}^{\mathrm{emission}}_{\mathrm{DeexHit}}, \tag{5.1}$$

where $\mathrm{t}^{\mathrm{emission}}$ is the time of a given hit corrected on TOF - subtracted by the time that photon needed to travel from the assumed position of the source to the reconstructed position of the hit. $\mathrm{Hit}_{\mathrm{Anni}}$ and $\mathrm{Hit}_{\mathrm{Deex}}$ corresponds to the only one annihilation hit and the only one

deexcitation hit in considered event.

$LF_{positron}$ distribution for events fulfilling TOT classification and not rejected by the scattering angle condition can be seen in Fig. 5.4. One can easily find long decaying tail coming from the o-Ps annihilations, and peak around zero coming from short decaying direct annihilations and the annihilations of p-Ps. However, clear decomposition onto different components can be obtained by fitting multi-exponential model, mentioned in the Sec. 4.2. To fit the model to obtained distribution PALS Avalanche was used.

As a first step of the fitting one needs to assume number of positron annihilation components that can be observed in the measured sample and the initial values of the components parameters like its mean lifetime and intensity. It may be helpful to measure the sample on another system that has already been checked for decomposition of positron lifetime distributions. The results of the positron lifetime analysis in XAD4 made on the standard PALS system [29] is given in Tab. 5.1. $LF_{positron}$ distribution with fit is shown in Fig. 5.4 and the results from fitting are given in Tab. 5.1.

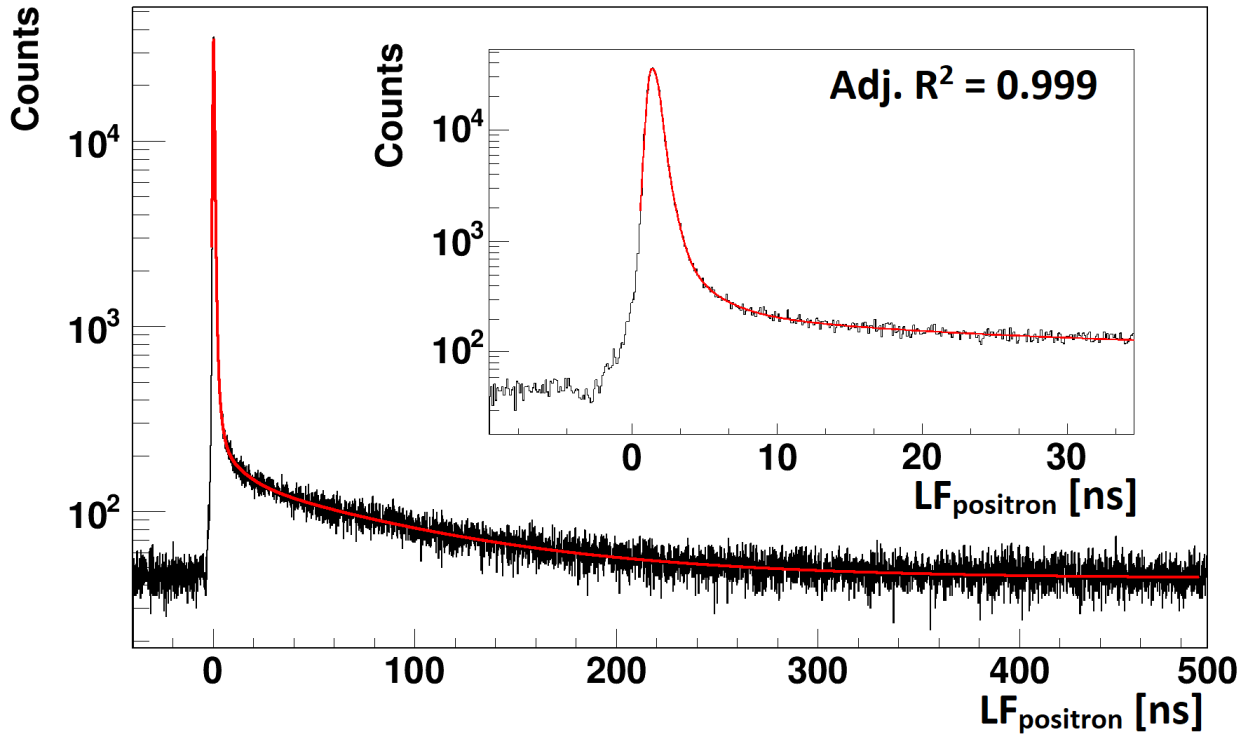


Figure 5.4: **$LF_{positron}$ distributon in the XAD4 [95].** Experimental data. Events with exactly one annihilation hit and the exactly one deexcitation hit, can be used for the collection of the $LF_{positron}$ distributon in the studied sample. Resulting $LF_{positron}$ distributon from the measurement with XAD4 is shown here. Red line indicate the fit from the PALS Avalanche software. The fit is quite good ($R^2 = 0.999$) as can be seen also for the distribution drawn in a narrower range. The fitting results are given in Tab 5.1.

Values obtained from the fit is in agreement with the results from the standard PALS system, proving that the J-PET detector allows to study positronium decays and differentiate between its different decay modes. It is important, as thanks to the geometry of the detector

Table 5.1: **Fit results from [29] and from the J-PET detector.**

| **Parameter** | **Result from [29]** | **Result from the J-PET detector** |
|---|---|---|
| $\sigma_1$ [ns] | 0.126 | 0.223 (01) |
| $I_1^g$ [%]] | 83.9 | 66.5 (0.1) |
| $\sigma_2$ [ns] | 0.202 | 0.518 (02) |
| $I_2^g$ [%]] | 16.1 | 33.5 (0.1) |
| $\tau_{\text{source}}$ [ns] (fixed) | 0.374 | 0.374 |
| $I^e_{\text{source}}$ [%] (fixed) | 10 | 10 |
| $\tau_1$ [ns] (fixed) | 0.125 | 0.125 |
| $I_1^e$ [%] | no information | 40.63 (01) |
| $\tau_2$ [ns] | no information | 0.527 (01) |
| $I_2^e$ [%] | no information | 26.88 (01) |
| $\tau_3$ [ns] | 2.45 (25) | 2.165 (01) |
| $I_3^e$ [%] | 3.3 (0.6) | 4.75 (01) |
| $\tau_4$ [ns] | 10.2 (0.6) | 10.92 (03) |
| $I_4^e$ [%] | 2.8 (0.5) | 2.55 (01) |
| $\tau_5$ [ns] | 90.8 (1.2) | 90.99 (04) |
| $I_5^e$ [%] | 44.8 (0.4) | 25.74 (01) |

it is possible to study all of the positronium decays geometries simultaneously and correlations between them. Next section will show how to select events that are coming from the 2G and 3G annihilation of positron-electron pair, and then such events will be further analyzed.

## 5.3 The distinction between two and three gamma decay

The basic distinction between different states of positronium can be the mean lifetime and the geometry of the decay. Mean lifetime can be a good discriminator due to a three-order of magnitude difference between p-Ps and o-Ps in a vacuum, however as shown in Fig. 5.8 the lifetime distribution of the p-Ps and o-Ps can overlap for very small values. Moreover, the mean o-Ps lifetime may be shortened in matter, due to the pick-off process or ortho-para conversion [54, 55]. In that situation, more strict may be the geometric criterion which is specific for different decays, to two or three photons. For the new geometric criterion distinguishing the different types of positronium decays it will be useful to define the angle ($\theta_{ij}$) between $i^{th}$ and $j^{th}$ hit as

$$\theta_{ij} = \text{acos}\left(\overrightarrow{\text{Position}_{\text{Hit}_i}} \circ \overrightarrow{\text{Position}_{\text{Hit}_j}}\right) / |\text{Position}_{\text{Hit}_i}||\text{Position}_{\text{Hit}_j}|, \tag{5.2}$$

where $\circ$ is scalar product, $\overrightarrow{\text{Position}_{\text{Hit}_i}}$ is a vector from the centre (0,0,0) to the $\text{Hit}_i$ position and $|\text{Position}_{\text{Hit}_i}|$ is the length of that vector. In other words $\theta_{ij}$ is the angle between two points measured from the center of the coordinate system. As it can be seen in Fig. 5.5 different types of events can be distinguished based on the sum of angles between annihilation hits.

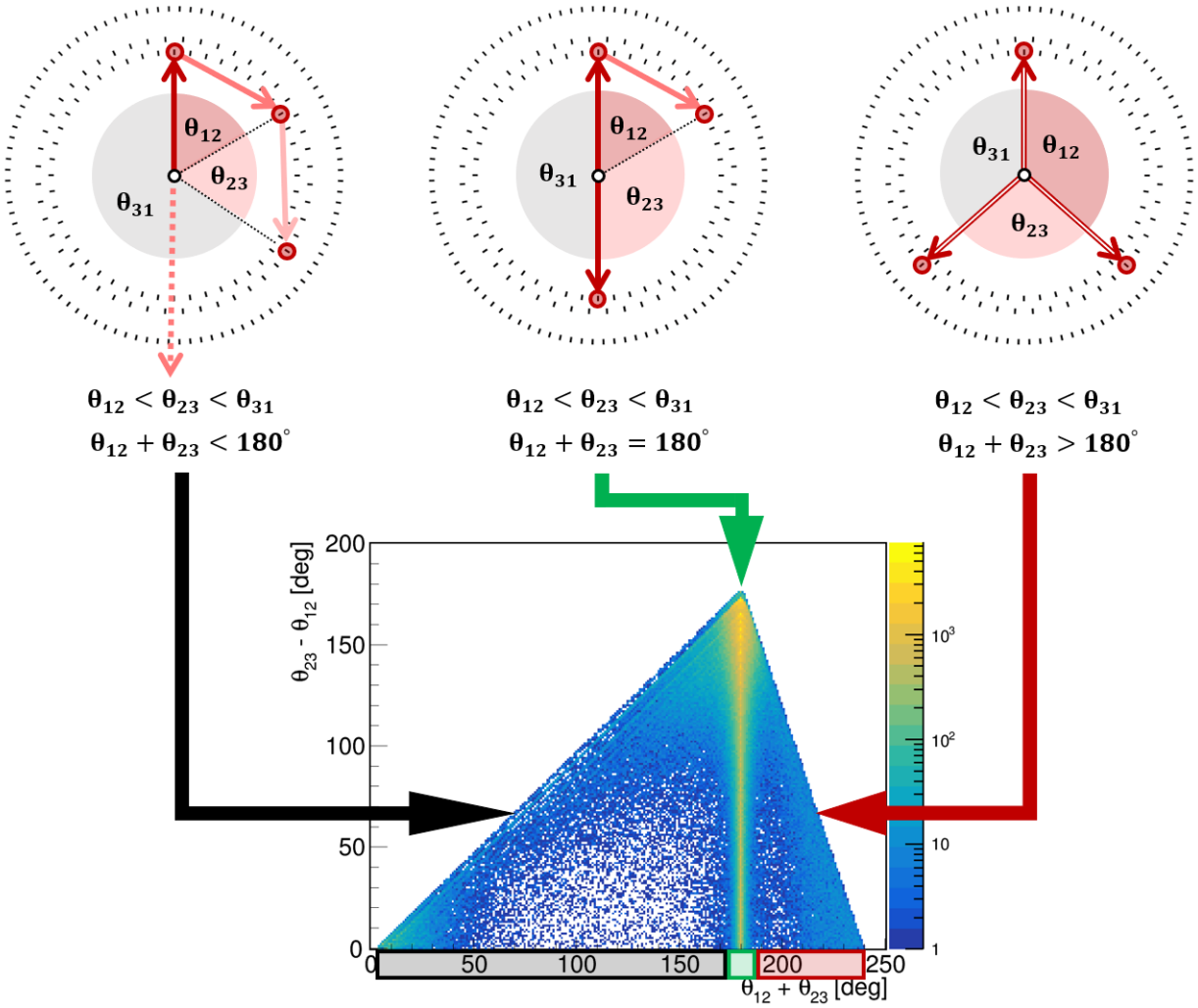


Figure 5.5: **Distinction between different decay modes based on the angle.** Experimental data. In the case of events with three annihilation hits, different modes of positronium decay and the double scattering of the annihilation photon can be distinguished. Given the three annihilation hits, the angles between their positions can be computed so that $\theta_{12}$, $\theta_{23}$ and $\theta_{31}$ are arranged in ascending order. This convention makes it possible to distinguish true three-photon decays ($\theta_{12} + \theta_{23} > 180^o$) from two-photon decays ($\theta_{12} + \theta_{23} = 180^o$) and from part of double scatterings ($\theta_{12} + \theta_{23} < 180^o$). Note that in the case of a two-photon decay, the third hit, which is not from the original annihilation photon, may also come from the deexcitation photon or its scattering, as it will not change the sum of the two smallest angles. The distribution of the sum of the two smallest angles relative to their difference shows how the previously described types of events are distributed.

The criterion defined in Fig. 5.5 can be applied not only to events with three annihilation hits. Considering (2G) the type of event, a hit from the deexcitation photon can be a third hit to calculate the angles between hits. Indeed, wherever the third hit is recorded, as long as the event has photons from the decay into two, the sum of the two smallest angles will

always be 180 degrees, calculated from the position of annihilation. Details of the position reconstruction algorithm was described in Sec. 2.1 for the two gamma decay, and in Sec. 4.1 covering three and higher gamma decays. The next section show the result and it will be focused on the analysis of the annihilation of positron-electron pair to two photons, in view of the lifetime analysis and position reconstruction.

## 5.4 Analysis of the annihilations into two photons

The key process that enables PET imaging is the decay of the positron-electron pair into two photons. Its decay geometry, consisting of two photons flying approximately in one straight line (LOR), makes it possible to determine the position of annihilation along LOR based on the time difference. Two-photon decays are also an important structural determinant. It is worth recalling that in addition to p-Ps and most of the direct annihilations of a positron with an electron, o-Ps can also decay into two photons, for example by pick-off or ortho-para conversion. It can be easily shown that the more decays into two photons, the shorter the mean lifetime of o-Ps, following Eq. 1.1. In inorganic matter, this would correspond to smaller pores (free volumes) [25–28]. In organic matter, the impact of changes in o-Ps mean lifetime is still under investigation [63, 79–82]. First hypothesis states, that it may be related more to the amount of free radicals or oxygen molecules in the tested sample, than to the size of free volumes.

Linking the o-Ps mean lifetime to an annihilation position distribution map may enable the so-called positronium imaging, introduced in Sec. 6. It will be an object of study in the next chapter showing the final results of the thesis. But first it is important to correctly select the events that make it possible to determine the position and lifetime of individual positrons. The first candidate for such events are (2G) events which, thanks to the presence of annihilation hits, allow to mark the position of annihilation, and an additional deexcitation hit allows to determine the time after which a given positron annihilated. This type of event is the most numerous of those meeting this criterion as it requires the observation of the smallest number of photons. The next event candidate - (3G) will be studied wider in the next section.

Another possible application of the separation of various types of positronium decays may allow for a closer examination of other properties of positronium, such as the determination of the decay constant described in Sec. 5.7. The selection process has already been presented previously by the appropriate selection criteria given in Sec. 2.4. (2G) events will be considered in these section consisting of two annihilation and one deexcitation hits in an event. From the previous section one can distinguish two photon from three photon decay based on the sum of the two smallest angles between annihilation hits. For the sake of completeness of the criterion, the deexcitation hit may be taken as the third hit, or simply instead of the sum of the two smallest angles, the smallest angle between the annihilation hits may be taken.

When the sum of the two smallest angles (smaller angle) between annihilation hits is in the range of $[175^o, 185^o]$ it will be treated as a two photon decay candidate and analyzed further. Also, by looking at the distribution shown in Fig. 5.5 one can see the diagonal pattern formed by the scattering between neighbouring scintillators, which is the most common as it can be

seen in blue and yellow range in Fig. 5.3. The schemes of such scatterings and their presence on the angle distribution defined in Fig. 5.5 are shown in Fig. 5.6. It is worth noting that if a scattering occurs between adjacent scintillators creating an angle between hits equal to $\theta_{12}$, then all such events will occur on the line given as $f(x) = f(\theta_{12} + \theta_{23}) = \theta_{23} - \theta_{12} = \theta_{12} + \theta_{23} - 2 \cdot \theta_{12} = x - 2\theta_{12}$. In addition, the resulting lines will be parallel to any other line formed by a different minimum angle. To reduce the impact of such scatterings, an additional

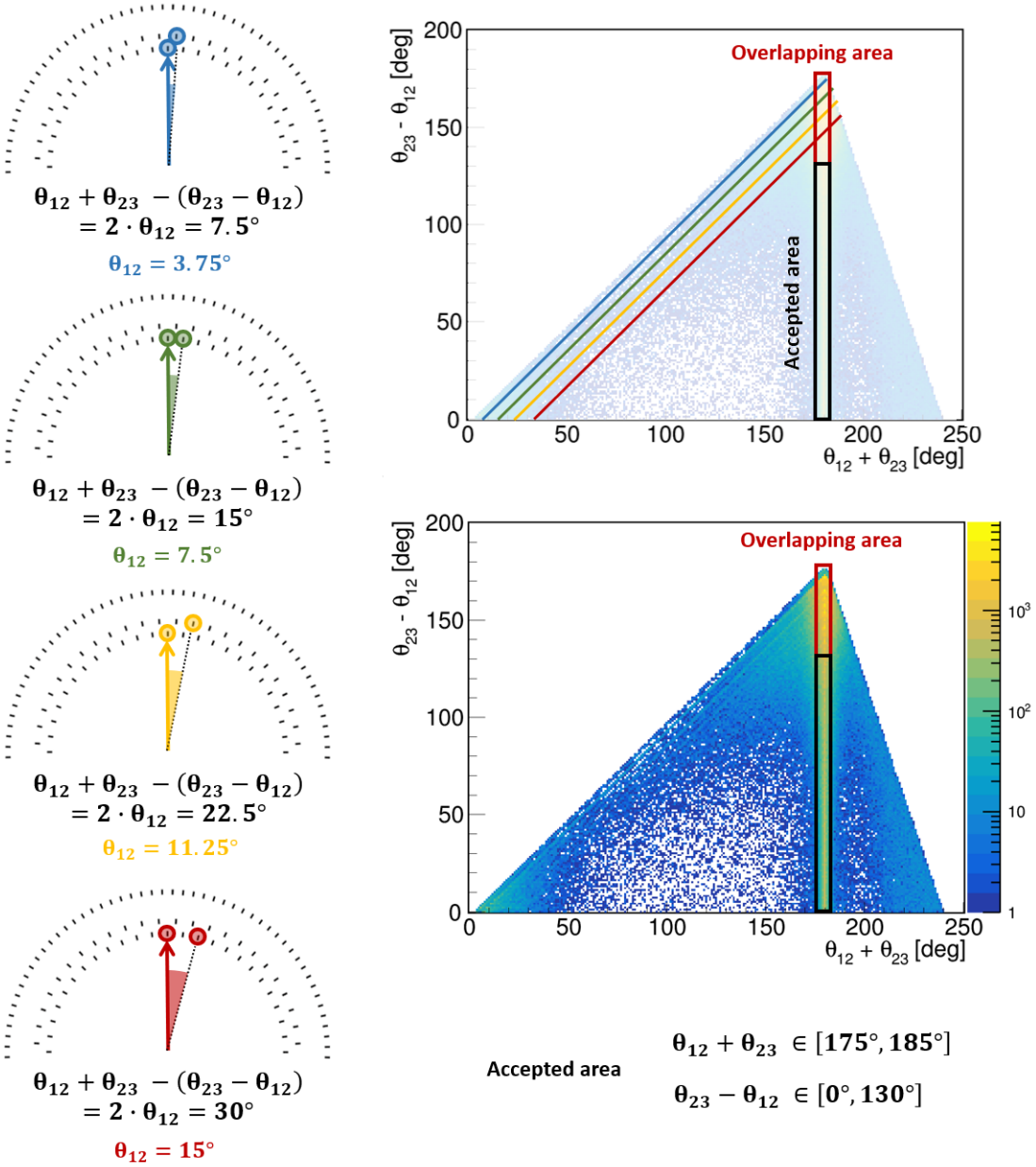


Figure 5.6: **Rejection of the scatterings for the (2G) events.** Experimental data. Four examples of scattering between adjacent scintillators, marked by blue, green, yellow, and red. Schematically marking where selected scatterings will be on the difference between the two smallest angles $(\theta_{23} - \theta_{12})$ over their sum $(\theta_{12} + \theta_{23})$ distribution.

cut was made on the difference between the two smallest angles to be less than 130°, yielding the final data sample for the analysis of the two photon decays.

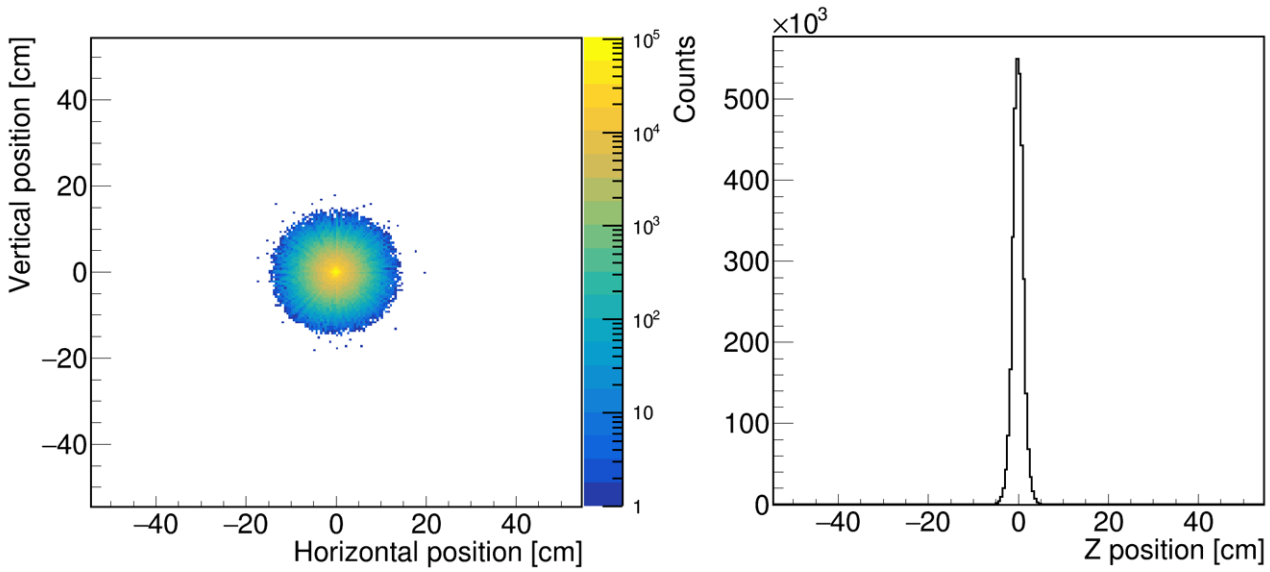


Mean Horizontal (X) position:
**-0.05972** cm
with SD: **2.623** cm

Mean Vertical (Y) position:
**-0.05454** cm
with SD: **2.65** cm

Mean Z position:
**-0.07683** cm
With SD: **1.195** cm

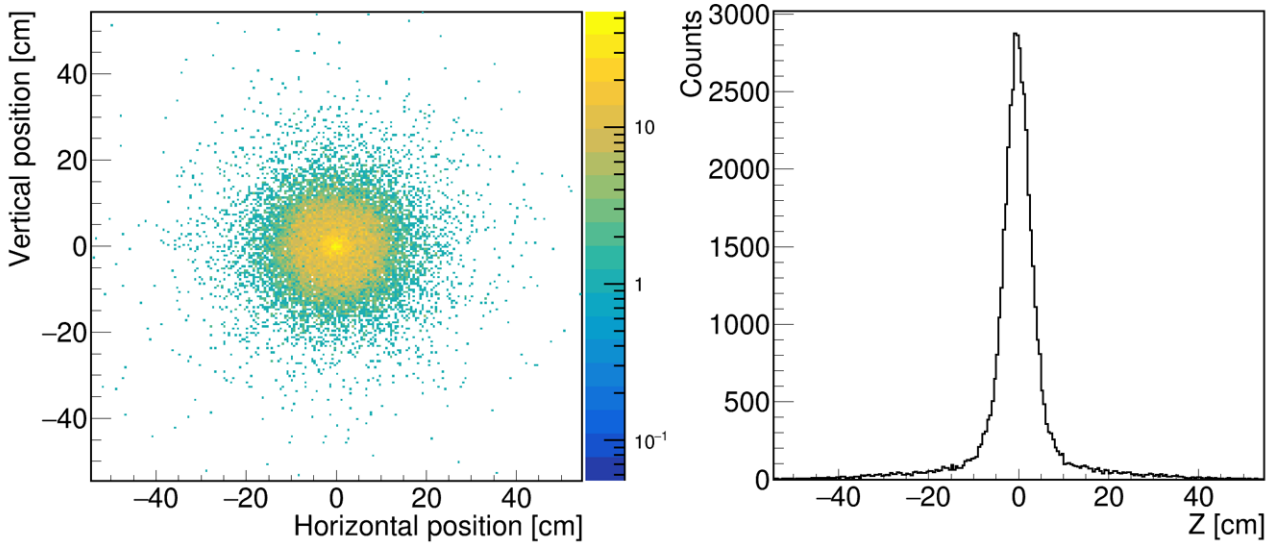


Mean Horizontal (X) position:
**-0.06472** cm
with SD: 8.815 cm

Mean Vertical (Y) position:
**-0.04211** cm
with SD: **8.721** cm

Mean Z position:
**-0.1618** cm
With SD: **8.51** cm

Figure 5.7: **Images of the annihilation position for the selected (2G) and (3G) events.** Experimental data. Distributions of the reconstructed annihilation positions for (2G) (top) and (3G) (bottom) events in the XY plane (left) and in Z (right).

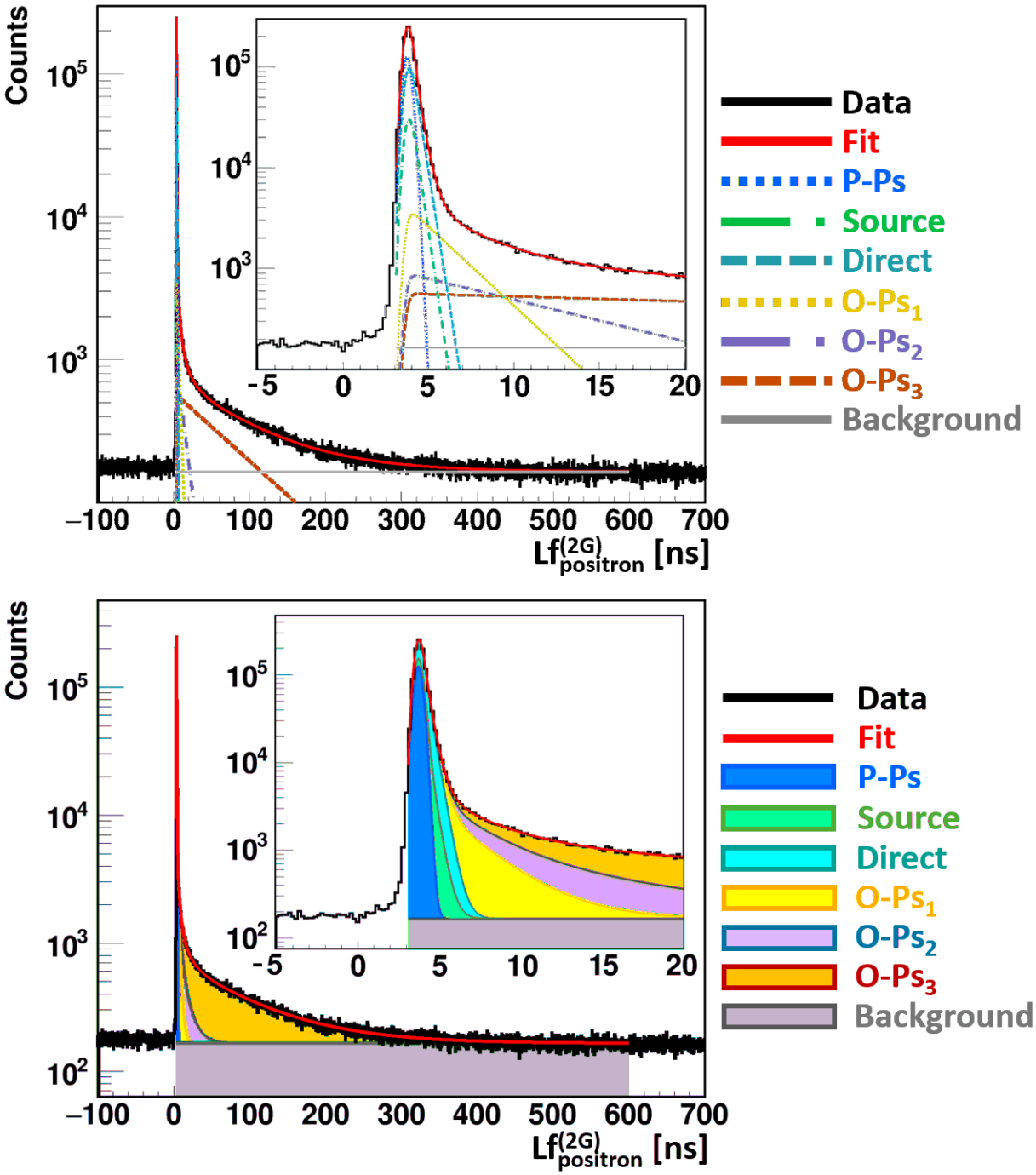


Figure 5.8: **Lifetime distribution from the analysis of the (2G) events.** Experimental data. Positron lifetime distribution with the fitted components drawn separately (top) and cumulatively (bottom)

For the selected data sample of (2G) events one can reconstruct position of every single annihilation of a positron with an electron, like it was shown in Fig. 2.1 and the lifetime of

positron as

$$\mathrm{LF}^{(2\mathrm{G})}_{\mathrm{positron}} = \frac{\mathrm{t}_{\mathrm{AnniHit1}} + \mathrm{t}_{\mathrm{AnniHit2}}}{2} - \mathrm{t}_{\mathrm{DeexHit}}. \tag{5.3}$$

In the above equation, $\mathrm{t}_{\mathrm{AnniHit1}}$ and $\mathrm{t}_{\mathrm{AnniHit2}}$ stands for the reconstructed time of the first and the second annihilation hit, respectively, where $\mathrm{t}_{\mathrm{DeexHit}}$ is the time of the only one deexcitation hit in an event.

Distribution of the annihilation positions is shown in Fig. 5.7 (top). It allowed to estimate the position of the chamber with the source and the tested sample as $(x, y, z) = (-0.06\ \mathrm{cm}, -0.06\ \mathrm{cm}, -0.08\ \mathrm{cm})$. In Fig. 5.8 there is positron lifetime distribution for (2G) events estimated as in Eq. 5.3 with fit performed in the PALS Avalanche software. Results from the fit is shown in Tab. 5.2. One can see that the results are smaller to one given in the [95] and the uncertainties are also smaller comparing to results given in Tab. 5.1. One can conclude, that the data sample after used selection criteria is much cleaner comparing to the events with the only one annihilation and deexcitation hits, and there may be some correlation of decay constant of the pick-off process over time, reducing effectively mean lifetime of such component. The next section will show the analysis for (3G) events, but the (2G) event will find another application in the determination of the decay constant in the Sec. 5.7.

Table 5.2: **Fit results for (2G) and (3G) events.** Intensity of the source component is subtracted from the total intensity of the lifetime components. High value of $\sigma$ for (3G) events is probably caused by low number of events creating lifetime spectrum, and the calculation of the time difference from four hits.

| **Parameter** | **Result for (2G)** | **Result for (3G)** |
|---|---|---|
| $\sigma$ [ns] | 0.243 (01) | 0.594 (09) |
| $\mathrm{I}^{g}$ [%] | 100 | 100 |
| $\tau_{\mathrm{source}}$ [ns] (fixed) | 0.374 | - |
| $\mathrm{I}^{e}_{\mathrm{source}}$ [%] (fixed) | 10 | - |
| $\tau_{\text{p-Ps}}$ [ns] (fixed) | 0.125 | - |
| $\mathrm{I}^{e}_{\text{p-Ps}}$ [%] | 33.72 (11) | - |
| $\tau_{\mathrm{direct}}$ [ns] | 0.404 (01) | 0.734 (17) |
| $\mathrm{I}^{e}_{\mathrm{direct}}$ [%] | 36.84 (04) | 34.08 (24) |
| $\tau_{\text{o-Ps}_1}$ [ns] | 2.77 (04) | 2.77 (fixed) |
| $\mathrm{I}^{e}_{\text{o-Ps}_1}$ [%] | 4.77 (04) | 0.26 (08) |
| $\tau_{\text{o-Ps}_2}$ [ns] | 10.50 (17) | 10.50 ((fixed) |
| $\mathrm{I}^{e}_{\text{o-Ps}_2}$ [%] | 3.85 (01) | 0.52 (23) |
| $\tau_{\text{o-Ps}_3}$ [ns] | 90.33 (05) | 90.33 (fixed) |
| $\mathrm{I}^{e}_{\text{o-Ps}_3}$ [%] | 20.82 (05) | 65.15 (44) |
| Adjusted $\mathrm{R}^2$ | 0.9991 | 0.9886 |
| Reduced $\chi^2$ | 1.0374 | 1.2275 |

## 5.5 Analysis of the annihilations into three photons

Analysis of the (3G) events will be no much different from the analysis of the (2G) events shown in the previous section. However, because a different type of positronium decay will be investigated - on three photons, some methods must be different, such as for example position reconstruction or the TOT cut. Because the mean photon energy for the three-photon decay is lower than it is for the two-photon decay, annihilation photon cut for analysis of the (3G) events was extended to 1 ns. It is worth to notice, that another area of the angle distribution shown in Fig. 5.5 - red one will be studied in this section.

After the correct data selection, the main part of (3G) events should be the decays of ortho-positronium into three photons. Of course, it is worth remembering that a small number of decays may occur from the direct annihilation of the positron-electron pair. From the fit to the (2G) lifetime distribution one can estimate that 36.84% of the positrons annihilate in XAD4 directly with an electron. In addition, with the assumption that 1/374 of the direct annihilations occurs with emission of three photons, that corresponds to $36.84\%/374 = 0.1\%$ positrons that can give signal to (3G) events. Data selection described in Sec. 2.4 were at first applied for (3G) events. Then the angle criterion shown in Fig. 5.5 was applied to choose proper decays of o-Ps into three photons. It allowed to reduce scatterings and events from different sources of background in the data sample. However, there can be still some part of the background not rejected by it what will be shown later based on the simulation results.

Before showing the results from the selected data sample one can start with highlighting why it is worth to study different types of decays of positronium separately. Having selection methods that allows to distinguish different decays one can not only find relative probabilities of a given decay but also to study its specific properties, like angular distribution. It can also help to find fractions of the forbidden and rare decays of the positronium, like p-Ps decay into three (forbidden) or four (rare) photons. An example of analysis and separation of positronium decays into three photons will prove that the J-PET detector is able to study and separate various positronium decays.

Method of the reconstruction of the position of the o-Ps three photon annihilation was already described in Sec. 4.1. It allowed to collect (3G) annihilation position distribution from the measurement, what is shown in Fig. 5.7 (bottom). Lifetime of positron calculated as

$$\mathrm{LF}^{(3\mathrm{G})}_{\mathrm{positron}} = \frac{\mathrm{t}_{\mathrm{AnniHit1}} + \mathrm{t}_{\mathrm{AnniHit2}} + \mathrm{t}_{\mathrm{AnniHit3}}}{3} - \mathrm{t}_{\mathrm{DeexHit}}, \tag{5.4}$$

was used for the selected event. Similar as in the previous section $\mathrm{t}_{\mathrm{AnniHit1}}$, $\mathrm{t}_{\mathrm{AnniHit2}}$ and $\mathrm{t}_{\mathrm{AnniHit3}}$ stands for the reconstructed time of the first, the second and the third annihilation hit, respectively, where $\mathrm{t}_{\mathrm{DeexHit}}$ is the time of the only one deexcitation hit in an event. Resulting lifetime distribution with fit is shown in Fig. 5.9.

Fitting of the lifetime spectrum, due to the low total number of counts in the spectrum was performed by fixing mean lifetime of the o-Ps components on the values obtained from fitting (2G) spectrum. Fitted spectrum is shown in Fig. 5.9. Surprisingly, the intensity of the component with a low average lifetime, interpreted as the one coming from the direct annihilation of the positron with the electron, is high. From the theory it should not exceed 1% of the total intensity of the o-Ps components. This is where simulations come in handy to

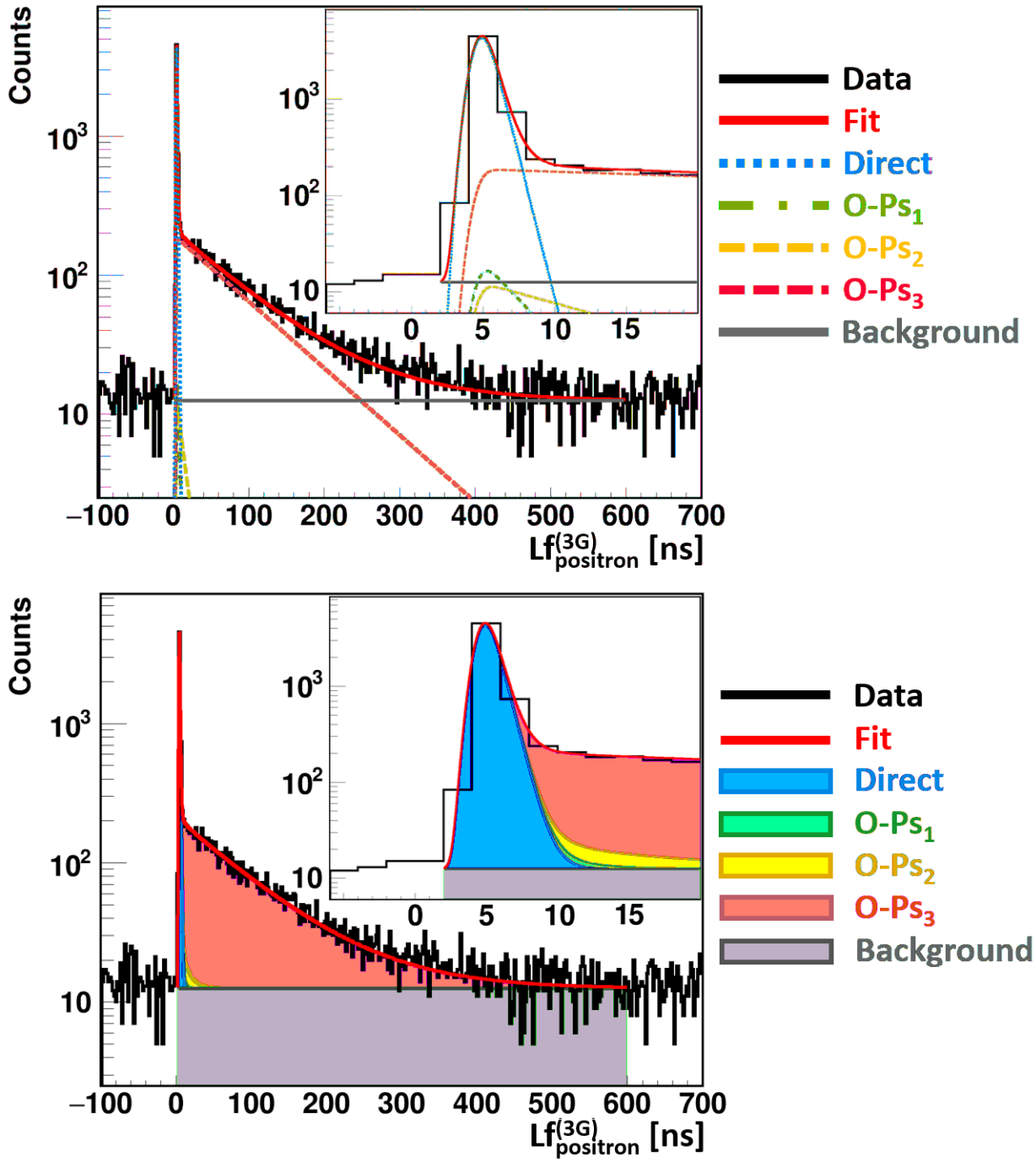


Figure 5.9: **Lifetime distribution from the analysis of the (3G) events.** Experimental data. Positron lifetime distribution with the fitted components drawn separately (top) and cumulatively (bottom).

estimate the effect of different background types on the final spectrum. Decomposition of the lifetime spectrum onto different background types listed in Sec. 4.6 based on the simulation is shown in Fig. 5.10. The high convergence of the obtained simulation results with the

measurement data allows to answer the question of the main origin of events with very low lifetimes. One can deduce, that the peak around zero in the lifetime spectrum is mainly due to event-related (2G) scattering. There is still some discrepancies between the data and the simulation in the peak ( 360 events), that were not explained by the simulations. However, as it will be shown in the next section, influence of the cosmic radiation may be the last piece of the puzzle. It is also the only background type that has not yet been simulated by the software used to simulate the J-PET detector measurement.

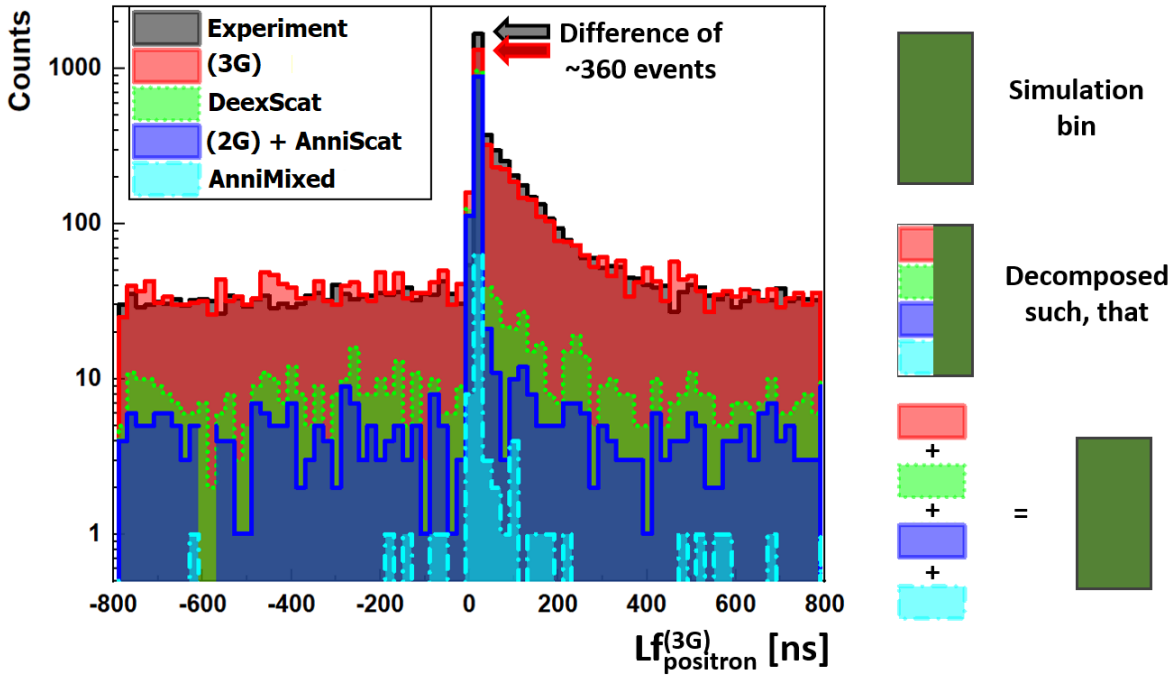


Figure 5.10: **Lifetime distribution decomposed onto different types of events [96].** Experimental data. Lifetime distribution for (3G) events from Fig. 5.9 is compared with the distribution coming from the simulations. The simulated bin is divided into bins from different event types, such that the sum of the divided bins gives the simulation bin value (drawn cumulatively). One can them decompose simulated distribution onto different components coming from the signal (3G) and the various types of backgrounds - scatterings with (2G) events, (3G) event but with at least one annihilation hit coming from the scattering of the deexcitation hit and the event with mixed origin (coincidences of (2G) and (3G) events). However there is still some difference in the peak, that was not explained by the simulations.

Nevertheless, it was possible to select three-photon decays from the data with fairly good accuracy, what was proven by the resulting lifetime distribution. The remaining remnants of other types of events were successfully separated on the basis of simulations. This is a promising finding in future studies of rare positronium decays or other defined unstable systems.

## 5.6 Cosmic rays influence

Cosmic rays consisting mostly of high-energy protons and nuclei originating from the sun, can create secondary particles in the high levels of the atmosphere. Secondary particles produced in this way (mainly muons) can be registered by detectors close to the Earth's surface. For example, $\mu^+$ with an energy of 4 GeV [111] can deposit in the plastic scintillators used in the J-PET detector with dimensions given in Section 2.1, an average energy of about 1.2 MeV. For this reason, they can be confused with annihilation or deexcitation photons studied in the measurement with XAD4. Due to the fact that cosmic rays can create the so-called particle showers, the J-PET detector is even able to register a few muons in a small time window. As a result, it is possible to reconstruct the entire event, which consists only of hits from cosmic rays.

If there are some events in the data that do not come from the analyzed decays, they may distort the analysis results if they are not filtered out. Just filtering out unwanted cosmic ray events is very difficult as the resulting muons do not have a simple timing or geometric correlation. The energy criterion in the absence of a signal from the photoelectric effect is also a weak condition for data selection. In the literature there is a method based on an additional detector, the so-called Veto detector that helps to find events with potential cosmic hits by studying coincidences between Veto and the rest of the detection modules.

For the J-PET detector, additional measurement was conducted, in order to estimate how the cosmic radiation can be reconstructed by the reconstruction procedures. The (cosmic) measurement without source in the detection chamber lasted 66 hours, compared to the 27-day measurement with XAD4. The influence of the cosmic radiation on the (3G) events was estimated, that possibly can help in explaining possible discrepancies between simulations and the data. The same cuts were applied on the data coming from the cosmic measurement as it was for the XAD4 measurement.

Resulting lifetime spectrum is shown in Fig. 5.11. One can notice, that all of the 37 events reconstructed from the cosmic run are concentrated around zero at 7 ns of the maximum difference from zero at the lifetime spectrum. It also shows that the selection criteria were not able to reject these events. However, obtained distribution can be used to estimate how much, and in which range, cosmic radiation can influence (3G) lifetime distribution.

For comparison between cosmic measurement and the measurement with the XAD4, obtained distributions must be multiplied by the fraction of time (FT) that will cover time difference between those two runs

$$\mathrm{FT} = \frac{66\ \mathrm{h}}{27\ \mathrm{days}} = \frac{66\ \mathrm{h}}{648\ \mathrm{h}} = 9.82. \tag{5.5}$$

Therefore, number of cosmic events that could be part of the (3G) selected events, will be around 383 events. It corresponds to the 2% fraction of the (3G) lifetime spectrum, but they will be most probably only in the range up to [-7.7] ns. When one take the differences between the simulated and measured lifetime distribution shown in Fig. 5.10, the 2% impact of the cosmic radiation allows to complete the interpretation of the whole spectrum (3G), at least in terms of the uncertainty of the simulations obtained.

It is worth mentioning that in the sourceless measurement used to estimate the effect of

cosmic rays, it also includes signals from other radiation unrelated to those originating from the $^{22}$Na radioisotope. Thus, additional measurement without source inside the detection chamber may allow the impact of all external sources to be estimated. In the last section final analysis of the decay constant from the comparison between lifetime spectra for (2G) and (3G) events.

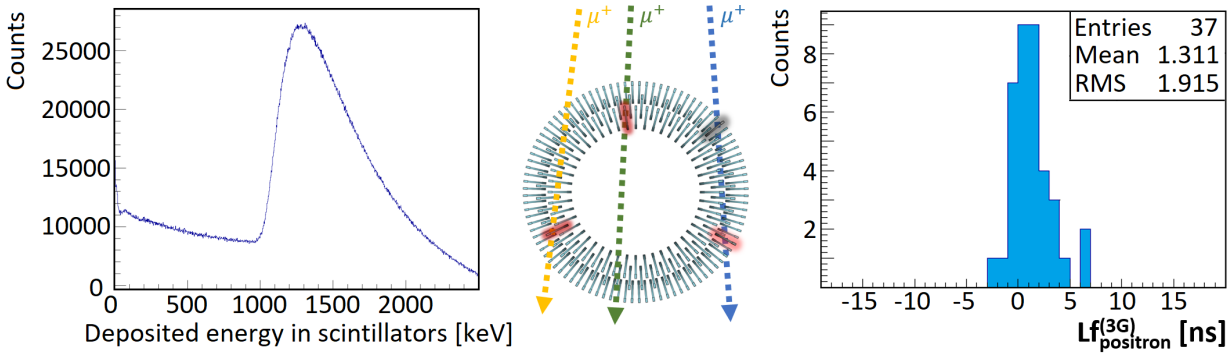


Figure 5.11: **Lifetime distribution obtained from the measurement with cosmic radiation only.** (left) Simulated energy distribution for muons ($\mu^+$) with initial energy of 4 GeV deposition energy in the J-PET detector. (middle) Diagram of the cosmic shower passing through the J-PET detector from above. (right) Experimental distribution of the events from the cosmic measurements that passed the selection criteria for (3G) events.

## 5.7 Decay constants determination

The one additional task that can be done in the context of the analysis of the lifetime distributions is the determination of the decay constant of the o-Ps. Precise experimental determination of the o-Ps decay constant may assist in verifying this value determined theoretically [41]. At the beginning, one can start by introducing a decay constant characterization. Namely, the mean lifetime ($\tau$) of some particle is related to the decay constant ($\lambda$) as follows

$$\tau = \frac{1}{\lambda}. \tag{5.6}$$

Given the positronium and its two states p-Ps and o-Ps, their decay constants in a vacuum are given as [112, 113]

$$7.9852 \frac{1}{\text{ns}} = \lambda_{\text{p-Ps}} \overset{\text{Eq. 5.6}}{=} \frac{1}{\tau_{\text{p-Ps}}} = \frac{1}{125.23 \text{ ps}}, \tag{5.7}$$

$$7.0399 \frac{1}{\mu\text{s}} = \lambda_{\text{o-Ps}} \overset{\text{Eq. 5.6}}{=} \frac{1}{\tau_{\text{o-Ps}}} = \frac{1}{142.05 \text{ ns}}. \tag{5.8}$$

In matter, mean o-Ps lifetime can be shorten due to the interaction with electrons (pick-off) or para-magnetic oxygen molecules (ortho-para conversion), what was wider described in

Sec. 1.3. However, when considering only the pick-off process the decay constant for o-Ps in matter ($\tau_{\text{o-Ps}}^{\text{matter}}$) can be expressed as

$$\tau_{\text{o-Ps}}^{\text{matter}} \overset{\text{Eq. 5.8}}{=} \frac{1}{\lambda_{\text{o-Ps}}^{\text{matter}}} = \frac{1}{\lambda_{\text{o-Ps}} + \lambda_{\text{pick-off}}}, \tag{5.9}$$

where $\lambda_{\text{pick-off}}$ is the decay constant of the pick-off process, resulting in the shortening of the mean lifetime of the o-Ps $\tau_{\text{o-Ps}}^{\text{matter}} < \tau_{\text{o-Ps}}$.

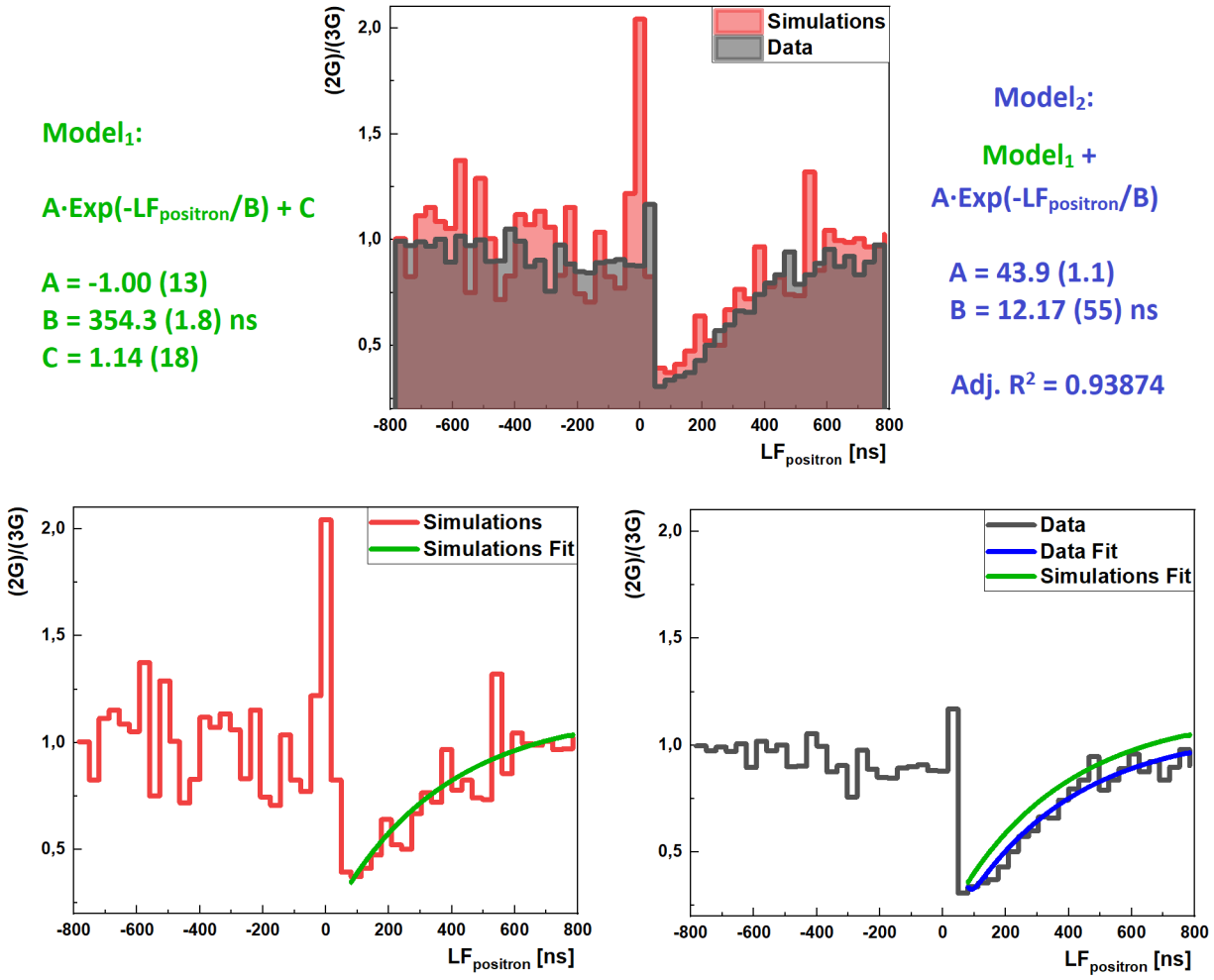


Figure 5.12: **Determination of the models describing (2G)/(3G) distributions.** (middle, top) Normalized distribution of (2G)/(3G) for the simulated (red) and the experimental (black) data. (left, bottom) Fitted distribution of (2G)/(3G) for the simulated data with $\text{Model}_1$ (green line). (right, bottom). Fitted distribution of (2G)/(3G) for the experimental data with $\text{Model}_2$ (blue line).

A common assumption during analysis of the positronium lifetime is that the decay constant of the pick-off process is constant over time. However, this assumption is not always true causing dependence of the decay constant - $\lambda_{\text{pick-off}}(\text{LF}_{\text{positron}})$. This relationship comes

from the interaction of o-Ps with electrons from matter at low o-Ps velocities. Indeed, the probability of o-Ps collision with the electron will depend on the o-Ps velocity and thus may affect the chance of the pick-off process. This has very serious consequences as the mean lifetime of o-Ps may be different in different parts of the lifetime spectrum $\tau_{\text{o-Ps}}^{\text{matter}}(\text{LF}_{\text{positron}})$. Some studies have already been carried out to determine this relationship [114–117].

It is worth reminding that the number of the decay into three photons for a given o-Ps component depends on the mean lifetime, following Eq. 1.1. This can be used for comparing the positronium lifetime distributions for two-photon (2G) and three-photon (3G) events. Distributions shown in Fig. 5.8 and 5.9 will be explained by the same decay constant set for different o-Ps components. It has already been shown in Tab. 5.2, that the relative intensities for different o-Ps components (2.5, 10.4 and 90.3 ns) are different for different type of the decay. The intensities of the short-lived o-Ps components will be lower for three-photon decays, which is also confirmed by the Eq. 1.1. When dividing distribution for (2G) events by distribution for (3G) events, it will results in different fraction of components for different ranges of time as it is shown in Fig. 5.12. The most interesting effects can be seen in the range where the influence of the longest component, in terms of mean lifetime, will start to be predominant. It can be observed for time differences larger than 50 ns, where the impact of the component with an average lifetime of 10 ns will be negligible, and the signal will only come from the longest component (90 ns). For larger time differences, the distribution for (2G) and (3G) should be then characterized by the same o-Ps component.

If one divide distribution of $\text{LF}_{\text{positron}}^{(2\text{G})}$ by distribution of $\text{LF}_{\text{positron}}^{(3\text{G})}$, the resulting distribution $\frac{(2\text{G})}{(3\text{G})}$ will be a function of $\lambda_{\text{pick-off}}$ and $\lambda_{\text{o-Ps}}$. Indeed, the loss of the $\frac{(2\text{G})}{(3\text{G})}$, comparing to the accidental coincidences level, is corresponding to those ortho-positronia, that should decay into two photons due to the pick-off process, but due to the low velocity of the o-Ps it self-decayed with emission of three photons. In addition, $\lambda_{\text{pick-off}}$ for a given time t corresponds to the number of o-Ps that annihilate via the pick-off process, so in other words the number of events in the $\text{LF}_{\text{positron}}^{(2\text{G})}$ with bin related with time t. Therefore, the division of the $\text{LF}_{\text{positron}}^{(2\text{G})}$ by distribution of $\text{LF}_{\text{positron}}^{(3\text{G})}$, should correspond to the fraction of the decay constants.

The pick-off decay rate $\lambda_{\text{pick-off}}$ as a function of time (t) can be divided into two components

$$\lambda_{\text{pick-off}}(\text{t}) = \lambda_{\text{pick-off}}^{\text{v}}(\text{t}) + \lambda_{\text{pick-off}}^{0} = \lambda_{\text{o-Ps}}\left(\text{F}_{\frac{(2\text{G})}{(3\text{G})}}(\text{t}) + \text{C}_{\text{b}}\right), \tag{5.10}$$

where $\text{F}_{\frac{(2\text{G})}{(3\text{G})}}$ is a function that expresses the dependence of the pick-off decay constant over time $\left(\lambda_{\text{pick-off}}^{\text{v}}\right)$ which can be extracted from the distribution derived from dividing the positron lifetime distribution for events (2G) by the corresponding distribution for events (3G). $\lambda_{\text{pick-off}}^{0}$ and $\text{C}_{\text{b}}$ are the parameters connected to the constant fraction of the $\lambda_{\text{pick-off}}$. It can be easily seen that

$$\text{C}_{\text{b}} \overset{\text{Eq.5.10}}{=} \frac{\lambda_{\text{pick-off}}^{0}}{\lambda_{\text{o-Ps}}}. \tag{5.11}$$

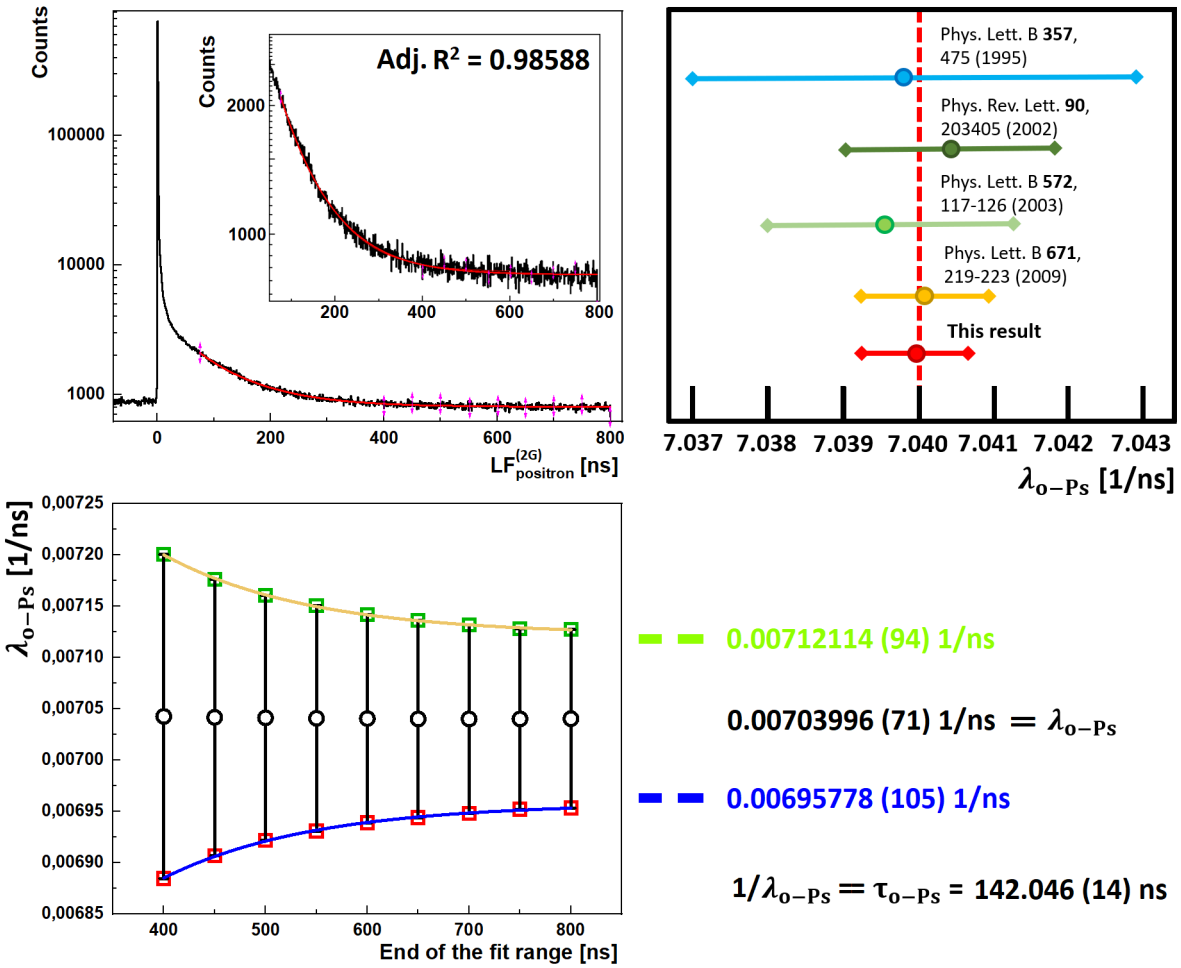


Figure 5.13: **Ortho-positronium decay constant determination by the J-PET detector.** Experimental data. (lfet, top) Positron lifetime distribution for (2G) event with fitted model given in Eq. 5.16, in different ranges from 80 ns to 400-800 ns. (left, bottom) $\lambda_{\text{o-Ps}}$ value and its uncertainty changes in different fitting ranges, characterized by end of the fit range. By extrapolating $\lambda_{\text{o-Ps}}$ with the uncertainties to the infinite ranges the limit value of the $\lambda_{\text{o-Ps}}$ was estimated to 0.00703996 (71) ns$^{-1}$, what correspond to the mean lifetime of the o-Ps in vacuum to 142.046 (14) ns. (right, top) Comparison of the other experimental values [114–117] of the $\lambda_{\text{o-Ps}}$ with the value obtained for the J-PET detector. The theoretical value of 0.00704 ns$^{-1}$ is marked by red, dashed line.

In particular, one can show that $C_b$ should be a function of $C_b(\lambda_{\text{bulk}})$. $\lambda_{\text{bulk}}$ is interpreted as a decay rate of the o-Ps in bulk (dense matter). Value of the $\lambda_{\text{bulk}}$ is often taken as 2 ns$^{-1}$, but it could change in various media and conditions, as it depends on the relative fraction of the formation probability of o-Ps to p-Ps [71]. Going back to the $C_b$, following definition from Eq. 5.9

$$\lambda^{\text{matter}}_{\text{o-Ps}} \overset{\text{Eq.5.9}}{=} \lambda_{\text{o-Ps}} + \lambda^{0}_{\text{pick-off}}, \tag{5.12}$$

when on the other hand $\lambda_{\text{o-Ps}}^{\text{matter}}$ can be also expressed as for example in [71]

$$\lambda_{\text{o-Ps}}^{\text{matter}} \overset{\text{Eq.5.9}}{=} \text{P} \cdot \lambda_{\text{bulk}} + (1 - \text{P}) \cdot \lambda_{\text{o-Ps}}, \tag{5.13}$$

where P is interpreted as the probability of the annihilation of the o-Ps via pick-off process. Parameter P will depend on the measured sample and can therefore be obtained with pick-off models [25–28] with a known value for the pore size in the sample. Comparing Eq. 5.12 and 5.13, one can obtain expression for the $\lambda_{\text{pick-off}}$ as a function of $\lambda_{\text{bulk}}$

$$\lambda_{\text{pick-off}}^{0} = \text{P}\left(\lambda_{\text{bulk}} - \lambda_{\text{o-Ps}}\right). \tag{5.14}$$

and therefore $\text{C}_\text{b}$ is given as

$$\text{C}_\text{b} \overset{\text{Eq.5.11,5.14}}{=} \frac{\text{P}\left(\lambda_{\text{bulk}} - \lambda_{\text{o-Ps}}\right)}{\lambda_{\text{o-Ps}}}. \tag{5.15}$$

In conclusion, the decay constant characterizing the measured o-Ps lifetime distribution can be expressed as a function of the two parameters, which are closely related to the properties of o-Ps in two opposite media - vacuum ($\lambda_{\text{o-Ps}}$) and matter ($\lambda_{\text{bulk}}$).

To estimate the fraction of the scatterings in the $\frac{(2\text{G})}{(3\text{G})}$ distribution that survived selection criteria and could also form an excess of the three-photon decays, comparing to the two-photons', simulated distribution was used. During the simulation, no dependence of the pick-off decay constant on time was assumed. To extract the real excess of the three-photon decays, the experimental distribution of $\frac{(2\text{G})}{(3\text{G})}$ was fitted by a sum of the simulated distribution of the scatterings and the exponential decay ($\text{F}_{\frac{(2\text{G})}{(3\text{G})}}$ = Model$_1$ - Model$_2$ from Fig. 5.13), that modelled $\frac{\lambda_{\text{pick-off}}}{\lambda_{\text{o-Ps}}}$. It allows to expand the model of the $\text{LF}_{\text{positron}}^{(2\text{G})}$ by introducing the dependence of the pick-off decay constant on time, from the fitted model as

$$f\left(\text{LF}_{\text{positron}}\right) = f(0) \cdot \exp\left(-\lambda_{\text{o-Ps}}\left(1 + \frac{\lambda_{\text{pick-off}}\left(\text{LF}_{\text{positron}}\right)}{\lambda_{\text{o-Ps}}}\right) \cdot \text{LF}_{\text{positron}}\right) \overset{5.10}{=}$$

$$= f(0) \cdot \exp\left(-\lambda_{\text{o-Ps}}\left(1 + \text{C}_\text{b} + \text{F}_{\frac{(2\text{G})}{(3\text{G})}}\left(\text{LF}_{\text{positron}}\right)\right) \cdot \text{LF}_{\text{positron}}\right). \tag{5.16}$$

One can fit the model given in Eq. 5.16 to different ranges of the $\text{LF}_{\text{positron}}^{(2\text{G})}$ distribution, which consists of the ortho-positronia that decays due to the pick-off process. One can especially look at the dependence of the estimated value of $\lambda_{\text{o-Ps}}$ on the value of the end of the fitting range in Fig. 5.13. For larger and larger fitting range the value of the $\lambda_{\text{o-Ps}}$ should be burdened with less and less error. With extrapolation to the infinite range the final value of the $\lambda_{\text{o-Ps}}$ was estimated to value 0.00703996 (71) ns$^{-1}$. Extrapolation was done by fitting exponential models to the ends of the uncertainty range for different values of $\lambda_{\text{o-Ps}}$ and calculating an average of horizontal asymptotes of the models. The uncertainty was calculated as the standard deviation of the sum of the random variables. Obtained value is in agreement with the theoretical value of 0.00704 ns$^{-1}$ and with the values obtained experimentally, as shown in Fig. 5.13. The precision of the obtained value of the o-Ps decay constant was estimated at $7.1 \cdot 10^{-7}$ ns$^{-1}$, which is an improvement in comparison to the previous experiments.

In addition one could also estimate the value of $\lambda_{bulk}$ from the fitted value of $C_b$, following Eq. 5.15. Parameter P was estimated from the known value of the pore size in the measured sample, given by the producer - radius equal to 5 nm. The value $\lambda_{bulk}$ of 1.986 (18) $ns^{-1}$ was obtained, which was in agreement with the value usually assumed in the literature (2 $ns^{-1}$).

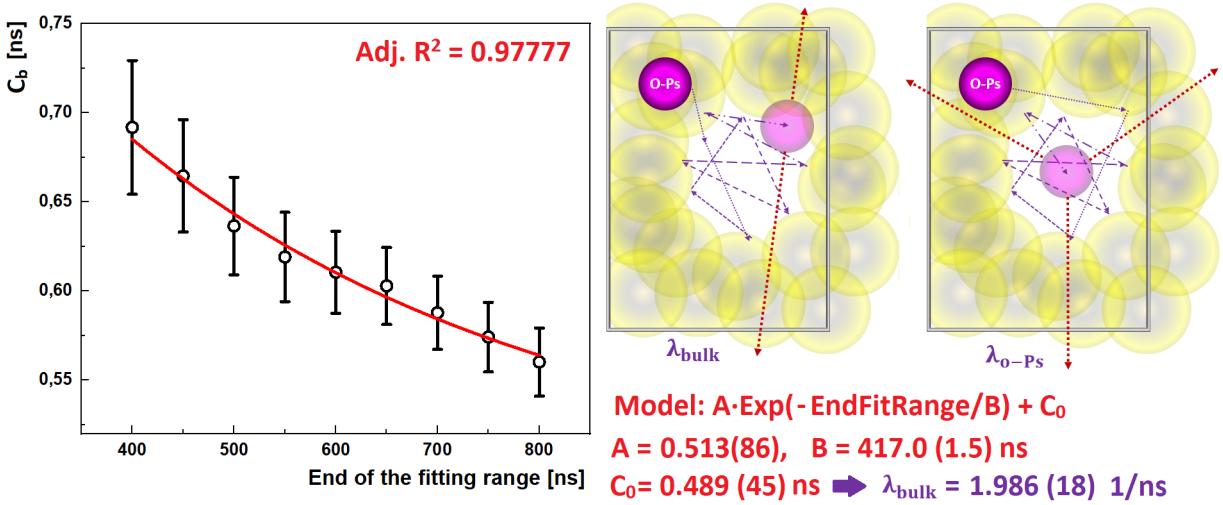


Figure 5.14: **Decay constant in bulk determination by the J-PET detector.** Experimental data. Dependence of the $C_b$ parameter from Eq. 5.16, over the end of the fit range with fit (red line) with the exponential model. Following Eq. 5.15 and the value of the P for the XAD4 used in the measurement (P (R = 5 nm) $\approx$ 0.00174) and the theoretical value of the $\lambda_{o\text{-}Ps} = 0.00704$ $ns^{-1}$ the value of the $\lambda_{bulk} = 1.986(18)$ $ns^{-1}$.

The result of the o-Ps decay constant completes the analysis of the measurement from XAD4. It is worth noting that the obtained result came only from a monthly measurement, which is quite small sample for the usual measurement on the J-PET detector, and still quite good compliance with the theoretical values was achieved. For a longer measurement and a larger amount of data from the simulation, the uncertainty of the obtained value of the o-Ps decay constant can be further improved. It is important to stress, that the only considered source of the obtained uncertainty was the statistical one. In future, complex studies of the systematic uncertainties of the obtained value of the o-Ps decay constants are planned. However, presented results are still very promising, showing the potential of the J-PET detector in fundamental studies field. The next chapter will focus on the imaging capabilities of the J-PET detector, particularly in the context of positronium imaging. It is worth noting that these are the first experimental images of this type, possible to obtain at that time only by the J-PET detector.

# Chapter 6

# Positronium imaging by the J-PET detector

As the final part and the main result of the thesis, positronium imaging by the J-PET detector of two kind of phantoms will be presented. It can be summarized so far that it has been shown how the data is reconstructed, then how the detector is calibrated to reconstruct the positron-electron annihilation position and time. The introduced selection criteria allowed for the selection of an appropriate data sample, which then allowed for the analysis of positronium lifetime for two types of decays - into two and three photons. It has been shown that the J-PET detector is able not only to determine the distribution of the annihilation position, but also to estimate the mean lifetime of each lifetime component. A voxel-by-voxel lifetime estimation method will be described here, which will then lead to positronium imaging.

## 6.1 Experimental setup description

An experimental setup other than that introduced in Sec. 2.2 will be used to evaluate positronium imaging. The new setup should allow to identify more than one material based on the mean lifetime of o-Ps. Additionally, these materials should be far enough apart that their positions can be correctly reconstructed as separate materials. Point-like $^{22}$Na sources encapsulated in the thin Kapton foil, surrounded by an appropriate sample, were used for the positronium imaging. Each sample with the source was inserted to the plastic chamber. In order to reduce scatterings in the holders of the chambers, Kapton scaffoldings were holding chambers in the chosen positions inside the detection chamber.

The first positronium phantom was designed to check whether the J-PET detector could distinguish between samples with large differences in o-Ps mean lifetime. To have that, samples with different porosity were used: IC3100 [118], XAD4 [98] and PVT (scintillator) [119]. They are characterized by the o-Ps component with the highest mean lifetime in vacuum equal to 131.9, 90.8 and 2 ns, respectively [29, 119]. The measurement was carried out under normal conditions (atmospheric pressure, room temperature) for the simplicity of the system and additionally not to introduce additional metal tubes that would have to be connected to each of the chambers to pump out the air. The differences in the measured lifetimes, despite

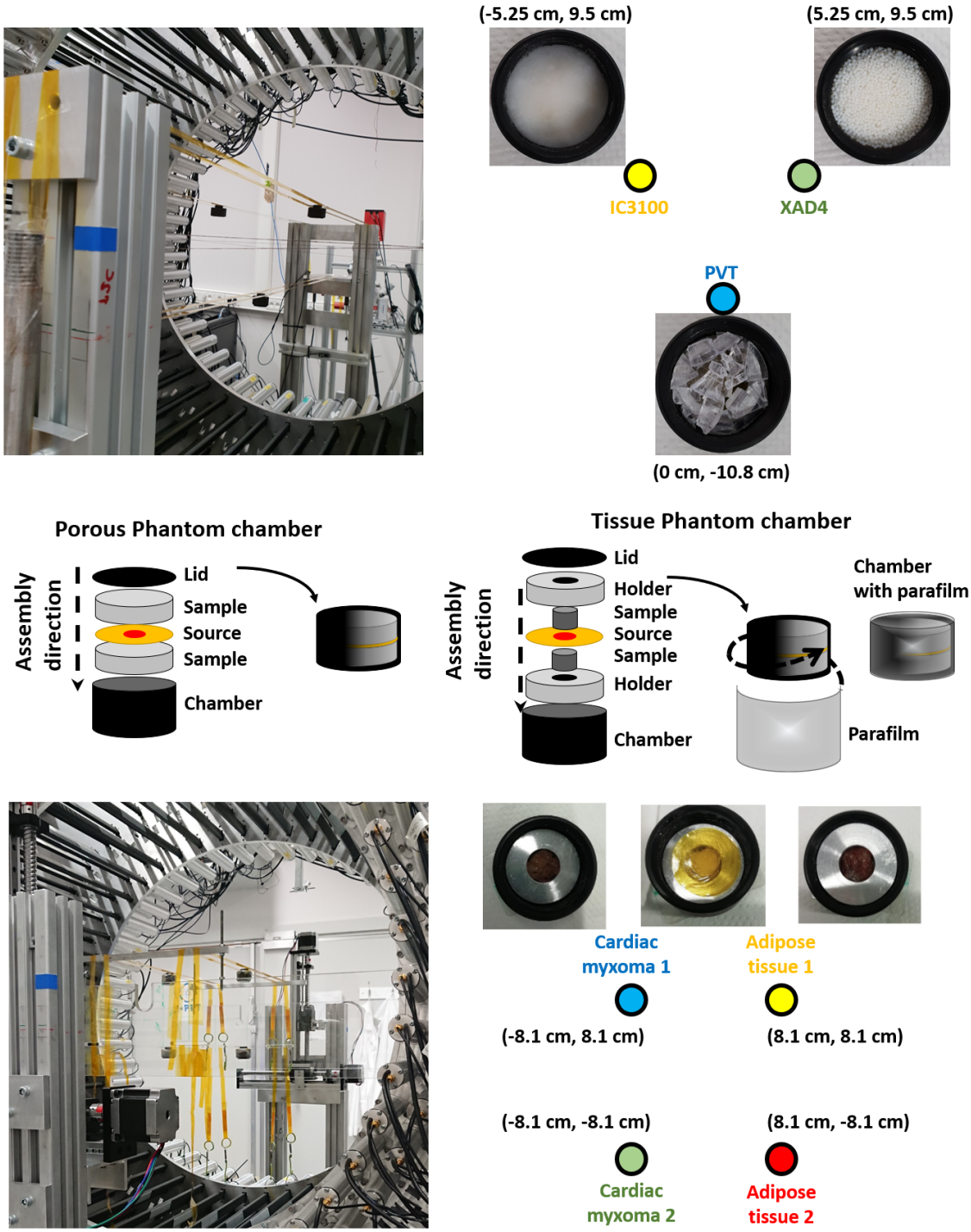


Figure 6.1: **Photograph of the phantoms used for the positronium imaging with the schematic view.** (top) Phantom with the porous materials - IC3100, XAD4 and PVT. Each sample is inserted into the plastic chamber with the radioactive $^{22}$Na source. Each chamber is equidistant from the center of the detector. (bottom) Phantom with the tissues - cardiac myxoma and adipose tissue from two patients. Each sample is inserted into the plastic chamber with the radioactive $^{22}$Na source and with the holder to hold the sample in the source position. Each chamber is equidistant from the center of the detector.

such system simplifications, should still be visible between different samples, what will be shown later. Measurement with the described setup, shown in Fig. 6.1 (top), lasted for 2 days and the results will be shown in Sec. 6.4.

The second positronium phantom focused on o-Ps lifetime studies for two different types of human tissues. The expected changes in the mean o-Ps lifetimes for different tissue types will be much smaller than for the previous phantom. For this reason, such a measurement may also help evaluate positronium imaging for slightly different samples in the positron lifetime domain. The test samples will be cardiac myxoma and the corresponding normal tissue in the form of adipose tissue. Two pairs of cardiac myxoma - adipose tissue from two patients will be the part of the phantom. Samples were fixed in the 10% formalin solution so that they do not change over the course of a long measurement. Similar to the previous phantom each sample was surrounding point-like $^{22}$Na source and inserted to the plastic annihilation chamber. Chambers were holding on Kapton scaffoldings like in Fig. 6.1 (bottom) and the measurement lasted for 8 days in the same conditions as in the measurement with porous samples.

The next section will describe specific analysis procedure, based on the selection criteria defined in Sec. 2.4 and 5.3, that will allow to create positronium image from the measured phantoms.

## 6.2 Data selection

After the data selection and reconstruction one needs to select proper data sample, that will represent events for the positronium imaging. The only difference in the data reconstruction, comparing to the description in Sec. 2.3, was the smaller event time window of 200 ns used. This was due to the fact that the measurements were carried out at atmospheric pressure, hence the mean o-Ps lifetime for any measured sample should be much lower than for the measurement with XAD4 in a vacuum. For the selection the criteria defined in Sec. 2.4 and 5.3 will be used. Following recipe for positronium imaging event given in Fig. 1.9 at first one needs to identify annihilation and deexcitation hits. It can be done by similar cuts as it is shown in Fig. 2.5. For the reconstruction of the annihilation position, like shown in Fig. 2.1, two annihilation hits are required in an event. To estimate lifetime of a positron in an event, single deexcitation hit can be used to set the positron formation time frame. Similar as in analysis of the decays into two photons, to reduce ambiguity in choosing proper hits, the only three hits in an event should create 2 Annihilation - 1 Deexcitation set, based on the $\mathrm{TOT_{hit}}$ value.

Next criteria will be focused on the first step of the scattering reduction and to restrict potential annihilation position to the inside of the detection chamber. One can use the annihilation time difference and the distance of the annihilation plane from the center, described in Sec. 2.4. However, different criterion will be introduced that will work in similar way, but it will be much quicker and simpler. This can be particularly beneficial in a imaging mode, where the simpler the algorithm, the shorter the analysis time will be, and thus the image reconstruction itself will be faster. Distance of the annihilation plane and time difference between annihilation hits will be replaced by a criterion based on calculating the angle bet-

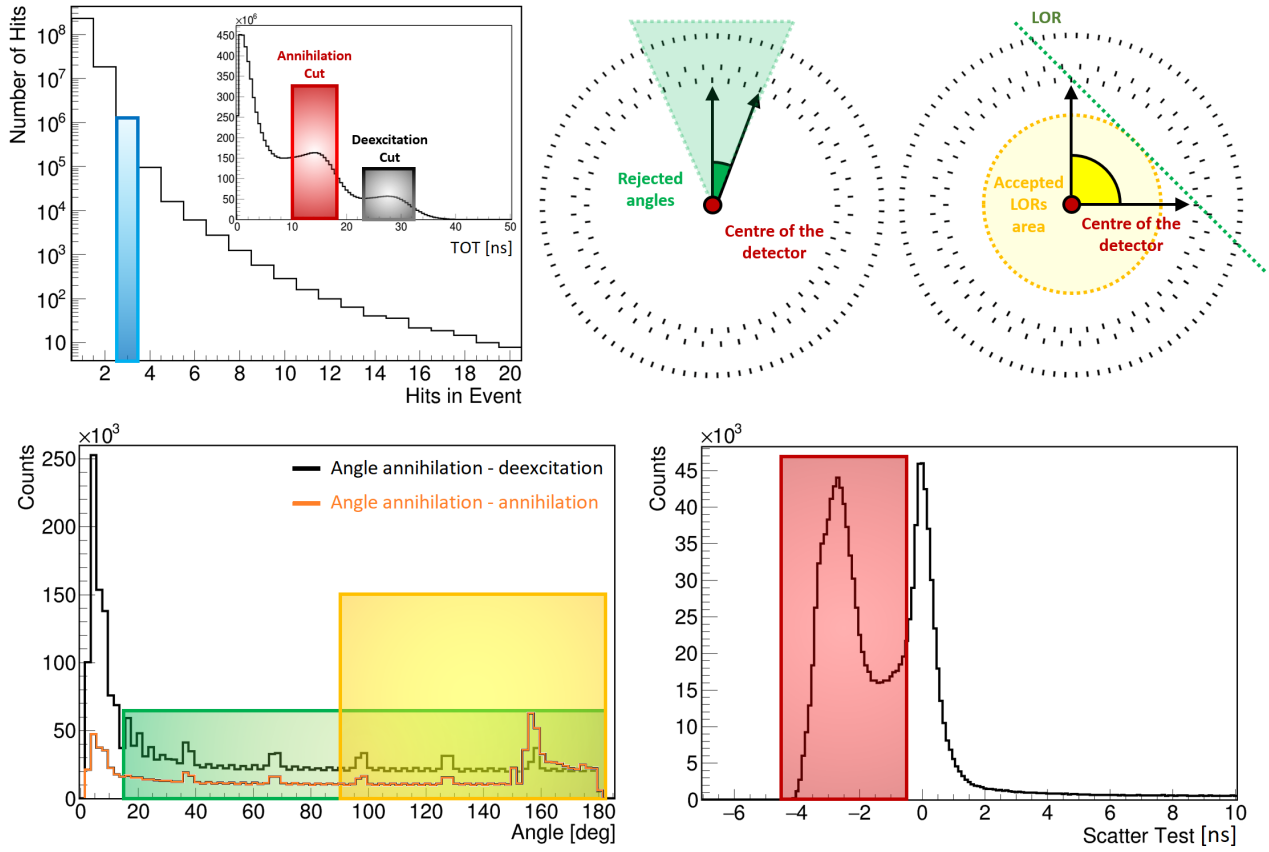


Figure 6.2: **Selection criteria for positronium imaging.** Experimental data. (left, top) Distribution of the hit multiplicity in an event with an insert of the TOT distribution. Blue rectangle indicates selected events with multiplicity 3, where red and black areas indicates selected TOT ranges for annihilation and deexcitation candidates, respectively. (right, top) Schemes of the selection of the angles, drawn on the cross-section of the scintillators in the J-PET detector, between any two hits (green) and annihilation hits (yellow). (left, bottom) Distribution of the angles between any two hits (green line) and annihilation hits (yellow line). Areas marked by yellow and green indicates selected angles for the analysis. (right, bottom) Distribution of the scatter test for the annihilation hits, with a red area indicating the selected events for analysis.

ween hits in the event. Indeed, by requiring that the minimal angle between two annihilation hits will be more than $90^o$ will restrict the created Line-of-Responses (LORs) to the area of the detection chamber as shown in Fig. 6.2. In addition, to reduce scatterings between the neighbouring scintillators, which is the most common as marked in Fig. 5.3 by blue and yellow areas, one can form a criterion on the minimal angle between any two hits in event. Requiring minimal angle between any two hits to be greater than $15^o$, should reject the major part of the scatterings in the data sample as shown in Fig. 6.2. Local enhancements on the angle distribution comes from the binning and the specific geometry of the J-PET detector, and it is described in detail in Appendix G .

The last part of the data selection will use the scatter test criterion, designed for the separation of the scatterings from the primary photons. As it was shown in Fig. 5.1 one needs to be careful when using this criterion not to disturb the lifetime distribution, crucial for the positronium imaging. This will be the case when the scatter test is applied to an annihilation deexcitation hits pair. In situation of the annihilation-annihilation pair, scatter test will no longer affect positron lifetime distribution. However, its use can help in selecting the appropriate pairs that will reproduce a better distribution of annihilation positions. Therefore, scatter test will be checked only on the pair of the annihilation hits in the selected events. The distribution of the scatter test for such pairs is shown in Fig. 6.2 with the similar cut-off equal to -0.5 ns, described in more detail in Sec. 2.4.

After the data selection process one will have events for which annihilation position can be calculated (as in Fig. 2.1) and the positron lifetime estimate, following Eq. 5.3. The next step of the analysis is to estimate the mean o-Ps lifetime in each voxel. The main problem to be overcome is the low lifetime spectrum statistics for single voxels, but it will be discussed in more detail in the next section.

## 6.3 Lifetime estimation for a single voxel

Having proper candidates for the positronium imaging in form of the selected events, one can start from dividing the area of the detection chamber (image space) into smaller cells called voxels. Single voxel represents $\mathbb{R}^3$ subset that will store all the annihilation positions which are contained within this subset. Additionally, all voxels are the same in all dimensions and intersect at most at the edges. Schematically division on voxels is shown in Fig. 6.3. After selection of the events for the positronium imaging, each annihilation position can be correlated with the single positron lifetime. Therefore, for a given voxel positron lifetime distribution can be created, from the lifetimes correlated with the annihilation positions contained in a given voxel. The process of obtaining lifetime spectrum for a single voxel is shown schematically in Fig. 6.3.

It is important to stress, that the dividing image space into voxels is also dividing total lifetime spectrum onto smaller samples. Therefore, the larger the number of voxels, the lower the lifetime spectrum statistic will be collected for a single voxel. As it was shown in the Sec. 4.3, the lower total number of counts in a PAL spectrum the higher the uncertainty of the determined lifetime parameters will be. In that case, it requires the development of a method that will focus on estimating the o-Ps component as accurately as possible for small statistics.

The proposed method will be iterative and will consist in gradually reducing the size of the voxels to stabilize the fit results. A similar approach is used, for example, in the confocal Raman spectroscopy technique, where at the first step pure components are determined in large voxels [120]. Then, in the next step pure components are fixed, voxels are reduced in size and relative intensities of each component is determined for a given voxel. However, with positron imaging, the components will not be fixed, but will be set as the initial parameters for fitting smaller voxels. The fitting procedure is schematically shown in Fig. 6.4.

The use of the described fitting procedure will be shown in the following sections. However,

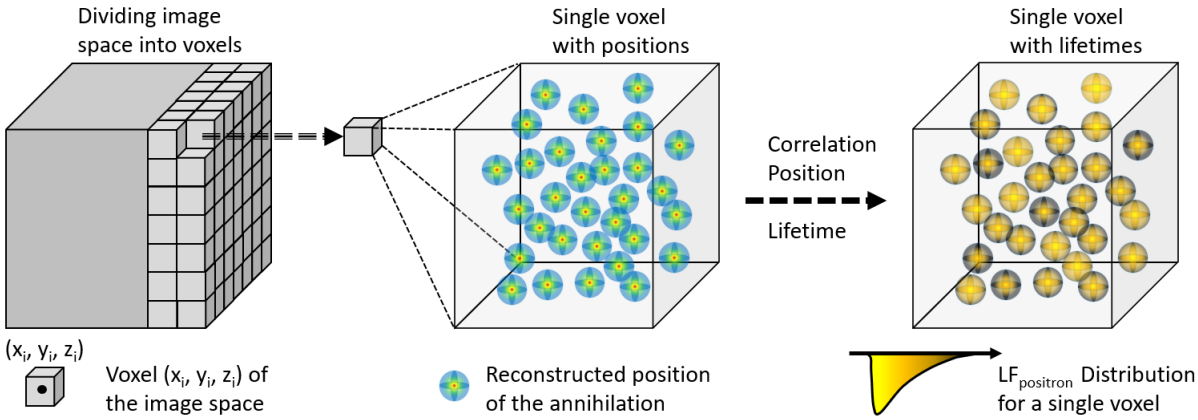


Figure 6.3: **Lifetime distribution for a single voxel of the image space.** Image space, representing all the possible annihilation position that can be reconstructed by the detector, can be divided into identical cuboids called voxels. Given voxel, identified by its center coordinates ($x_i$, $y_i$, $z_i$), contains all the annihilation positions which are contained within the area bounded by the voxel. In a standard imaging single voxel with positions is the final result. However, in positronium imaging each annihilation position inside the voxel can be correlated with the positron lifetime collected from the same event. Correlated lifetimes forms the positron lifetime distribution in a given voxel, which then can be analyzed to estimate mean o-Ps lifetime.

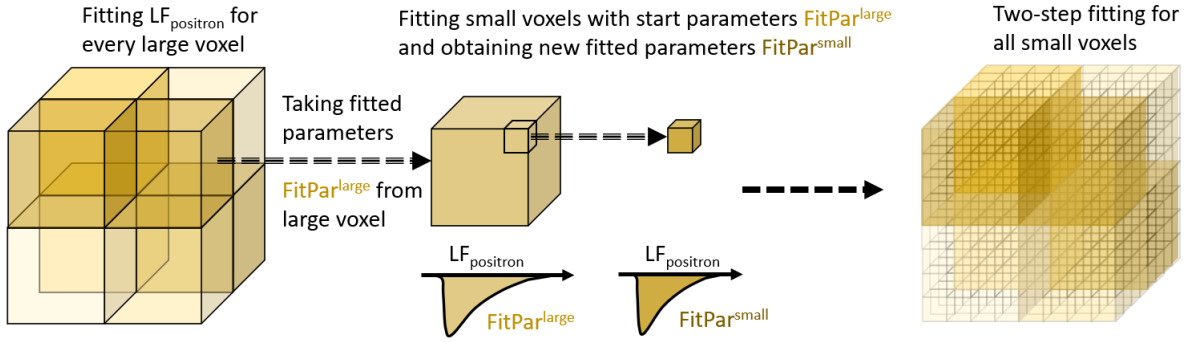


Figure 6.4: **Lifetime fitting procedure.** In the first stage of fitting, the image space is divided into large voxels. In large voxels total number of counts of the $LF_{positron}$ distribution will be sufficient to properly estimate lifetime components represented by $FitPar^{large}$. Next, each voxel is divided into smaller voxel, and the $LF_{positron}$ distribution for small voxels is fitted once again using $FitPar^{large}$ as initial parameters. The described two-step fitting procedure allows to stabilize the results for distributions with small statistics.

the main focus will be on finding the mean o-Ps lifetime, that should be separated from the short-lived components, as it can be seen for example in Fig. 5.9 where red long component and blue short-lived component are dominating in different ranges. Indeed, the structural indicator that will be most sensitive will be o-Ps, so focusing on determining it will be most effective in the structural analysis.

## 6.4 Porous phantom imaging

After entering the details of the measurement and analysis, one can proceed to the presentation of the final results. The first will come from the measurement with the phantom with porous materials. This will allow to check whether the J-PET detector and the analysis methods used are able to separate materials with significantly different mean o-Ps lifetimes in the positronium image. The data from the measurement of the phantom with the three materials was selected by the methods given in the previous sections. The resulting annihilation position distribution from the measurement, the SUV analogue can be seen in Fig. 6.5. It is worth noting, that those positions are calculated based on a naive approach without any sophisticated image reconstruction algorithm. This is due to the lack of such reconstruction algorithms for positronium imaging, where it is necessary to correlate changes in the image during the reconstruction with changes in the lifetime distributions in a given voxel. For this reason, it will be much better to compare the image of annihilation positions and the lifetime image, which are reconstructed in the same way - by naive approach.

Checking how each of the criteria used for positronium imaging affects the distribution of annihilation points is shown in Appendix H. In particular, one can see that the angle criterion allows to reduce the scatterings and scatter test allows to reject some of the accidental coincidences. However, based on the reconstructed image one can see clearly three areas with the higher uptake, which corresponds to each chamber used for the measurement. Additional restriction of the image to three cylinders with centre in (-5.25 cm, 9,5 cm), (5.25 cm, 9.5 cm) and (0 cm, -10.8 cm), where coordinates are in the format (horizontal position, vertical position), will correspond to the possible annihilation positions for IC3100, XAD4, and PVT, respectively. Those cylinders has radius equal to 2 cm and the Z position in the range [-5 cm, 5 cm]. Considering every cylinder separately one can plot the positron lifetime distribution from the positions which are included in the created cylinders. Resulting distributions are shown in Fig. 6.5, where it is possible to see that the IC3100 is characterized by the well pronounced exponential tail coming from the long-lived o-Ps, in contrast to PVT, which has no such tail visible. Indeed, it is reasonable as the o-Ps in the IC3100 should live the longest and in PVT the shortest, looking at the theoretical mean lifetime of o-Ps in those samples in vacuum.

Selected cylinders can be treated as large voxels, introduced in Fig. 6.4. Therefore, Fitting the positron lifetime spectra created for such voxels can be the first step towards the estimation of the o-Ps mean lifetime in every small voxel. Spectra were fitted with the PALS Avalanche software and the results from fitting are given in Tab. 6.1 and each fit with the separation onto different components and some exemplary distributions for small voxels are shown in Appendix I. Obtained values of the o-Ps mean lifetime differ from the theoretical values [62, 119] as the measurement were conducted in the atmospheric pressure, which increases probability of ortho-para conversion process. However, the longest lived o-Ps components is significantly different for different samples. Deriving from that, it was possible to distinguish three samples inserted to the J-PET detector by the correlation of the annihilation position and positron lifetime. Having that, image of the cylinders coloured with the colour corresponding to the o-Ps mean lifetime value, estimated for a given cylinder, is the first

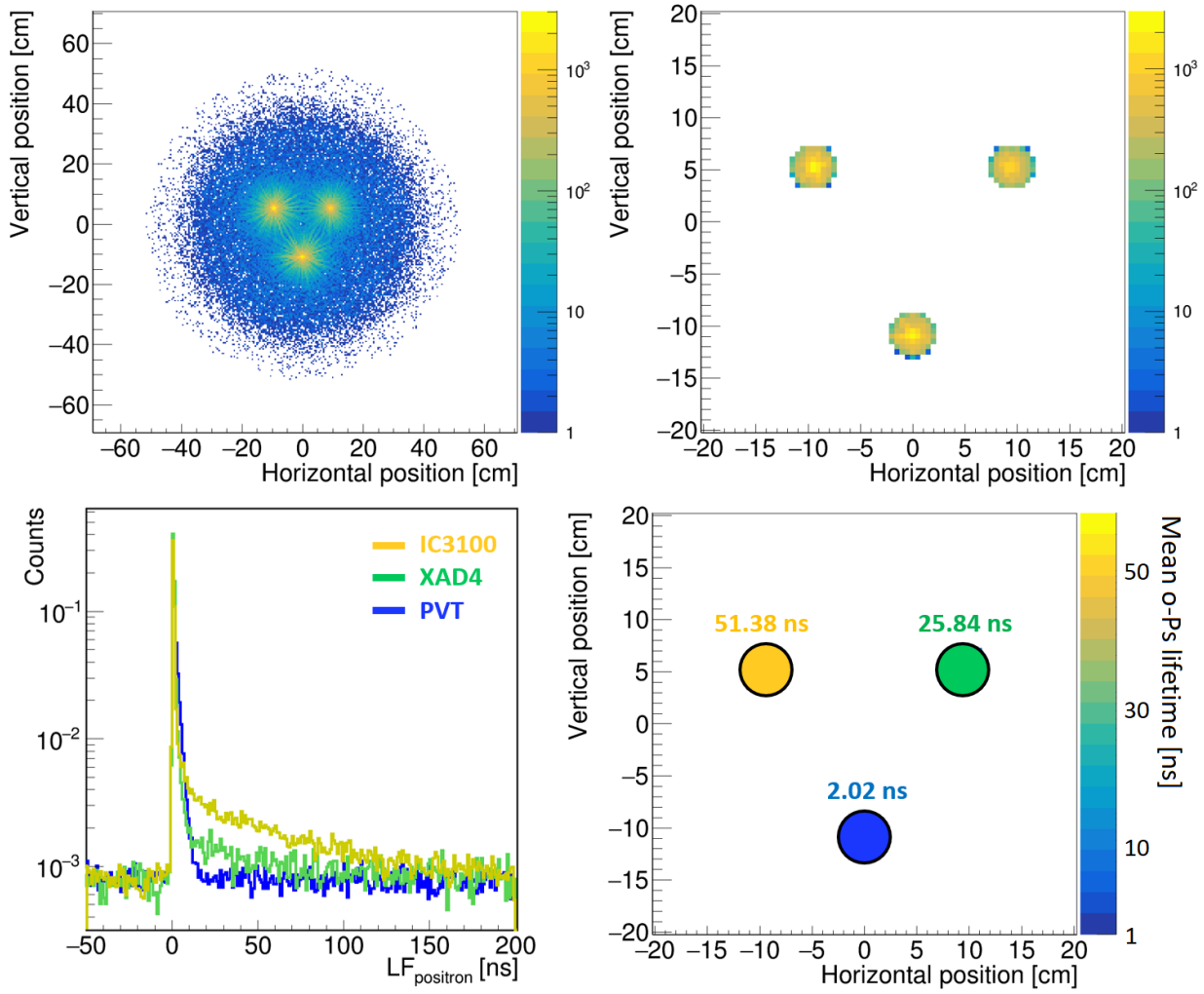


Figure 6.5: **Results from the analysis of the data with the porous phantom.** Experimental data. (top) Annihilation points distribution for the porous phantom after applying selection criteria in diffetent ranges: (left) full and (right) restricted to the assumed positions of the samples. (left, bottom) Normalized positron lifetime distribution for each sample in a given restricted range. (right, bottom) Mean o-Ps lifetime image, estimated from the lifetime distributions for large voxels - restricted ranges.

positronium image obtained by the J-PET detector. However, the desired voxel size should be as small as possible, to properly show the capabilities of the detector for the positronium imaging. Individual fits for each cylinder, with the separation onto different components are shown in Appendix I.

It is also worth adding in terms of the obtained results that the theoretical ratio of p-Ps to o-Ps (1: 3) was not fixed during the analysis. Indeed, as can be seen in Tab. 6.1, the ratio of the fitted intensities p-Ps to o-Ps for any material does not agree with the theoretical ratio. This may be due to direct annihilations in the chamber and the metal holder in which the source was located, which artificially increased the intensity of the p-Ps component due to having similar mean lifetimes. No additional components were fitted that could separate

Table 6.1: **Results from fitting positron annihilation lifetime spectra for three materials used for the measurement with the porous phantom - IC3100, XAD4, PVT.** Total number of counts is equal to the number of events, included in the selected voxel. Normalized total number of counts is the value of the total number of counts divided by the activity of the source used for a given chamber with a sample. The lower value of the normalized total counts for the IC3100 may have come from a time window that was a bit too narrow, which may have cut out some good events. Obviously, this will affect the sample with the highest o-Ps mean lifetime the most, but looking at the lifetime distributions for the different samples in Fig. 6.6, it was not a significant change to re-analyze the data with a slightly larger time window. Fitted lifetime components are shown with the measures of the goodness of the fit $R^2$ and $\chi^2$. Component derived from annihilation in the source was estimated from a different measurement on the standard PALS system. The intensity of the source component was not included in the total intensity.

| **Parameter name** | **IC3100** | **XAD4** | **PVT** |
|---|---|---|---|
| Total number of counts | 53542 | 35313 | 52408 |
| Normalized total number of counts (1/Bq) | 0.136 | 0.152 | 0.148 |
| $\sigma$ [ns] | 0.312 (02) | 0.305 (03) | 0.305 (02) |
| $\tau_{\text{source}}$ [ns] (fixed) | 0.374 | 0.374 | 0.374 |
| $I^e_{\text{source}}$ [%] (fixed) | 10.00 | 10.00 | 10.00 |
| $\tau_{\text{p-Ps}}$ [ns] (fixed) | 0.125 | 0.125 | 0.125 |
| $I^e_{\text{p-Ps}}$ [%] | 35.98 (53) | 23.99 (93) | 29.52 (52) |
| $\tau_{\text{direct}}$ [ns] | 0.435 (09) | 0.404 (07) | 0.452 (15) |
| $I^e_{\text{direct}}$ [%] | 31.13 (28) | 55.89 (28) | 25.76 (53) |
| $\tau_{\text{o-Ps}_1}$ | 3.64 (23) | 1.65 (05) | 2.02 (02) |
| $I^e_{\text{o-Ps}_1}$ [%] | 6.65 (07) | 15.29 (02) | 44.71 (52) |
| $\tau_{\text{o-Ps}_2}$ | 51.4 (1.2) | 25.8 (2.6) | - |
| $I^e_{\text{o-Ps}_2}$ [%] | 26.24 (35) | 4.82 (29) | - |
| Adjusted $R^2$ | 0.9961 | 0.9958 | 0.9976 |
| Reduced $\chi^2$ | 0.942 | 1.094 | 1.113 |

the p-Ps component from the non-sample direct annihilation, due to the relatively low total counts of the resulting distributions $\approx 50,000$. Additionally, the only component analyzed was the longest-lived o-Ps component whose mean lifetime is one or two orders of magnitude greater than any p-Ps or direct annihilation component. For this reason, any uncertainties obtained from incorrect estimation of the short-life components should not significantly affect the obtained results of the mean o-Ps lifetime.

In the next step of the analysis, the voxels will be reduced to 2 cm vertically and horizontally. All samples were approximately in the same Z position, so the Z dimension will not be sensitive to different materials and therefore different lifetime distributions. For this reason, the Z-dimension voxels will not be reduced. Each small voxel will be fitted according to the procedure shown in Fig. 6.4, so using the results for large voxels given in Tab. 6.1 as

a initial lifetime parameters. Exemplary comparison of the positron lifetime distribution for two chosen voxels for each sample is shown in Appendix in Fig. I.5, I.6 and I.7. The final positronium image for the porous phantom with small voxels is shown in Fig. 6.6. In addition, for the inorganic matter it is possible to estimate the size of the pores, based on the mean o-Ps lifetime, by for example the pick-off models described in section 1.4. Using Tao-Eldrup and Goworek-Gidley model, mean o-Ps lifetime in each voxel was recalculated to the pore size, resulting in the porosity image shown in Fig. 6.6.

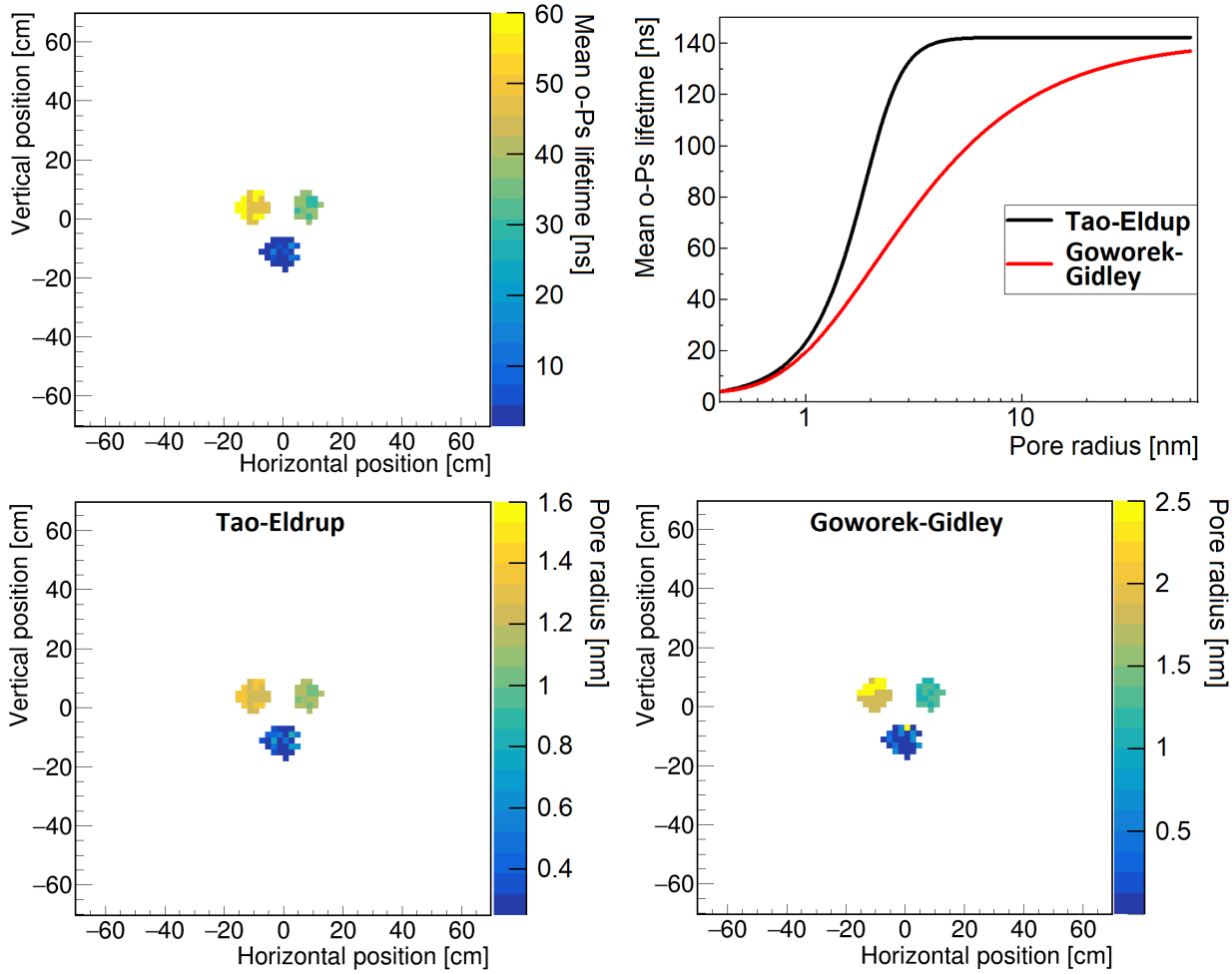


Figure 6.6: **Final positronium image and porosity image of the porous phantom.** Experimental data. (left, top) Positronium image for the 2 cm x 2 cm voxels. Only voxels with the total number of counts greater than the 5 % of the maximum total number of counts are shown to improve clarity of the image. (right, top) Pick-off models allowing to correlate mean o-Ps lifetime with the pore size. Using (left, bottom) Tao-Eldrup and (right, bottom) Goworek-Gidley models for sphercial pores, described in section 1.4, porosity image was obtained for the porous phantom.

The obtained positronium and porosity images for the porous phantom have shown that it is possible to obtain such images during standard scanning with a TOF-PET detector. Additionally, it has been possible to use positronium lifetime as a useful structural indicator

during standard measurement of radioisotope distribution. On the basis of the mean o-Ps lifetime, it was possible to distinguish spatially different samples of different porosity. Simultaneous determination of porosity in three spatial dimensions could lead to the birth of a new technique that could be used in the future for structural studies and phase transitions in different parts of the sample. In addition, it can be a complementary technique to previously known methods of determining porosity, such as Transmission Electron microscopy (TEM) [121], Micro Computer Tomography ($\mu$-CT) [122, 124] or Laser Scanning Confocal Microscopy (LCSM) [123, 124], as the positronium lifetime provides information about the nanostructure that so far has not been extensively researched with the techniques mentioned.

The next chapter, which will also conclude the main part of the work, will show the use of positronium imaging to characterize different tissue types based on the tissue phantom used for the measurement. This may be particularly important when using positronium in a standard PET scan to determine, for example, early stages of cancer, or to improve the efficiency of PET diagnostics by applying additional structural information. The possibilities of examining various tissues with the J-PET detector will be based on tissues derived from the cardiac myxoma.

## 6.5 Tissue phantom imaging

In the previous section the first positronium and porosity image collected by the J-PET detector were presented for the porous phantom. It was shown, that the difference in mean o-Ps lifetime in order of 20 ns (or even lower) is possible to distinguish, by the analysis procedure for the positronium image. However, the main life-changing application of positronium imaging would be to distinguish different tissues during PET scanning, thus enabling early diagnosis. However, the differences in the average lifetime of positronium in human tissues should differ only within a few dozen or several hundred ps [79–88], resulting from small structural changes and different concentration of the bio-active molecules, like free radicals or oxygen molecules. For this reason, it would be advisable to check whether the J-PET detector is able to distinguish neoplastic tissues from healthy tissues in the positronium image. As it was firstly mentioned in Sec. 6.1 two types of tissues (cardiac myxoma and adipose tissue) were measured in the next phantom - tissue phantom.

Data from the measurement were reconstructed and analyzed by the procedure described in Sec. 6.2. Distribution of the annihilation position at different stages of the analysis is shown in Appendix H in Fig. H.4, H.5 and H.6. Each selection criterion was applied as it was for the analysis of the porous phantom. Resulting distribution of the annihilation points is shown in Fig. 6.7. Four areas with higher uptake, corresponding to four chambers consiting of tissue phantom, can be see on the SUV analogue of the tissue phantom. Similar to the analysis of the porous phantom image, one can divide obtained image onto four cylinders, around the assumed positions of the chambers. Such division is shown in Fig. 6.7, where the radius of the base of the cylinder equal to 3 cm and the interval of the given position in Z [-5.5] cm were used. The reason for widening the base radius of the cylinder is the greater amount of data collected for the tissue phantom. This increases the area for which a sufficient number of events can be obtained to estimate the mean lifetime o-Ps, and thus to test the possibility

of analyzing lifetimes for lower statistics.

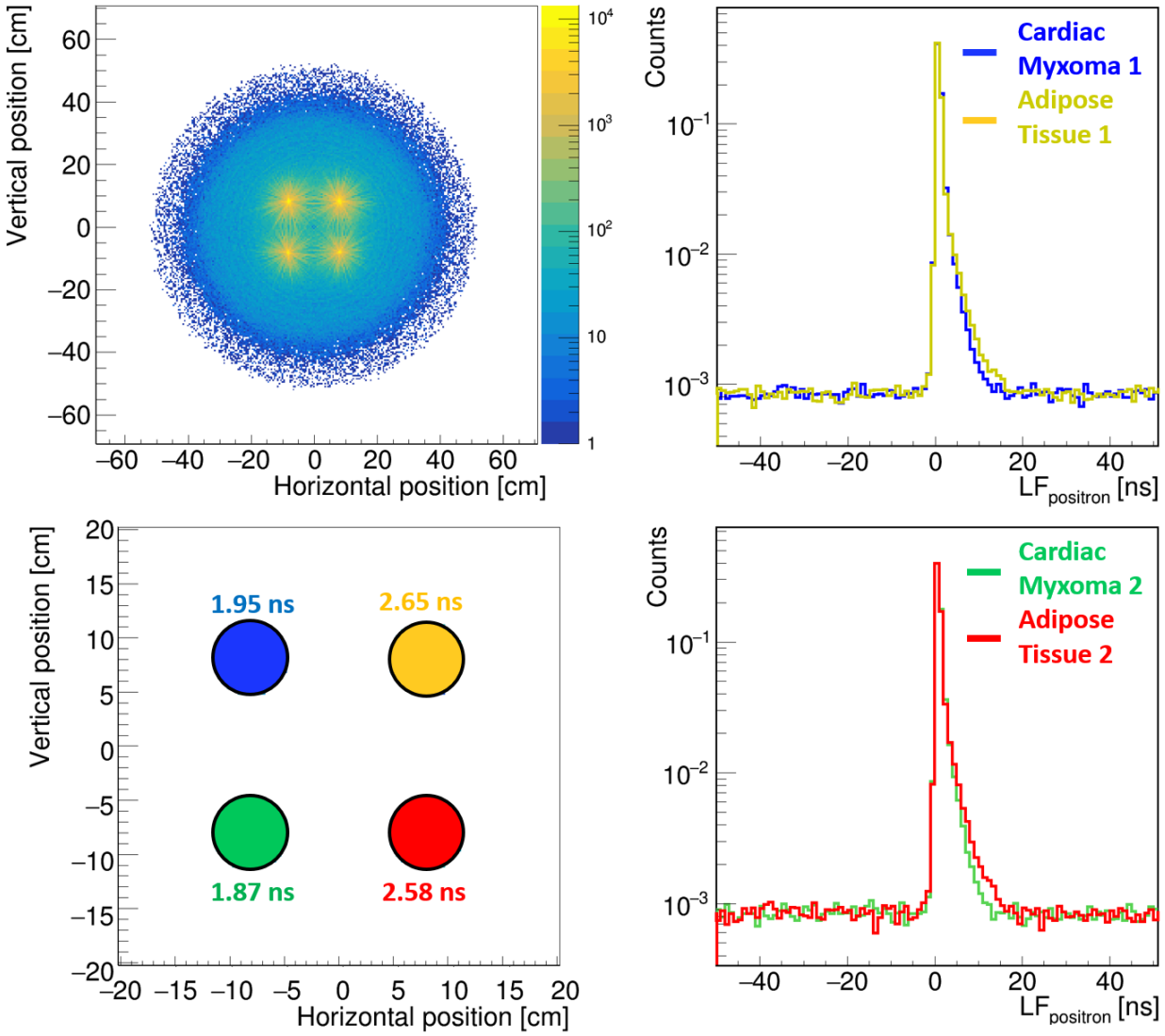


Figure 6.7: **Results from the analysis of the data with the tissue phantom.** Experimental data. (left, top) Annihilation points distribution for the tissue phantom after applying selection criteria. (right) Normalized positron lifetime distribution for each pair of samples for a given patient with ID equal to (top) 1 and (bottom) 2. (left, bottom) Mean o-Ps lifetime image, estimated from the lifetime distributions for large voxels.

The comparison of the sample pair cardiac myxoma - adipose tissue, from the same patient is shown in Fig. 6.7. It is clearly visible, that adipose tissue is characterized by broader lifetime spectrum, than it is for the cardiac myxoma. This is also confirmed by the o-Ps mean lifetimes obtained, from fitting by PALS Avalanche software, shown in Tab. 6.2. Fits to each sample and separation onto different components are shown in Appendix J. Results from fitting shows, that the resolution of the distributions represented by $\sigma$ value, was better

for the measurement with the tissue phantom that in case of the porous phantom. It can come from the higher total number of counts in the fitted spectra for tissues and the smaller area of the samples, what decreased the smearing of the $LF_{positron}$ distribution due to the narrower annihilation position distribution. The difference of the mean o-Ps lifetime between cancer (cardiac myxoma) and normal tissue (adipose tissue) was approximately equal to 800 ps. This is quite a difference, proving quite significant structural differences between the examined tissues. Differences from different concentrations of free radicals and other bioactive molecules for different tissues cannot explain such significant differences, alone.

Table 6.2: **Results from fitting positron annihilation lifetime spectra for four samples used for the measurement with the tissue phantom - Cardiac Myxoma 1, 2 and Adipose Tissue 1, 2.** Total number of counts is equal to the number of events, included in the selected voxel. Normalized total number of counts is the value of the total number of counts divided by the activity of the source used for a given chamber with a sample. Values of the normalized total number of counts were similar for every sample. Mean lifetime of the direct component was fixed in order to decrease fluctuations of the fit and obtain the most accurate value of the only parameter-of-interest - mean o-Ps lifetime. Fitted lifetime components are shown with the measures of the goodness of the fit $R^2$ and $\chi^2$. Component derived from annihilation in the source was estimated from a different measurement on the standard PALS system. The intensity of the source component was not included in the total intensity.

| **Parameter name** | **Cardiac Myxoma 1** | **Cardiac Myxoma 2** | **Adipose Tissue 1** | **Adipose Tissue 1** |
|---|---|---|---|---|
| Total number of counts | 197340 | 136434 | 231149 | 134346 |
| Normalized total number of counts (1/Bq) | 0.572 | 0.573 | 0.588 | 0.584 |
| $\sigma$ [ns] | 0.265 (02) | 0.269 (03) | 0.263 (02) | 0.263 (03) |
| $\tau_{source}$ [ns] (fixed) | 0.374 | 0.374 | 0.374 | 0.374 |
| $I^e_{source}$ [%] (fixed) | 10.00 | 10.00 | 10.00 | 10.00 |
| $\tau_{p\text{-}Ps}$ [ns] (fixed) | 0.125 | 0.125 | 0.125 | 0.125 |
| $I^e_{p\text{-}Ps}$ [%] | 13.26 (18) | 12.21 (21) | 17.18 (16) | 17.14 (20) |
| $\tau_{direct}$ [ns] (fixed) | 0.388 | 0.388 | 0.388 | 0.388 |
| $I^e_{direct}$ [%] | 65.35 (22) | 64.52 (27) | 61.34 (20) | 61.31 (23) |
| $\tau_{o\text{-}Ps}$ | 1.950 (19) | 1.874 (20) | 2.645 (27) | 2.581 (30) |
| $I^e_{o\text{-}Ps}$ [%] | 21.39 (47) | 23.27 (45) | 21.49 (41) | 21.56 (54) |
| Adjusted $R^2$ | 0.9999 | 0.9999 | 0.9999 | 0.9999 |
| Reduced $\chi^2$ | 0.999 | 1.067 | 1.039 | 1.253 |

As a next step, mean o-Ps lifetime will be estimated for every small voxels, following procedure from Fig. 6.4, already used for the analysis of the porous phantom. The resulting positronium image is shown in Fig. 6.8. Exemplary comparison of the positron lifetime distribution for two chosen voxels for each sample is shown in Appendix in Fig. J.3, J.4, J.5 and J.6. It is shown, that it is possible to differentiate types of the tissues, for individual

voxels based on the mean o-Ps lifetime. Indeed, even for small statistics in small voxels it was possible to successfully estimate mean o-Ps lifetime, and the resulting value is close to the value obtained for large voxels shown in Fig. 6.7. This is a very interesting result showing that positronium images can become an additional image type produced during a standard PET scan that can provide information on the structure of a given tissue. If the structural differences between neoplastic and normal tissues are large enough, it will also be possible to extend the diagnostic capabilities of TOF-PET detectors. It is worth mentioning that positronium imaging does not require any additional mechanical modules, but only consists in appropriate energy selection of photons and the possibility of measuring the time of photon arrival. For this reason, it is possible to introduce positronium imaging to already existing TOF-PET detectors, changing only the analysis of the data collected during the scan. The only change in comparison to the previously determined measurement details in PET will be the appropriate selection of a radiopharmaceutical that will provide an additional photon, signaling the formation of a positron. However, as suggested in Sec. 1.6 there are already some substances that could solve this problem.

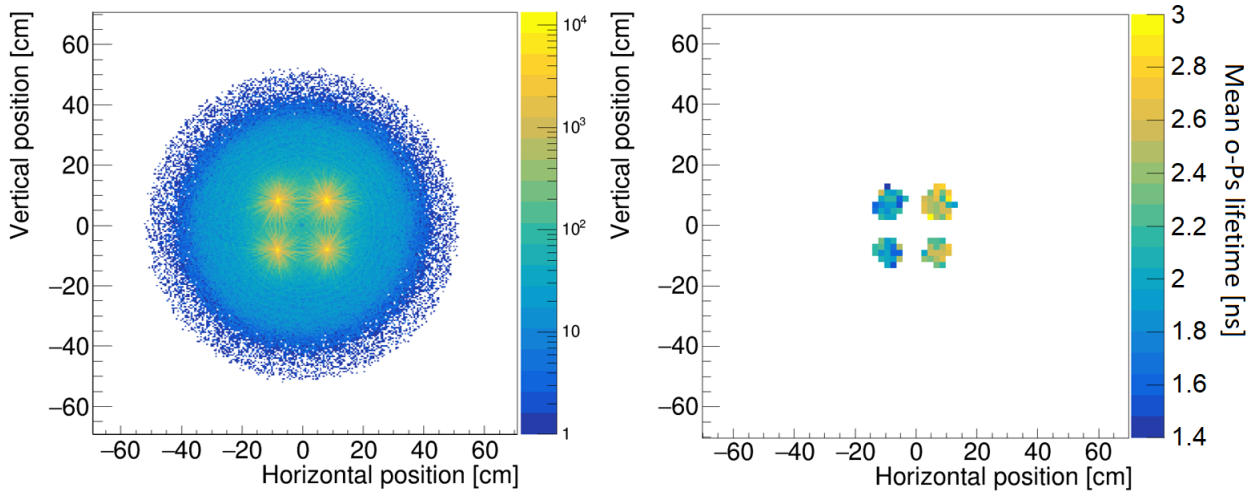


Figure 6.8: **Final positronium image of the tissue phantom.** Experimental data. (left) Reconstructed annihilation position distribution for the tissue phantom. (right) Positronium image for the 2 cm x 2 cm voxels for the tissue phantom. Only voxels with the total number of counts greater than the 5 % of the maximum total number of counts are shown to improve clarity of the image.

Of course, the presented results came from the weekly measurement of fixed tissues. However, only sources with a total activity of 1 MBq were used when the activity administered to a patient during a standard PET scan is hundred times greater. In addition, the length of the detection modules was only 50 cm and the geometry itself ensured only the sensitivity to event detection for positronium imaging at the level of $1.17 \cdot 10^{-6}$, as shown in Tab. 4.3. However, future prototypes of J-PET detectors with more densely populated detectors in space, increasing detector acceptance, and in particular the Total-Body prototype, could significantly increase detection sensitivity and thus enable positronium imaging in a reasonable

time. Additionally, there is also the issue of positronium image reconstruction, which can increase the spatial resolution of the images obtained. It will be quite difficult because the positronium lifetime - annihilation position correlation should be kept, which is not possible with the previously known PET image reconstruction methods.

Regarding the obtained results for the tissue phantom and porosity image presented for the porous phantom. It is difficult to talk about any pores in tissues, because there should not be a predetermined porous structure in the tissue, as is the case with inorganic matter with structure defects. Obviously, tissues contain certain structures such as extracellular matrix, cell membranes and others, but these are not sufficiently studied for positronium mean lifetimes to adequately correlate existing structures with mean o-Ps lifetime. Perhaps in the future, appropriate models will be developed to characterize the structure of tissues based on positronium. Certainly there is still some hidden potential in the positronium that can be mined for human purposes.

# Summary and conclusions

The aim of the thesis was to present the experimental test of a completely new imaging technique based on positron-electron annihilation - positronium imaging [2, 3], in view of material and medical research. The 192-strip J-PET detector [4–6] was used for positronium imaging, the only device capable of this type of imaging. Two phantoms, consisting of different types of samples - porous and tissue, were measured with a J-PET detector in order to test the research hypothesis stated in this work.

The work focuses on the demonstration of the 192-strip J-PET detector as an imaging system that allows also to study of positronium properties in each voxel of the image. In particular, its characteristics, calibration methods and data reconstruction and selection were presented. Time calibration method, based on the positron lifetime spectra, introduced for the J-PET detector allowed to achieve time resolution equal to 0.223 (01) ns for the time difference. In addition a method for estimating the speed of light signals in a scintillator was also developed, based on the correlation of signal time and position along the scintillation strip. This method were based on minimizing the dispersion of time calibration constants and it does not require the use of additional calibration systems. Obtained mean velocity of light in the scintillating strip, used in the 192-strip J-PET detector, was equal to 12.49 (14) cm/ns, which was in agreement with the measurement with the same scintillators done by the different detection setup [4] and close to the results obtained for the plastic scintillators [104–106]. Spatial resolution were estimated to approximately 0.72 cm in standard deviation for the vertical and horizontal dimensions, which comes only from the reconstruction of the position inside the scintilalting strip in these dimensions, as the position of the center of the strip. For the reconstructed position along the strip (Z position), value of standard deviation equal to 2.45 (19) cm was obtained.

Presented methods of the data reconstruction and selection were tested by analyzing two most common decays of positronium - into two and three photons, from the measurement with the porous polymer (XAD4 [98]) and from the data generated by dedicated simulations software [101]. The selection criteria introduced for the J-PET detector [96], based on geometrical and timing correlations, allowed to separate these two types of the decays in two disjoint sets of events. High purity of the data sample was maintained - 94.71% and 56.27% for the two- and three-photon decays of the positron-electron pair respectively, with an additional requirement of having photon coming from the deexcitation of the radioisotope. It was also possible to estimate the sensitivity of the 192-strip J-PET detector to a given positronium decay channel - $1.17 \cdot 10^{-6}$ and $0.41 \cdot 10^{-6}$ for the two- and three-photon decays respectively, allowing access to the characterization of measurement conditions in the context of the re-

quired statistics of the analyzed decays. The annihilation position reconstruction methods were tested for two different decays of positronium. Obtained images were consistent with the assumed sample position inside the detection chamber.

Analysis of positron lifetime spectrum for each of the set of selected events allowed for additional decomposition into individual positronium decay channels - para-positronium, ortho-positronium and the direct annihilation, and estimation of its relative intensity and mean lifetime. In addition, it was possible to estimate the influence of the introduced background types (scatterings) for each set of events, and in particular to fully explain the structure of the lifetime distribution of selected events with decays into three photons, based on additional information from measurements with cosmic rays. Finally, the information contained in the lifetime distributions for each decay type was connected, allowing an estimate of the o-Ps decay constant by the J-PET detector. The obtained value of the o-Ps decay constant equal to 0.00703996 (71) 1/ns was consistent with the theoretical predictions (0.0070399 1/ns [113]) and the results of previous experiments, but with better accuracy [114–117].

As the final proof of concept of the positronium imaging by the 192-strip J-PET detector, the results of the measurement analysis with the use of phantoms developed for this purpose were presented. The first phantom consisting of three samples with different porosity - IC3100 [118], XAD4 [98] and PVT [119], allowed to show how well the J-PET detector is able to estimate the structural index - mean o-Ps lifetime, in different areas of the image space and for different statistics of the lifetime distribution. The developed method of positronium lifetime analysis for small voxels has successfully shown that it is possible to distinguish in space samples of significantly different porosity expressed by the mean o-Ps lifetime. The demonstrated methodology may give rise to a new technique of imaging the structure of samples, in particular nanoporosity, which may complement currently known methods such as for example Transmission Emission Tomography (TEM) [121], Micro Computer Tomography ($\mu$-CT) [122, 124] or Laser Scanning Confocal Microscopy (LCSM) [123, 124]. The second phantom focused on testing positronium imaging sensitivity for samples where the difference in the mean o-Ps lifetime is relatively small (on the order of 0.5 ns). Additionally, these samples came from the fixed neoplastic (Cardiac Myxoma) and normal (Adipose tissue) human tissue, thus the obtained image was the first in-vitro positronium image of human tissues. The result of the measurement analysis with the second phantom also confirmed the research hypothesis about the possibilities of positronium imaging, characterizing the structure of the sample in space, and additionally showed that it is possible to distinguish tissues of different types on the basis of the mean o-Ps lifetime. This may be of particular importance in extending the diagnostic possibilities of PET measurement with a new contrast based on the positronium lifetime, which may not only distinguish neoplastic tissue from normal but possibly characterize different stages of cancer.

Overall, this work demonstrated the potential of the 192-strip J-PET detector to characterize positronium. In particular, the use of positron-electron pair annihilation for the simultaneous characterization of a nanostructure in three spatial dimensions has been presented for the first time. Currently, the J-PET detector is the only detection system that allows obtaining positronium images. In the future, new positronium image reconstruction algorithms as well as future J-PET prototypes could lead to its further improvement.

# Appendices

# Appendix A

# Calibration methods for TOF-PET scanners

There are several established methods for calibrating the TOF-PET scanner. The main difference between them is the design of a specific phantom or specific measurement conditions. Phantom methods focus on making possible LORs, having their source in the phantom, able to connect as many pairs of detection modules as possible. The first method benefits from using a large phantom [125, 126], while the second method uses a small phantom or an additional detector that rotates [127, 128], imitating using a large phantom. These types of methods can be used prior to examining the patient in order to maintain optimal scanner operating conditions. Another method, without any phantom, use a natural source of radiation, which is cosmic rays, and collect such events in which a single particle from the cosmic shower reacts in at least two detection modules [129]. In addition, this method requires a long measurement to collect a sufficient number of events to perform the calibration, which makes it less effective than the methods described above. However, it shows a good direction for the development of calibration methods that do not use complicated circuits and can even be used during a patient scan.

All described phantom methods, shown schematically in Fig. A.1, are based on the known position of the phantom and the resulting time difference distribution between a given pair of the detection modules. Large phantoms produce a wide distribution of time differences, but it is possible to calibrate multiple detectors in a single iteration. On the other hand, a rotating reference detector / phantom allows to obtain a narrow distribution of time differences, but for a given position of this detector, a limited number of module pairs is possible to calibrate. Calibration using cosmic rays requires a lot of time to test each pair of detection modules, due to the relatively low frequency of their occurrence (around 10000 / $s \cdot m^2$) [130].

In addition each method with phantoms require an additional calibration measurement which must be conducted before proper scan, where for phantoms, they must be localized in the centre of the detection chamber. Therefore, a new method that is comparable in performance and can be performed during scanning, or at least does not require the precise localization of complex setups, will be beneficial for future scanners. One of the candidate for such method is the calibration procedure described in Chapter. 3. The presented method is fast, efficient (takes about 1 hour of scanning) and can generally be performed during scanning,

because only the position of the source is used in the calibration process and knowing the position of the annihilation one can make a TOF correction.

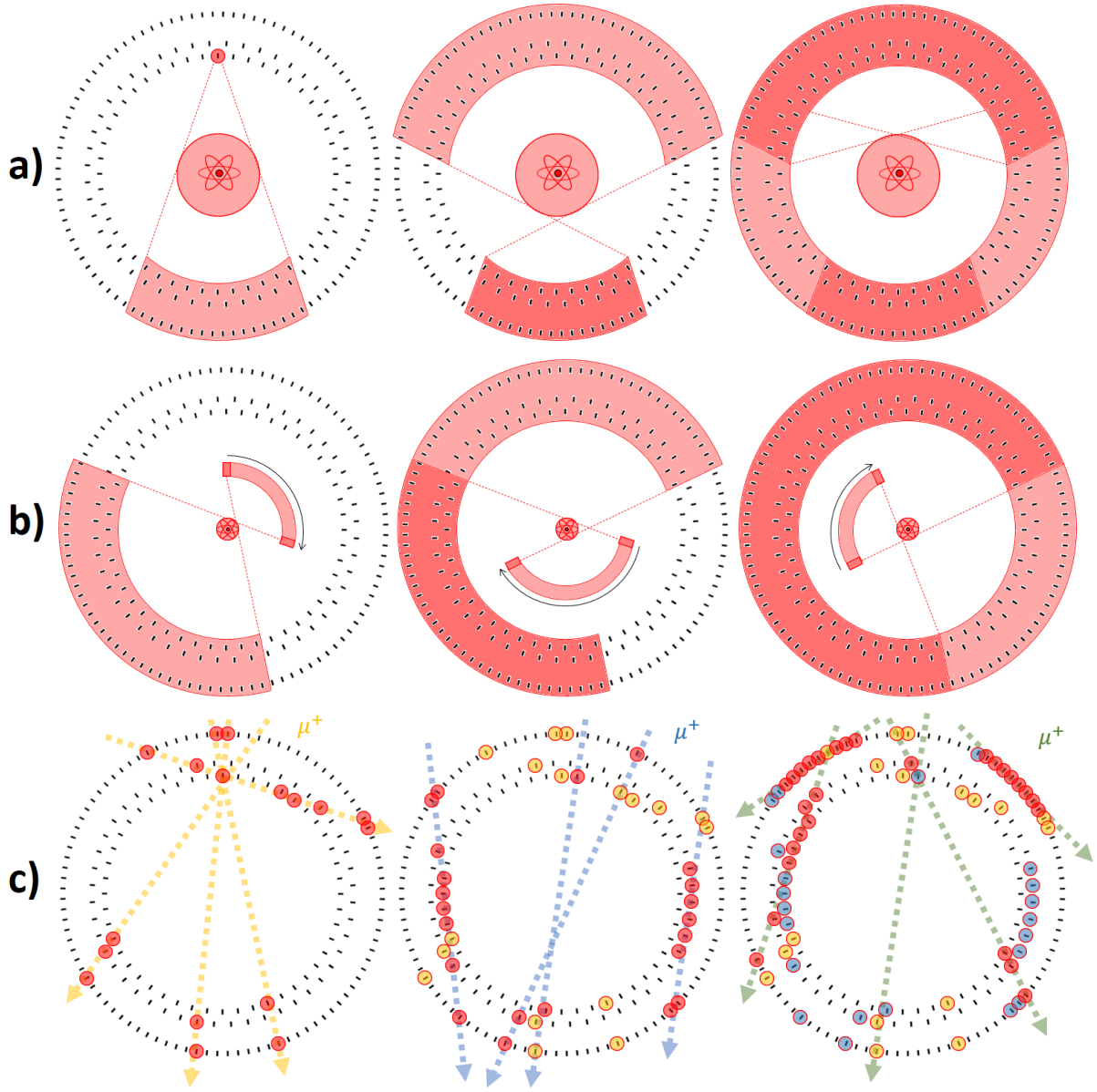


Figure A.1: **TOF-PET calibration methods.** On the schematic view of the J-PET detector (black rectangles), three TOF-PET scanners calibration methods are depicted usind: a) Large phantom and one module selected as reference - red rectangle. Pink area indicates calibrated modules in a given iteration, where red area indicates already calibrated modules. b) Rotating detector/phantom -red rectangle. Pink area indicates calibrated modules in a given iteration, where red area indicates already calibrated modules. c) Cosmic radiation ($\mu^+$) - dashed lines. Red circles indicate modules which are calibrated in a given iteration, where other circles indicate already calibrated modules. Each scheme is limited to three iterations.

# Appendix B

# Calibration corrections for different iterations

Calibration procedure described in Sec. 3.3 was constructed based on the iterative approach, which in general tend to minimize the miscalibration between different detection modules. In order to check, whether the calibration procedure works as designed one can look at the corrections calculated at the beginning (first iteration) and at the end (last iteration) of the calibration. For the calibration performed from the measurement with XAD4, that results are shown in Fig. 3.8 and 3.9, correction as a function of the scintillator in different iterations are shown in Fig. B.1, B.2, B.3, B.4 and B.5. The figures are split for different thresholds and the mean correction in the first iteration was around 200 ps, where for the seventh iteration it is around 10 ps. It can be seen, that the correction proportional to the miscalibration measure is actually lower in the seventh iteration than in the first.

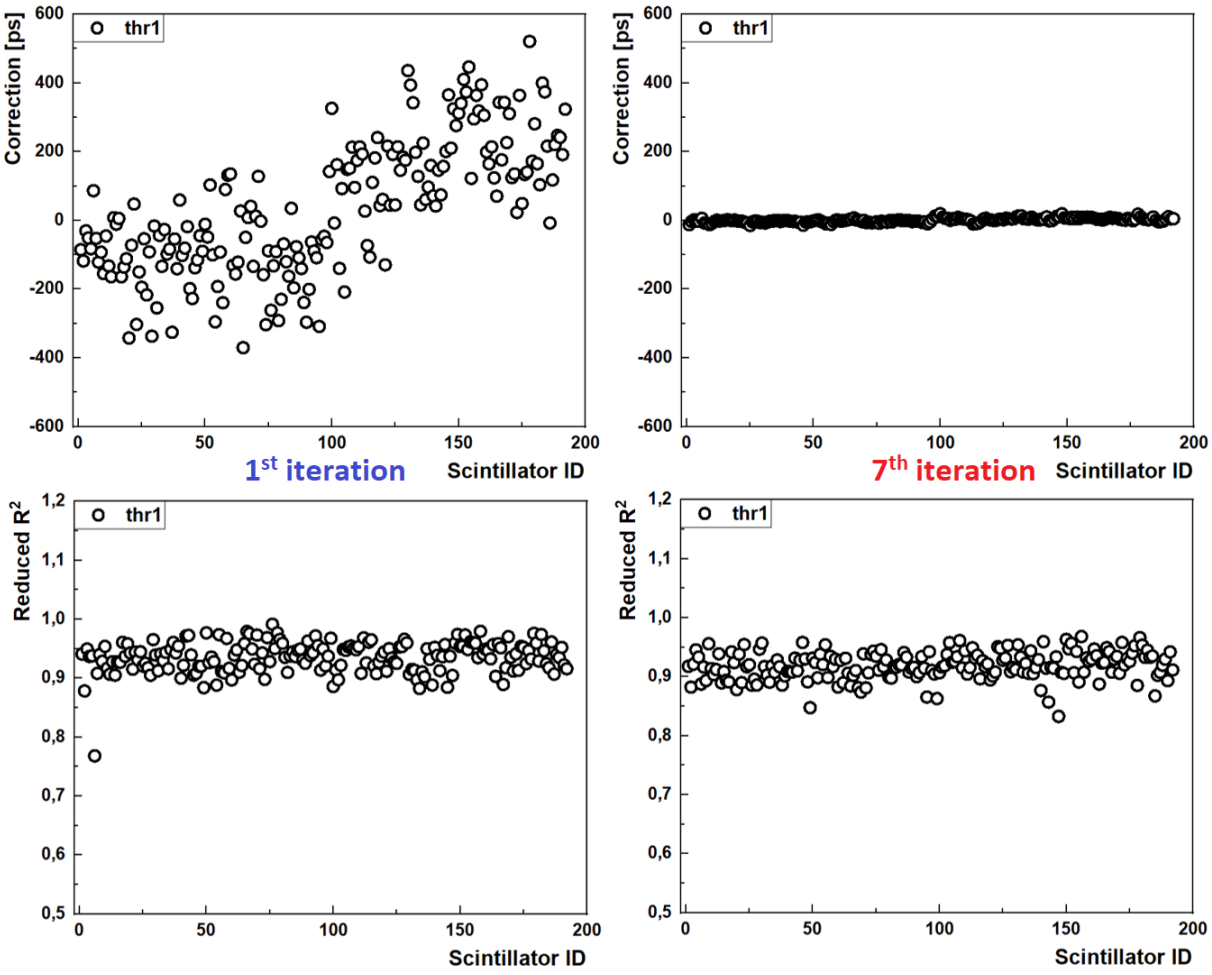


Figure B.1: **Correction for a given scintillator for the first and seventh iteration, for the first threshold.** Correction calculated as in Eg. 3.4 for a given scintillator calculated for the first and the seventh iteration. Corrections only for the first threshold is shown. After the seventh iteration, corrections varies in the 10 ps range. Closer look of the seventh iteration corrections is in Fig. B.5.

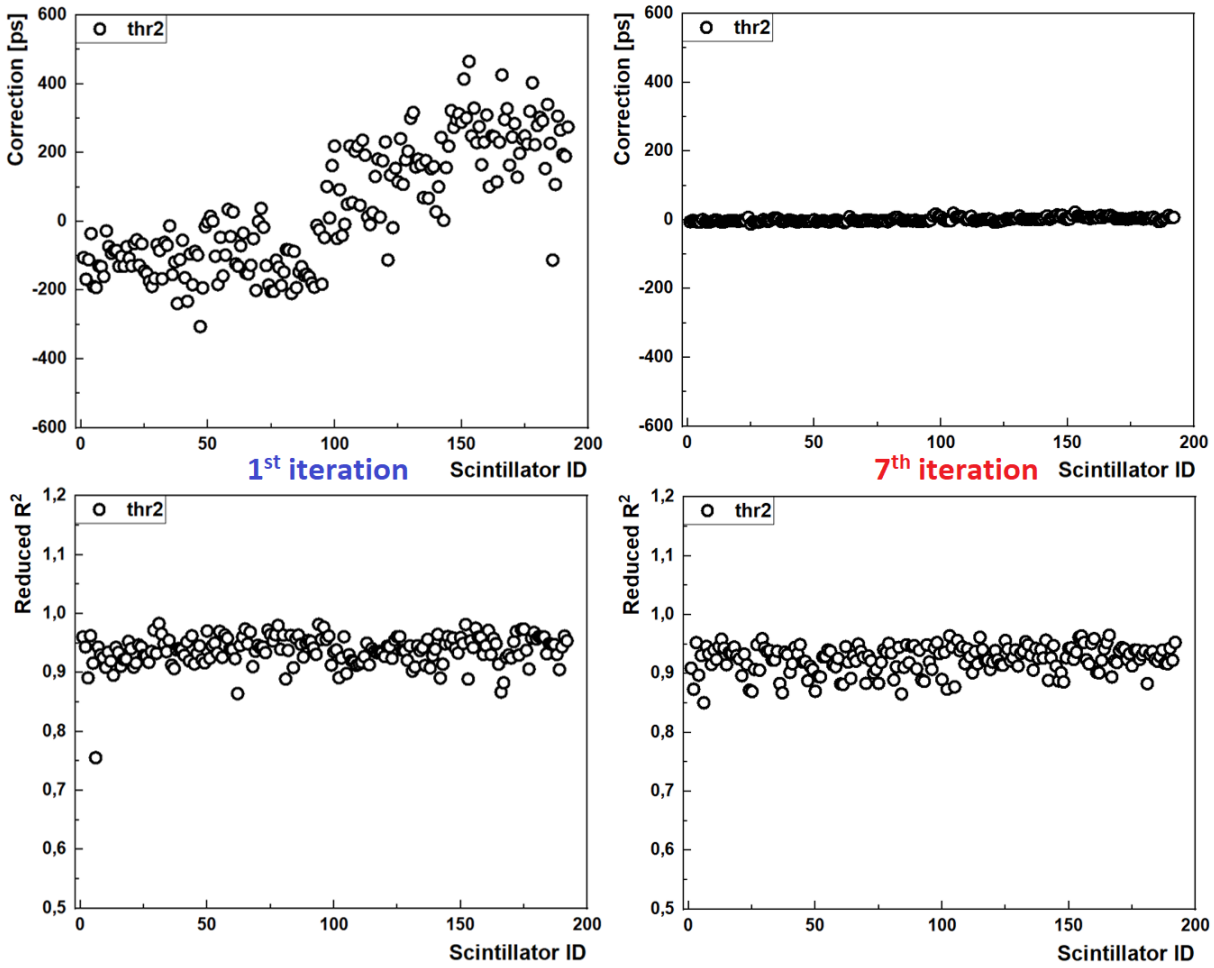


Figure B.2: **Correction for a given scintillator for the first and seventh iteration, for the second threshold.** Correction calculated as in Eg. 3.4 for a given scintillator calculated for the first and the seventh iteration. Corrections only for the second threshold is shown. After the seventh iteration, corrections varies in the 10 ps range. Closer look of the seventh iteration corrections is in Fig. B.5.

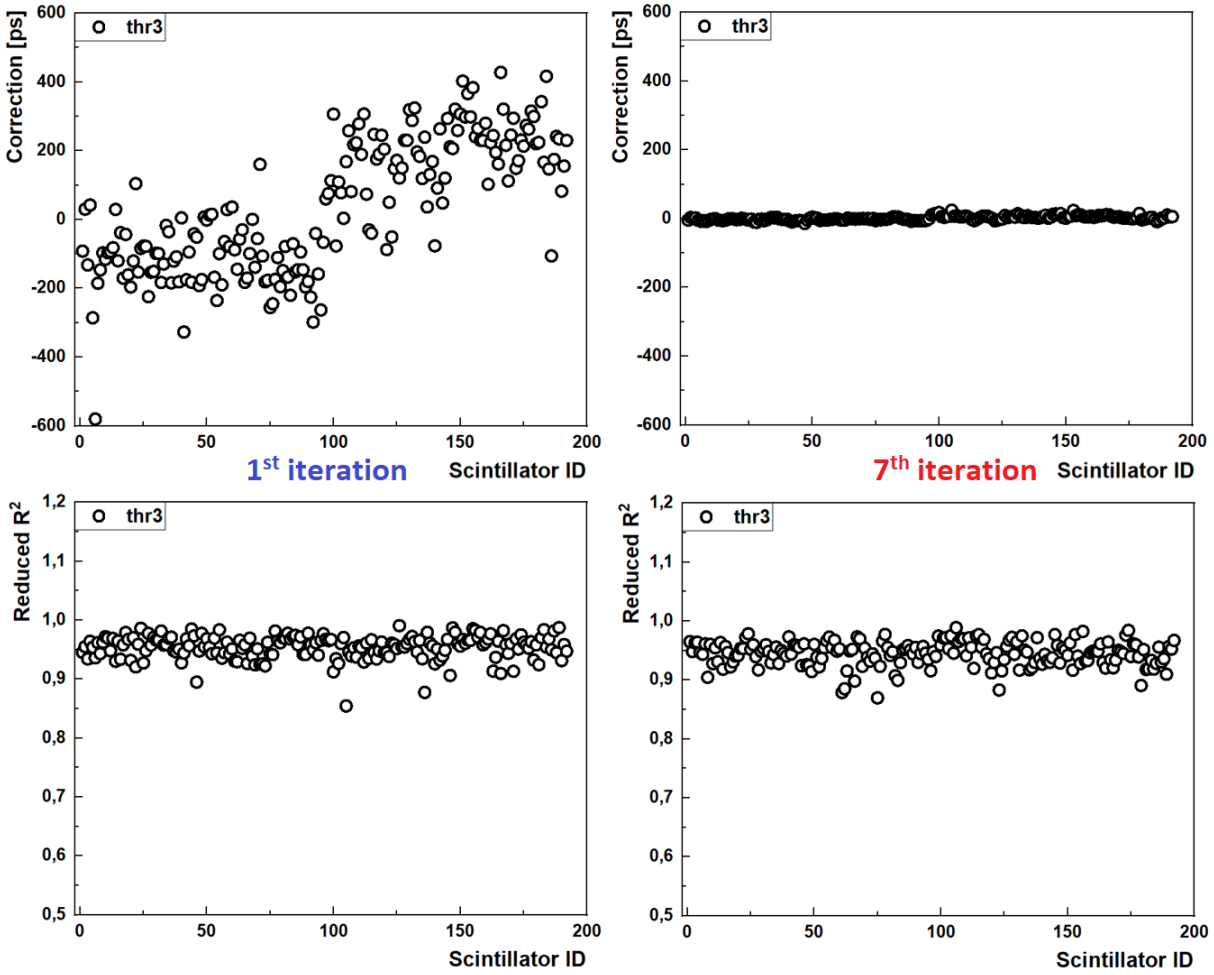


Figure B.3: **Correction for a given scintillator for the first and seventh iteration, for the third threshold.** Correction calculated as in Eg. 3.4 for a given scintillator calculated for the first and the seventh iteration. Corrections only for the third threshold is shown. After the seventh iteration, corrections varies in the 10 ps range. Closer look of the seventh iteration corrections is in Fig. B.5.

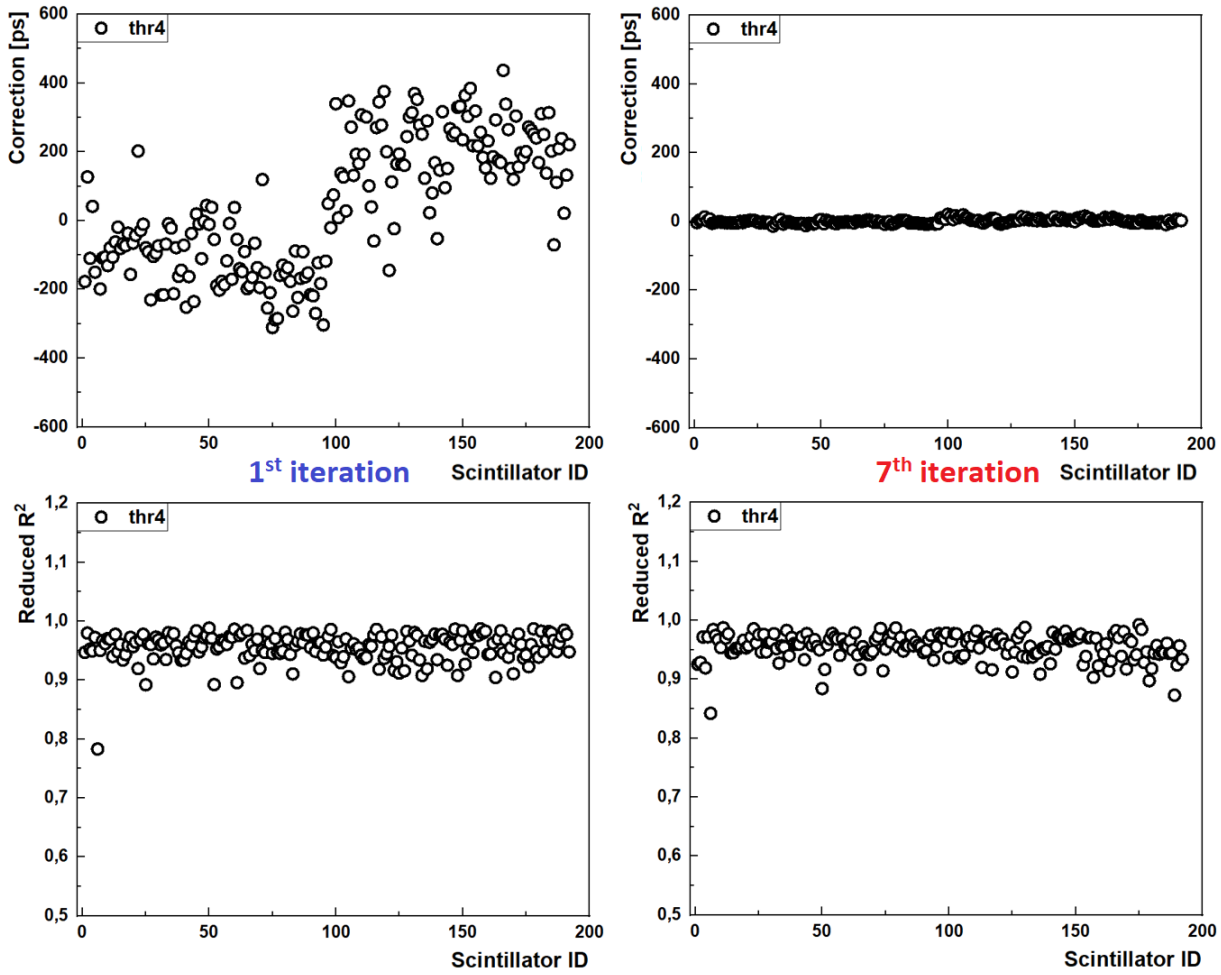


Figure B.4: **Correction for a given scintillator for the first and seventh iteration, for the fourth threshold.** Correction calculated as in Eg. 3.4 for a given scintillator calculated for the first and the seventh iteration. Corrections only for the fourth threshold is shown. After the seventh iteration, corrections varies in the 10 ps range. Closer look of the seventh iteration corrections is in Fig. B.5.

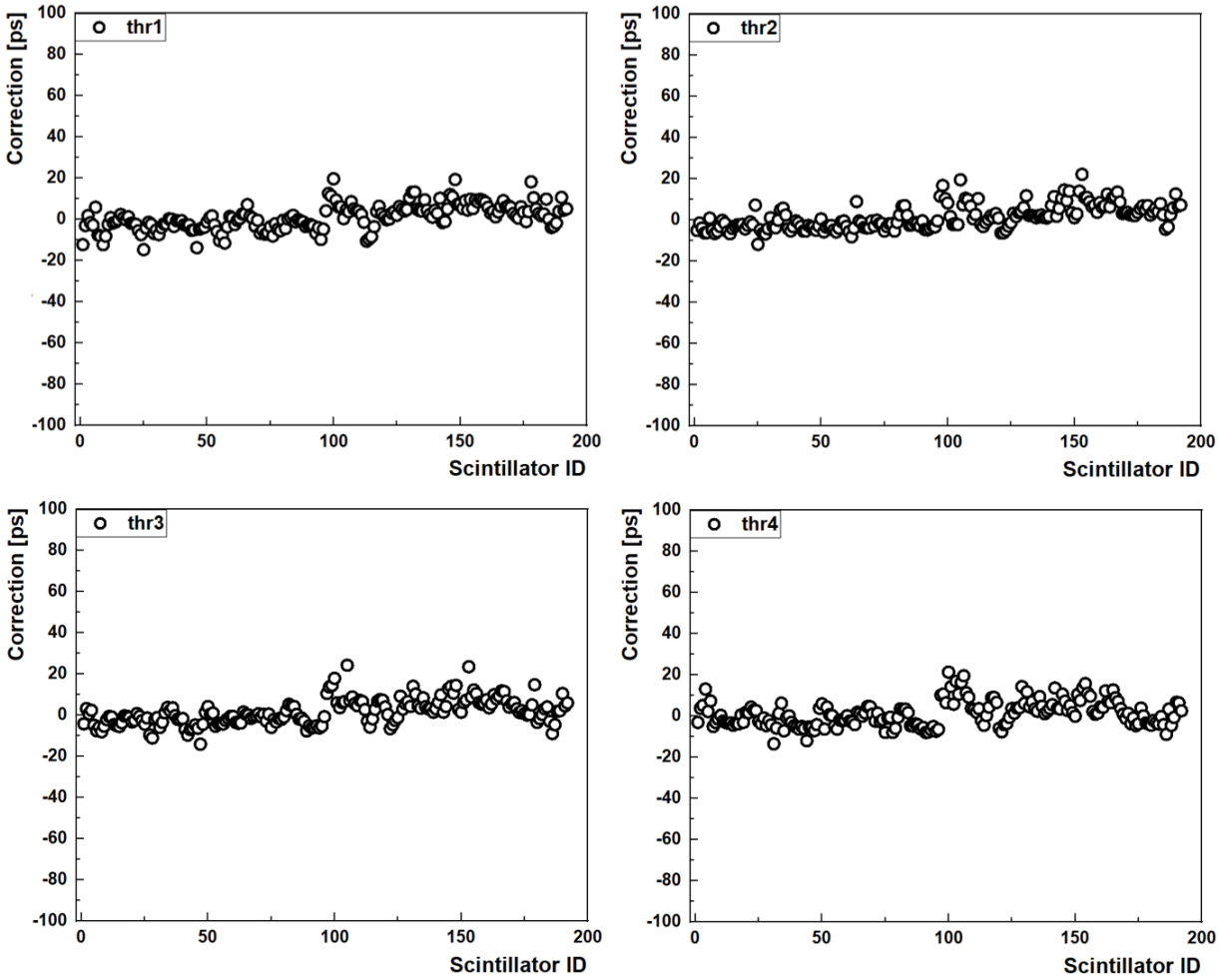


Figure B.5: **Correction for a given scintillator seventh iteration, for all thresholds.** Correction calculated as in Eg. 3.4 for a given scintillator and for each threshold calculated for the seventh iteration. After the seventh iteration, corrections varies in the 10 ps range.

# Appendix C

# Effective length supplement

To show that the value of the reference length is not important for the estimation of the optimal effective length, the same calculations as described in Fig. 3.10 was done, assuming that the reference length is equal to 49 cm. The values of the obtained optimal effecitve lengths is different by those extracted for 50 cm reference effective length by 0.1 cm. However, they are the same at the error limit, so one can assume that the effective length is the same for both reference effective lengths.

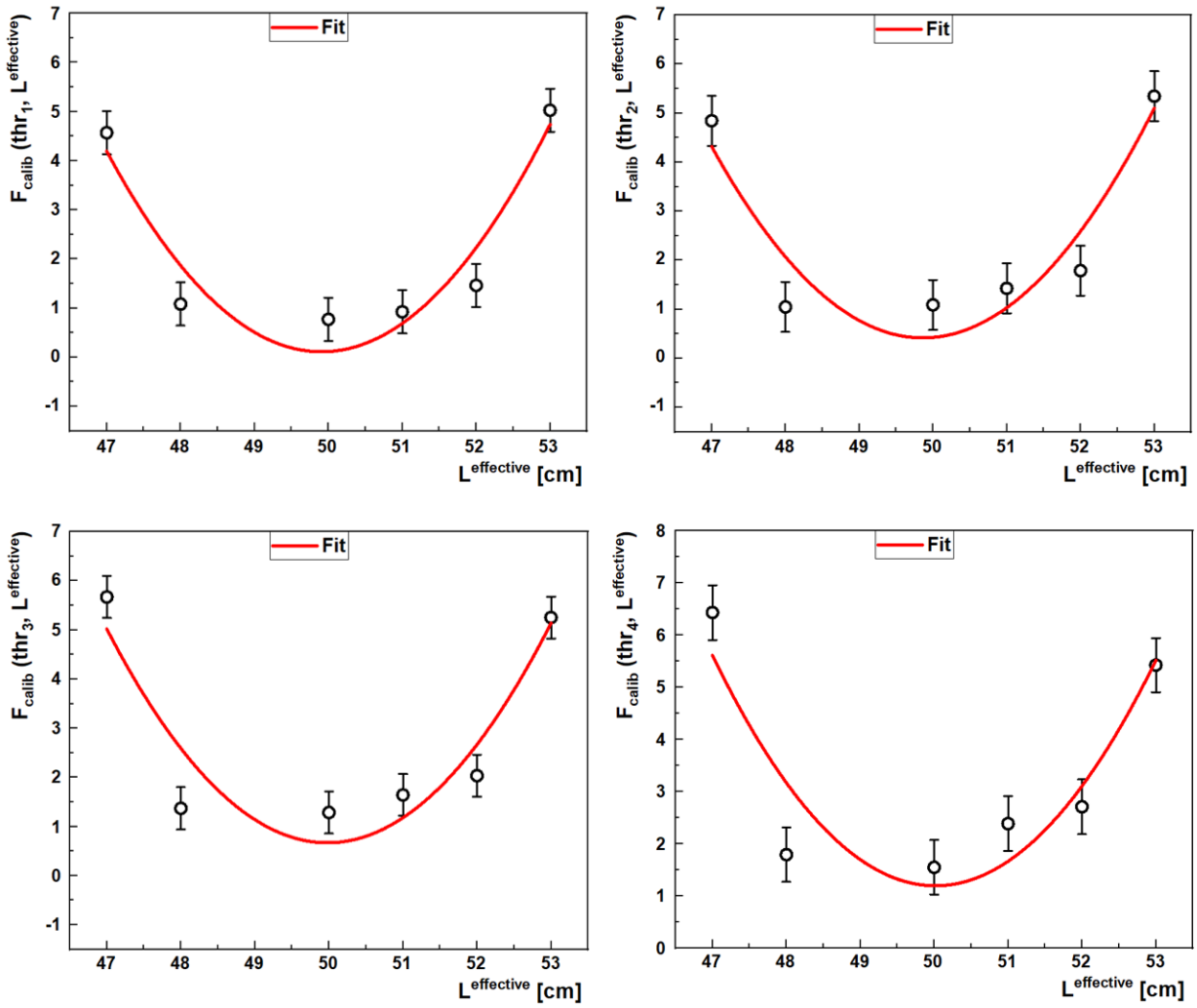


Figure C.1: **Mean difference of the calibration constants from the reference value of effective length as 49 cm.** Dependence of the inaccuracy of the calibration ($F_{calib}$) as a function of assumed value of the effective length ($L^{effective}$) for four different thresholds ($thr_1$, $thr_2$, $thr_3$ and $thr_4$). To estimate optimal value of the effective length $L^{optimal}$ quadratic function $f\left(L^{effective}\right) = A\left(L^{effective} - L^{optimal}\right)^2 + f_0$ has been fitted to each plot. Values of $L^{optimal}$ for different thresholds from fitting: 49.91 (16) Adjusted $R^2 = 0.832$ - $thr_1$, 49.86 (19) Adjusted $R^2 = 0.773$ - $thr_2$, 49.98 (19) Adjusted $R^2 = 0.764$ - $thr_3$ and 50.02 (21) Adjusted $R^2 = 0.729$ - $thr_4$. Comparing to the values for reference value of effective length as 50 cm, here the inaccuracies and the uncertainties of the fitted parameters are worst. Additionally, it proves that taking an effective length of 50 cm as a reference does not spoil the final estimate of the optimal effective length.

# Appendix D

# Z position resolution

Method of determination of the edge of the $t_{BA}$ distribution allows also to estimate resolution of the position along the strip. Indeed, the zero of the second derivative ($t^0_L$ or $t^0_R$) of the $t_{BA}$ distribution, treated as the measure of the edge is not the only fixed point, that can be determined. As shown in Fig. D.1 an additional point that can be estimated is the time of the closest extreme ($t^S_L$ or $t^S_R$) on the second derivative to the zero point. If one assumes that the edge of the $t_{BA}$ distribution is coming from the convolution of the rectangular distribution and Gaussian distribution interpreted as the resolution function, then the sum of the time differences between fixed points will correspond to the Full Width at Half Maximum (FWHM) of the resolution function, as shown in Fig. D.1. Because the Z position is estimated based on the time on the first threshold, the Z position resolution can be estimted from the first threshold only. For a given scintillator $i$ sum of $d^Z_L$ and $d^Z_R$ ($d^Z_i$) can be estimated, using velocity for a given scintillator, or the mean velocity ($\overline{v}$), given in Fig. 3.12. Then, the Z resolution, expressed by $\sigma_Z$ can be estimated from mean $d^Z$ value, calculated as a mean over all detection modules ($d^Z_i$), as

$$\sigma_Z = d^Z \cdot \frac{\overline{v}}{2.35}, \tag{D.1}$$

where 2.35, comes from the translation of FWHM to $\sigma$ for the Gaussian distribution. Resulting value of the Z resolution was equal to 2.45 (19) cm.

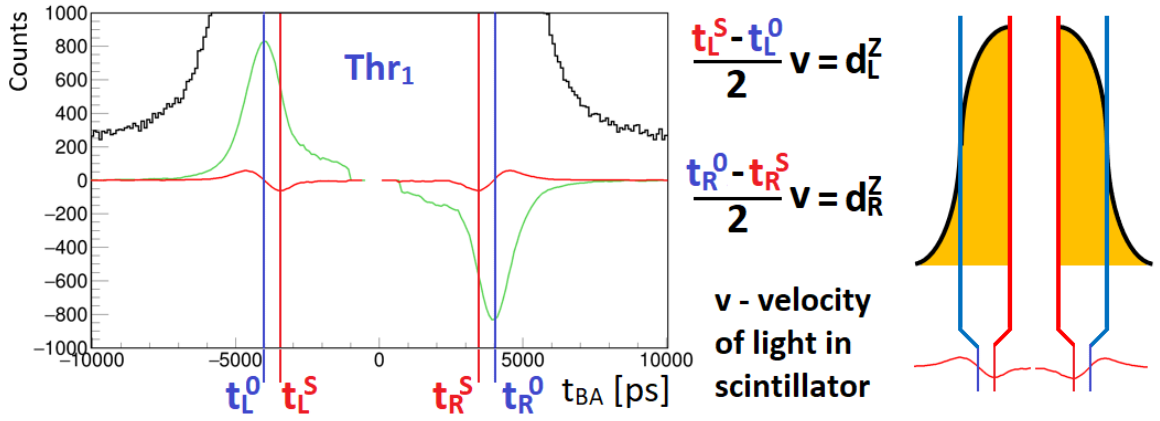


Figure D.1: **Procedure of determining Z position resolution.** Distribution for the first threshold from Fig. 3.2 (black curve) with the first (green curve) and the second derivative (red curve) shown with the marked fixed points: zero point (blue line) and the closest extreme (red line). Sum of the differences between fixed point for a given side of the edge - left (L) and right (R), can be translated to the FWHM of the Z position for a given side ($d_L^Z$, $d_R^Z$), by using velocity of light in scintillator (v). In fact the second derivatives can be glued in the positions expressed by red lines, therefore mean of the $d_L^Z$ and $d_R^Z$ value will correspond to the sigma of the resolution function.

# Appendix E

# Generalization of the position reconstruction algorithm

Algorithm for the position reconstruction described in Sec. 4.1, can be generalized to decays into N photons, where $N > 3$. Schematic example for the $N = 4$ is shown in Fig. E.1, but the example can be expanded for higher decays, while adding another spheres, which creates more vertices of the minimized shape. Each sphere corresponds to the potential annihilation positions, from a perspective of a given hit. Radius for each sphere is calculated as it was shown in Fig. 4.2, and it is based on the time of hits. For each sphere, two other spheres are sought which are closest to the position of their centers, and their intersections are determined - creating N different circles for all N hits. It is worth noting that the centers of the circles lie on the vectors connecting the centers of two adjacent spheres. Single fixed point for a given circle is determined as the intersection of the circle and the vector connecting two spheres, shifted to the centre of the circle. Vector for the fixed point determination is chosen such, that it is coming from the adjacent circle. Connecting fixed points creates a shape that should contain the actual position of the annihilation. By varying the minimal radius $R_0$, one can find the shape with minimal perimeter. The reconstructed position of the annihilation is calculated as a middle of the shape with minimal perimeter. The method of the minimization of the shape is the same as it was shown in Fig. 4.2.

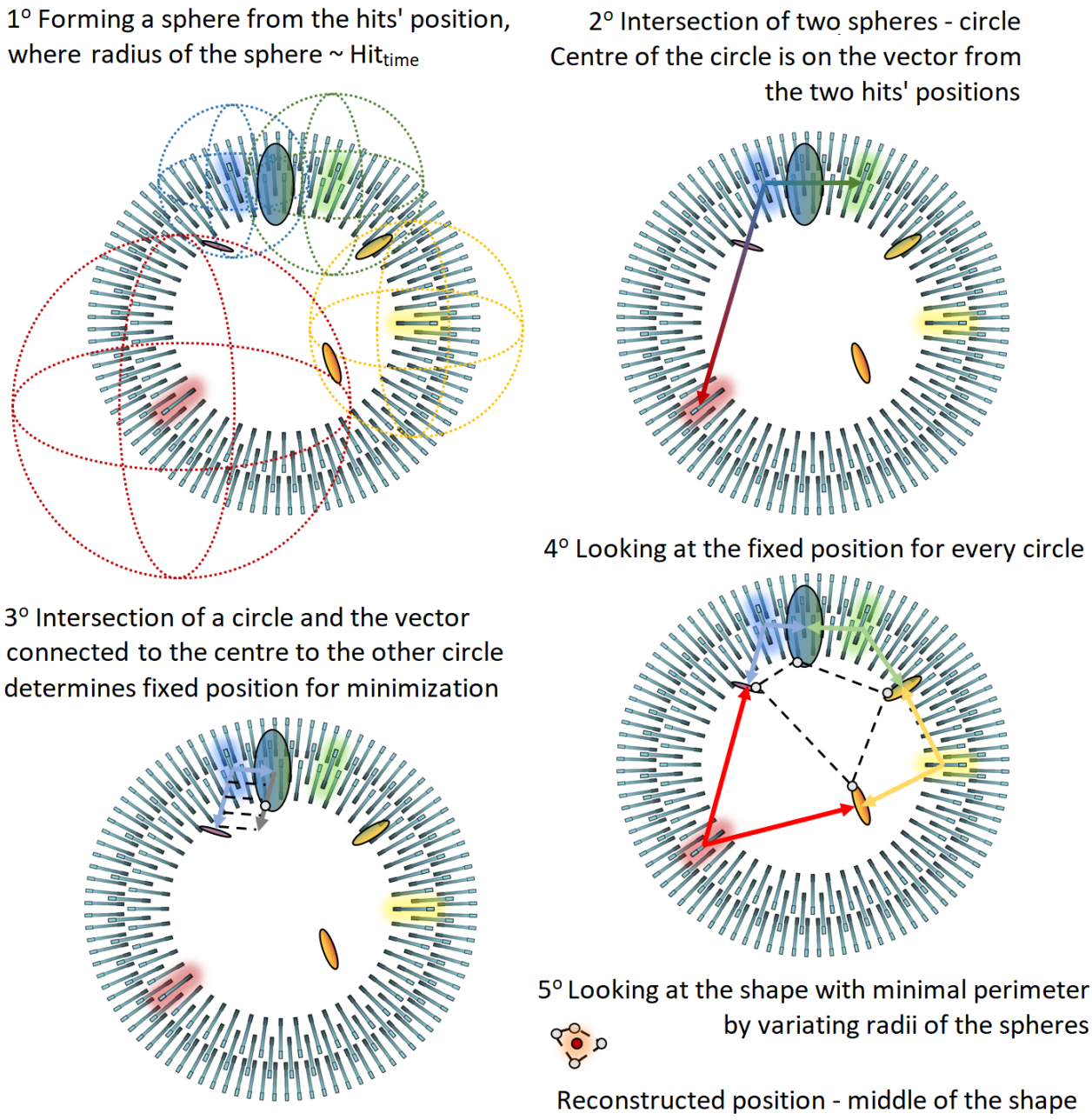


Figure E.1: **Position reconstruction concept for decays into 4 photons.** Having four hits registered in a single event that is coming from the same annihilation, one can create spheres from each hits' positions. For every adjacent sphere pair one can create a circle, which corresponds to the intersection of two spheres. Fixed point of each circle is determined as a intersection of the circle and a proper vector. Fixed points creates a shape, which can be minimzed by looking at the shape with minimal perimeter. Reconstructed position is estimated as a middle of the shape.

# Appendix F

# Comparison of the three-photon decay position reconstruction methods

In the thesis an algorithm for the reconstruction of the position of the decay of three photons, was described in Sec. 4.1. It was based on the trilateration algorithm described elsewhere. The comparison of the reconstructed annihilation position distribution for the trilateration method and the proposed algorithm was done by means of the simulations. Simulated events allows to extract the real annihilation position, and compare it with the reconstructed position. As the reconstruction error value, the position difference between true and reconstructed was introduced as $\Delta$P (algorithm). Simulation data for the XAD4 measurement was used for the comparison. Images of the reconstructed positions using trilateration and iterative algorithms are shown in Fig. F.1. In addition in Fig. F.1 there is a comparison of the $\Delta$P distribution between those two algortihms. One can see, that the image reconstructed by the iterative method looks more centered around real position at zero, than the image created by the trilateration method. The standard deviation of the reconstructed points was improved by 20% and 40% for the iterative algorithm comparing to the trilateration algorithm, by looking at the standard deviations and the selected region with the highest counts on the $\Delta$P (iterative) vs $\Delta$P (trilateration).

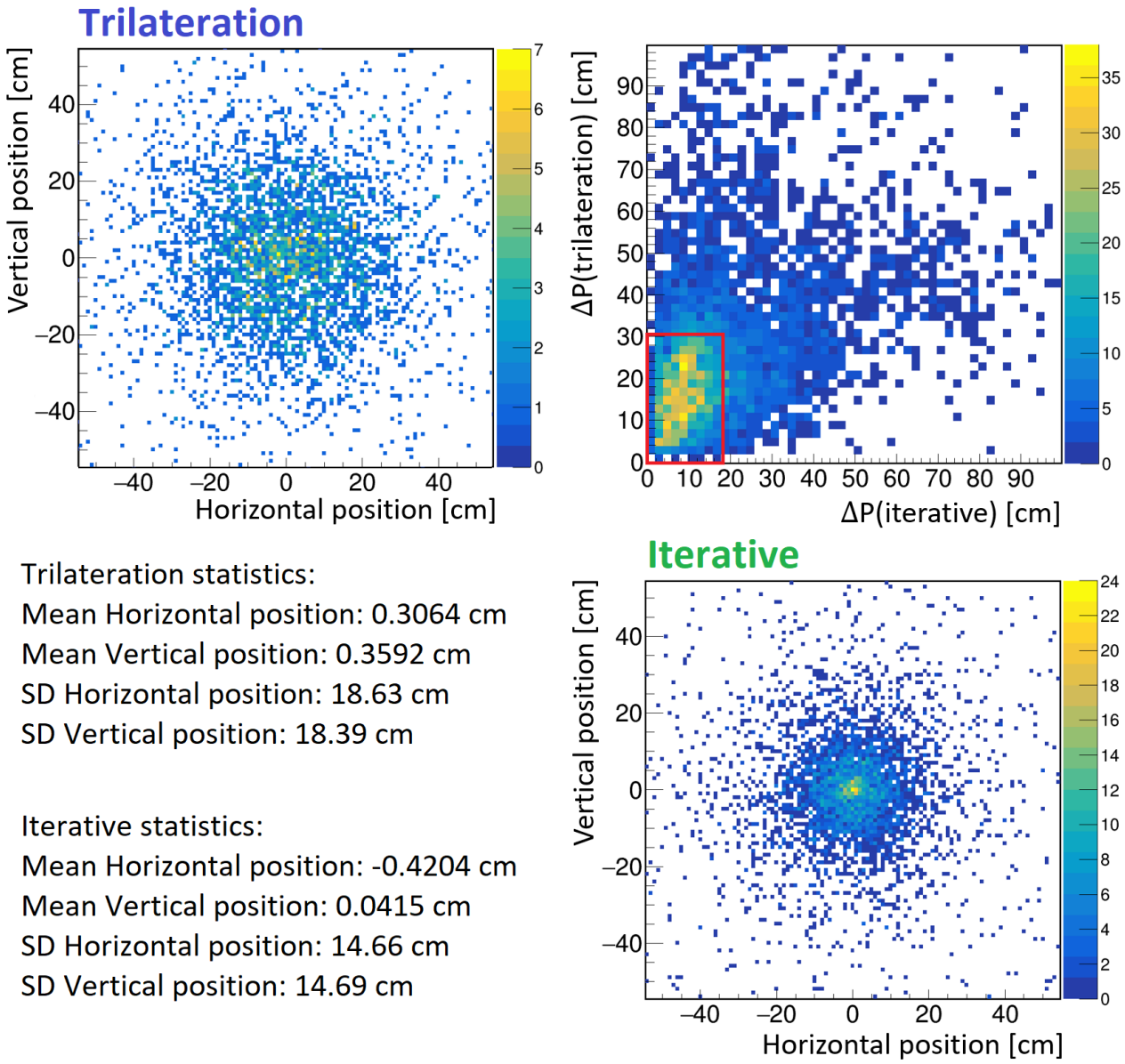


Figure F.1: **Position reconstruction comparison between trilateration and introduced iterative algorithms.** Reconstructed annihlation position shown in the horizontal-vertical plane for the simulated data, using trilateration and iterative algorithm. In addition there is a comparison of those two methods shown as ΔP (iterative) vs ΔP (trilateration) distribution. One can see, that the iterative method produces positions closer to the real annihilation position. By looking just at the standard deviations of the reconstructed positions iterative method was better by 20% than the trilaterion method for the experimental smearings described in Fig. 4.5. Red rectangle on the ΔP (iterative) vs ΔP (trilateration) distribution indicates the closest reconstructed positions for both methods. By looking at the red rectangle iterative method is better than trilateration method by 40% ((30-18)/30).

# Appendix G

# Explanation of the structure on the angle distribution

In Fig. 6.2 there is a structure on the angle distribution between two hits. It can be explained by the specific geometry of the J-PET detector and the bin width used for the visualization of the data - $2^o$. One can start from the description of the detecion modules geometry. The detection modules in the J-PET detector are distributed evenly in each layer - by $7.5^o$ in the first and the second layer and by $3.75^o$ in the third layer, like it is shown in Fig. G.1. In addition, detection modules in the second and the third layer are shifted by $3.75^o$ and $1.875^o$, so the modules do not overlap.

The division angles on $2^o$ in some situations, can be artificially enhanced, when in the single bin two detection modules are included. Those situations, due to the geometry of the J-PET detector occur every $30^o$, starting with $8^o$. Bin with the centre equal to $38^o$ is shown in Fig. G.1, in which two detection modules, from the third layer and from the first layer, are in it. Artificial structure can be muted by appropriately binning the angle distribution. Using bin width equal to $7.42^o$ does not show any structure not derived from true scattering and not from the radioisotope inside the detection chamber, as shown in Fig. G.2. However, wider bins blur the shapes of the distribution, and thus make it difficult to determine such a cut that will reduce scatterings and at the same time maximize the sensitivity of the selection criteria. From that reason angle distributions for $2^o$ were used to formulate cut-offs for the selection of the events for the positronium imaging.

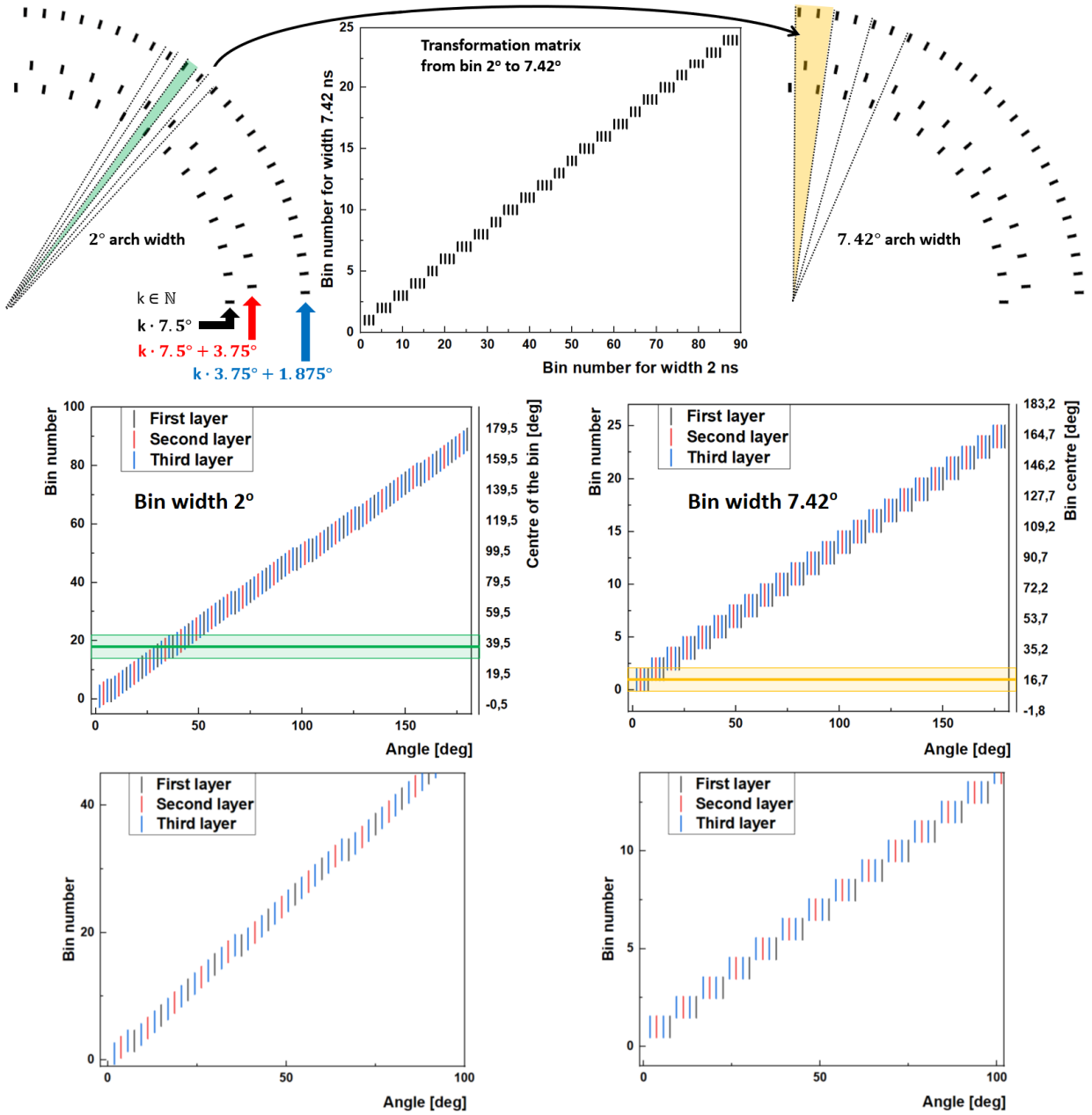


Figure G.1: **Different division of the detection modules in the J-PET detector based on the angle.** Division of detectors with respect to angles for two different arch widths - $2^o$ (left, top) and $7.42^o$ (right, top) marked on the scheme of the J-PET detector. Distribution of the bin number as a function of angle of the detector for $2^o$ (left, middle and left, bottom) and $7.42^o$ (right, middle and right, bottom). For the $2^o$ division one can see a characteristic edge, which disturbs the homogeneity of the angle distribution. In particular, the edge at the $38^o$ (green area) corresponds to the situation, when two detection modules are cumulated in the same bin, marked as the green area on the scheme of the J-PET detector. This effect is increasing the content of the bins at $8^o$, $38^o$, $68^o$, $98^o$, $128^o$ and $158^o$, so it is periodic every $30^o$. When using the bin equal to $7.42^o$, the effect is nivelated, grouping exactly four detection modules (yellow area) in a given bin, which homogenizes the distribution of angles.

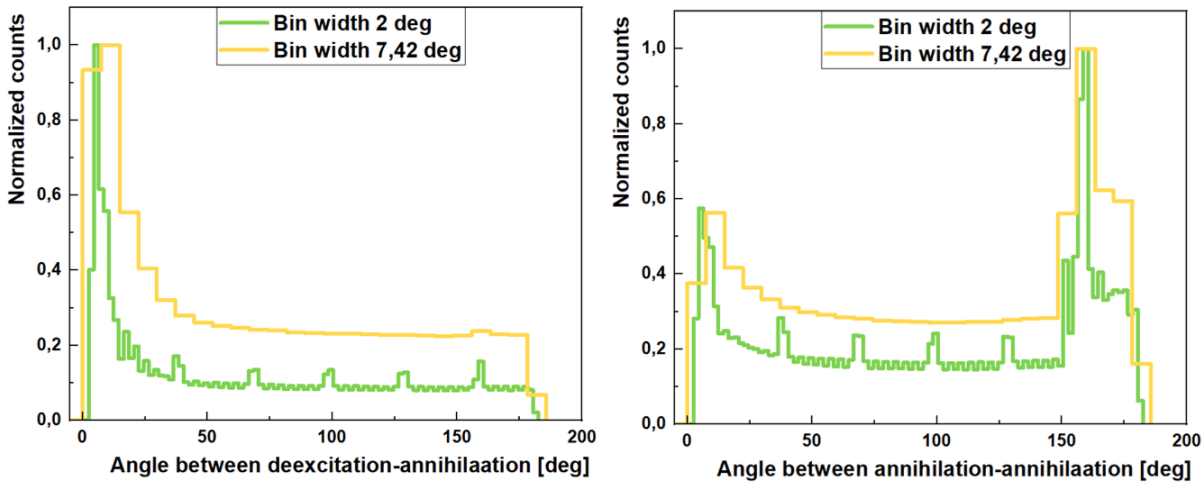


Figure G.2: **Angle distribution for different binnings.** Angle between deexcitation-annihilation and annihilation-annihilation pairs in event shown for two different bin widths - $2^o$ (green) and $7.42^o$ (yellow). The additional structure seen in the green distribution is nivelated on the yellow one, by simply rebinning the distribution. However, wider bin weakens the possibility of estimating the correct scatterings cut-off.

# Appendix H

# Image of the annihilation positions on each step of the analysis

To test the selection procedure for the positronium imaging one can plot the distribution of the annihilation positions at different stages of the analysis. Annihilation position can be estimated based on the algorithm shown in Fig. 2.1, where the selection criteria was as described in Sec. H. The selection criteria were tested for the porous phantom (Sec. 6.4) and for the tissue phantom (Sec. 6.5). The results for the porous phantom are shown in Fig. H.1, H.2 and H.3 where the results for the tissue phantom is shown in Fig. H.4, H.5 and H.6. Enhancements on the distribution of the annihilation positions in the position of the detectors are coming from the scatterings between two scintillators. Indeed, the time difference between primary photon and the first scattering will be equal to the distance between two scintillators multiplied by the speed of light. Therefore, the reconstructed position will be the position of the detection module, where the primary photon deposited energy. Regarding the selection criteria one can also see, that the most scatterings are reduced when the requirement on the minimal angle between annihilation hits is applied. In addition, scatter test allows also to reduce the impact of the accidental coincidences.

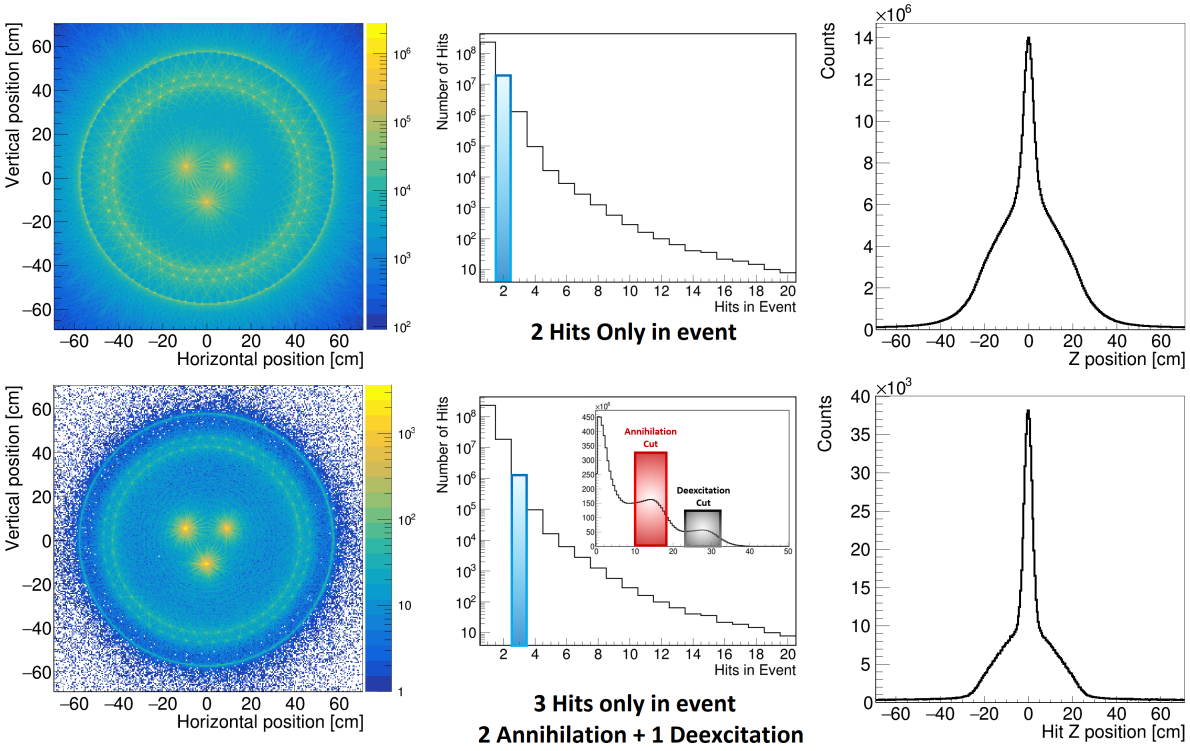


Figure H.1: **Impact of the hit multiplicity and the TOT cut on the annihilation position distribution for the porous phantom** (top) Annihilation position distribution for the events with two hits only. The reconstruction of the position for such events is done based on the two hits positions and times. (bottom) Annihilation position distribution for the events with three hits only, where one of the hit was classified as the deexcitation hit and the other two are classified as the annihilation hits based on the TOT value. The reconstruction of the position for such events is done based on the two annihilation hits positions and times.

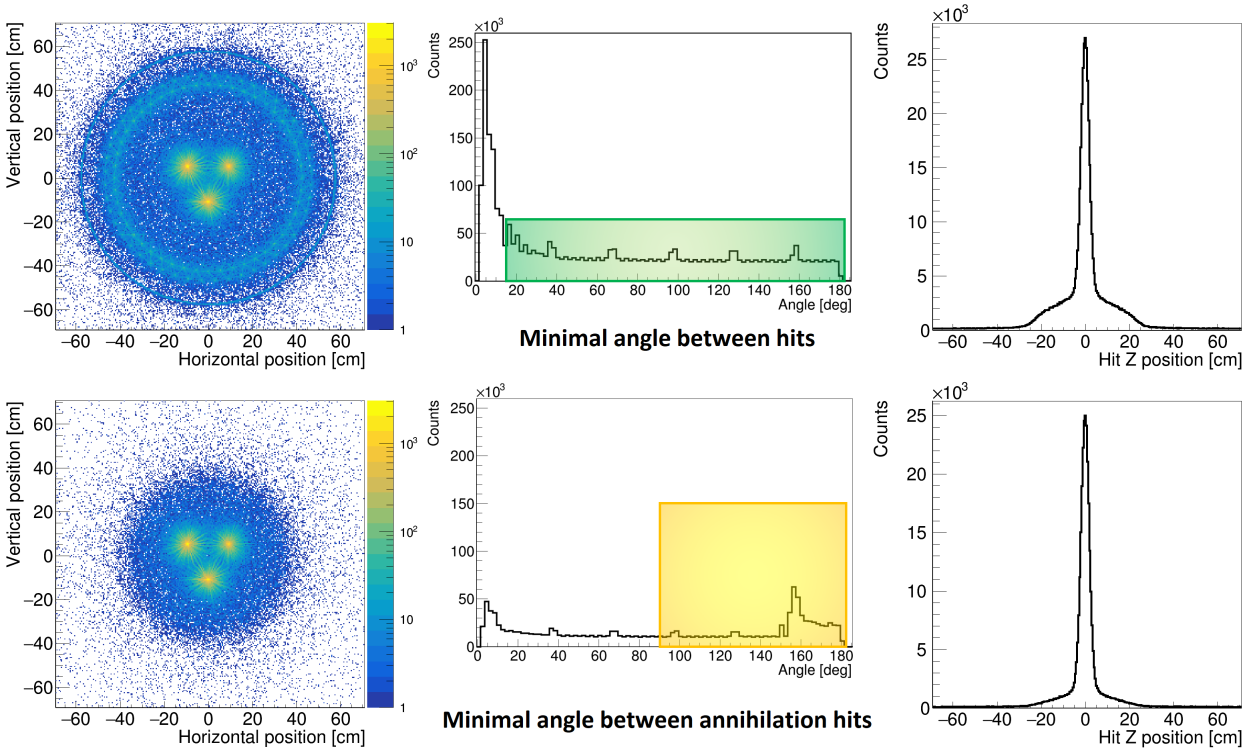


Figure H.2: **Impact of the angle between hits cuts on the annihilation position distribution for the porous phantom** (top) Annihilation position distribution for the events with three hits only, where one of the hit was classified as the deexcitation hit and the other two are classified as the annihilation hits based on the TOT value. In addition, the angle between any two hits in an event must be greater than $15^o$. The reconstruction of the position for such events is done based on the two annihilation hits positions and times. (bottom) Annihilation position distribution for the events with three hits only, where one of the hit was classified as the deexcitation hit and the other two are classified as the annihilation hits based on the TOT value. In addition, the angle between any two hits in an event must be greater than $15^o$ and angle between the annihilation hits must be greater than $90^o$. The reconstruction of the position for such events is done based on the two annihilation hits positions and times.

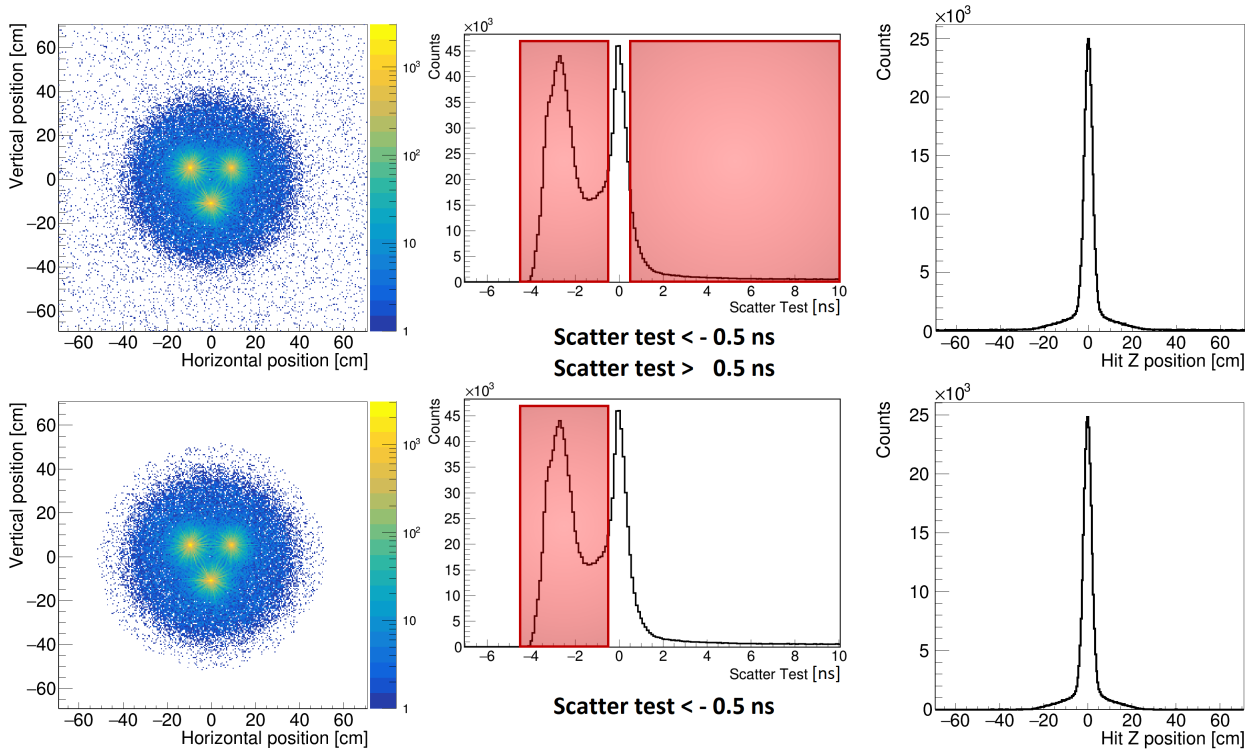


Figure H.3: **Impact of the scatter test cuts on the annihilation position distribution for the porous phantom** (top) Annihilation position distribution for the events with three hits only, where one of the hit was classified as the deexcitation hit and the other two are classified as the annihilation hits based on the TOT value. In addition, the angle between any two hits in an event must be greater than $15^o$ and angle between the annihilation hits must be greater than $90^o$ and the scatter test calculated for the annihilation hits must be lower than -0.5 ns or greater than 0.5 ns. The reconstruction of the position for such events is done based on the two annihilation hits positions and times. (bottom) Annihilation position distribution for the events with three hits only, where one of the hit was classified as the deexcitation hit and the other two are classified as the annihilation hits based on the TOT value. In addition, the angle between any two hits in an event must be greater than $15^o$ and angle between the annihilation hits must be greater than $90^o$ and the scatter test calculated for the annihilation hits must be lower than -0.5 ns. The reconstruction of the position for such events is done based on the two annihilation hits positions and times.

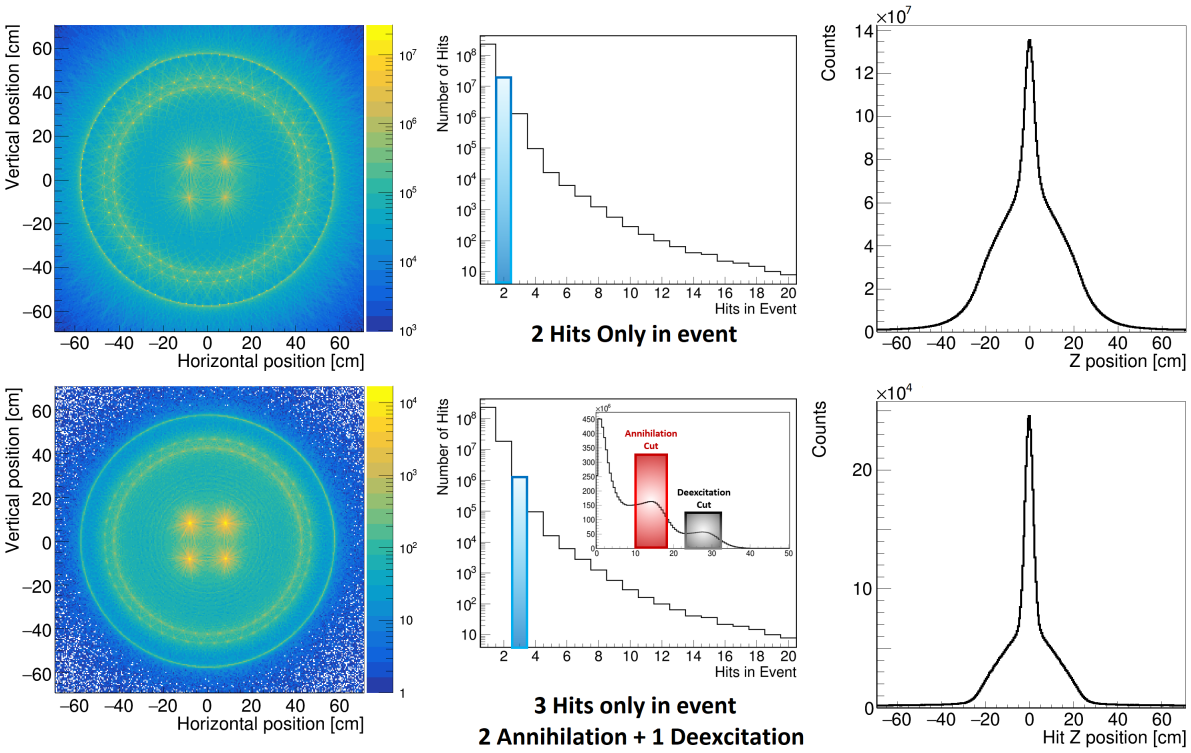


Figure H.4: **Impact of the hit multiplicity and the TOT cut on the annihilation position distribution for the tissue phantom** (top) Annihilation position distribution for the events with two hits only. The reconstruction of the position for such events is done based on the two hits positions and times. (bottom) Annihilation position distribution for the events with three hits only, where one of the hit was classified as the deexcitation hit and the other two are classified as the annihilation hits based on the TOT value. The reconstruction of the position for such events is done based on the two annihilation hits positions and times.

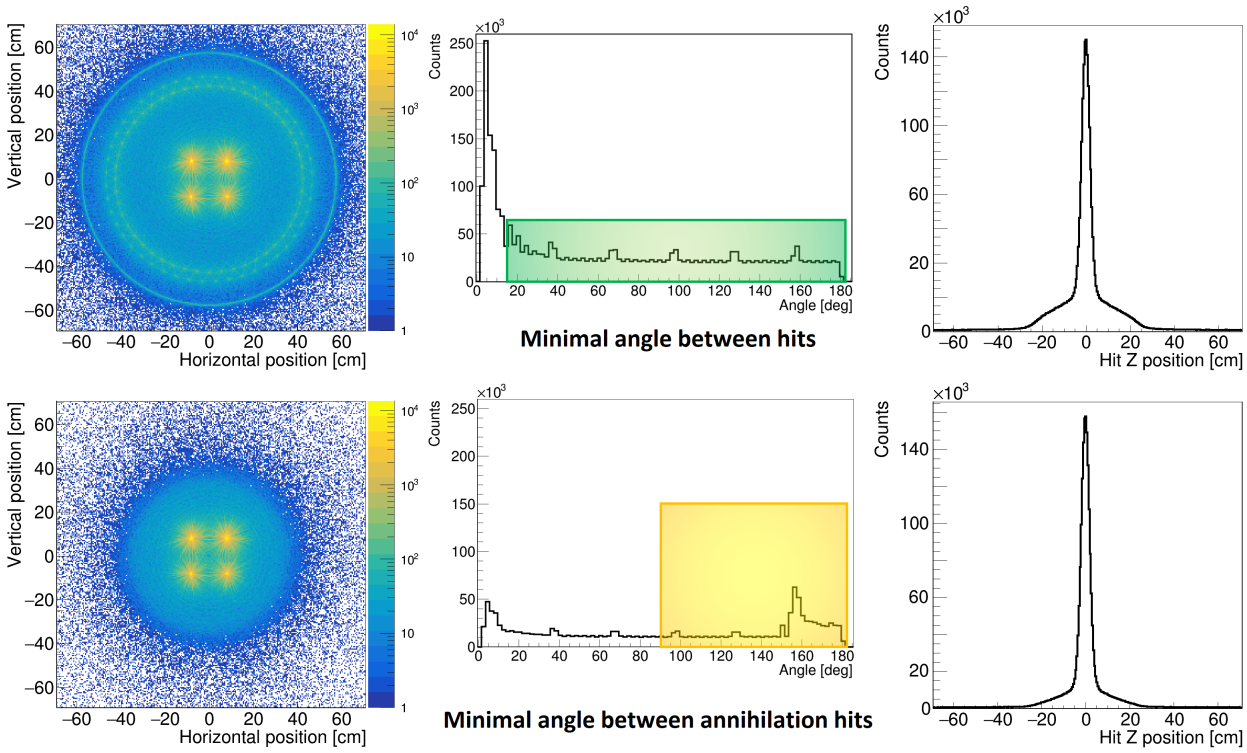


Figure H.5: **Impact of the angle between hits cuts on the annihilation position distribution for the tissue phantom** (top) Annihilation position distribution for the events with three hits only, where one of the hit was classified as the deexcitation hit and the other two are classified as the annihilation hits based on the TOT value. In addition, the angle between any two hits in an event must be greater than $15^o$. The reconstruction of the position for such events is done based on the two annihilation hits positions and times. (bottom) Annihilation position distribution for the events with three hits only, where one of the hit was classified as the deexcitation hit and the other two are classified as the annihilation hits based on the TOT value. In addition, the angle between any two hits in an event must be greater than $15^o$ and angle between the annihilation hits must be greater than $90^o$. The reconstruction of the position for such events is done based on the two annihilation hits positions and times.

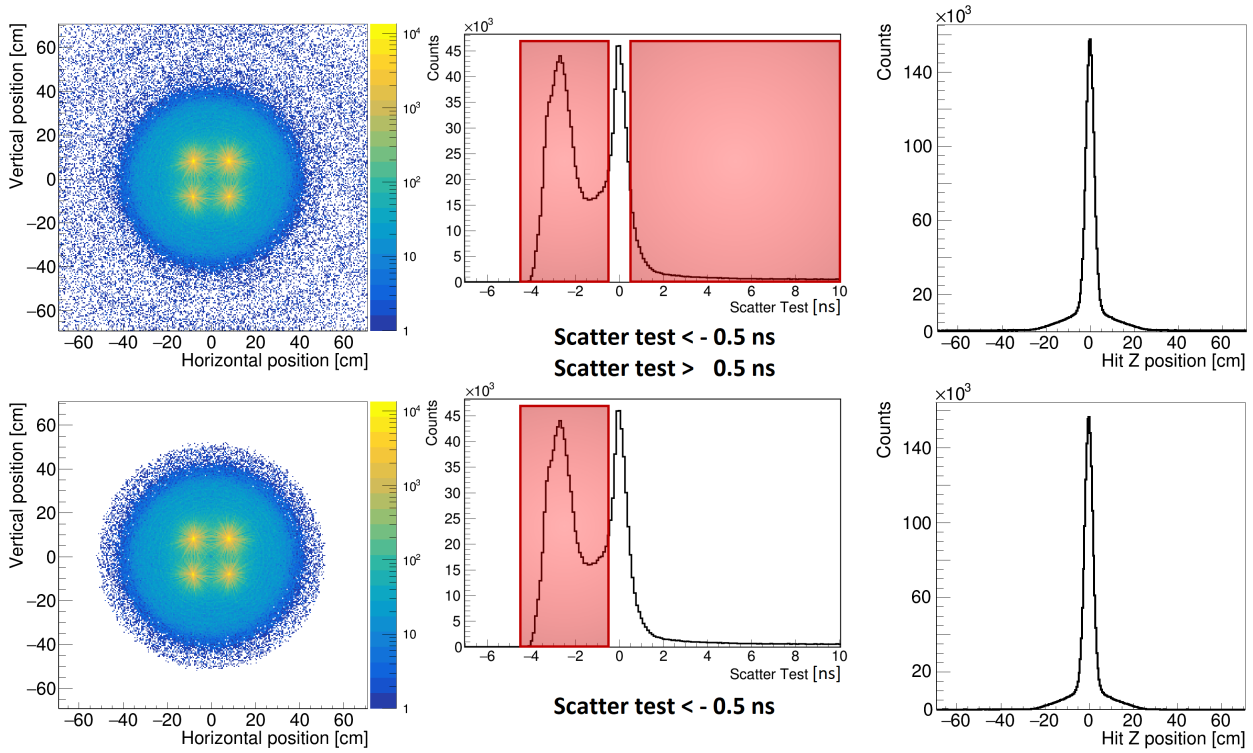


Figure H.6: **Impact of the scatter test cuts on the annihilation position distribution for the tissue phantom** (top) Annihilation position distribution for the events with three hits only, where one of the hit was classified as the deexcitation hit and the other two are classified as the annihilation hits based on the TOT value. In addition, the angle between any two hits in an event must be greater than $15^o$ and angle between the annihilation hits must be greater than $90^o$ and the scatter test calculated for the annihilation hits must be lower than -0.5 ns or greater than 0.5 ns. The reconstruction of the position for such events is done based on the two annihilation hits positions and times. (bottom) Annihilation position distribution for the events with three hits only, where one of the hit was classified as the deexcitation hit and the other two are classified as the annihilation hits based on the TOT value. In addition, the angle between any two hits in an event must be greater than $15^o$ and angle between the annihilation hits must be greater than $90^o$ and the scatter test calculated for the annihilation hits must be lower than -0.5 ns. The reconstruction of the position for such events is done based on the two annihilation hits positions and times.

# Appendix I

# Porous phantom analysis supplement

Division of the image of the porous phantom, shown in Fig. 6.5, allows to create positron lifetime distribution for each large voxel. These distributions were fitted by PALS Avalanche software, resulting in the longest-lived component with an mean o-Ps lifetime of 51.38 ns, 25.84 ns, and 2.02 ns for IC3100, XAD4, and PVT, respectively as shown in Tab. 6.1 and Fig. I.1. Fits with decomposition onto different component are shown for each sample in Fig. I.2, I.3 and I.4. Lifetime spectrum for small voxels for a given sample are shown in Fig. I.5, I.6 and I.7, where voxel with the highest statistic is compared with the voxel with the lowest statistic.

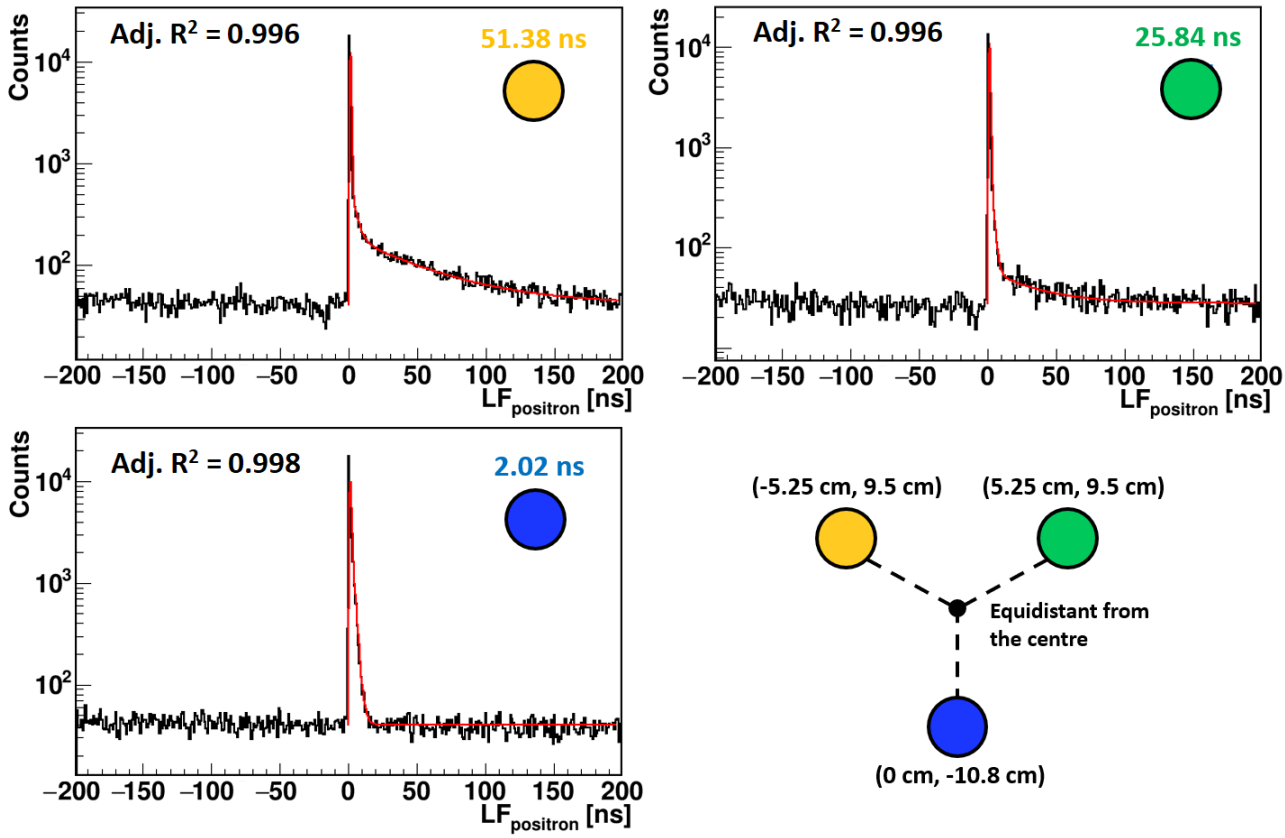


Figure I.1: **Fit to the positron lifetime spectrum for the porous phantom.** Positron lifetime distribution from large voxels corresponding to a given sample - IC3100 (yellow), XAD4 (green) and PVT (blue), with fitted model drawn as a red line. Models are in good agreement with the data, confirmed by the high values of the adjusted $R^2$ parameter.

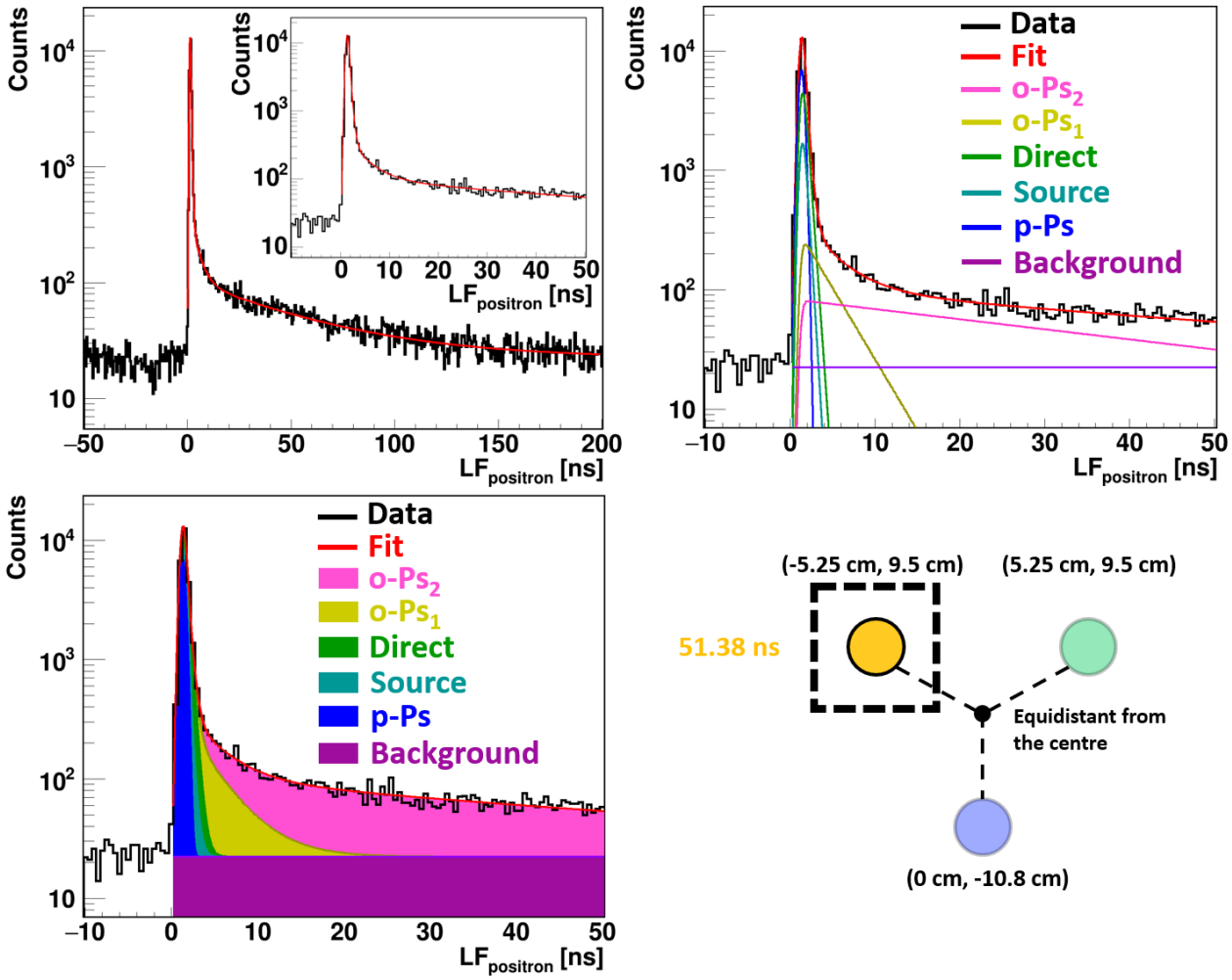


Figure I.2: **Fit to the positron lifetime spectrum for IC3100 and separation for different components.** Positron lifetime distribution from large voxel corresponding to a given sample - IC3100 with fitted model drawn as a red line. In addition, separation onto different component drawn separately and cummulatively is shown.

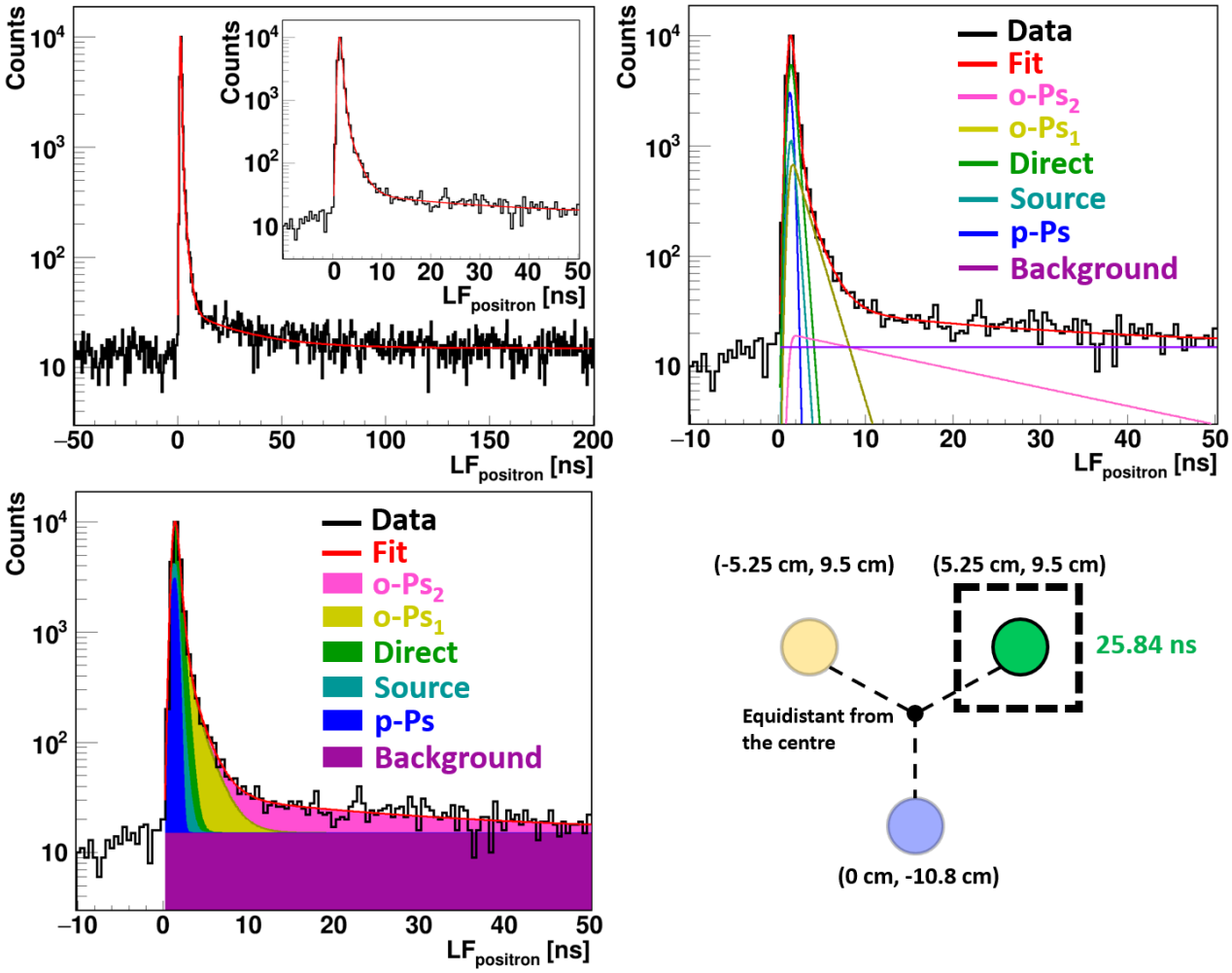


Figure I.3: **Fit to the positron lifetime spectrum for XAD4 and separation for different components.** Positron lifetime distribution from large voxel corresponding to a given sample - XAD4 with fitted model drawn as a red line. In addition, separation onto different component drawn separately and cummulatively is shown.

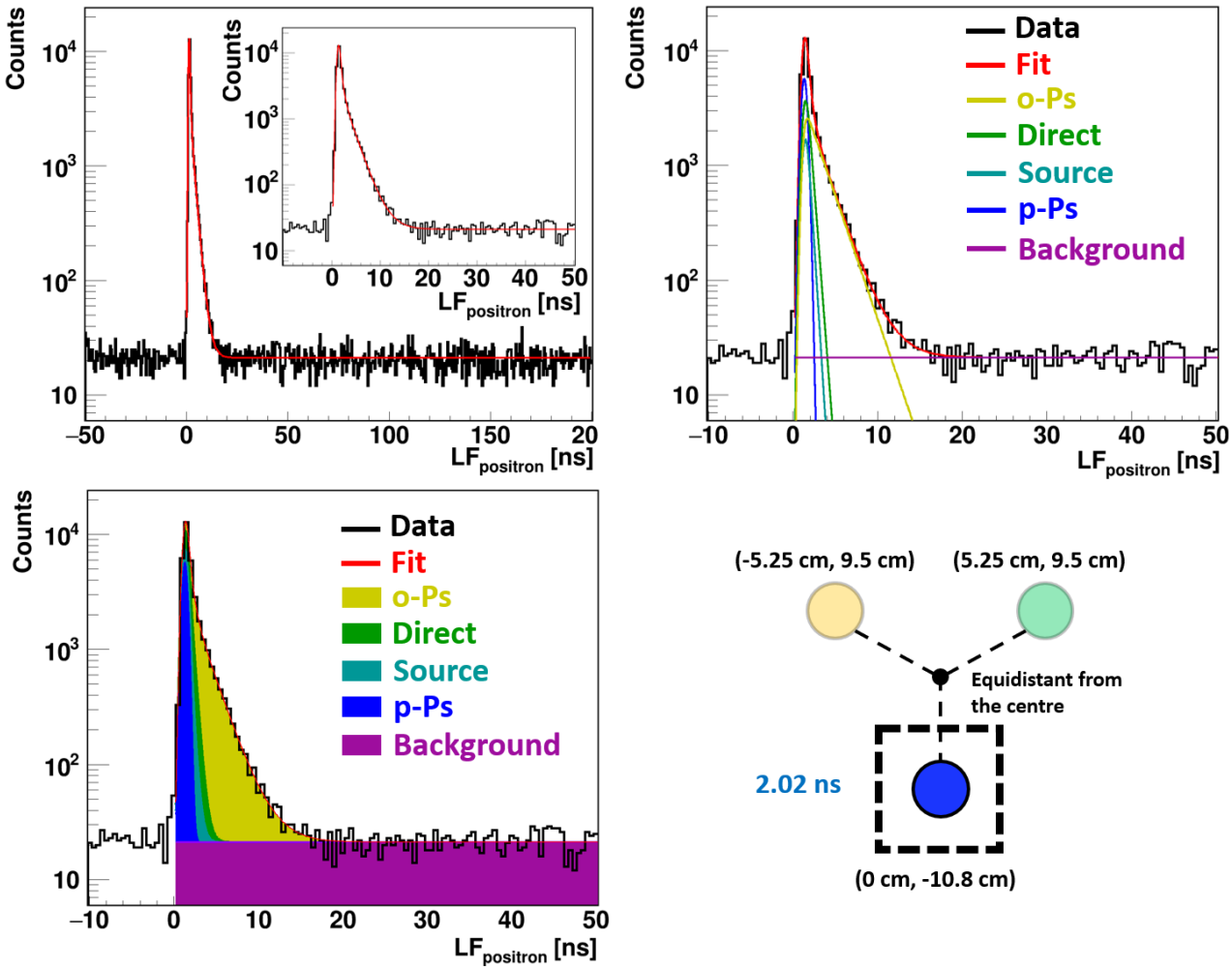


Figure I.4: **Fit to the positron lifetime spectrum for PVT and separation for different components.** Positron lifetime distribution from large voxel corresponding to a given sample - PVT with fitted model drawn as a red line. In addition, separation onto different component drawn separately and cummulatively is shown.

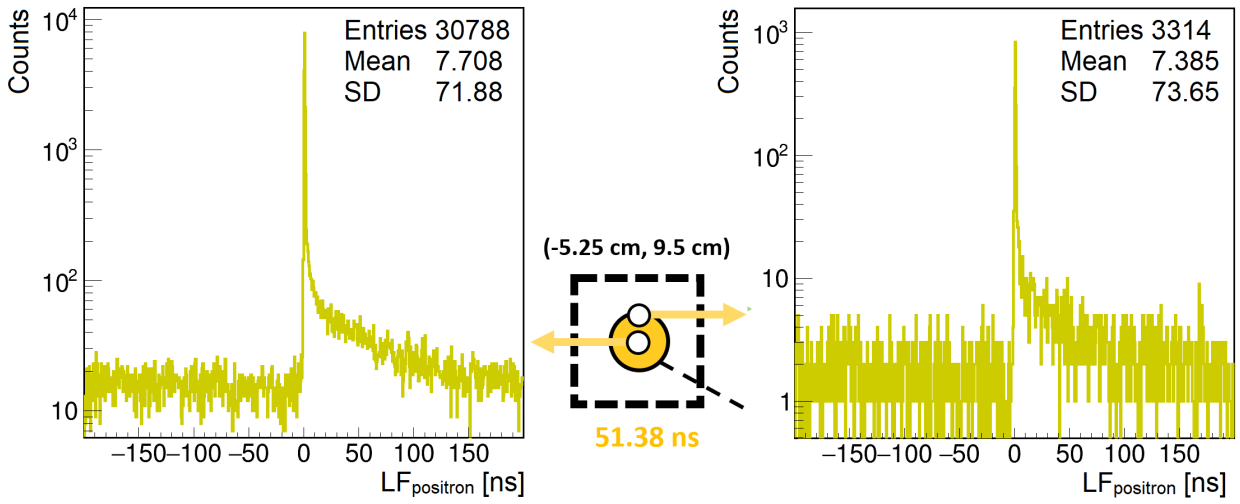


Figure I.5: **Comparison of the positron lifetime distribution between two chosen voxels for IC3100.** (left) Lifetime distribution from the voxel with the highest total number of counts, regarding position of the chamber with IC3100. (right) In contrast, voxel with the lowest total number of counts is shown

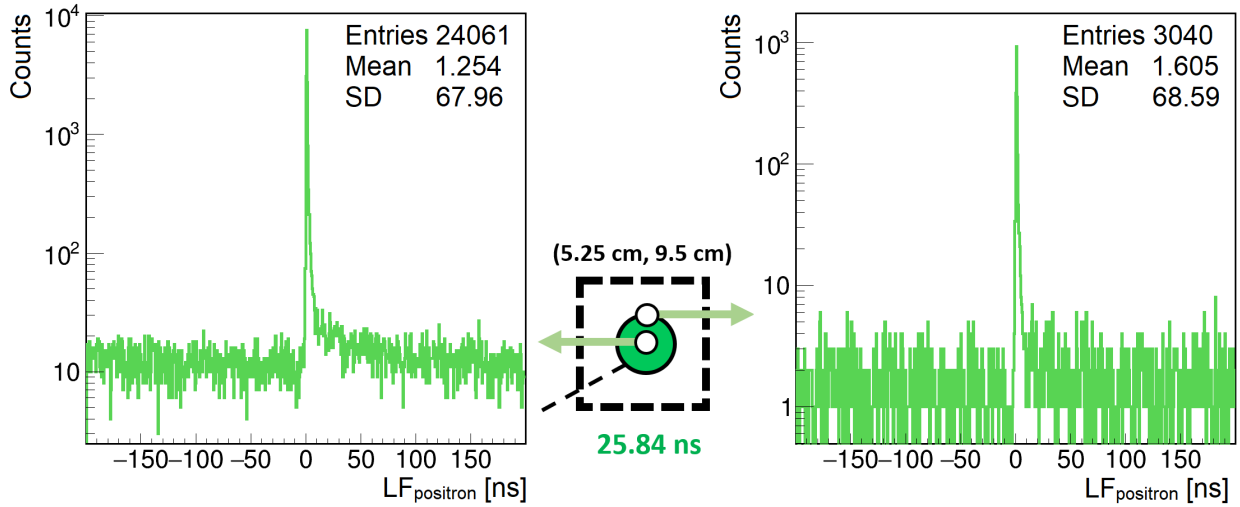


Figure I.6: **Comparison of the positron lifetime distribution between two chosen voxels for XAD4.** (left) Lifetime distribution from the voxel with the highest total number of counts, regarding position of the chamber with XAD4. (right) In contrast, voxel with the lowest total number of counts is shown.

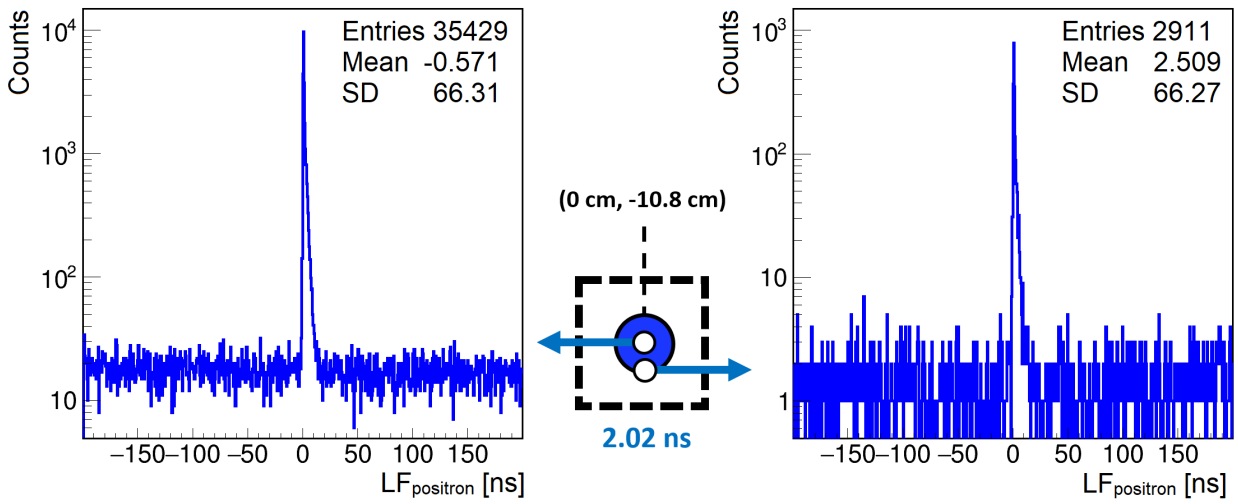


Figure I.7: **Comparison of the positron lifetime distribution between two chosen voxels for PVT.** (left) Lifetime distribution from the voxel with the highest total number of counts, regarding position of the chamber with PVT. (right) In contrast, voxel with the lowest total number of counts is shown.

# Appendix J

# Tissue phantom analysis supplement

Division the image of the tissue phantom, shown in Fig. 6.7, allows to create positron lifetime distribution for each large voxel. These distributions were fitted by PALS Avalanche software, resulting in the longest-lived component with an mean o-Ps lifetime of 1.950 ns, 1.874 ns, 2.645 ns and 2.581 ns for Cardiac Myxoma 1, Cardiac Myxoma 2, Adipose Tissue 1 and Adipose Tissue 2, respectively as shown in Tab. 6.2. Fits with decomposition onto different component are shown for each sample in Fig. J.1 and J.2. Lifetime spectrum for small voxels for a given sample are shown in Fig. J.3, J.4, J.5 and J.6, where voxel with the highest statistic is compared with the voxel with the lowest statistic.

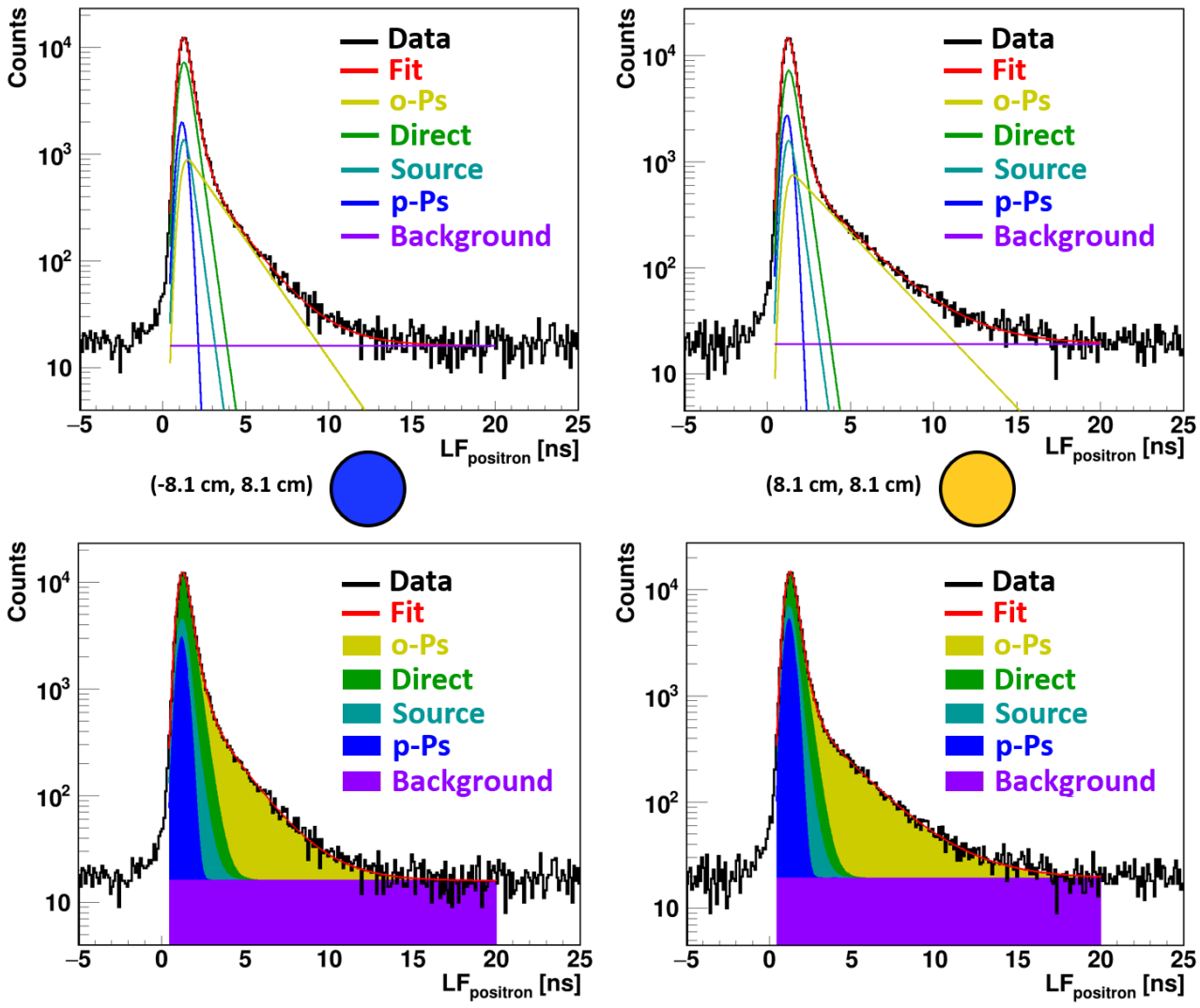


Figure J.1: **Fit to the positron lifetime spectrum for tissues from the first patient and separation for different components.** Positron lifetime distribution from large voxel corresponding to a given sample - cardiac myxoma (blue) and adipose tissue (yellow) for the first patient with fitted model drawn as a red line. In addition, separation onto different component drawn separately and cummulatively is shown.

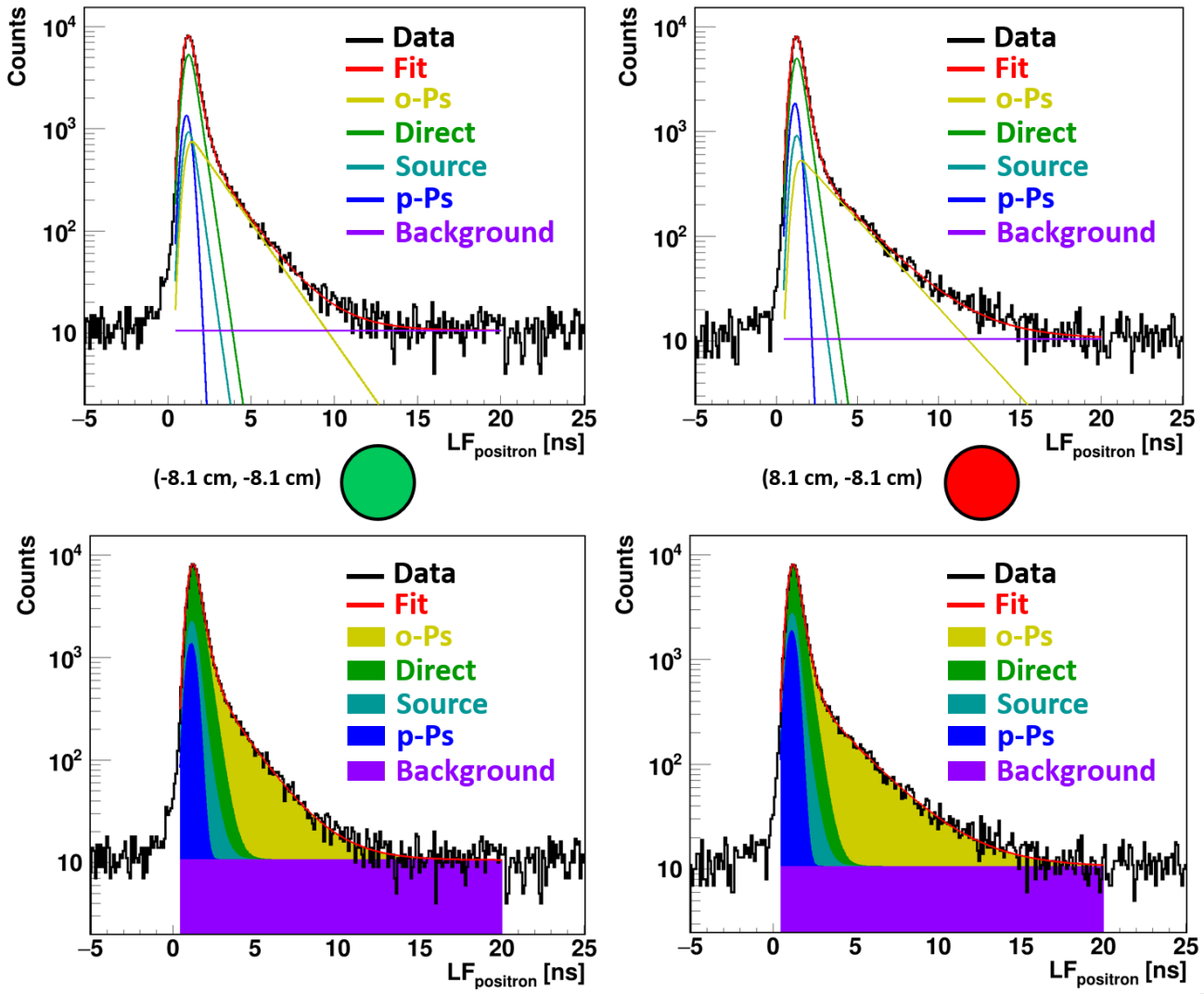


Figure J.2: **Fit to the positron lifetime spectrum for tissues from the second patient and separation for different components.** Positron lifetime distribution from large voxel corresponding to a given sample - cardiac myxoma (green) and adipose tissue (red) for the second patient with fitted model drawn as a red line. In addition, separation onto different component drawn separately and cummulatively is shown.

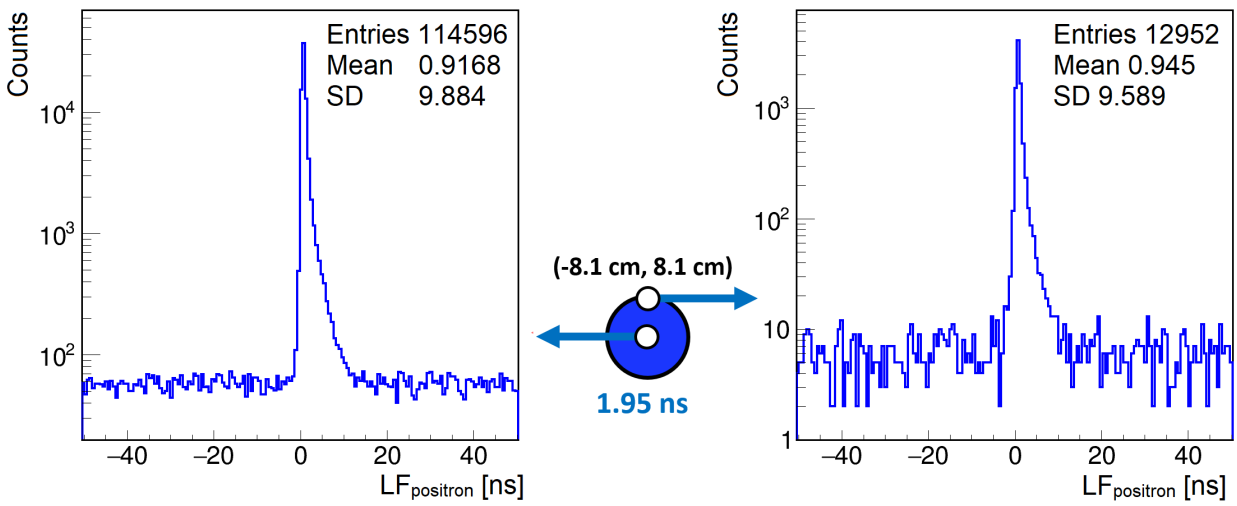


Figure J.3: **Comparison of the positron lifetime distribution between two chosen voxels for cardiac myxoma for the first patient.** (left) Lifetime distribution from the voxel with the highest total number of counts, regarding position of the chamber with Cardiac Myxoma 1. (right) In contrast, voxel with the lowest total number of counts is shown

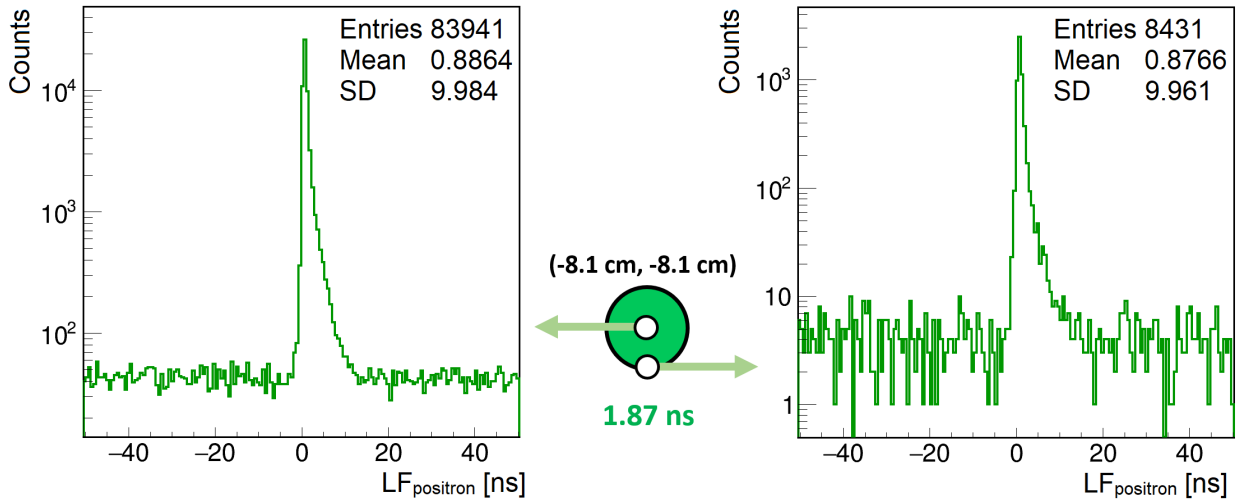


Figure J.4: **Comparison of the positron lifetime distribution between two chosen voxels for cardiac myxoma for the second patient.** (left) Lifetime distribution from the voxel with the highest total number of counts, regarding position of the chamber with Cardiac Myxoma 2. (right) In contrast, voxel with the lowest total number of counts is shown

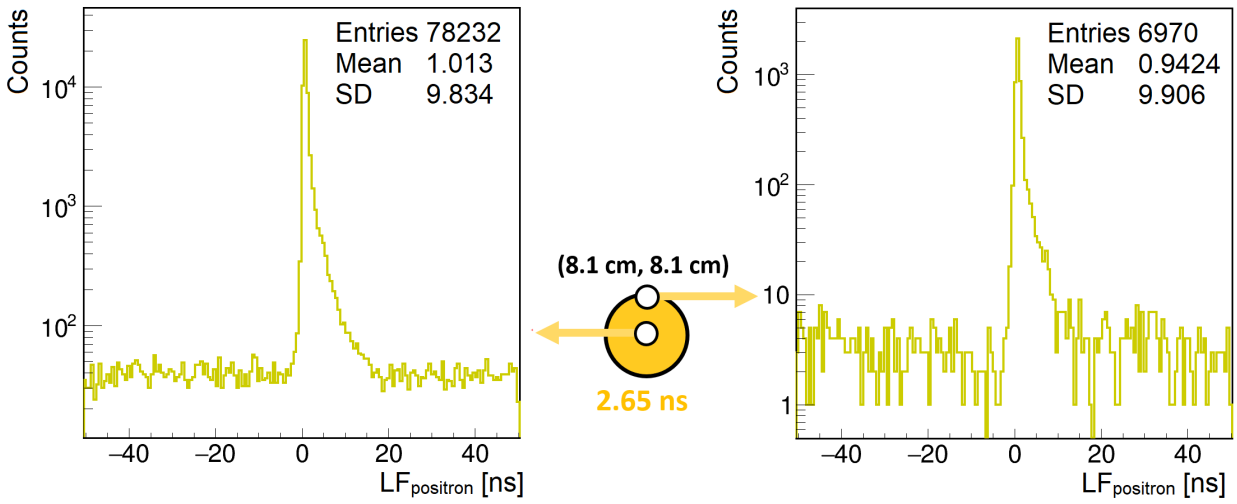


Figure J.5: **Comparison of the positron lifetime distribution between two chosen voxels for adipose tissue for the first patient.** (left) Lifetime distribution from the voxel with the highest total number of counts, regarding position of the chamber with Adipose Tissue 1. (right) In contrast, voxel with the lowest total number of counts is shown

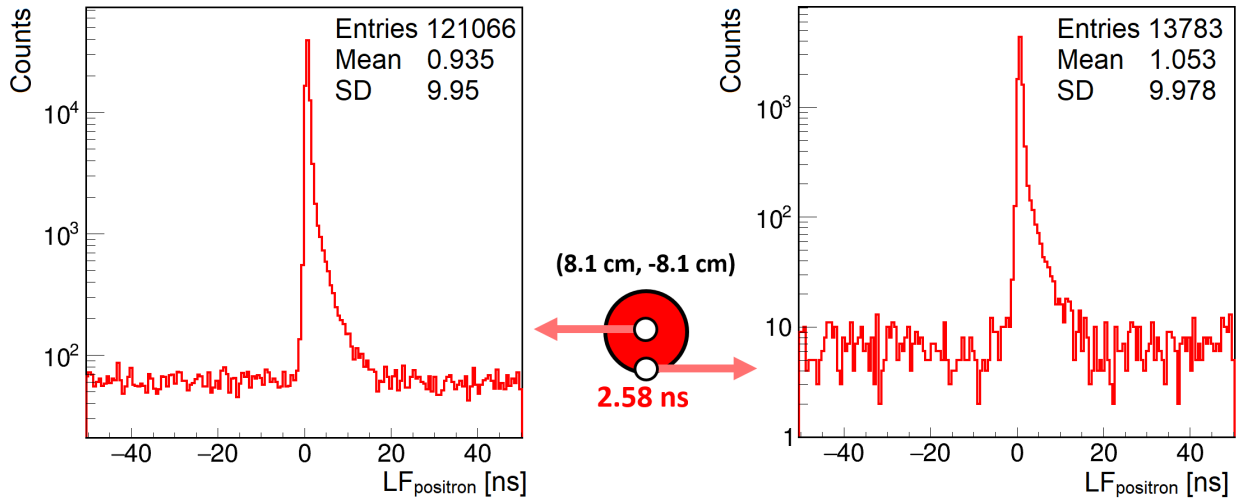


Figure J.6: **Comparison of the positron lifetime distribution between two chosen voxels for adipose tissue for the second patient.** (left) Lifetime distribution from the voxel with the highest total number of counts, regarding position of the chamber with Adipose Tissue 2. (right) In contrast, voxel with the lowest total number of counts is shown

# Bibliography


[1] P. Moskal, K. Dulski, N. Chug *et al.*, Positronium imaging with the novel multiphoton PET scanner *Science Advances* ***7***, eabh4394 (2021)

[2] P. Moskal, Positronium Imaging. *2019 IEEE Nuclear Science Symposium and Medical Imaging Conference (NSS/MIC)*, 1-3 (2019)

[3] P. Moskal, Towards total-body modular PET for positronium and quantum entanglement imaging. *2018 IEEE Nuclear Science Symposium and Medical Imaging Conference Proceedings (NSS/MIC)*, 1-4 (2019)

[4] P. Moskal, S. Niedźwiecki, T. Bednarski *et al.*, Test of a single module of the J-PET scanner based on plastic scintillators. *Nucl. Instr. and Meth. A* ***764***, 317-321 (2014)

[5] P. Moskal, N. Zoń, T. Bednarski *et al.*, A novel method for the line-of-response and time-of-flight reconstruction in TOF-PET detectors based on a library of synchronized model signals. *Nucl. Inst. and Meth. A* ***775***, 54-62 (2015)

[6] S. Niedźwiecki, P. Białas, C. Curceanu, ...K. Dulski *et al.*, J-PET: A New Technology for the Whole-body PET Imaging. *Acta Phys. Pol. B* ***48***, 1567-1576 (2017)

[7] P. Moskal, P. Kowalski, R.Y. Shopa, ...K. Dulski *et al.*, Simulating NEMA characteristics of the modular total-body J-PET scanner - an economic total-body PET from plastic scintillators. *Phys. Med. Biol.* ***66***, 175015 (2021)

[8] W.W. Moses, Fundamental Limits of Spatial Resolution in PET. *Nucl. Instr. and Meth. A* ***648***, S236-S240 (2011)

[9] S. Vandenberghe, E. Mikhaylova, E. D'Hoe, P. Mollet and J.S. Karp, Recent developments in time-of-flight PET. *EJNMMI Phys.* ***3***, 3 (2016)

[10] S. Vandenberghe, P. Moskal and J. Karp, State of the art in total body PET. *EJNMMI Phys.* ***7***, 35 (2020)

[11] P. Moskal and E.Ł. Stępień, Prospects and clinical perspectives of total-body PET imaging using plastic scintillators. *PET Clin.* ***15***, 439 (2020)

[12] E. Miele, G.P. Spinelli, F. Tomao *et al.*, Positron Emission Tomography (PET) radiotracers in oncology – utility of 18F-Fluoro-deoxy-glucose (FDG)-PET in the management

of patients with non-small-cell lung cancer (NSCLC). *J. Exp. Clin. Cancer Res.* ***27***, 52 (2008)

[13] M. Sitarz, J. Cussonneau, T. Matulewicz and F. Haddad, Radionuclide candidates for $\beta + \gamma$ coincidence PET: An overview. *Appl. Radiat. Isot.* ***155***, 108898 (2020)

[14] T. Matulewicz, Radioactive nuclei for $\beta + \gamma$ PET and theranostics: selected candidates. *Bio-Algorithms and Med-Systems* ***17***, DOI:10.1515/bams-2021-0142 (2021)

[15] J. Choiński and M. Łyczko, Prospects for the production of radioisotopes and radiobioconjugates for theranostics. *Bio-Algorithms and Med-Systems* ***17***, DOI:10.1515/bams-2021-0136 (2021)

[16] S. Sharma, J. Chhokar, C. Curceanu, ... K. Dulski *et al.*, Estimating relationship between the Time Over Threshold and energy loss by photons in plastic scintillators used in the J-PET scanner. *EJNMMI Phys.* ***7***, 39 (2020)

[17] M. Pałka, P. Strzempek, G. Korcyl, ... K. Dulski *et al.*, Multichannel FPGA based MVT system for high precision time (20 ps RMS) and charge measurement. *JINST* ***12***, P08001 (2017)

[18] G. Korcyl, P. Białas, C. Curceanu, ... K. Dulski *et al.*, Evaluation of Single-Chip, Real-Time Tomographic Data Processing on FPGA - SoC Devices. *IEEE Trans. Med. Imaging* ***37***, 2526-2535 (2018)

[19] P. Moskal, D. Alfs, T. Bednarski *et al.*, Potential of the J-PET detector for studies of discrete symmetries in decays of positronium atom – a purely leptonic system. *Acta Phys. Pol. B* ***47***, 509-535 (2016)

[20] E. Czerwiński, K. Dulski, P. Białas *et al.*, Comissionning of the J-PET detector for studies of decays of positronium atoms. *Acta Phys. Pol. B* ***47***, 1961-1968 (2016)

[21] P. Moskal, N. Krawczyk, B.C. Hiesmayr, ... K. Dulski *et al.*, Feasibility studies of the polarization of photons beyond theoptical wavelength regime with the J-PET detector. *Eur. Phys. J. C* ***78***, 970-978 (2018)

[22] S.D. Bass, QED and fundamental symmetries in positronium decays. *Acta Phys. Pol. B* ***50***, 1319-1333 (2018)

[23] B.C. Hiesmayr and P. Moskal, Witnessing entanglement In Compton scattering processes Via Mutually Unbiased Bases. *Scientific Reports* ***9***, 8166 (2019)

[24] J. Raj, K. Dulski and E. Czerwiński, Towards time reversal symmetry test with o-Ps decays using the J-PET detector. *Acta Phys. Pol. B* ***51***, 149-152 (2020)

[25] S.J. Tao, Positronium Annihilation in Molecular Substances. *J. Chem. Phys.* ***56***, 5499-5510 (1972)

[26] M. Eldrup, D. Lightbody and J.N. Sherwood, The temperature dependence of positron lifetimes in solid pivalic acid. *Chem. Phys.* ***63***, 51-58 (1981)

[27] T. Goworek, K. Ciesielski, B. Jasińska and J. Wawryszczuk, Positronium Annihilation in Molecular Substances. *Chem. Phys.* ***230***, 305-315 (1998)

[28] D.W. Gidley, W.E. Frieze, T.L. Dull *et al.*, Positronium annihilation in mesoporous thin films. *Phys. Rev. B* ***60***, 5157-5160 (1999)

[29] B. Jasińska, M. Gorgol, M. Wiertel, ...K. Dulski *et al.*, Determination of the 3gamma Fraction from Positron Annihilation in Mesoporous Materials for Symmetry Violation Experiment with J-PET Scanner. *Acta. Phys. Pol. B* ***47***, 453-460 (2016)

[30] P. Moskal, E. Kubicz, G. Grudzień, ...K. Dulski *et al.*, Developing a Novel Positronium Biomarker for Cardiac Myxoma Imaging. https://www.biorxiv.org/content/10.1101/2021.08.05.455285v1

[31] C.D. Anderson, The apparent existence of easily deflectable positives. *Science New Series* ***76***, 238-239 (1932)

[32] R.M. Santilli, Does antimatter emit a new light? *Hyperfine Interact.* ***109***, 63-81 (1997)

[33] R.G. Greaves and C.M. Surko, Antimatter plasmas and antihydrogen. *Physics of Plasmas* ***4***, 1528-1543 (1997)

[34] S. Pascoli and J. Turner, Matter–antimatter symmetry violated. *Nature* ***580***, 323-324 (2020)

[35] B.S. Xie, Z.L. Li and S. Tang, Electron-positron pair production in ultrastrong laser fields. *Matter and Radiation at Extremes* ***2***, 225-242 (2017)

[36] M. Deutsch, Evidence for the Formation of Positronium in Gases. *Phys. Rev.* ***82***, 455-456 (1951)

[37] A. Ore, *Univ. Bergen Arbok. Naturvitenskapelig rekke* ***9*** , (1949)

[38] A.P. Mills Jr., Positron and Positronium Sources. *Meth. Exp. Phys.* ***29*** , 39-68 (1995)

[39] P. Dirac, Theory of Protons and Electrons. *Proceedings of the Royal Society of London A* ***126*** , 360-365 (1930)

[40] J.A. Wheeler, Polyelectron. *Ann. N.Y. Acad. Sci.* ***48***, 219–238 (1946)

[41] A. Ore and J.L. Powell, Three-photon annihilation of an electron–positron pair. *Phys. Rev.* ***75***, 1696–1699 (1949)

[42] A. Czarnecki, K. Melnikov and A. Yelkhovsky, a2 Corrections to Parapositronium Decay. *Phys. Rev. Lett.* ***83***, 1135-1138 (1999)

[43] S.C. Pevovar, M.H. Weber and K.G. Lynn, Ratio of positron annihilation into three photons versus two. *Phys. Stat. Sol.* ***4***, 3447–3450 (2007)

[44] S. Marder, V. W. Hughes, C. S. Wu, and W. Bennett, Effect of an Electric Field on Positronium Formation in Gases: Experimental. *Phys. Rev.* ***103***, 1258-1265 (1985)

[45] W. Teutsch and V.W. Hughes, Effect of an Electric Field on Positronium Formation in Gases: Experimental. *Phys. Rev.* ***103***, 1266-1281 (1956)

[46] O.E. Mogensen, Spur reaction model of positronium formation. *J. Chem. Phys.* ***60***, 998-1004 (1974)

[47] S.J. Tao, The Formation of Positronium in Molecular Substances. *Appl. Phys.* ***10***, 998-1004 (1976)

[48] V.M. Byakov and S.V. Stepanov, Common features in the formation of Ps, Mu, radiolytic hydrogen and solvated electrons in aqueous solutions. *J. Radioan. Nucl. Chem.* ***210***, 371-405 (1996)

[49] S.V. Stepanov and V.M. Byakov, Electric field effect on positronium formation in liquids. *J. Chem. Phys.* ***116***, 6178-6195 (2002)

[50] S.V. Stepanov, V.M. Byakov, D.S. Zvezhinskiy, G. Duplâtre, R.R. Nurmukhametov, and P.S. Stepanov, Positronium in a Liquid Phase: Formation, Bubble State and Chemical Reactions. *Adv. Phys. Chem.*, 431962 (2012)

[51] R.A. Ferrell, Long lifetime of positronium in liquid helium. *Phys. Rev.* ***108***, 167–168 (1957)

[52] R.L. Garwin, Thermalization of Positron in Metals. *Phys. Rev.* ***91***, 1571-1572 (1956)

[53] M.J. Puska and R.M. Nieminen, Theory of positrons in solids and on solid surfaces. *Rev. Mod. Phys.* ***66***, 841-897 (1994)

[54] A. Karbowski, K. Fedus and G. Karwasz, Positronium formation in molecular gases - from experiment to modeling. *Acta Phys. Pol. B* ***48***, 1593-1599 (2017)

[55] A. Karbowski, K. Fedus, K. Służewski, J. Bruzdowska and G. Karwasz, Positronium Formation in Organic Liquids. *Acta Phys. Pol. A* ***132***, 1466-1469 (2017)

[56] A. Bisi, G. Consolati, G. Gambarini and L. Zappa, Positronium-oxygen interaction in hexane. *Il Nuovo Cimento D* ***6***, 725-736 (1982)

[57] A. Dupasquier, G. Kögel and A. Somoza, Studies of light alloys by positron annihilation techniques. *Acta Materialia* ***52***, 4707-4726 (2004)

[58] X. Jiang, Y. Zhang, J. Jiang *et al.*, Characterization of Oxygen Vacancy Associates within Hydrogenated TiO2: A Positron Annihilation Study. *J. Phys. Chem. C* ***116***, 22619-22624 (2012)

[59] M.P. Petkov, M.H. Weber and K.G. Lynn, Probing capped and uncapped mesoporous low-dielectric constant films using positron annihilation lifetime spectroscopy. *Appl. Phys. Lett.* ***77***, 2470-2472 (2000)

[60] C.L. Wang, T. Hirade, F.H.J. Maurer, M. Eldrup and N.J. Pedersen, Free-volume distribution and positronium formation in amorphous polymers: Temperature and positron-irradiation-time dependence. *J. Chem. Phys.* ***108***, 4654-4661 (1998)

[61] P. Moskal, B. Jasińska, E.Ł. Stępień and S.D. Bass, Positronium in medicine and biology. *Nature Rev. Phys.* ***1***, 527-529 (2019)

[62] B. Jasińska, B. Zgardzińska, G. Chołubek ... K. Dulski *et al.*, Human tissues investigation using PALS Technique. *Acta Phys. Pol. B* ***48***, 1737-1747 (2017)

[63] H. Chen, J. Van Horn and Y. Ching Jean, Applications of positron annihilation spectroscopy to life science. *Defect and Diffusion Forum* ***331***, 275-293 (2012)

[64] E. Kubicz, B. Jasińska, B. Zgardzińska, *et al.*, Studies of unicellular micro-organisms Saccharomyces cerevisiae by means of positron annihilation lifetime spectroscopy. *Nukleonika* ***60***, 749-753 (2015)

[65] R. Suzuki, Y. Kobayashi, T. Mikado *et al.*, Slow Positron Pulsing System for Variable Energy Positron Lifetime Spectroscopy. *Jap. J. Appl. Phys.* ***30***, 532-534 (1991)

[66] C. Hugenschmidt, B. Lowe, J. Mayer *et al.*, Unprecedented intensity of a low-energy positron beam. *Nucl. Instr. and Meth. A* ***593***, 616-618 (2008)

[67] W. Hung, M. De Guzman, S. Huang *et al.*, Characterizing Free Volumes and Layer Structures in Asymmetric Thin-Film Polymeric Membranes in the Wet Condition Using the Variable Monoenergy Slow Positron Beam. *Macromolecules* ***43***, 6127–6134 (2010)

[68] S. De Benedetti, C.E. Cowan, W.R. Konneker and H. Primakoff, On the Angular Distribution of Two-Photon Annihilation Radiation. *Phys. Rev.* ***77***, 205-212 (1950)

[69] S. B. Dugdale, H. M. Fretwell, M. A. Alam *et al.*, Direct Observation and Calipering of the "Webbing" Fermi Surface of Yttrium. *Phys. Rev. Lett.* ***79***, 941-944 (1997)

[70] A. Biganeh, O. Kakuee, H. Rafi-Kheiri *et al.*, Positron Annihilation Lifetime and Doppler Broadening Spectroscopy of polymers. *Radi. Phys. Chem.* ***166***, 108461 (2020)

[71] T. Goworek, Comments on the relation: positronium lifetime – free volume size parameters of the Tao–Eldrup model. *Chem. Phys. Lett.* ***366***, 184-187 (2002)

[72] H. Nakanishi, Microscopic surface tension studied by positron annihilation *Int. Symp. on Positron Annihilation Studies of Fluids*, 292-298 (1988)

[73] T. Goworek, Positronium as a probe of small free volumes in crystals, polymers and porous media. *Annales Universitatis Mariae Curie-Sklodowska sectio AA – Chemia* ***69***, 1-110 (2014)

[74] A. Alavi, T.J. Werner, E.Ł. Stępień and P. Moskal, Unparalleled and revolutionary impact of PET imaging on research and day to day practice of medicine. *Bio-Algorithms and Med-Systems* ***17***, DOI:10.1515/bams-2021-0186 (2021)

[75] R.D. Badawi, H. Shi, P. Hu, *et al.*, First human imaging studies with the EXPLORER total-body PET scanner. *J. Nucl. Med.* ***60***, 299-303 (2019)

[76] J.S. Karp, V. Viswanath, M.J. Geagan, *et al.*, PennPET explorer: design and preliminary performance of a whole-body imager. *J. Nucl. Med.* ***61***, 136-143 (2020)

[77] P. Moskal, D. Kisielewska, C. Curceanu, ...K. Dulski *et al.*, Feasibility study of the positronium imaging with the J-PET tomograph. *Phys. Med. Biol.* ***64***, 055017 (2019)

[78] P. Moskal, D. Kisielewska, Z. Bura, ...K. Dulski *et al.*, Performance assessment of the 2gamma positronium imaging with the total-body PET scanners. *EJNMMI Phys.* ***7***, 44 (2020)

[79] P.V. Stepanov, F.A. Selim, S.V. Stepanov, *et al.*, Interaction of positronium with dissolved oxygen in liquids. *Phys. Chem. Chem. Phys. 22*, 5123-5131 (2020)

[80] K. Shibuya, H. Saito, F. Nishikido, *et al.*, Oxygen sensing ability of positronium atom for tumor hypoxia imaging. *Comm. Phys.*, 173 (2020)

[81] B. Jasińska, B. Zgardzińska, G. Chołubek, *et al.*, Human tissue investigations using PALS technique - free radicals influence. *Acta Phys. Pol. A* ***132***, 1556-1558 (2017)

[82] D. Kilburn, S. Townrow, V. Meunier, *et al.*, Organization and mobility of water in amorphous and crystalline trehalose. *Nat. Mater* ***5***, 632-635 (2006)

[83] Y.C. Jean, Y. Li, G. Liu, *et al.*, Applications of slow positrons to cancer research: search for selectivity of positron annihilation to skin cancer. *Appl. Surf. Sci.* ***252***, 3166-3171 (2006)

[84] Y. Jean, H. Chen, G. Liu, *et al.*, Life science research using positron annihilation spectroscopy: UV-irradiated mouse skin. *Radiat. Phys. Chem.* ***76***, 70-75 (2007)

[85] G. Liu, H. Chen, L. Chakka, *et al.*, Applications of positron annihilation to dermatology and skin cancer. *Phys. Status Solidi C* ***4***, 3912-3915 (2007)

[86] G. Liu, H. Chen, L. Chakka, *et al.*, Further search for selectivity of positron annihilation in the skin and cancerous systems. *Appl. Surf. Sci.* ***255***, 115-118 (2008)

[87] R.M. Yas, A.H. Al-Mshhdani, M.M. Elias, *et al.*, Detection of line shape parameters in normal and abnormal biological tissues. *Iraqi J. Phys.* ***10***, 77-82 (2012)

[88] E. Axpe, T. Lopez-Euba, A. Castellanos-Rubio, *et al.*, Detection of atomic scale changes in the free volume void size of three-dimensional colorectal cancer cell culture using positron annihilation lifetime spectroscopy. *PLoS One* ***9***, e83838 (2014)

[89] R. Pietrzak, S. Borbulak and R. Szatanik, Influence of neoplastic therapy on the investigated blood using positron annihilation lifetime spectroscopy. *Nukleonika* ***58***, 199-202 (2013)

[90] E. Kubicz, Potential for biomedical applications of positron annihilation lifetime spectroscopy (PALS). *AIP Conf. Proc.* ***2182***, 050004 (2019)

[91] Z. Bura, K. Dulski, E. Kubicz, *et al.*, Studies of the ortho-Positronium lifetime for cancer diagnostic. *Acta Phys. Pol. B* ***51***, 377-382 (2020)

[92] https://eljentechnology.com, Plastic scintillator EJ-230

[93] Ł. Kapłon, Technical Attenuation Length Measurement of Plastic Scintillator Strips for the Total-Body J-PET Scanner. *IEEE Trans. Nucl. Sci.* ***67***, 2286-2289 (2020)

[94] http://hamamatsu.com, Photomultiplier tube R9800s

[95] K. Dulski, C. Curceanu, E. Czerwiński *et al.*, Commissioning of the J-PET detector in view of the positron annihilation lifetime spectroscopy. *Hyperfine Interact.****239***, 40-45 (2018)

[96] K. Dulski, S.D. Bass, J. Chhokar *et al.*, The J-PET detector—a tool for precision studies of ortho-positronium decays. *Nucl. Instr. and Meth. A* ***1008***, 165452 (2021)

[97] M. Gorgol, B. Jasińska, M. Kosior, E. Stępień, P. Moskal, Construction of the Vacuum Chambers for J-PET Experiments with Positron Annihilation. *Acta Phys. Pol. B* ***51***, 293 (2020)

[98] https://www.sigmaaldrich.com, CAS Number 37380-42-0.

[99] W. Krzemień, A. Gajos A., K. Kacprzak *et al.*, J-PET Framework: Software platform for PET tomography data reconstruction and analysis. *SoftwareX* ***11***, 100487 (2020)

[100] R. Brun and F. Rademakers, ROOT — An object oriented data analysis framework. *Nucl. Instr. and Meth. A* ***389***, 81-86 (1997)

[101] D. Kisielewska, K. Dulski https://github.com/JPETTomography/J-PET-geant4

[102] K. Dulski, M. Silarski and P. Moskal, A method for time calibration of PET systems using fixed $\beta^+$ radioactive source. *Acta Phys. Pol. B* ***51***, 195-200 (2020)

[103] K. Dulski, P. Moskal, System i sposób kalibracji czasowej układu detekcyjnego tomografu ToF-PET, Polish patent number: PL434697

[104] G. Chrapak, L. Dick and L. Feuvrais, Location of the position of a particle trajectory in a scintillator. *Nucl. Instr. and Meth. A* ***15***, 485-488 (1962)

[105] Y. Shikaze, S. Orito, T. Mitsui *et al.*, Large-area scintillator hodoscope with 50 ps timing resolution onboard BESS. *Nucl. Instr. and Meth. A* ***455***, 596-606 (2000)

[106] V. Kouznetsov, A. Lapik, S. Churikova *et al.*, Large-area scintillator hodoscope with 50 ps timing resolution onboard BESS. *Nucl. Instr. and Meth. A* ***487***, 396-406 (2002)

[107] A. Gajos, D. Kamińska, E. Czerwiński, *et al.*, Trilateration-based reconstruction of ortho-positronium decays into three photons with the J-PET detector. *Nucl. Instr. and Meth. A* ***819***, 54-59 (2016)

[108] K. Dulski, B. Zgardzińska, P. Białas *et al.*, Analysis procedure of the positronium lifetime spectra for the J-PET detector. *Acta Phys. Pol. A* ***132***, 1637-1640 (2017)

[109] K. Dulski, PALS Avalanche — A New PAL Spectra Analysis Software. *Acta Phys. Pol. A* ***137***, 167-170 (2020)

[110] K. Dulski, Assembly and calibration of apparatus for Positron Annihilation Lifetime Spectroscopy, Master thesis, Defence year: 2016

[111] Particle Data Group Review, accessible in https://pdg.lbl.gov/2011/reviews/rpp2011-rev-cosmic-rays.pdf (July 2021)

[112] G.S. Adkins, Radiative corrections to positronium decay*. *Ann. Phys.* ***146***, 78-128 (1983)

[113] G.S. Adkins, R.N. Fell and J. Sapirstein, Two-loop correction to the orthopositronium decay rate. *Ann. Phys.* ***295***, 136-193 (2002)

[114] S. Asai, S. Orito and N. Shinohara, New measurement of the orthopositronium decay rate. *Phys. Lett. B* ***357***, 475-480 (1995)

[115] R.S. Vallery, P.W. Zitzewitz and D.W. Gidley, Resolution of the Orthopositronium-Lifetime Puzzle. *Phys. Rev. Lett.* ***90***, 203402 (2003)

[116] O. Jinnouchi, S. Asai and T. Kobayashi, Precision measurement of orthopositronium decay rate using $SiO_2$ powder. *Phys. Lett. B* ***572***, 117-126 (2003)

[117] Y. Kataoka, S. Asai, T. Kobayashi, First test of $O(\alpha^2)$ correction of the orthopositronium decay rate. *Phys. Lett. B* ***671***, 219-223 (2009)

[118] https://www.cabotcorp.com, CAS Number 102262-30-6

[119] A. Wieczorek, K. Dulski, S. Niedźwiecki *et al.*, Novel scintillating material 2-(4-styrylphenyl)benzoxazole for the fully digital and MRI compatible J-PET tomograph based on plastic scintillators. *PLoS ONE* ***12***, e0186728 (2017)

[120] C. Kallepitis, M.S. Bergholt, M.M. Mazo *et al.*, Quantitative volumetric Raman imaging of three dimensional cell cultures. *Nat. Comm.* ***8***, 14843 (2017)

[121] S. Sadamatsu, M. Tanaka, K. Higashida and S. Matsumura, Transmission electron microscopy of bulk specimens over 10 µm in thickness. *Ultramicroscopy* ***162*** 10-16 (2016)

[122] M. Madadi, A.C. Jones, C.H. Arns and M.A. Knackstedt, 3D Imaging and Simulation of Elastic Properties of Porous Materials. *IEEE: Comp. Sci. Eng.* ***11*** 65-73 (2009)

[123] M.H.N. Yio, M.J. Mac, H.S. Wong and N.R. Buenfeld, 3D imaging of cement-based materials at submicron resolution by combining laser scanning confocal microscopy with serial sectioning. *J. Micro.* ***258*** 151-169 (2015)

[124] L. Salvo, M. Suéry, A. Marmottant, N. Limodin and D. Bernard, 3D imaging in material science: Application of X-ray tomography. *Compt. Rendus Phys.* ***11*** 641-649 (2010)

[125] W.W. Moses and C.J. Thomson, Timing Calibration in PET Using a Time Alignment Probe. *IEEE Trans. Nucl. Sci.* ***53*** 2660-2665 (2006)

[126] G. Wang, X. Li, X. Niu, H. Du, K. Balakrishnan, H. Ye and K. Burr, PET Timing Performance Measurement Method Using NEMA NEC Phantom. *IEEE Trans. Nucl. Sci.* ***63*** 1335-1342 (2016)

[127] A.E. Perkins, M. Werner, A. Kuhn, S. Surti, G. Muehllehner and J.S. Karp, Time of flight coincidence timing calibration techniques using radioactive sources. *IEEE Nucl. Sci. Symp. Conf. Rec.* 2488-2491 (2005)

[128] M. Skurzok, M. Silarski, D. Alfs, ...K. Dulski *et al.*, Time Calibration of the J-PET Detector. *Acta Phys. Pol. A* ***132*** 1641-1643 (2017)

[129] M. Silarski, E. Czerwiński, T. Bednarski *et al.*, A novel method for calibration and monitoring of time synchronization of TOF-PET scanners by means of cosmic rays. *Bio-Algorithms and Med-Systems* ***10*** 19-25 (2014)

[130] https://web.archive.org/web/20121012090629/http://www.auger.org/cosmic_rays/faq.html